Engineering of Grain-Based Materials with Mechanical Agitation

Aram Bahmani

Department of Mechanical Engineering
McGill University
Montreal, Canada

August 2024

A dissertation submitted to McGill University in partial fulfillment of the requirements for the degree of Doctor of Philosophy

© 2024 Aram Bahmani

Table of Contents

Table of Contents	i
Abstract	iv
Résumé	vi
Acknowledgements	viii
Contribution to Original Knowledge	xi
Contribution of Authors	xiii
List of Figures	XV
List of Tables	XXV
List of Abbreviations	xxvi
CHAPTER 1 Introduction	1
1.1 Dissertation Organization	1
1.2 Dissertation Motivation and Challenges	3
1.3 Literature Survey	7
1.3.1 Architectured Materials	8
1.3.2 Intersection of Granular and Architectured Materials	10
1.3.3 Fabrication Methods for TIMs	15
1.3.4 Self-assembly	17
1.3.5 Computational Modeling	21
1.3.6 Mechanisms of Hemostasis, Fibrinolysis, and Wound Healing	24
1.3.7 Soft Cellular Inclusions within Clot-like Materials	28
1.4 Dissertation Objectives	32
CHAPTER 2 Materials and Methods	34
2.1 Fabrication and Synthesis	34
2.1.1 Polyhedral Blocks	35
2.1.2 Clots Laden with Cellular Inclusions	39
2.2 Setups and Configurations	41
2.2.1 Vibrating Platform for Hard Architectured Materials	41
2.2.2 Vibrating Platform for Clot-like Materials	43
2.2.3 In-vivo	46
2.2.4 Fibrinolysis	48

2.3	Mechanical Characterizations	49
2	3.1 Elastic and Fracture Toughness Properties	49
2	3.2 Rheological Properties	49
2.4	Cell Culture and Confocal Imaging	50
2.4	4.1 Fibroblast Cells	50
2.4	4.2 Blood Clots	51
2.5	Spatial Analysis	52
2.:	5.1 Vibration-mediated Cell Organization	52
2.:	5.2 Microstructure of Fibrin Networks	52
2.6	Simulations	55
2.0	6.1 Discrete Element Modeling	55
2.0	6.2 Finite Element Modeling	58
СНАРТЕ	R 3 Agitation-Driven Fabrication of Dense Architectured Panels	60
3.1	Experimental Assembly	61
3.2	Discrete Element Modeling	65
3.3	Bouncing of Individual Grains	66
3	3.1 Bouncing Model	66
3	3.2 Rotation Model	69
СНАРТЕ	R 4 Agitation-Induced Assembly of Topologically Interlocked Materials	70
4.1	Experimental Interlocking	71
4.2	Discrete Element Models.	77
4.2	2.1 Rotation Mechanism	79
СНАРТЕ	R 5 Agitation-Mediated Structure-Property Relation of Biopolymers Lader	n with Soft
Cellular I	nclusions	81
5.1	Agitation-mediated Mechanical Properties of Blood Clots	82
5.2	In-vivo Experiments	86
5.3	Extending to Clot-like Materials	88
5.4	Microstructure Characterization	90
5.5	Hybrid Element Modeling	102
СНАРТЕ	R 6 Discussions	107
6.1	Similarities and Differences between Hard and Soft Inclusions	107

Copyrig	ht and Licence Permissions	139
Bibliog	aphy	124
CHAPT	ER 7 Concluding Remarks	120
6.6	Discussion on Limitations and Scale-Up Challenges	118
6.5	Clot-like Materials	114
6.4	Assembly of Polyhedral Blocks	111
6.3	Assembly Phase Diagram Assessments with Individual Block Mechanics	109
6.2	Predicting Many-cube Transition Lines with Single-grain Models	108

Abstract

Architectured materials represent an emerging class of materials characterized by unconventional structural behavior, often surpassing the performance of traditional materials. Fully dense architectured materials consist of polyhedral blocks interconnected by weaker interfaces, posing challenges in their assembly into functional materials and structures, thus hindering broader applications. These materials, including dense architectured and granular systems, offer mechanical responses not typically achievable in monolithic materials. By adjusting the geometry, packing arrangement, and jamming states of blocks, the performance of these materials can be tailored and enhanced. Despite their potential, the widespread use of architectured materials remains limited due to fabrication challenges and scalability issues. Mechanical agitation-induced assembly at the macro-scale presents a promising yet unused fabrication pathway. However, the understanding of the assembly process and mechanisms is still incomplete. Optimizing agitation-driven assembly can provide insights into the physics and mechanics of complex granular and active media.

We investigated vibration-induced assembly to rapidly fabricate and assemble granular grains into crystalline structures. By exploring vibration-driven assembly methods, we achieved periodic arrangements of convex polyhedral blocks into large, free-standing topologically interlocked panels. Our study delved into the physics and mechanics involved in the crystallization and interlocking of far-from-equilibrium granular systems, considering different grain geometries and basic medial section shapes. Combining experiments with discrete element modeling, we analyzed how vibration influences the states of polyhedral blocks—static, assembly, and fluttering—and their phase transitions. Our findings elucidated the role of normalized relative acceleration, bouncing, and rotation mechanisms in packing and phase transitions. Rotation predominantly influences packing, while bouncing affects both packing and phase transitions. Chaotic phase transitions facilitate self-crystallization and interlocking processes. Geometries with lower out-of-plane moments of inertia exhibit broader ranges of interlocking under varied vibration conditions. This study provides insights into the geometry-dependency, re-fragmentation, re-crystallization, and re-configurability of athermal out-of-equilibrium material systems.

Transitioning from hard and stiff active granular media to soft active matter, we explored clot-like materials resembling soft cellular inclusions within a biopolymeric matrix. These

materials, mimicking blood clots, present unique challenges for engineering and medicine due to their relatively unexplored formation and structure-property relations. Mechanical agitation emerges as a promising strategy for modulating clot-like material properties without inducing cytotoxicity or other side effects associated with chemical alterations. Through tailored agitation platforms and blood clots as a model system, we demonstrate the effectiveness of mechanical agitation in modulating material properties and mechanical performance, including stiffness, fracture toughness, lysis, and active contraction. Experimental and simulation results highlight the role of agitation-mediated cellular organization in influencing both microscopic structure and macroscopic mechanical responses within fibrin networks. Our approach offers new avenues for engineering living materials, with potential applications in biofabrication, tissue engineering, and the treatment of clot-related diseases.

Résumé

Les matériaux architecturés sont une classe émergente de matériaux avec un comportement structurel non conventionnel, souvent supérieur aux matériaux traditionnels. Les matériaux architecturés denses, composés de blocs polyédriques reliés par des interfaces plus faibles, posent des défis d'assemblage en structures fonctionnelles, limitant leurs applications. Ces matériaux, y compris les systèmes architecturés denses et granulaires, offrent des réponses mécaniques inaccessibles aux matériaux monolithiques. En ajustant la géométrie, l'agencement et les états de blocage des blocs, la performance de ces matériaux peut être optimisée. Malgré leur potentiel, l'utilisation des matériaux architecturés reste limitée par des défis de fabrication et d'échelle. L'assemblage par agitation mécanique à grande échelle est une voie prometteuse mais encore inexploitée. Cependant, la compréhension des processus et mécanismes d'assemblage reste incomplète. L'optimisation de l'assemblage par agitation pourrait fournir des informations précieuses sur la physique et la mécanique des médias granulaires et actifs complexes.

Nous avons étudié l'assemblage par vibration pour fabriquer rapidement des grains granulaires en structures cristallines. En explorant les méthodes d'assemblage par vibration, nous avons obtenu des arrangements périodiques de blocs polyédriques convexes en grands panneaux autoportants topologiquement verrouillés. Notre étude a exploré la physique et la mécanique de la cristallisation et du verrouillage des systèmes granulaires loin de l'équilibre, en considérant différentes géométries de grains et formes de sections médiales. En combinant expériences et modélisation par éléments discrets, nous avons analysé comment la vibration influence les états des blocs polyédriques—statique, assemblage et flottement—et leurs transitions de phase. Nos résultats ont éclairé le rôle de l'accélération relative normalisée, des mécanismes de rebond et de rotation dans le compactage et les transitions de phase. La rotation influence principalement le compactage, tandis que le rebond affecte à la fois le compactage et les transitions de phase. Les transitions de phase chaotiques facilitent les processus d'auto-cristallisation et de verrouillage. Les géométries avec des moments d'inertie hors du plan plus faibles présentent des plages plus larges de verrouillage sous diverses conditions de vibration. Cette étude fournit des informations sur la dépendance à la géométrie, la re-fragmentation, la re-cristallisation et la re-configurabilité des systèmes matériels athermiques hors d'équilibre.

En passant des médias granulaires actifs durs et rigides à la matière active douce, nous avons exploré des matériaux de type caillot ressemblant à des inclusions cellulaires molles dans une matrice biopolymérique. Ces matériaux, imitant les caillots sanguins, posent des défis uniques pour l'ingénierie et la médecine en raison de la formation et des relations structure-propriété peu explorées. L'agitation mécanique émerge comme une stratégie prometteuse pour moduler les propriétés des matériaux de type caillot sans induire de cytotoxicité ni d'autres effets secondaires associés aux altérations chimiques. Grâce à des plateformes d'agitation adaptées et en utilisant les caillots sanguins comme système modèle, nous démontrons l'efficacité de l'agitation mécanique pour moduler les propriétés matérielles et la performance mécanique, incluant la rigidité, la ténacité à la fracture, la lyse et la contraction active. Les résultats expérimentaux et de simulation mettent en évidence le rôle de l'organisation cellulaire médiée par agitation dans l'influence de la structure microscopique et des réponses mécaniques macroscopiques au sein des réseaux de fibrine. Notre approche offre de nouvelles avenues pour l'ingénierie des matériaux vivants, avec des applications en biofabrication, ingénierie tissulaire et traitement des maladies liées aux caillots.

Acknowledgements

The completion of this dissertation and the research it represents would not have been possible without the consistent support I received from my mentors, friends, and family. Although the Covid-19 pandemic may now seem like a distant memory for many, this work serves as a reminder of its impact and challenges.

I am deeply grateful to my supervisors, Prof. Jianyu Li and Prof. Francois Barthelat, for their invaluable support, guidance, and mentorship throughout this journey. In addition to their exceptional knowledge, they have imparted numerous life lessons that have enriched both my academic and personal growth. It has been an honor to work under their supervision, and I take immense pride in the opportunity.

Prof. Li once shared with me in his office, "In the pursuit of success, the debate often arises: which is more crucial, hard work or luck? Without diligent effort, luck remains inaccessible. Only through hard work can one elevate themselves to a level where fortuitous opportunities can manifest."

Similarly, during one of our individual meetings, Prof. Barthelat offered valuable advice, saying, "Stay focused, avoid comparing your work with others, and remain true to your identity as a mechanical engineer."

Their words serve as a constant reminder to uphold integrity and authenticity in my work. I am deeply indebted to Prof. Li and Prof. Barthelat for their consistent support and wisdom throughout this academic endeavor.

I am honored to begin by acknowledging the alumni of McGill's Laboratory for Advanced Materials & Bioinspiration: Dr. Ali Shafiei, Dr. Ahmed Dalaq, Dr. Zhen Yin, Dr. J William Pro, Dr. Najmul Abid, Dr. Florent Hannard, Dr. Siyu Liu, and Dr. Mohammad Mirkhalaf.

I am also honored to acknowledge the members and alumni of McGill's Lab of Biomaterials Engineering: Dr. Guangyu Bao, Dr. Shiyu Liu, Dr. Xuan Li, Dr. Ran Huo, Dr. Zhen Yang, Alex Nottegar, Christopher Chung, Evan Johnston, Portia Rayner, Dr. Farshid Ghezelbash, and Dr. Baolin Huang.

These exceptional individuals have been not only great friends, mentors, and colleagues but also invaluable sources of learning. Their guidance and support have profoundly influenced my journey, although this dissertation can only offer a glimpse of the lessons I have learned from them.

I also appreciate the generous support from various funding agencies, including Natural Sciences and Engineering Research Council (NSERC), Fonds de recherche du Québec - Nature et technologies (FRQNT), and McGill Faculty of Engineering.

I also acknowledge the support from the Centre de Recherche sur les Systèmes Polymères et Composites à Haute Performance. Image acquisition (Confocal, Fluorescence and Brightfield) and analysis (Columbus, Harmony, Imaris, Volocity) were performed with the McGill University Imaging and Molecular Biology Platform (IMBP) equipment and/or services.

Finally, I would like to express my deepest gratitude to my family for their unconditional support and love. To mom, my gratitude is beyond words. Thank you so much for supporting me all these years and always believing in me.

To all those who, with unwavering determination and relentless effort, dare to pursue the seemingly unattainable.
To Mitra, my beautiful and brilliant wife, whose support, encouragement, and belief in me have been the cornerstone of this journey.
Lastly, to Covid-19, which failed to disrupt our steadfast commitment to our research.

Contribution to Original Knowledge

The body of work presented in this dissertation contributed to the advancement of original knowledge to the fields of granular materials, architectured materials, and biopolymers laden with soft cellular inclusions materials. The outlined original contributions of this research are as follows: (i) An advanced self-assembly fabrication system using mechanical vibration for architectured and block-based materials; (ii) an efficient procedure to study the physics and mechanics underlying the shape-dependency of athermal out-of-equilibrium material systems systems across different length scales; (iii) a unique agitation-mediated system to modulate structure-property relation of clot-like materials; (iv) a new approach to demonstrating that the principles and underlying mechanisms of stiff grains and soft cellular inclusions are universal within different media under external mechanical stimuli; (v) an innovative discrete element model to study vibration-induced interlocking of polyhedra blocks; (vi) an innovative hybrid finite elements model to simulate clot-like materials.

Each one of these contributions is briefly summarized in the following:

- (i) Development of a novel self-assembly fabrication system using mechanical vibration for architectured and block-based materials. Polyhedral convex blocks can be crystalized into free-standing topologically interlocked materials using a combination of mechanical vibration and gravity.
- (ii) Proposing of an efficient procedure for studying the physics and mechanics underlying the shape-dependency of athermal, out-of-equilibrium material systems across various length scales. The effect of vibration amplitudes and frequencies on the crystallization and phase transition of different granular block geometry or shapes can be determined. This process can be characterized by varying amplitudes, frequencies, or acceleration of the agitating system. This protocol assesses the underlying mechanisms including blocks bouncing and rotation, both individually and with their neighboring blocks, extending beyond their exclusion volume to find positions of minimal energy.
- (iii) Establishment of a novel agitation-mediated system to modulate the structure-property relation of clot-like materials. The micro-scale mechanical properties of clots can be tuned through agitation-mediated organization of different soft cellular inclusions including red blood cells,

fibroblast cells and microgels within a natural fibrous biopolymer such as poor-platelet-plasma during clotting.

- (iv) Examination of the effects of external mechanical stimuli on the assembly of various granular materials with different mechanical properties, including soft cellular inclusions and stiff grains, across different length scales, such as micrometric and millimetric, within various fluidic media, including air and plasma. There exist strong universal links between the principles and underlying mechanisms governing stiff grains and soft cellular inclusions within different media under external mechanical stimuli.
- (v) Creation of an innovative discrete element model for duplicating the vibration-induced assembly process of polyhedral convex blocks and capturing the crystallization and phase transitions of granular materials using the single-block mechanisms models.
- (vi) Implementation of an innovative hybrid finite elements model for simulating clot-like materials to study the effect of agitation-mediated cell organizations and geometrical features of fibrin polymeric network such as number of connectivity, fibrin diameter and fibrin length.

The contributions have been consolidated in the preparation or publication of the following peer-reviewed journal articles:

- 1. **Bahmani, A.**, Pro, J. W., Hannard, F., & Barthelat, F.* (2022). Vibration-driven fabrication of dense architectured panels. *Matter*, *5*(3), 899-910.
- 2. **Bahmani**, A., Pro, J. W., & Barthelat, F.* (2022). Vibration-induced assembly of topologically interlocked materials. *Applied Materials Today*, *29*, 101601.
- 3. **Bahmani, A.**, Liu, S., Johnston, E., Wan, W., Nottegar, A., Huo, R., Jiang, S., Li, J.* (2024). Engineering clot-like materials with mechanical agitation. (Under review)

In addition, the author has contributed to the following work during his Ph.D. Unpublished works are not included here.

- Peer-reviewed journal articles
 - 1. Liu, S.†, **Bahmani, A.**†, Ghezelbash, F., & Li, J.* (2024). Fibrin Clot Fracture under Cyclic Fatigue and Variable Rate Loading. *Acta Biomaterialia*. (Co-first author †)

2. Liu, S., **Bahmani**, A., Sugerman, G.P., Yang, Z., Rausch, M., Ghezelbash, F., & Li, J.* (2024). Adhesive and Cohesive Fracture of Blood Clots: Experiments and Modeling. (Under review)

Contributions: Conceptualization, Methodology, Software, Validation, Formal analysis, Investigation, Data curation, Writing – original draft, Writing – review & editing.

Contribution of Authors

The successful completion of this dissertation could not have been realized without the collaborative research efforts from my Ph.D. advisor, colleagues, and collaborators. This section listed the specific contributions.

The author of this dissertation is responsible for conceptualization of the material systems and fabrication techniques, synthesis of materials, design and execution of experimentation, programming and modeling of computational simulations, theoretical modeling, image analysis, data analysis and visualization, as well as writing, editing, and reviewing of all the chapters in this dissertation. Note that my Ph.D. advisors, Prof. Jianyu Li and Prof. Francois Barthelat offered invaluable insights that contributed to the conception of the materials and the design of the experiments and simulations as well as deciphering both experimental and computational results throughout this dissertation. Other coauthors' contributions are described below.

In Chapters 2, 3, and 4, Dr. J. William Pro played a pivotal role in conceptualizing and laying the foundation for our discrete element simulations. This included tasks such as running and debugging the C++ Granoo code solver, reprogramming and customizing existing plug-in codes within Granoo, and developing basic codes in Matlab to generate input files for Granoo. Additionally, Dr. Pro contributed to the extraction of computational results and the execution of our codes and programs on Linux platforms. Dr. Florent Hannard made significant contributions to conceptualizing and establishing the foundation for programming image analysis, object tracking, and correlation codes in Matlab. Additionally, Dr. Hannard played an important role in our experimental image analysis measurements conducted in Matlab.

In Chapters 2 and 5, Dr. Shiyu Liu played a substantial role in the conceptualization of the material system and its synthesis, as well as in designing and implementing experiments. Dr. Liu was also instrumental in analyzing experimental data. Furthermore, Dr. Liu contributed significantly to all experiments pertaining to clot-like materials, which included mechanical agitation experiments, in-vitro and in-vivo experiments, mechanical testing, and the extraction of experimental data. Additionally, Dr. Liu was involved in confocal imaging of these material systems and extracting data from the obtained confocal images. Evan Johnston and Weiyi Wan played vital roles in conducting in-vitro cell culture experiments and performing confocal imaging of the material systems. They were also responsible for extracting data from the obtained confocal images. Additionally, Evan Johnston made contributions to in-vivo experiments, further enhancing the scope of the research conducted in these chapters. Alexander Nottegar contributed to preparing the whole blood fluorescently labelled by decorating the red blood cells surface with a fluorescent probe using a click reaction. Dr. Ran Huo contributed to synthesizing and preparing microgels experiments. Shuaibing Jiang also contributed to in-vivo experiments.

List of Figures

Figure 1. 1. Different biological materials composed of the high volume fraction of stiff and hard
blocks interlocked together within the low volume fraction of weak and soft interfaces. (A) The
nacreous layer of mollusc shell ^[28] (Reproduced with permission, Copyright 2011, Springer Nature
BV); (B) tooth enamel ^{29]} (Reproduced with permission, Copyright 2001, Elsevier); (C) the spicules
of glass sponge skeleton ^[30] (Reproduced with permission, Copyright 2005, AAAS). The dashed
red line illustrates the border of blocks. (D) The turtle shell skeleton comprises multiple bone plates
interconnected by a network of interlocked interfaces, with soft tissue integrated between them ^[31]
(Reproduced with permission, Copyright 2021, Elsevier)
Figure 1. 2. Typical force-displacement curves for a brittle monolithic material, a ductile material,
and their longitudinal, transverse, and architectured compositions ^[35] (Reproduced with permission
Copyright 2018, Elsevier)
Figure 1. 3. Comprehensive depiction of the 15 architectured topologically interlocked materials
panel designs: Each group presents the geometric configuration of the individual block alongside
an assembly schematic and visual representations of panels constructed from CaSO4 blocks. The
designs include: (A) truncated tetrahedra with a square medial section base; (B) truncated
octahedra featuring a hexagonal medial section base; and (C) dodecahedra[2] (Reproduced with
permission, Copyright 2018, National Academy of Sciences).
Figure 1. 4. Three-dimensional granular crystals: (A) Individual grains—spherical, rhombic
dodecahedral, and truncated octahedral—in millimeter scales with uniform volumes. These grains
possess the potential to crystallize into close-packed spheres or fully dense crystals. The enclosing
box served as a crystallization template, resulting in two distinct crystallographic orientations ^[39] .
(Reproduced with permission, Copyright 2022, National Academy of Sciences)
Figure 1. 5. Various proposed fabrication methods for topologically interlocked materials. (A)
Pick-and-place method employing human hand ^[33] (Reproduced with permission, Copyright 2019,
Elsevier); (B) Parallel method utilizing internal wires ^[4] ; (C) Laser engraving method ^[79] ; (D, E)
Magnetic-based self-assembly method ^[4] ; (F) 3D printing method ^[4] (Reproduced with permission,
Copyright 2016, American Society of Mechanical Engineers ASME); (G) Pick-and-place method
employing a robot ^[4] (Reproduced with permission, Copyright 2010, Emerald Publishing Limited).
16

rigure 1. 6. A general nowchart mustrating the fabrication process of engineering objects across
varying length scales, ranging from nano- to kilometer-level dimensions. The figure highlights the
potential applicability of self-assembly as an alternative to conventional fabrication techniques $[800]$
83]
Figure 1. 7. Systems comprising 2048 polyhedra assembled from a disordered fluid state. Each
subfigure includes several elements: a snapshot of the simulation box (left), a bond-order diagram
for nearest neighbors (inset), the shape and ID of the polyhedron (top right), a small group of
particles or a diffraction pattern (middle right), and crystallographic characterization details such
as name or atomic prototype, Pearson symbol, and Strukturbericht designation (bottom right). The
snapshots illustrate various crystal structures (A-D), plastic crystals (E-I), and liquid crystals (J-
L). Different colors highlight specific features in the simulation snapshots, such as low index
planes (A-C, E, F), tiling descriptions consisting of squares and triangles (D, G-I), and structural
features (K, L) ^[9] (Reproduced with permission, Copyright 2012, AAAS)
Figure 1. 8. The effect of the shape, topography, and topology of non-spherical particles is
demonstrated to exert control over their packing and assembly through directional entropic forces.
These forces lead to the alignment of particle faces that share similarities in one of these
characteristics, resulting in parallel orientation. This phenomenon underscores the significant
influence of directional entropic forces in guiding the organization of non-spherical particles [10]
(Reproduced with permission, Copyright 2014, National Academy of Sciences)
Figure 1. 9. The packing configurations of 250 particles of six different shapes within a cylindrical
container using discrete element modeling (DEM) for (A) spheres, (B) cylinders, (C) cubes, (D)
tetrahedra, (E) 2D cross and (F) 3D cross ^[125] (Reproduced with permission, Copyright 2018,
Springer Nature)
Figure 1. 10. Schematic representation illustrating the mechanisms of bleeding, primary and
secondary hemostasis, and coagulation cascades
Figure 1. 11. Schematic representation illustrating (A) clot lysis process and (B) rebleeding due
to clot rupture
Figure 1. 12. Schematic representation illustrating the phases of wound healing ^[11, 12] (Reproduced
with permission, Copyright 2021, Springer Nature)
Figure 1. 13. Blood clot contraction and its analogy with active elastic solid behavior. (A)
Progression from initiation of blood clot contraction to linear contraction phase and final

mechanical stabilization. (B) Sequential steps involving fibrin receptor activation, activated
platelet binding, spreading, deformation, and contraction, leading to fibrin collapse. (C) Analogy
between the blood clot contraction process and the behavior of active elastic solid matter 29
Figure 1. 14. Schematic of possible microstructures of clot-like materials under external
mechanical agitations and experimental configurations. (A) Soft inclusions (cells) within
biopolymeric medium; (B) inclusions clustering under low energy vibrations within biopolymeric
medium; (C) non-uniformly dispersed inclusions under high energy vibrations within
biopolymeric medium; (D) fixing the position of clustered inclusions due to clotting under low
energy vibration; (E) fixing the position of randomly dispersed inclusions due to clotting under
high energy vibration; (F) large porosities within biopolymeric network due to the inclusions
clusters; G) homogenous porosities within biopolymeric network due to inclusion random
dispersion. 32
Figure 2. 1. Overview of four blocks categorized based on their medial section (A) square-based
tiling; (B) hexagon-based tiling: For each category, the tessellation from the basic prism geometry
to the truncated version; (C) the crystal and/or interlocked conditions for each geometry; (D) the
to the truncated version, (C) the crystal and/or interlocked conditions for each geometry, (D) the
limited geometries for vibration-driven assembly generated by increasing α in each medial section.
. , , , , , , , , , , , , , , , , , , ,
limited geometries for vibration-driven assembly generated by increasing α in each medial section.
limited geometries for vibration-driven assembly generated by increasing α in each medial section.
limited geometries for vibration-driven assembly generated by increasing α in each medial section. 37 Figure 2. 2. Replica casting technique used for producing calcium sulfate polyhedral blocks 39
limited geometries for vibration-driven assembly generated by increasing α in each medial section. 37 Figure 2. 2. Replica casting technique used for producing calcium sulfate polyhedral blocks 39 Figure 2. 3. Obtaining poor-platelet plasma (PPP) from whole blood clot (WB). Platelet rich
limited geometries for vibration-driven assembly generated by increasing α in each medial section. 37 Figure 2. 2. Replica casting technique used for producing calcium sulfate polyhedral blocks 39 Figure 2. 3. Obtaining poor-platelet plasma (PPP) from whole blood clot (WB). Platelet rich plasma (PRP) first is separated from red blood cells (RBC) and then PPP is separated from platelets
limited geometries for vibration-driven assembly generated by increasing α in each medial section. 37 Figure 2. 2. Replica casting technique used for producing calcium sulfate polyhedral blocks 39 Figure 2. 3. Obtaining poor-platelet plasma (PPP) from whole blood clot (WB). Platelet rich plasma (PRP) first is separated from red blood cells (RBC) and then PPP is separated from platelets (PLT). 40
limited geometries for vibration-driven assembly generated by increasing α in each medial section. 37 Figure 2. 2. Replica casting technique used for producing calcium sulfate polyhedral blocks 39 Figure 2. 3. Obtaining poor-platelet plasma (PPP) from whole blood clot (WB). Platelet rich plasma (PRP) first is separated from red blood cells (RBC) and then PPP is separated from platelets (PLT). 40 Figure 2. 4. Synthetized microgels under microscope; the scale bar is 50 μm
limited geometries for vibration-driven assembly generated by increasing α in each medial section. 37 Figure 2. 2. Replica casting technique used for producing calcium sulfate polyhedral blocks 39 Figure 2. 3. Obtaining poor-platelet plasma (PPP) from whole blood clot (WB). Platelet rich plasma (PRP) first is separated from red blood cells (RBC) and then PPP is separated from platelets (PLT). 40 Figure 2. 4. Synthetized microgels under microscope; the scale bar is 50 μm
limited geometries for vibration-driven assembly generated by increasing α in each medial section. 37 Figure 2. 2. Replica casting technique used for producing calcium sulfate polyhedral blocks 39 Figure 2. 3. Obtaining poor-platelet plasma (PPP) from whole blood clot (WB). Platelet rich plasma (PRP) first is separated from red blood cells (RBC) and then PPP is separated from platelets (PLT). 40 Figure 2. 4. Synthetized microgels under microscope; the scale bar is 50 μm. 41 Figure 2. 5. (A) Schematic of the vibration-driven assembly process integrated with a high-speed camera and laser vibrometer. (B) Polyhedral blocks are randomly dropped on the tilted assembly
limited geometries for vibration-driven assembly generated by increasing α in each medial section. 37 Figure 2. 2. Replica casting technique used for producing calcium sulfate polyhedral blocks 39 Figure 2. 3. Obtaining poor-platelet plasma (PPP) from whole blood clot (WB). Platelet rich plasma (PRP) first is separated from red blood cells (RBC) and then PPP is separated from platelets (PLT). 40 Figure 2. 4. Synthetized microgels under microscope; the scale bar is 50 μm. 41 Figure 2. 5. (A) Schematic of the vibration-driven assembly process integrated with a high-speed camera and laser vibrometer. (B) Polyhedral blocks are randomly dropped on the tilted assembly platform with block-like walls (template) while it is vibrating. (C) Crystalline (interlocked)
limited geometries for vibration-driven assembly generated by increasing α in each medial section. 37 Figure 2. 2. Replica casting technique used for producing calcium sulfate polyhedral blocks 39 Figure 2. 3. Obtaining poor-platelet plasma (PPP) from whole blood clot (WB). Platelet rich plasma (PRP) first is separated from red blood cells (RBC) and then PPP is separated from platelets (PLT). 40 Figure 2. 4. Synthetized microgels under microscope; the scale bar is 50 μm. 41 Figure 2. 5. (A) Schematic of the vibration-driven assembly process integrated with a high-speed camera and laser vibrometer. (B) Polyhedral blocks are randomly dropped on the tilted assembly platform with block-like walls (template) while it is vibrating. (C) Crystalline (interlocked) packing at steady-state condition measured by image analysis through overlaid bounding contour.
limited geometries for vibration-driven assembly generated by increasing α in each medial section. 37 Figure 2. 2. Replica casting technique used for producing calcium sulfate polyhedral blocks 39 Figure 2. 3. Obtaining poor-platelet plasma (PPP) from whole blood clot (WB). Platelet rich plasma (PRP) first is separated from red blood cells (RBC) and then PPP is separated from platelets (PLT). 40 Figure 2. 4. Synthetized microgels under microscope; the scale bar is 50 μm. 41 Figure 2. 5. (A) Schematic of the vibration-driven assembly process integrated with a high-speed camera and laser vibrometer. (B) Polyhedral blocks are randomly dropped on the tilted assembly platform with block-like walls (template) while it is vibrating. (C) Crystalline (interlocked) packing at steady-state condition measured by image analysis through overlaid bounding contour. 43

Figure 2. 7. Pure shear specimen within sonication bath to generated blood clots
Figure 2. 8. Demonstration of agitation-mediated clotting with a rodent liver bleeding model in
vivo. The agitation is applied with a customized in vivo agitating platform (A) and a cup-like
biopsy tube (B). A volumetric injury is made with a biopsy punch (C) and receives agitation on
site (D). The resulting clots (E) are tested with a rheometer (F)
Figure 2. 9. Blood clots fibrinolysis test using a transwell. 48
Figure 2. 10. Actual fibrin network confocal images of native and agitation-generated blood clots
with their 3D reconstruction morphometric quantification. (A-C) Actual fibrin network confocal
images for blood clots with high (agitation-enhanced), native, and low (agitation-degraded). (D-F)
3D reconstructed geometries of fibrin network from their confocal images for blood clots with
high (agitation-enhanced), native, and low (agitation-degraded)
Figure 2. 11. Coefficients of friction tests using the ASTM D1894 standard for calcium sulfate
(CaCo4) on either the same calcium sulfate (CaSO4) or polymethyl methacrylate (PMMA)
material 56
Figure 2. 12. Force-displacment curves in the ASTM D1894 standard tests and obtained frinction
coefficients for calcium sulfate (CaCO4) on either the same calcium sulfate (CaSO4) or
polymethyl methacrylate (PMMA) material
Figure 2. 13. Schematic of an individual sphere bouncing on a vibrating rigid platform 57
Figure 2. 14. Schematics of the single-block DEM models rotating due to the vibration of the tilted
rigid platform. 58
Figure 2. 15. Hybrid element computational models—geometry generation, verification and
validation, and results. (A) non-uniformly dispersed RBCs within a representative volume element
(RVE); (B) Clustered (agglomerated) RBCs beside non-uniformly distributed RBCs within an
RVE; (C) RBC model includes RBCs and connected linkage networks
Figure 3. 1. Example of results obtained on 9 cubes dropped on a vibrating platform (A=10 μm
and f=600 Hz). (A) Trajectories of individual cubes by video recording and tracking the trajectory;
(B) packed position of each cube; (C) instantaneous and average (filled color markers) speed of
each cube; (D) evolution of packing factor versus duration of the vibrations
Figure 3. 2. Experimental phase diagram showing the different states of the cubes as function of
dimensionless frequency and dimensionless amplitude. This man show three main regimes: static
THE TRANSPORM AS LICENSELLY AND THE CONTROLLEY ADDITIONS. THIS HISD SHOW THERE HAVE TRAINED AND THE

packing (contoured region showing final packing factor) and fluttering. The two green lines show
the predictions from fitted relative acceleration models
Figure 3. 3. The self- crystallization and/or assembly process of hard cubes into dense free-
standing monolayer as a large piece material and/or structure
Figure 3. 4. (A) DEM phase diagram showing the different states of the cubes as function of
dimensionless frequency and dimensionless amplitude. This map show three main regimes: static,
packing (contoured region showing final packing factor) and fluttering. The two green lines show
the predictions from fitted relative acceleration models; (B) comparisons between experimental
and DEM assembly maps; the contoured region shows the percent error between experimentally
measured packing factor and packing factor predicted from DEM simulation
Figure 3. 5. Bouncing of single spherical grain as function of different vibration parameters. (A)
Schematic of an individual sphere bouncing on a vibrating rigid platform; (B-D) predictions from
the DEM model under various regimes; (E and F) DEM-predicted average bounce height and
bounce duration for the sphere as function of amplitude and frequency with fitted 3D surfaces; (G
and H): Bounce height and bounce duration as function of Γ , together with curve fit
Figure 3. 6. (A) Schematic of the single-cube DEM model rotating due to the vibration of the rigid
platform; θ is the initial cube rotation angle; (B) cube rotation map as function of dimensionless
relative acceleration and its initial rotation angle. The rotation map shows the three main regimes:
static, rotating, and fluttering regimes
Figure 4. 1. Experimental assembly phase diagrams demonstrating the various states of the blocks
based on normalized vibration amplitude and frequency (A) square prism; (B) truncated
tetrahedron; (C) hexagonal prism; (D) octahedron. These assembly diagrams indicate three main
regimes: static, assembly (contoured region representing normalized steady-state packing factor
quantified by the colorbar) and fluttering, as well as two phase transitions: static-assembly and
assembly-fluttering. The two dash lines exhibit the predictions of fitted critical relative
acceleration criterion normalized by gravitational acceleration. For each geometry, the snapshots
show the blocks in different regimes: fluttering, high and low packing factor, and static regime.
Figure 4. 2. Comparisons between experimental assembly phase diagrams for two different

Figure 4. 3. The self-interlocking and/or crystallization process of (A) square prism, (B) truncated
tetraheron, (C) hexagon prism, and (D) octahedron blocks into dense free-standing TIM
monolayer as a large piece material and/or structure
Figure 4. 4. DEM-generated phase diagrams indicating the various states of the blocks based on
normalized vibration amplitude and frequency (A) square prism; (B) truncated tetrahedron; (C)
hexagonal prism; (D) octahedron. These assembly phase diagrams show three main regimes: static,
assembly and fluttering. as well as two phase transitions: static-assembly and assembly-fluttering.
The contours quantified by the colorbar represent the variation of the steady-state normalized
average packing factor, which was measured by the bounding contour the same as experiments.
The two dash lines exhibit the predictions of fitted critical relative acceleration criterion
normalized by gravitational acceleration. For each geometry, the snapshots show the blocks in
different regimes: fluttering, high and low packing factor, and static regime
Figure 4. 5. Schematics of the single-block DEM models rotating due to the vibration of the tilted
rigid platform. Radial phase diagrams computed by these single-block DEM models as function
of dimensionless critical relative acceleration (Γ) and initial misaligned angle (θ) for each block.
(A) Square prism; (B) truncated tetrahedron; (C) hexagonal prism; (D) octahedron 80
Figure 4. 6. The constant values of the rotation model for each block geometry and phase
transitions

released from the gelling mold. Data are shown as means \pm SD for n=3 independent experiments.
Figure 5. 3. Elastic modulus and fracture toughness of native and sonication bath-generated blood
clots
Figure 5. 4. (A-F) Demonstration of agitation-mediated clotting with a rodent liver bleeding model
in vivo. The agitation is applied with a customized in vivo agitating platform (A) and a cup-like
biopsy tube (B). A volumetric injury is made with a biopsy punch (C) and receives agitation on site (D). The resulting clots (E) are tested with a rheamster (E), displaying permelized starges
site (D). The resulting clots (E) are tested with a rheometer (F), displaying normalized storage
moduli of native and in-vivo agitation-mediated blood clots (G). Typical obtained storage modulus
curves in rheology testes for in-vivo agitation generated blood clots
Figure 5. 5. (A) normalized elastic modulus and fracture toughness of native and agitation-
mediated plasma clots. (B) Normalized elastic properties and fracture toughness of native and
agitation-mediated plasma/microgel clots. (C) normalized average storage modulus of native and
agitation-mediated plasma/fibroblast clots. (D) Typical obtained storage modulus curves in
rheology testes for plasma/fibroblast cells clots. Data are shown as means \pm SD for n=5
independent experiments
Figure 5. 6. Confocal images of native and agitation-generated blood clots. (A) Fibrin network of
agitation-enhanced blood clots; (B) click-chemistry labelled RBCs for agitation-enhanced blood
clots; (C) merged image of agitation-enhanced blood clots. (D-F) Fibrin network, RBCs and
merged image of native group. (G-I) Fibrin network, RBCs and merged image of agitation-
degraded group. Scale bars are 30µm. Fibrin fibers and RBCs were stained as green and red
respectively
Figure 5. 7. Three-dimensional confocal microscopy image stacks with morphometric
quantifications and spatial analyses. (A) Blood clot (BC) with low (agitation-degraded)
mechanical properties; (B) native blood clot group; (C) blood clot with high (agitation-enhanced)
mechanical properties. The scale bars are 30µm and fibrin fibers and RBCs were stained as green
and red respectively. First (D), second (E), and third (F) nearest neighbor distance (NND) density
distributions of RBCs and their box-and-whisker diagram (G). (H) Radial distribution function g(r)
(pair correlation function) as function of a long-range normalized distance of RBCs; (I) kernel
density estimation of radial distribution function g(r) for RBCs. CSR denotes complete spatial
random. Nucleus and actin structure confocal images for agitation-degraded (Low) (J), native (K),

and agitation-enhanced (High) (L) plasma/fibroblast cells clots (FC) on day 1. Scale bars are 40μm
and Fibrin fibers, nucleus, and actin were stained as green, blue, and red respectively. (M) The
normalized average porosity area in plasma/fibroblast cells clots for agitation-degraded (Low),
native, and agitation-enhanced (High) groups. Data are shown as means \pm SD for n=3 independent
experiments. 94
Figure 5. 8. The histograms of first, second, and third nearest neighbor distance (NND) density
distributions of RBCs. (A-C) Agitation-degraded (low), (D-F) native and (G-I) agitation-enhanced
(high) blood clots, where d is centroid-to-centroid nearest neighbor distances and \overline{R} is the average
of RBC radii95
Figure 5. 9. The histograms of kernel density estimations of radial distribution function g(r) (pair
correlation function) of RBCs. (A) Agitation-degraded (low), (B) native and (C) agitation-
enhanced (high) blood clots
Figure 5. 10. Nucleus and actin member confocal images of native and agitation-generated
plasma/fibroblast cells clots. (A-C) Agitation-enhanced (high), (D-F) native, and (G-I) agitation-
$degraded \ (low) \ plasma/fibroblast \ cells \ clots \ on \ day \ 1. \ Scale \ bars \ are \ 40 \mu m. \ Fibrin \ fibers, \ nucleus,$
and actin were stained as green, blue, and red respectively
Figure 5. 11. Cell viability confocal images for the agitation-generated plasma/fibroblast cells
clots on day 1. (A) agitation-enhanced (high) and (B) agitation-degraded (Low) groups; (C) dead
reference control group. Scale bars are $80\mu m$. Fibrin fibers, live cells, and dead cells were stained
as green, blue, and red respectively. (D) The fibroblast cells viability percentages within the
crosslinked plasma for both agitation-degraded (low) and agitation-enhanced (high) groups 98
Figure 5. 12. Actual fibrin network confocal images of native and agitation-generated blood clots
with their 3D reconstruction morphometric quantification. (A-C) Actual fibrin network confocal
images for blood clots with high (agitation-enhanced), native, and low (agitation-degraded). (D-F)
3D reconstructed geometries of fibrin network from their confocal images for blood clots with
high (agitation-enhanced), native, and low (agitation-degraded)
Figure 5. 13. Box-and-whisker diagram of fiber diameters (A) and lengths (B). Cumulative
frequency of fiber orientations as function $\theta\left(C\right)$ and $\phi\left(D\right)$ angles. CSR stands for complete spatial
random. Data are shown as means \pm SD for n=3 independent experiments

versus incubation duration for fibrinolysis tests of agitation-mediated and native blood clots. Data
are shown as means \pm SD for n=3 independent experiments
Figure 5. 15. Hybrid element computational models of blood clots. (A) Randomly dispersed RBCs
within a representative volume element (RVE); (B) clustered (agglomerated) RBCs beside
randomly distributed RBCs within an RVE; (C) RBC model includes RBCs and connected linkage
networks; (D) statistical analysis of linkage networks length distribution for both random and
clustered cases (L _{sf} , fibrin segment length); (E) size assessment of RVEs for both randomly
dispersed and clustered distributions for RBC model; (F) comparisons of computed normalized
elastic (Young's) moduli for random and cluster dispersion models and experiments native clots
versus RBCs volume fractions; (G) stress contours within RBC model and (H) linkage networks
model under tensile loading (indicated by arrows); (I) variation of normalized elastic (Young's)
modulus of linkage networks model as function of linkage number and normalized linkage length
and diameter. Data are shown as means \pm SD for n=3 independent simulations and experiments.
and diameter. Data are shown as means \pm SD for n=3 independent simulations and experiments
•
•
Figure 6. 1. Comparison between experimental phase transition boundaries (i.e., static-packing
Figure 6. 1. Comparison between experimental phase transition boundaries (i.e., static-packing and packing-fluttering) and packing regime with relative acceleration, bounce height, bounce
Figure 6. 1. Comparison between experimental phase transition boundaries (i.e., static-packing and packing-fluttering) and packing regime with relative acceleration, bounce height, bounce duration, and rotation models.
Figure 6. 1. Comparison between experimental phase transition boundaries (i.e., static-packing and packing-fluttering) and packing regime with relative acceleration, bounce height, bounce duration, and rotation models
Figure 6. 1. Comparison between experimental phase transition boundaries (i.e., static-packing and packing-fluttering) and packing regime with relative acceleration, bounce height, bounce duration, and rotation models
Figure 6. 1. Comparison between experimental phase transition boundaries (i.e., static-packing and packing-fluttering) and packing regime with relative acceleration, bounce height, bounce duration, and rotation models
Figure 6. 1. Comparison between experimental phase transition boundaries (i.e., static-packing and packing-fluttering) and packing regime with relative acceleration, bounce height, bounce duration, and rotation models

Figure 6. 4. Schematic of possible microstructures of clot-like materials under external mechanical agitations. (A) Soft inclusions (cells) within biopolymeric medium; (B) inclusions clustering under low energy vibrations within biopolymeric medium; (C) non-uniformly dispersed inclusions under high energy vibrations within biopolymeric medium; (D) fixing the position of clustered inclusions due to clotting under low energy vibration; (E) fixing the position of randomly dispersed inclusions

due to clotting under high energy vibration; (F) large porosities within biopolymeric network of	due
to the inclusions clusters; G) homogenous porosities within biopolymeric network due to inclus	ior
random dispersion.	115

List of Tables

Table 1. Effective interactions and forces of significant magnitude in the self-assembly	of
components with molecular-to-millimeters length scales.	. 19
Table 2. Examples of self-assembled functional systems.	. 20

List of Abbreviations

2D Two-dimensional

3D Three-dimensional

DEM Discrete element modeling

FEM Finite element modeling

TIM Topologically interlocked material

MD Molecular dynamics

MC Monte Carlo

vWF von Willebrand factor

TF Tissue factor

FXa Activated factor X

RBC Red blood cell

PPP Poor-platelet plasma

PRP Platelet rich plasma

PLT Platelet

WB Whole blood

ECM Extracellular matrix

PMMA Polymethyl methacrylate

PF Packing factor

PBS Phosphate-buffered saline

t-PA Tissue plasminogen activator

NHS N-Hydroxysuccinimide

DMSO Dimethyl sulfoxide

NND Nearest neighbor distance

CSR Complete spatial random

GJK Gilbert–Johnson–Keerthi distance algorithm

EPA Expanding Polytope Algorithm

NSMP Non-uniform sequential mobile packing

RVE Representative volume element

IQR Interquartile range

Q1 First quartile

Q1 Third quartile

CaSO4 Calcium sulfate

A Applied vibration amplitude

a Edge length of hexagonal medial section

C Rotation constant value

n Rotation constant value

D Diameter of red blood cell

D' The diameter of sphere

D₁ Linkage cross-section diameter

Df Fibrin fiber diameter

d Centroid-to-centroid nearest neighbor distance

E Elastic modulus

G' Storage modulus

W Strain energy density function

S Area of medial section

V Volume of one block

Length of representative volume element

 $L_{\rm I}$ Length of linkage

 $L_{\rm sf}$ Length of fiber segment

 H_0 Height of sample in pure shear specimen

t Bounce duration

f Applied vibration frequency

g Gravitational acceleration

g(r) Radial distribution function (pair correlation function)

h Height of blocksh' Bouncing height

 I_{zz} In-plane moment of inertia

 I_{xx} , I_{yy} Normalized out-of-plane moment of inertia

l Edge length of square medial section

λ_c Critical stretch

Poisson's ratio v Interlocking angle α Critical relative acceleration Γ Γ' Fracture toughness Critical relative acceleration Ψ $\boldsymbol{\theta}$ Initial rotation angle of the block Initial rotation angle of the block θ_{i} Orientation of fibrin fibers φ Density p Compressive strength $\sigma_{
m c}$ Tensile strength σ_{t} Angular velocity w

CHAPTER 1

Introduction

This general introduction begins with a section on dissertation organization, outlining the structure of the dissertation and providing a concise summary for each chapter. It is followed by a dissertation motivations and challenges section to explain the necessary backgrounds and highlight the primary difficulties and limitations associated with fabricating and engineering hard blockbased and soft cellular inclusion-based materials that need to be tackled and understood. Afterward, there is a comprehensive literature review section focusing on the previous studies related to different experimental and theoretical aspects of this dissertation and summarizing the current relevant gaps. The necessity for implementing this dissertation is rationalized in the detailed aims and objectives section.

1.1 Dissertation Organization

This dissertation has been written in traditional monograph style, including 7 chapters: Introduction, Materials and Methods, Agitation-Driven Fabrication of Dense Architectured Panels, Agitation-Induced Assembly of Topologically Interlocked Materials, Agitation-Mediated Structure-Property Relation of Biopolymers Laden with Soft Cellular Inclusions, Discussions, and Concluding remarks – overviewed as follows.

Chapter 1 serves as a comprehensive introduction to the dissertation. It begins by outlining the motivations and challenges existed in block-based archtectured materials and cellular inclusion-laden clot-like materials addressed within this study. Followed by a literature review section which explores the background of architectured materials and their intersection with granular materials. The literature survey then discusses the fabrication methods employed for architectured materials, along with the current challenges associated with these methods. It then provides an overview of self-assembly techniques and their applications. Furthermore, it explains the background of computational modeling utilized for grain-based materials. It subsequently details the mechanisms of hemostasis, fibrinolysis, and wound healing, followed by an exploration of the implications of clot-like materials, which encompass biopolymers laden with high-volume

fraction cellular inclusions. The aims, objectives and essential implications and applications of this dissertation are described at the end.

Chapter 2 focuses on detailing the experiments and computations utilized across the entirety of the dissertation. The experimental materials and methodology sections cover the fabrication of polyhedral blocks, including their geometrical design and casting, as well as the synthesis of clots such as blood clot, plasma clot, fibroblast cells/plasma clot, and microgels/plasma clot. Subsequently, the chapter elaborates on the mechanical agitating platforms, object tracking image analysis, mechanical and rheological tests, including pure shear specimen characterization. It also discusses fibrolysis procedures, in-vitro cell culture, and their confocal imaging, along with the implementation and characterization of customized in-vivo experiments. Spatial analyses, which are integral to microstructural characterization, are then described. Following the experimental methodologies, the chapter delves into computational simulations, including discrete element (DEM) and finite element (FEM) models. It outlines the geometry generation, geometrical and physical properties, constraints, boundary conditions, and verifications of all DEM and FEM models utilized throughout the dissertation. Additionally, the chapter discusses the required experimental tests to validate different DEM and FEM simulations. Overall, Chapter 2 serves as a comprehensive guide to the experimental and computational methodologies employed in the research.

The main body of the dissertation comprises Chapters 3, 4, and 5, which explore the findings derived from consecutive studies aimed at addressing the research challenges. Chapter 3 initiates by presenting the DEM and experimental results. Subsequently, various single-grain mechanisms are examined through bouncing and rotating DEM models, leading to the capture of experimental phase transitions using the models obtained from single-grain DEM results.

Expanding upon the findings of Chapter 3, Chapter 4 investigates the interlocking of different polyhedral blocks, emphasizing the impact of block geometry and the tilting angle of the agitating platform on the assembly phase diagram. This chapter also showcases the feasibility of self-interlocked architectured monolayers to be free-standing. Furthermore, it compares DEM-generated interlocking phase diagrams for various polyhedral blocks and illustrates single-block DEM results for rotation mechanisms, capturing packing efficiency using this mechanism.

Chapter 5 explores the effects of mechanical agitation on the elastic modulus and fracture toughness of blood clots. It provides a comprehensive analysis of various mechanical properties of agitation-mediated and native (non-treated) blood clots, including results from in-vivo experiments. Additionally, it demonstrates how agitation-mediated mechanical properties of blood clots can extend to other clot-like material systems, highlighting the influence of micro-scale cell organizations on macro-scale mechanical properties. Microstructure characterization of the fibrous network is also presented, showcasing the effects of agitation-mediated cell organizations on the fibrous network and, thus, macro-scale mechanical properties. Furthermore, the chapter explores the impacts of these agitation-mediated microstructural and mechanical characteristics on the lysis of clot-like materials. Lastly, the chapters will be ended by presenting the results from FEM computational simulations, alongside their verifications and validations.

Chapter 6 comprehensively discusses the findings, applications, and future works of mechanical agitation-based engineering of granular stiff polyhedral blocks and soft active cell-laden clot-like materials. The chapter is divided into six sections; the first section highlights the links and connections between hard and soft active inclusions subjected to mechanical stimuli; the following three sections discuss the mechanics and physics of vibration-driven fabrication and assembly of stiff polyhedral granular blocks. The underlying mechanisms of agitation-mediated structure-property of cell-laden clot-like materials are discussed. Lastly, the potential and feasible future works based on understating from this dissertation are discussed.

The final chapter is devoted to presenting the conclusions and remarks. It summarizes the outcomes of the dissertation in relation to the proposed objectives, as well as its contributions to advancing knowledge in the field of engineering of hard granular materials and soft active materials.

1.2 Dissertation Motivation and Challenges

In contemporary materials science, specific microstructures, heterogeneities, and hybrid compositions are widely embraced to enhance performance. This pursuit has culminated in the development of architectured materials, characterized by meticulously engineered structures and morphological features at intermediate length scales between traditional microstructures and whole components. These architectured materials offer a realm of possibilities, allowing for the

precise design of architectures, geometries, and interfaces to achieve unique combinations of properties and functionalities, such as negative Poisson's ratio, exceptional stiffness, or remarkable toughness^[1-5]. While lattice materials have been extensively investigated, possessing only a small fraction of solid material, dense architectured materials, a less-explored domain, comprise fully solid structures built from well-defined blocks arranged in two or three dimensions. The arrangement and geometry of these blocks can be tailored to facilitate interlocking, as demonstrated in topologically interlocked materials (TIMs). TIMs are a novel category of architectured materials, featuring stiff blocks with precisely controlled geometries capable of collective sliding, rotation, or interlocking. These properties afford a myriad of tunable mechanisms, ensuring precise structural properties and diverse functionalities^[1-5]. Dense architectured, granular, and other material systems assembled from discrete blocks offer mechanical responses not typically observed in monolithic materials. The performance of these systems can be finely tuned and expanded by adjusting the geometry of the blocks, their packing arrangement, and/or their jamming states. Despite their promising characteristics, the applications of these material systems have been constrained, primarily due to challenges related to fabrication and scalability^[1-5].

In recent years, novel and innovative fabrication methods have emerged for creating complex materials with finely tuned architectures, morphological features, and interfaces at the meso-scale—sitting between grain size and the whole component. Examples of such methods include freeze casting, 3D printing, laser engraving, and centrifugation^[1-5]. Notably, some of these techniques were designed to mimic natural materials like nacre or bone, characterized by intricate assemblies of hard blocks bonded by softer biopolymers (proteins and/or polysaccharides) ^[1-5]. Interestingly, the concept of block-based materials joined by weaker interfaces finds application in topologically interlocked materials, capable of transforming brittle components like ceramics or glasses into tough, impact-resistant systems, or materials exhibiting unique mechanisms and precise structural responses not typically found in monolithic solid^[1-5]. The assembly of blocks in TIMs presents distinct challenges, with methods such as pick-and-place assembly, parallel assembly, magnetic assembly, 3D printing, and segmentation proposed to address these challenges^[1-5]. Self-assembly emerges as a promising pathway for fabricating such materials, with significant implications in chemistry, biology, and engineering. Despite its importance, most theoretical and experimental studies on self-assembly focus on nano- and microscale structures,

such as dense packing of colloids^[6-10]. Several numerical methods, including Monte Carlo and molecular dynamics, have been employed to study phase transitions and crystallization in thermal equilibrium systems^[6-10]. It is noteworthy to draw parallels between block-based materials and granular materials, as both systems operate athermally and far from thermodynamic equilibrium, with frictional and inertial forces playing prominent roles. While granular crystallization studies primarily focus on spherical grains, fewer reports delve into the assembly of polyhedral blocks. Mechanisms underlying packing and phase transitions of granular matter have been extensively described in the literature, yet detailed understanding of mechanical agitation-driven assembly of non-spherical blocks remains unexplored. Further research into these mechanisms is crucial for enabling large-scale fabrication of complex materials.

The primary challenge is to explore and examine how mechanical agitation can be used to assemble, crystallize, and interlock polyhedral blocks in order to fabricate topologically interlocked materials/structures. This involves developing experimental measurement instruments to characterize and analyze the packing and phase transitions of the system by decoupling the effects of the mechanical agitator and the blocks dynamics. Additional challenge is to use this experimental system to study the physics and mechanics underlying the transition of discrete polyhedral blocks into dense, segmented macro-scale interlocked material systems. Further challenge is to generate reliable computational tools to replicate the experiments and further evaluate and understand these processes and governing mechanisms at the grain length scale level.

The agitation-driven assembly of stiff polyhedral block-based architectured materials involves a process where athermal, far-from-equilibrium hard active grains transform into stable, reversible, or reconfigurable crystals at minimum potential energy conditions. However, soft active grains also can have the same behavior. Although the mechanical properties of hard and soft grains/inclusions are utterly different, the underlying mechanism of agitation-driven assembly can be universal. One of the primary motivations and challenges of this work is to explore and understand the analogous behaviors of hard and soft grains/inclusions subjected to mechanical stimuli within different media. The challenge is to extend these understandings to far-from-equilibrium active soft inclusions, aiming to achieve similar stabilization for translating the application of this system.

Soft active matter constitutes a class of materials far from equilibrium, characterized by soft active inclusions that interact with each other, their surrounding matrix, and external environments, leading to emergent behaviors such as dynamic collective motions, self-organization, and mechanical reactions. Many soft active materials consist of a significant volume fraction of cellular inclusions embedded within fibrous biopolymeric networks. Examples include blood clots, where a fibrin network envelops and undergoes deformation by blood cells such as red blood cells and platelets. Clot-like materials also encompass biological tissues, tumors, organoids, and bacterial biofilms. Their formation often involves the self-assembly of cellular inclusions within a biopolymer fluid medium, a process sensitive to external stimuli. However, unlike conventional polymeric materials, the formation and structure-property relations of clot-like materials under external stimulation remain relatively unexplored, despite their profound implications in engineering and medicine. For instance, understanding and controlling how blood clots deform and fracture could significantly advance treatments for hemorrhage and thrombosis^[11-23]

Engineering clot-like materials presents several challenges, with chemical strategies often limited by adverse side effects, toxicity, and specificity to the material system. In contrast, physical strategies such as magnetic manipulation, shearing, wave, and ultrasound have been utilized to manipulate soft active and/or granular material systems, facilitating the assembly and patterning of cells^[11-23]. However, modulating the three-dimensional structure and mechanical properties of clot-like materials across length scales remains unexplored. Mechanical agitation emerges as a promising yet underexplored strategy, offering a facile, biocompatible, low-frequency, and cost-effective method of stimulation. Unlike ultrasound, agitation produces no cavitation or thermal effects while enabling ordering, disordering, and phase transitioning of cellular, granular, and organoid inclusions^[11-23]. By extending the application of mechanical agitation to clot-like materials, it becomes possible to modulate their structure and mechanical properties without altering their chemical compositions.

Another main challenge is to devise a physical strategy based on mechanical agitation for engineering cellular inclusion-laden biopolymer (clot-like) materials. This entails examining and exploring the effects of mechanical agitation on the organization of cellular inclusions during polymerization (clotting) and the resulting microstructural impacts on the fibrous biopolymer network, thereby modulating the macroscopic mechanical behavior of the clot-like materials.

Another challenge is to understand how to tune a wide spectrum of material properties of clot-like materials, including stiffness, toughness, contraction, and lysis, using mechanical agitation. Further challenges include assessing the cytocompatibility and efficacy for real-time adjustment of clot-like material properties through in vitro cell culture and in vivo animal experiments. Lastly, there is the challenge of experimentally and computationally characterizing and studying processes such as agitation-mediated mechanical properties of clot-like materials to understand the leading mechanisms in modulating the assembly and structure-property relations of clot-like materials.

Lastly, there exists a significant gap and motivation to explore the effects of similar mechanical stimuli on hard and soft inclusions. For example, mechanical stimuli for hard blocks within air can include vibrations or oscillating shearing, where the applied mechanical energy is not dissipated due to the rigidity of the system. In contrast, the same mechanical stimulus for soft inclusions within fluid can be dissipated due to fluid perturbation and the softness of the inclusions. Therefore, instead of vibration for hard inclusions, applied agitation needs to be studied for soft inclusions to understand the different responses and behaviors under similar mechanical stimuli.

1.3 Literature Survey

This literature review provides a brief overview of the mechanics of both biological and bio-inspired architectured materials. A specific focus is placed on a subclass of bio-inspired architectured materials known as topologically interlocked materials (TIMs), encompassing discussions on fabrication techniques and mechanical properties. Notably, considerable attention is devoted to self-assembly, an underutilized yet promising strategy for fabricating this class of materials. The mechanics and physics of various self-assembly methods and resultant products at different length scales are described, including theoretical frameworks, modeling approaches, and experimental investigations. Additionally, a brief overview is provided on the mechanisms of hemostasis, fibrinolysis, and wound healing, followed by an exploration of the biophysics and mechanics of clot-like materials, specifically blood clots. Analogies are drawn between active soft cellular inclusions within their biopolymer media and active far-from-equilibrium materials such as granular materials.

1.3.1 Architectured Materials

Architectured materials are characterized by stiff blocks arranged periodically in two or three dimensions. Due to the unique nonlinear mechanisms inherent in such structures, architectured materials present novel avenues for meeting contemporary structural performance requirements, particularly in achieving simultaneous strength, toughness, and light weight. Intriguingly, certain hard biological materials, such as mollusk shells and bone, can also be conceptualized as architectured materials^[1-5, 24-28]. Hard biological materials and their bio-inspired counterparts are characterized by the presence of stiff and hard blocks, alongside elements of compliance and weak interfaces^[1]. While these blocks possess inherent material properties and microstructures, their individual deformation remains negligibly small and predominantly within the linear elastic regime^[1-5, 24-28]. In architectured biological materials, the mineral blocks often contain protein chains staggered at the boundaries of nano-grains^[25]. Although protein chains may enhance the strength of mineral blocks, they generally do not alter the elastic properties of the mineral components^[26]. Figure 1.1 illustrates various examples of architectured biological materials, showcasing the diverse shapes of blocks arranged in complex two- or three-dimensional segmented multilayer configurations. Despite the non-uniformity of segmentations in biological materials, they exhibit a high degree of periodicity^[1-5, 24-28].

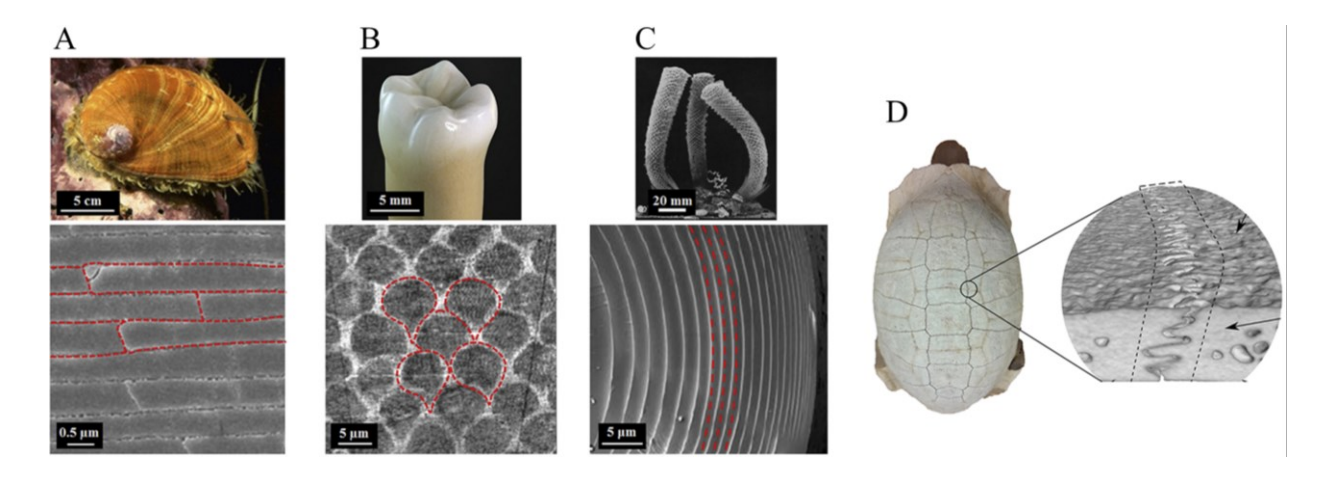


Figure 1. 1. Different biological materials composed of the high volume fraction of stiff and hard blocks interlocked together within the low volume fraction of weak and soft interfaces. (A) The nacreous layer of mollusc shell^[28] (Reproduced with permission, Copyright 2011, Springer Nature BV); (B) tooth enamel^{29]} (Reproduced with permission, Copyright 2001, Elsevier); (C) the spicules of glass sponge skeleton^[30] (Reproduced with permission, Copyright 2005, AAAS). The dashed red line illustrates the border of blocks. (D) The turtle shell skeleton comprises multiple bone plates interconnected by a network of interlocked interfaces, with soft tissue integrated between them^[31] (Reproduced with permission, Copyright 2021, Elsevier).

In architectured hard biological materials, interfaces between blocks incorporate protein chains and/or polysaccharides, typically constituting up to 5% of the volume^[1, 24, 25]. These interfaces are intricately structured, promoting interlocking through geometric features and enabling stiffening under higher loads^[1-5, 24-35]. The behavior of block interfaces, including sliding or opening, is evaluated through methodologies such as contact mechanics, fracture mechanics, and analysis of interface material deformation^[1-5, 24-35]. While the nonlinearity of these mechanisms contributes to energy dissipation and toughness, additional hardening mechanisms at the interfaces are necessary^[1-5, 24-35]. This hardening can be achieved through progressive jamming of the blocks, strain hardening, or strain rate hardening at the interfaces^[1-5, 24-35]. However, these intricate mechanisms have yet to be implemented in bio-inspired architectured materials^[1-5, 24-35]. In bio-inspired architectured materials, blocks exhibit uniform dimensions and are arranged in a periodic fashion. Analogous to architectured biological materials, the volume fraction of blocks in architectured bio-inspired materials substantially exceeds that of interfaces^[1-5, 24-35]. Figure 1.2 depicts typical force-displacement curves for various materials, including brittle monolithic materials, longitudinal and transverse composite materials, architectured materials, and ductile

materials with identical constituents. In hard bio-inspired architectured materials, individual blocks exhibit minimal deformation, whereas the structure as a whole undergoes substantial displacements attributed to the collective movements of blocks relative to one another. Consequently, the mechanical responses of these materials are primarily governed by the overall structure, composition, and mechanics of interfaces^[1-5, 24-35].

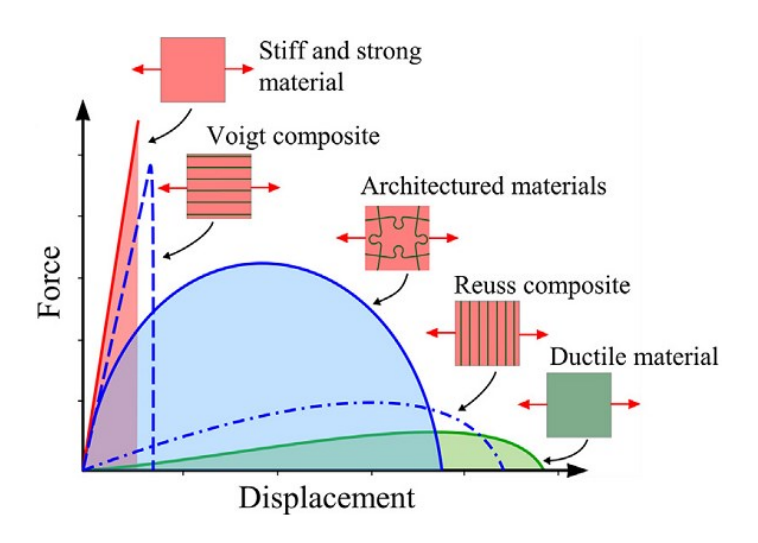


Figure 1. 2. Typical force-displacement curves for a brittle monolithic material, a ductile material, and their longitudinal, transverse, and architectured compositions^[35] (Reproduced with permission, Copyright 2018, Elsevier).

1.3.2 Intersection of Granular and Architectured Materials

Architected materials, alongside other mechanical metamaterials, leverage intricate and adaptable microstructures to induce nonlinearities, instabilities, and unconventional mechanical responses^[1-5, 33-42]. Another category within architected materials comprises fully dense structures composed of stiff, millimeter-scale blocks, employing frictional contact and topological interlocking to confer impact resistance and damage tolerance^[1-5, 33-42]. These structures, known as "topologically interlocked materials" (TIMs), feature meticulously designed individual blocks arranged in periodic arrays and can be assembled into panels. TIMs exhibit exceptional structural characteristics; they not only surpass monolithic plates of equivalent material in toughness by up to 50 times but also demonstrate strength improvements of up to 1.2 times^[2]. While the principles underlying TIMs are well-established for planar configurations such as flat panels, curved panels, domes, and walls, the exploration of these construction strategies and mechanisms in fully three-dimensional materials remains limited^[1-5, 33-42]. TIMs represent a noteworthy example of bio-

inspired architectured materials. Figure 1.3 showcases assembled panels of various TIMs constructed using diverse polyhedra blocks, with no adhesive employed at the interfaces between these blocks. Stiffness and strength are conferred by the geometric interference and interlocking of the blocks^[1-5, 33-42]. To facilitate these mechanisms, the blocks must be held together by an external ligament, typically achieved through a stiff external frame^[1-5, 33-42]. TIMs exhibit several mechanical properties and characteristics that render them superior to monolithic structures, including high energy absorption under both static and dynamic loading conditions, interlocking toughening mechanisms against crack propagation, resistance to local failure, tunable bending resistance, and negative elastic stiffness during unloading^[1-5, 33-42]. Moreover, TIMs can be composed of identical blocks with vastly different material properties, encompassing metallic, ceramic, and polymeric materials^[1-5, 33-42]. A defining feature of TIMs is their ability to generate segmented structures and materials without significant stress concentration.

Hard convex polyhedral blocks can be assembled and/or fabricated into crystal-like arrangements to create TIMs (Figure 1.3) [1-5, 33-42]. This emerging concept of block-based architectured materials produces materials with a rich set of tunable mechanisms and properties, based on morphological and interfaces at length scales intermediate between block size and component size^[1-5, 33-42]. In addition, block-based materials and structures provide ample tunable mechanisms, precise compositional and structural gradients, functionalities, and stiff-to-flexible transitions not ordinarily found in monolithic solids^[1-5, 33-42]. The performance of these information-rich materials have been pushed to the extreme by manipulating geometry and/or functionalizing the surface of blocks resulting in more architectural complexity^[1-5, 33-42]. For example, U-shape^[43], Z-shape^[44], hexapod^[45] blocks were used to create tensile strength, but these efforts remain limited by randomness and/or poor packing density of blocks.

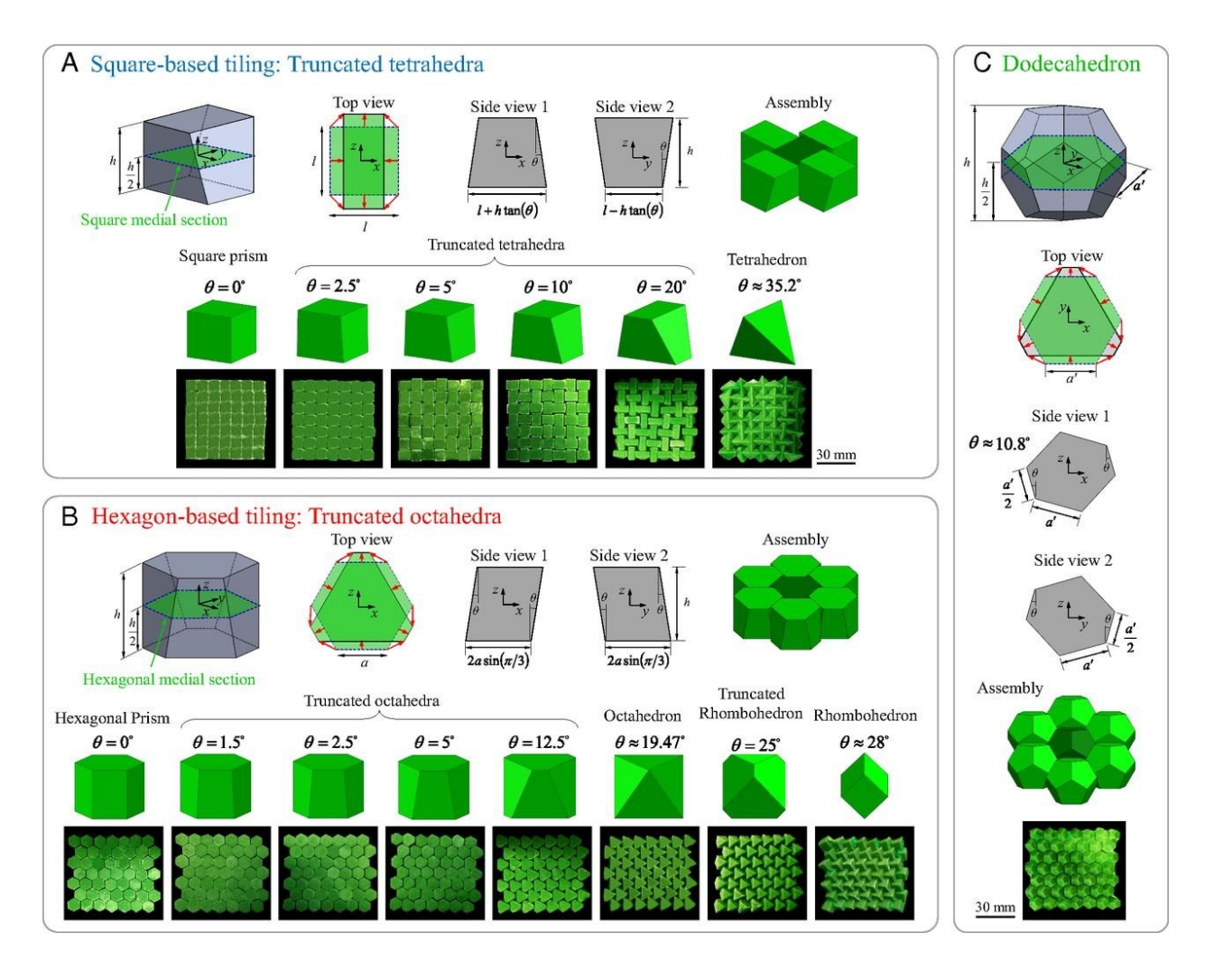


Figure 1. 3. Comprehensive depiction of the 15 architectured topologically interlocked materials panel designs: Each group presents the geometric configuration of the individual block alongside an assembly schematic and visual representations of panels constructed from CaSO4 blocks. The designs include: (A) truncated tetrahedra with a square medial section base; (B) truncated octahedra featuring a hexagonal medial section base; and (C) dodecahedra[2] (Reproduced with permission, Copyright 2018, National Academy of Sciences).

Block-based materials and structures are at the intersection between composite materials, masonry, architectured materials and granular materials, with which they share many similarities: they can temporarily have phase transitions and therefore, they are out-of-thermodynamic equilibrium in their amorphous state while they can be crystallized and stay in a state of equilibrium (the lowest possible potential energy is reached for each block). Granular materials exhibit several key characteristics similar to those found in TIMs, as they are also composed of

millimeter-sized blocks interacting through frictional contact, albeit within full three-dimensional space. Granular substances, such as sand, manifest a diverse array of complex mechanical behaviors that have yet to be fully leveraged in TIMs. For instance, depending on the degree of confinement, sand can exhibit fluid-like flow or possess the stiffness and strength characteristic of solids^[46], showcasing a spectrum of phenomena including cluster formation, localized stress transfer regions, jamming, shear banding, and shear-induced dilatation^[47, 48]. However, the inherent randomness present in typical granular configurations poses challenges in designing, optimizing, and effectively harnessing these deformation mechanisms for broader engineering applications. Moreover, granular materials typically consist of spherical or ellipsoidal grains^[47, 48], yet from a mechanical standpoint, spherical shapes are suboptimal. The packing efficiency, measured by the packing factor or solid volume fraction, for randomly packed spheres ranges only from 0.55 to 0.64^[49], significantly lower than the theoretical upper bound volume fraction of 0.74 achievable with densely packed spheres. However, this upper bound is inherently limited as spheres are not space-filling shapes. Consequently, when subjected to mechanical loads, typical granular materials transmit stress predominantly along narrow "force chains," occupying only a small fraction of the material volume^[50], leaving the majority of grains devoid of significant stress. The mechanical behavior of one-dimensional granular chains^[51, 52] and granular crystals composed of spherical grains^[53] under small deformation regimes exhibits unique and practical characteristics concerning elastic wave propagation, acoustics, and shock wave attenuation. Remarkably, the shape of individual grains can be intentionally tailored to manipulate mechanical responses and improve material properties^[40, 54]. For instance, granular materials utilizing convex platonic shapes (such as cubes, tetrahedra, and octahedra) demonstrate a significant increase in shear strength, ranging from 40% to 80% compared to materials composed of spherical grains, attributed to restricted grain rotation and enhanced jamming effects^[55]. However, despite these advancements, the arrangement of such grains remains random, thereby constraining their packing density and overall mechanical performance (Figure 1.4).

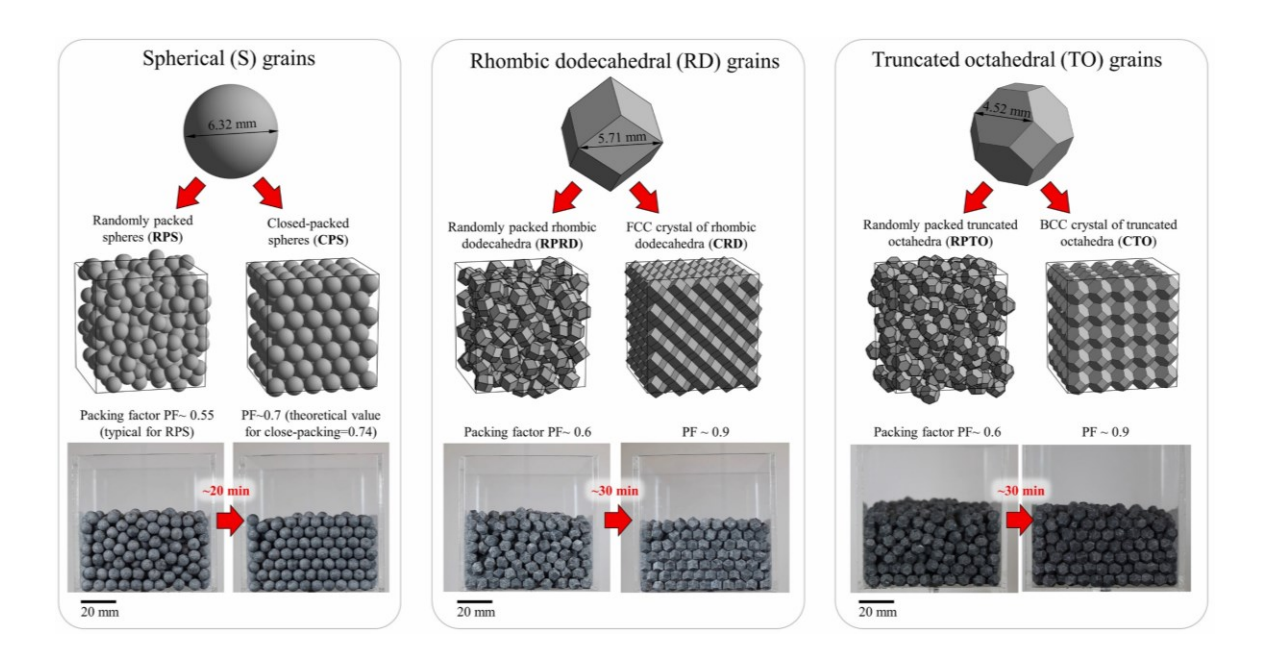


Figure 1. 4. Three-dimensional granular crystals: (A) Individual grains—spherical, rhombic dodecahedral, and truncated octahedral—in millimeter scales with uniform volumes. These grains possess the potential to crystallize into close-packed spheres or fully dense crystals. The enclosing box served as a crystallization template, resulting in two distinct crystallographic orientations^[39]. (Reproduced with permission, Copyright 2022, National Academy of Sciences)

TIMs can be fabricated using various approaches, including both bottom-up and top-down methods. However, the broader application of these complex material systems is also hampered by fabrication challenges; for example, for polyhedral blocks, the most common assembly method is manual^[1-5]. An underused yet potential approach for fabricating these materials is self-assembly which is intrinsically driven by thermal fluctuations at nanoscales and/or colloidal scales^[6-10]. Thermal fluctuations, however, do not affect the larger scales (meso- and macro-scales) and athermal systems; therefore, a promising alternative can be mechanical agitating and/or shearing^[56-73]. The vast majority of meso- and macro-scale granular assembly studies have sought the packing and phase transition of spherical grains^[46-66], and much fewer studies have focused on the polyhedral blocks^[56-73], while self-interlocking and/or -crystallization of these geometries has yet been explored particularly at the meso- and macro-scales. Various governing mechanisms underlying packing and temporary phase transitions of granular materials have been explained in the literature; for instance, the "magnitude" of the mechanical agitation has often been characterized by a single parameter: the critical acceleration normalized by the gravitational

acceleration^[56-58]. However, the effective mechanisms involved in self-interlocking and/or - crystallization of polyhedral blocks have yet been established.

1.3.3 Fabrication Methods for TIMs

Recent advancements in fabrication methods have introduced novel techniques for creating complex materials with finely-tuned architectures, morphological features, and interfaces at the meso-scale, which bridges the gap between grain-size and the entire component^[1-5]. These methods encompass a range of techniques such as freeze casting, 3D printing, laser engraving, and centrifugation^[1-5, 74-79]. Notably, some of these techniques were specifically devised to mimic natural materials like nacre or bone, which exhibit intricate assemblies of hard blocks bonded by softer biopolymers such as proteins and polysaccharides^[1-5, 74-79]. Interestingly, the concept of materials composed of blocks joined by weaker interfaces is also utilized in topologically interlocked materials. TIMs have the capability to transform brittle components like ceramics or glasses into tough, impact-resistant systems or materials with tunable mechanisms, precise structural responses, and functionalities not typically found in monolithic solids ^[1, 2, 4, 5, 33, 34, 36-38]. The assembly of these blocks poses unique challenges, with methods ranging from pick-and-place assembly to magnetic assembly, 3D printing, and segmentation^[1, 2, 4, 5, 33, 34, 36-38]. Self-assembly emerges as a promising pathway for fabricating these materials, leveraging the intrinsic capabilities of the blocks to autonomously organize into desired configurations.

The initial step in fabricating a TIMs structure involves the production of the primary polyhedral blocks. These blocks can be manufactured using various techniques such as computer numerical control, machining, casting, and additive manufacturing^[1, 2, 4, 5, 33, 34, 36-38]. Several bottom-up strategies, involving assembly methods, have been proposed for fabricating TIMs. These include pick-and-place assembly, parallel assembly, self-assembly, and 3D printing. In contrast, the sole method available for fabricating TIMs using a top-down approach is segmentation, typically achieved through laser engraving techniques ^[1, 2, 4, 5, 33, 34, 36-38]. Figures 1.5A illustrate the pick-and-place assembly methods, wherein human intervention is employed to pick individual blocks and position them in their predetermined locations to enable interlocking. For certain shapes, such as tetrahedrons, a specialized pre-manufactured template may also be required (Figures 1.5A,B). Figure 1.5B demonstrate the parallel assembly method utilizing internal wires for various polyhedral block shapes. Figure 1.5C illustrates a glass panel segmented using

laser engraving techniques. Figures 1.5D,E depict a self-assembly method utilizing magnetic forces, while Figure 1.5F showcases homogenous 3D-printed TIMs. Figure 1.5G illustrate the pick-and-place assembly method using a robot to pick and position individual blocks in their predetermined interlocking locations.

The primary challenge in TIMs lies in fabrication, with all the described methods having inherent shortcomings. They are generally time-consuming, require additional work on the polyhedral blocks, involve complex assembly setups, and necessitate specific pre-defined templates. Moreover, they may not be suitable for various types of materials and shapes of polyhedral blocks.

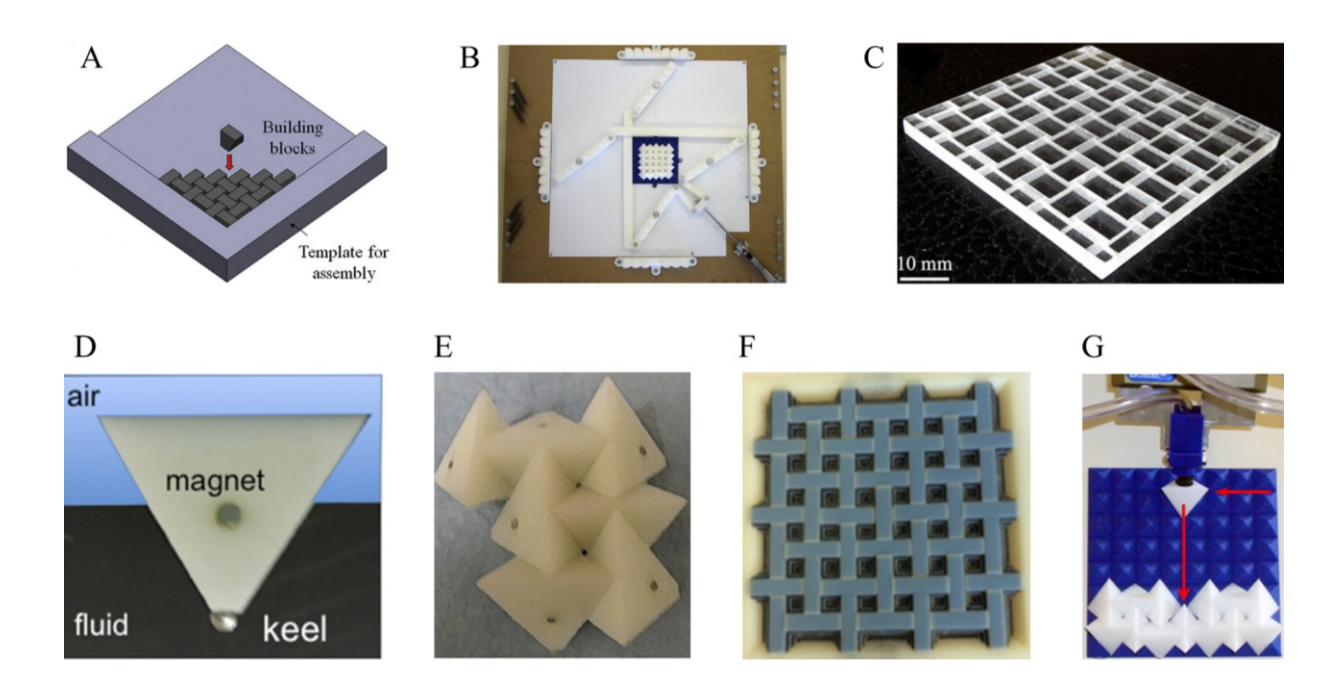


Figure 1. 5. Various proposed fabrication methods for topologically interlocked materials. (A) Pick-and-place method employing human hand^[33] (Reproduced with permission, Copyright 2019, Elsevier); (B) Parallel method utilizing internal wires^[4]; (C) Laser engraving method^[79]; (D, E) Magnetic-based self-assembly method^[4]; (F) 3D printing method^[4] (Reproduced with permission, Copyright 2016, American Society of Mechanical Engineers ASME); (G) Pick-and-place method employing a robot^[4] (Reproduced with permission, Copyright 2010, Emerald Publishing Limited).

1.3.4 Self-assembly

Numerous methodologies have been devised for manipulating various materials, facilitating the fabrication of engineering objects across scales ranging from nano- to macro-level. Among these methods, four primary categories emerge: (i) chemical synthesis, involving the manipulation of atoms to form molecules; (ii) photolithography, utilizing light patterns to pattern materials; (iii) mechanical manufacturing, employing manufacturing techniques and machinery for part creation and assembly to serve functional purposes; and (iv) construction, leveraging materials to erect expansive structures^[80-83]. A common requirement and characteristic shared by these methods are the necessity for human intervention. Indeed, the fruition of engineering products through these methods necessitates either direct human involvement or the operation of a device — such as a robot — in place of human hands^[80-83]. However, engineering objects can also be realized through a distinct method devoid of human intervention, termed self-assembly (Figure 1.6). Self-assembly represents a system wherein components autonomously arrange themselves into predefined structures without human intervention^[80-83].

The concept of self-assembly originated from the arrangement of molecular systems based on their non-covalent interactions^[84-89]. Examples of such formations encompass crystals and micelles, leading to the creation of organic and organometallic structures^[84-86]. Moreover, self-assembly processes are ubiquitous in various natural and biological systems. For instance, protein molecules utilize linear chains to construct intricate 3D functional structures^[87-89]. Historically, self-assembly has primarily been explored by biologists, chemists, and material scientists in the context of molecular systems^[80-83]. However, self-assembly extends beyond molecular systems and can also be harnessed to fabricate components spanning from nano- to millimeter length scales, offering a novel approach for producing previously unattainable engineering objects. This fabrication technique holds particular promise for generating structures that fall between the size range achievable through chemical synthesis (i.e., bottom-up) and conventional manufacturing or assembly strategies (i.e., top-down) [80-83].

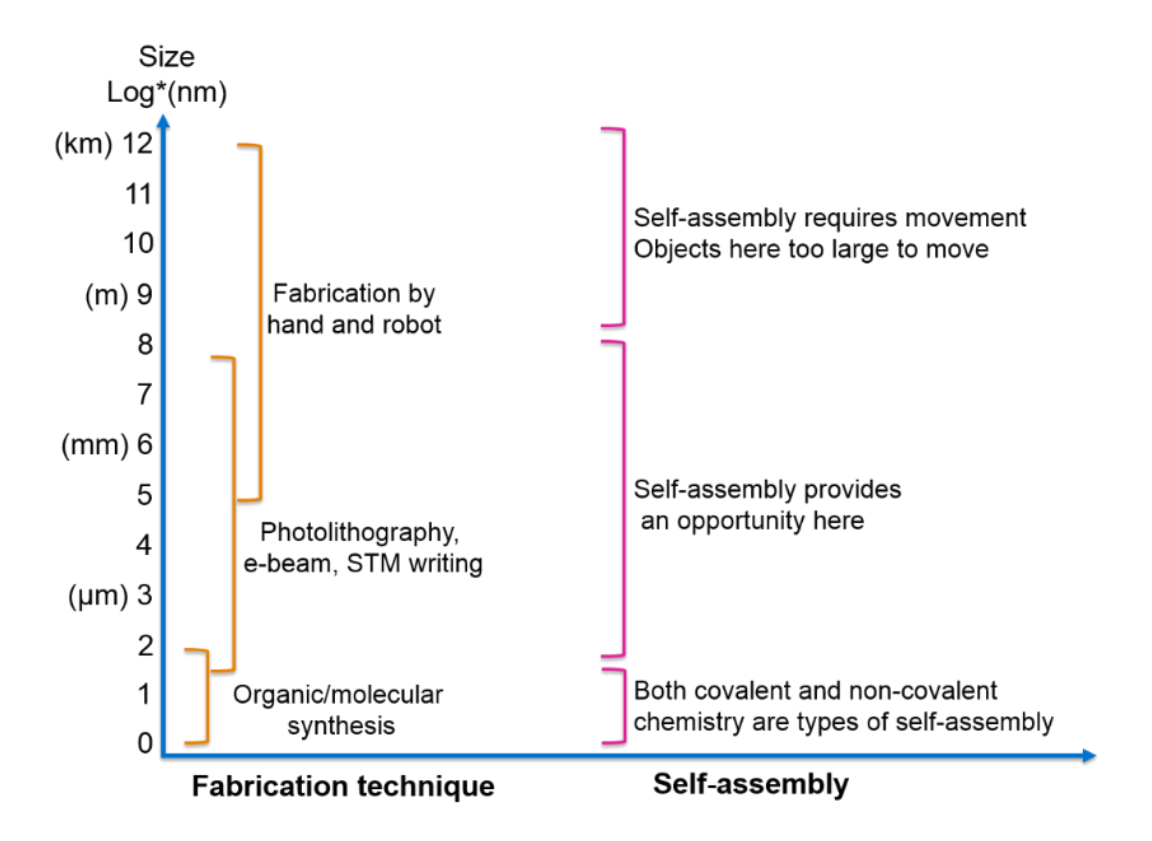


Figure 1. 6. A general flowchart illustrating the fabrication process of engineering objects across varying length scales, ranging from nano- to kilometer-level dimensions. The figure highlights the potential applicability of self-assembly as an alternative to conventional fabrication techniques^[80-83].

Molecules possess inherent rigidity, limiting the customization of potential interactions among their components. This constraint arises from the dependence of their covalent and non-covalent interactions on their electronic configuration. Notably, non-covalent interactions, such as van der Waals forces, electrostatic interactions, hydrophobic interactions, and hydrogen bonding, play pivotal roles in the self-assembly process. The majority of self-assembly concepts and principles have predominantly been explored within the realm of molecular systems, primarily for nano- and micro-scale structures. However, components at larger length scales, specifically the meso-scale, are also capable of self-assembling under meso-scale forces and interactions^[80-83]. Self-assembly at the meso-scale offers unprecedented flexibilities and functionalities that are not achievable with molecular-scale systems. Three key characteristics distinguish meso-scale self-assembly as an exceptional tool: (i) it enables the utilization of a broad spectrum of interactions, including capillary, electrostatic, magnetic, optical, fluidic shear, and gravitational forces; (ii) it facilitates the creation of a diverse array of three-dimensional structures that are challenging to

fabricate rapidly through alternative techniques; and (iii) it allows for a wide range of compositions to be employed, thereby enabling the creation of various functionalities within different structures^[80-83]. Subsequently, a comprehensive summary of effective interactions and forces in both molecular- and meso-scale self-assembly is provided in Table 1.

Table 1. Effective interactions and forces of significant magnitude in the self-assembly of components with molecular-to-millimeters length scales.

Meso-scale self-assembly	Molecular-scale self-assembly
Gravitational ^[90]	van der Waals ^[94, 95]
Electrostatic ^[91]	Centrifugal ^[82]
Magnetic ^[92]	Osmotic ^[96]
Capillary ^[93]	Entropic ^[97]
Fluid Shear ^[82]	Light ^[98, 99]
Hydrodynamic ^[91]	Casimir ^[100]
Hydrophobic ^[85]	Bio-specific (e.g., protein: ligand, DNA:DNA) ^[82]

Various research groups have investigated self-assembly within molecular systems and applied their findings to non-molecular and meso-scale structures and systems^[80-83]. Notable similarities and differences between fundamental characteristics of meso-scale and molecular-scale self-assembly are elucidated. (i) Parameters such as the size, number, fabrication, structure, and functionality of components hold greater significance in meso-scale self-assembly compared to molecular-scale self-assembly^[80-83]. (ii) Motion capability of components, facilitating collisions, is essential in both scales; however, molecular-scale self-assembly involves a higher frequency of collisions among colloids compared to millimetric components in the meso-scale, necessitating external sources such as vibration, stirring, magnetic, or gravitational forcing for motion in meso-scale self-assembly^[80-83]. (iii) Collisions and interactions among components, whether molecular or millimetric, must be reversible, indicating the necessity for components to adjust positions through a balance of attractive and repulsive forces. Consequently, geometry of colliding components plays a crucial role in both molecular- and meso-scale self-assembly processes^[80-83].

(iv) Templating, employed to control the number of structures and prevent defect formations, can be utilized in self-assembly at both molecular and millimetric scales. Templating can involve establishing connections among components or creating structural directors to guide them through the process. While templating is readily feasible in meso-scale self-assembly using containers of appropriate size and shape, it is rarely achievable at the molecular-scale due to the scarcity of suitable containers. Additionally, both molecular and millimetric length scales are sensitive to wall effects during templating, which extend over dimensions of 10-100 component layers from the walls. While the active wall effects distance differs in molecular- and meso-scale self-assembly processes, the scaled distance may remain equivalent^[80-83].

Various methods have been employed in meso-scale self-assembly for diverse engineering applications^[80-83]. For instance, a range of capillary, magnetic, electrostatic, vibration, and gravitational systems have been utilized to facilitate the self-assembly of electronic devices, circuits, and integrated LEDs^[80-83]. Additionally, to create crystal structures using spherical or polyhedral blocks, capillary and acoustic vibrational systems have been employed^[101-103]. The effectiveness of acoustic-vibration-assisted gravitational systems in facilitating the self-assembly of anisotropic and polyhedral blocks suggests the potential applicability of this method to assemble the blocks utilized in 2D and 3D TIMs. Such an approach could address many of the fabrication challenges associated with existing methods for this class of materials. In the subsequent section, various simulation approaches proposed for assessing and predicting the packing and self-assembly of polyhedral blocks are briefly reviewed and discussed.

Table 2. Examples of self-assembled functional systems.

Application	Driving force
3D structures by folding of 2D precursors	Capillarity ^[104, 105]
J G I	Electrical activation ^[106]
Microelectromechanical	
and	Capillarity ^[107-109]
microoptoelectromechanical	Cupmanty
systems	

Integrated LEDs, Si arrays	Fluidic and gravitation ^[110]
	Vibration and gravitation ^[111, 112]
	Magnetism ^[113]
	Electrostatic interactions ^[114]
Electronic device	Capillarity ^[115]
Electric circuit	Hydrophobic effect ^[116]
Positioning of micro-mirrors	Capillarity ^[117]
Part-to-substrate assembly	Capillarity ^[118]
2D arrays	Magnetic and hydrodynamic forces ^[119]
	Magnetic and electrostatic forces ^[120]
	Capillarity ^[121]

1.3.5 Computational Modeling

The exploration of particle packing and self-assembly across scales, from the nanoto macro-level, has long been a focal point in scientific inquiry. This section provides a succinct review of diverse modeling approaches employed in understanding particle packing and self-assembly phenomena. Molecular dynamics (MD) has emerged as a widely utilized tool for predicting the packing and self-assembly behaviors of colloidal and patchy particles at both molecular and atomic scales^[122, 123]. However, while MD techniques excel in capturing molecular-scale forces and interactions, they are predominantly employed for modeling spherical particles^[122, 123].

In contrast, the packing of particles with complex shapes, such as polyhedra, presents unique challenges. For instance, Monte Carlo (MC) simulations have been used to investigate the packing and crystallization of various polyhedral structures. These studies encompassed the modeling of four distinct crystal phases, including liquid crystals, plastic crystals, glassy crystals, and other crystalline configurations. MC simulations offer a powerful approach for exploring the

packing behavior of non-spherical particles, providing valuable insights into the assembly of complex structures. Figure 1.7 illustrates the potential structures resulting from the packing of various polyhedra within a representative volume element. Additionally, it presents the bond-order diagrams depicting the nearest neighbors for each polyhedron configuration^[9, 10]. The influential role of shape, topography, and topology of blocks in governing the self-assembly process.

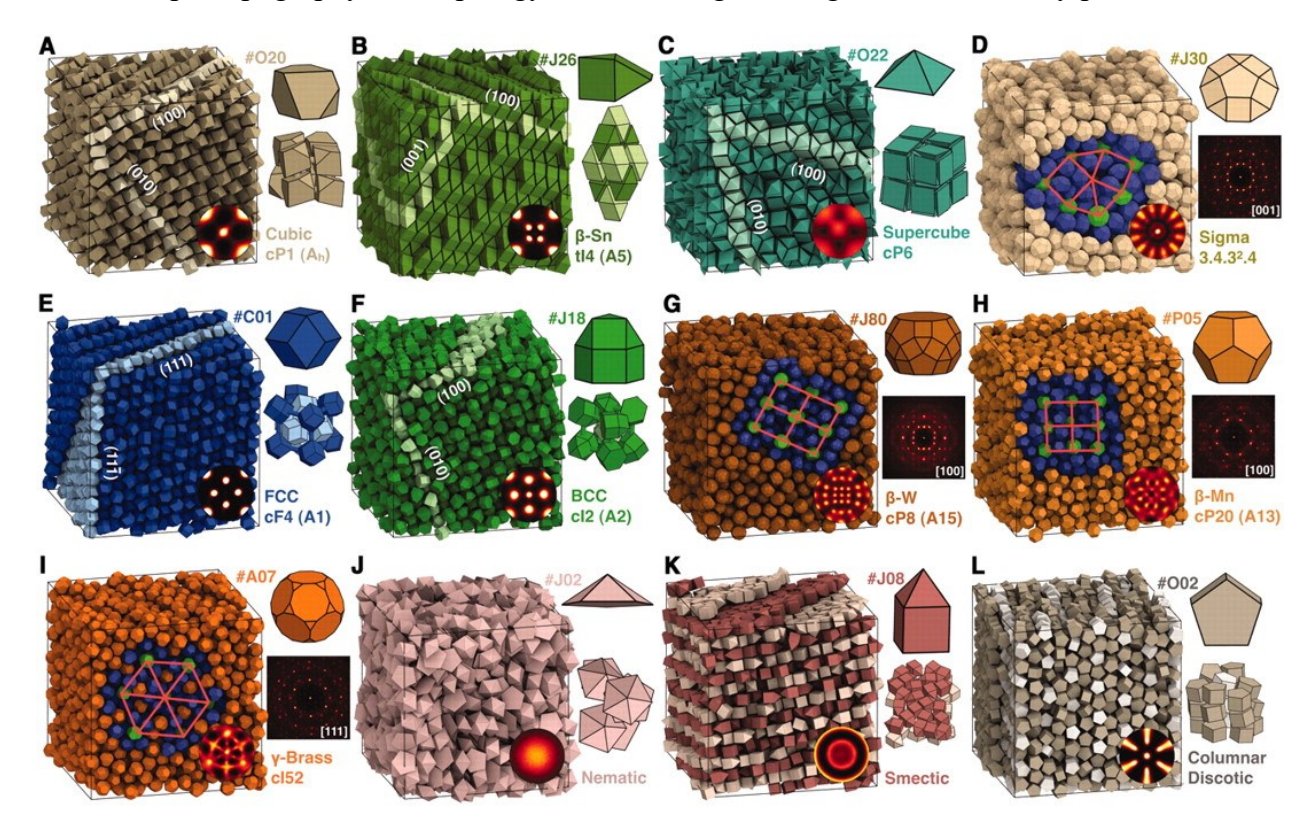


Figure 1. 7. Systems comprising 2048 polyhedra assembled from a disordered fluid state. Each subfigure includes several elements: a snapshot of the simulation box (left), a bond-order diagram for nearest neighbors (inset), the shape and ID of the polyhedron (top right), a small group of particles or a diffraction pattern (middle right), and crystallographic characterization details such as name or atomic prototype, Pearson symbol, and Strukturbericht designation (bottom right). The snapshots illustrate various crystal structures (A-D), plastic crystals (E-I), and liquid crystals (J-L). Different colors highlight specific features in the simulation snapshots, such as low index planes (A-C, E, F), tiling descriptions consisting of squares and triangles (D, G-I), and structural features (K, L)^[9] (Reproduced with permission, Copyright 2012, AAAS).

The concept of shape entropy has also been assessed by investigating the packing of polyhedra using MC simulations. These findings revealed that to maximize system entropy, polyhedral blocks tend to experience a directional entropic force, aligning their faces in parallel and bringing them closer together (Figure 1.8). Moreover, in regions comprising blocks of different shapes, interactions among them can be managed through anchoring forces[9, 10].

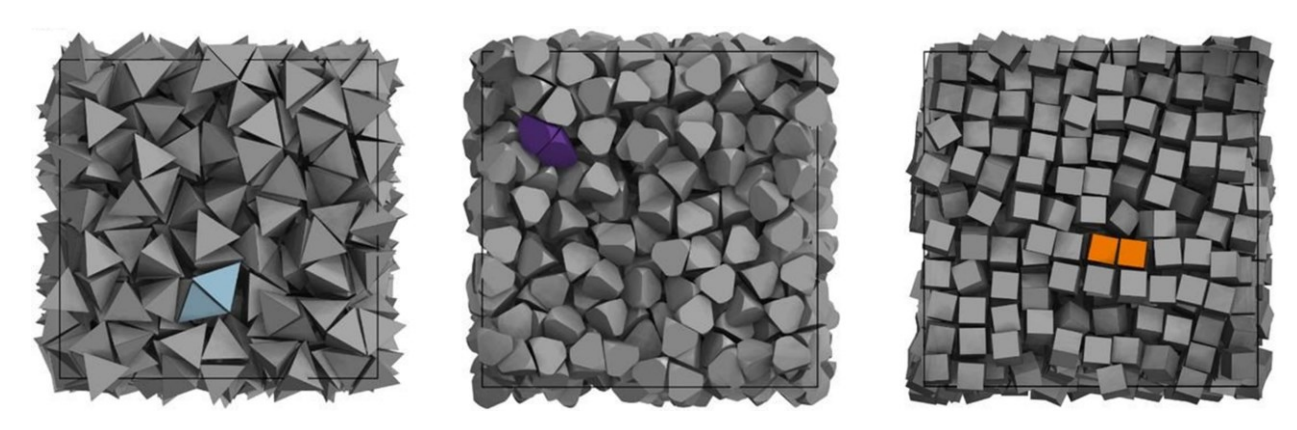


Figure 1. 8. The effect of the shape, topography, and topology of non-spherical particles is demonstrated to exert control over their packing and assembly through directional entropic forces. These forces lead to the alignment of particle faces that share similarities in one of these characteristics, resulting in parallel orientation. This phenomenon underscores the significant influence of directional entropic forces in guiding the organization of non-spherical particles^[10] (Reproduced with permission, Copyright 2014, National Academy of Sciences).

The computational studies mentioned above have primarily focused on thermal systems, where crystallization and entropy are driven by length scale and thermal fluctuations. However, granular material systems are athermal and far-from-equilibrium. Therefore, discrete element modeling (DEM) has emerged as a key tool for simulating granular polyhedra in such systems. Several research groups have employed DEM to assess the packing behavior of polyhedral blocks[124-128]. In the DEM approach, these blocks are treated as rigid bodies. Different DEM codes specifically designed to rapidly simulate the dynamics of both spherical and non-spherical blocks, as illustrated in Figure 1.9. Similarly, the packing behavior and contact forces among various polyhedral blocks have been simulated using DEM. In the context of predicting self-assembly processes, DEM models have been used to forecast the self-assembly of magnetic spherical nanoparticles[112-116]. These studies demonstrated the potential of DEM in efficiently and accurately modeling the dynamic behavior of polyhedral blocks. Despite these advancements,

it is noteworthy that the self-assembly of meso-scale non-spherical and polyhedral blocks has not yet been extensively simulated based on the studies reported in the literature.

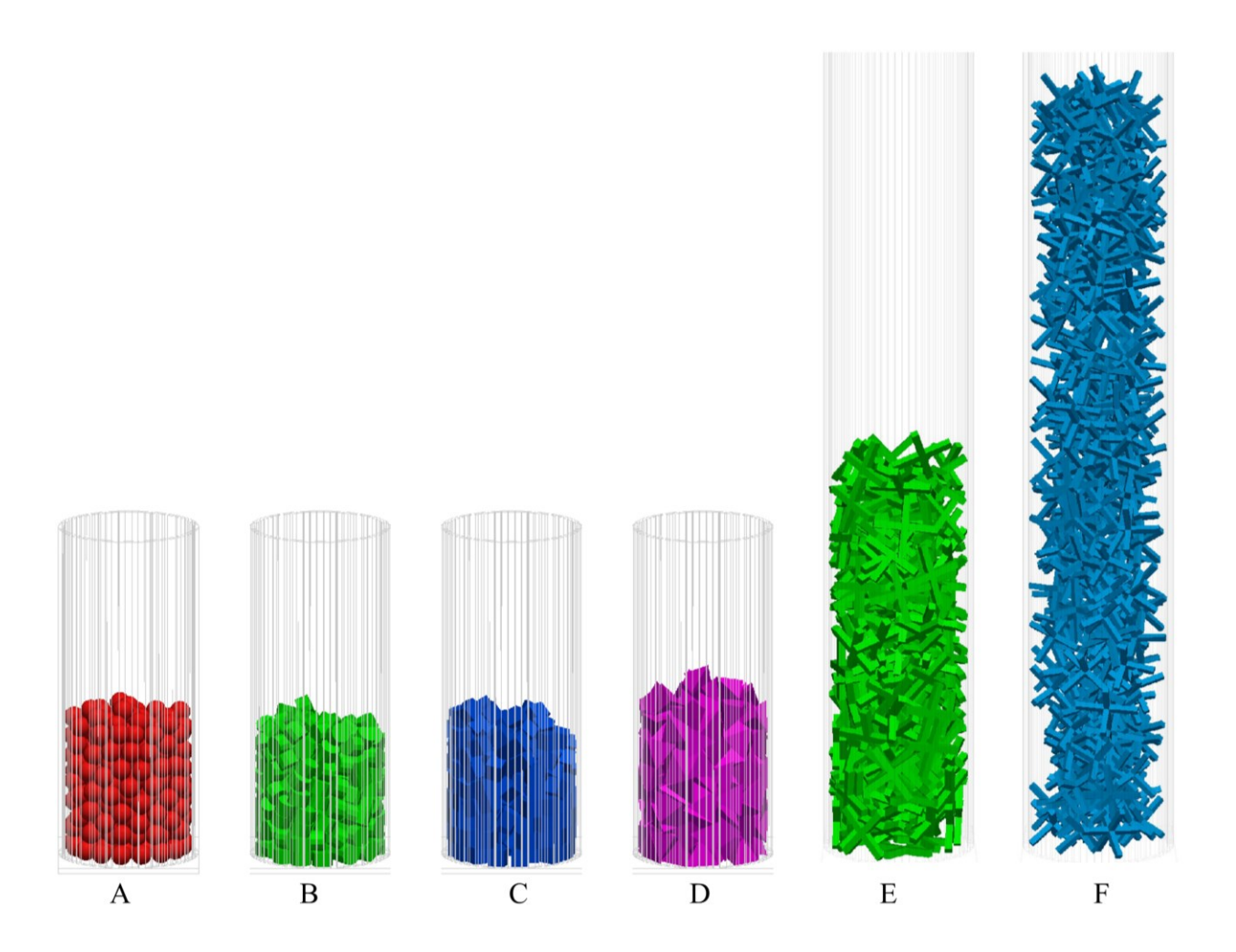


Figure 1. 9. The packing configurations of 250 particles of six different shapes within a cylindrical container using discrete element modeling (DEM) for (A) spheres, (B) cylinders, (C) cubes, (D) tetrahedra, (E) 2D cross and (F) 3D cross^[125] (Reproduced with permission, Copyright 2018, Springer Nature).

1.3.6 Mechanisms of Hemostasis, Fibrinolysis, and Wound Healing

In response to injuries, a cascade of events orchestrates hemostasis, preventing excessive blood loss. These mechanisms involve primary and secondary hemostasis, alongside fibrinolysis, each essential for maintaining vascular integrity (Figure 1.10). Primary Hemostasis: Upon injury, subendothelial collagen and von Willebrand factor (vWF) are exposed, along with tissue factor (TF) from surrounding cells. Platelets adhere to these exposed surfaces via interactions with

collagen and vWF. Subsequent platelet activation and aggregation, facilitated by fibrinogen-mediated bridging, culminate in the formation of a platelet plug at the bleeding sites. Secondary Hemostasis: Simultaneously, the coagulation cascades, intrinsic and extrinsic, are activated. The intrinsic pathway is initiated when blood contacts negatively charged surfaces, triggering a series of reactions leading to the activation of factor X (FX). Similarly, the extrinsic pathway is initiated by TF exposed at the injury site, which activates FX directly. Both pathways converge into a common pathway where activated factor X (FXa), along with factor Va and thrombin (VIIa), forms the prothrombinase complex on the platelet surface. Thrombin generated in this process acts as a key player, converting fibrinogen into fibrin. Fibrin molecules polymerize and assemble into a fibrous network, further stabilized by crosslinking mediated by factor XIII (FXIII), ultimately reinforcing the platelet plug and forming a stable clot [11, 12].

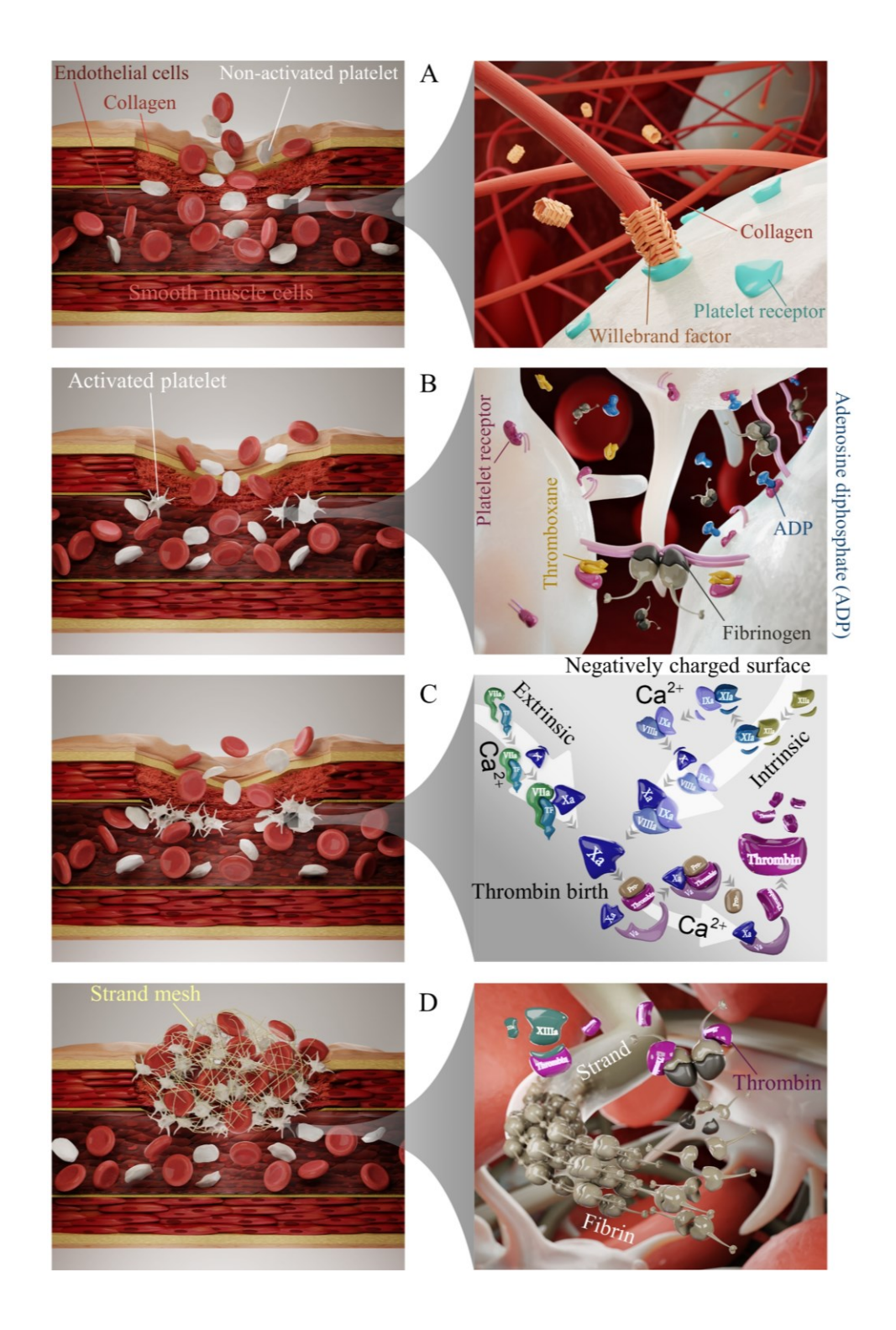
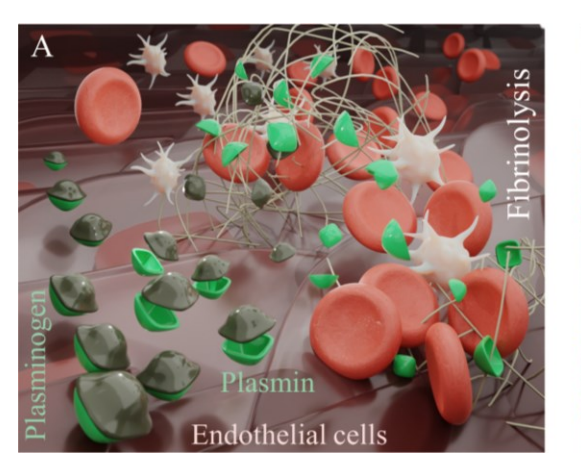


Figure 1. 10. Schematic representation illustrating the mechanisms of bleeding, primary and secondary hemostasis, and coagulation cascades.

Fibrinolysis: Fibrin, the main component of blood clots, is subject to fibrinolysis, a process mediated by plasmin, leading to the degradation of blood clots. Fibrinolysis acts as a crucial counterbalance to coagulation, preventing excessive clot formation and promoting clot resolution^[11, 12] (Figure 1.11A). Blood Clot Rupture: Blood clots, formed to seal the defect, experience mechanical loading from the blood flow and surrounding tissue, which might result in clot rupture (Figure 1.11B). Such ruptures can cause rebleeding, necessitating further hemostatic responses to maintain vascular integrity^[11, 12].



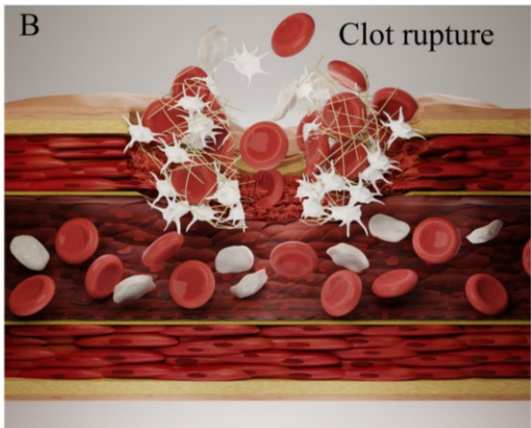


Figure 1. 11. Schematic representation illustrating (A) clot lysis process and (B) rebleeding due to clot rupture.

The process of wound healing unfolds through four consecutive yet overlapping phases (Figure 1.12): hemostasis, inflammation, proliferation, and remodeling. Hemostasis, the initial phase, comprises two primary stages. In the first stage, platelets adhere to the injured site and become activated, subsequently aggregating to form a platelet plug. In the second stage, thrombin generated via extrinsic and intrinsic coagulation pathways converts fibrinogen into fibrin, facilitating the formation of a thrombus with platelet clots and blood cells. The transition from hemostasis to the inflammation phase is marked by the release of mediators and cytokines that stimulate fibroblast proliferation, leading to collagen production. Concurrently, inflammatory cells adhere to the fibrin network established during the hemostatic phase, facilitating wound clearance by eliminating phagocytic cell debris and bacteria. The inflammatory phase typically persists for the initial days of wound healing. Subsequently, the proliferation phase unfolds over several weeks, characterized by the formation of granulation tissue, angiogenesis-driven neovascularization, and

epidermal regeneration. Lastly, the remodeling phase commences approximately 2–3 weeks postinjury, extending for a year or more. During this phase, the wound healing processes gradually diminish, while tissue remodeling occurs, ultimately restoring the mechanical properties of the skin^[11, 12].

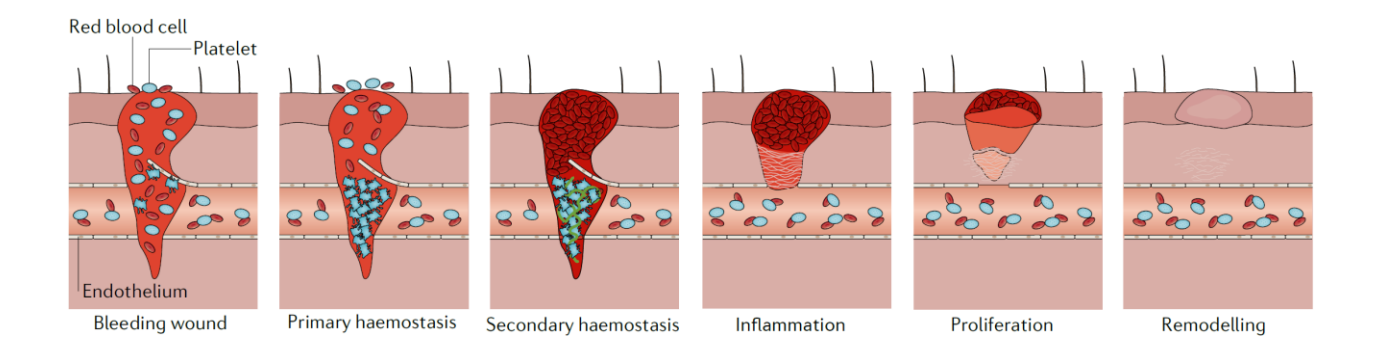


Figure 1. 12. Schematic representation illustrating the phases of wound healing^[11, 12] (Reproduced with permission, Copyright 2021, Springer Nature).

1.3.7 Soft Cellular Inclusions within Clot-like Materials

Active matter is a ubiquitous far-from-equilibrium class of condensed systems existing in living and nonliving materials. These material systems consist of active inclusions interacting with each other and their living medium enabling dynamic collective motions, self-organization, and mechanical reactions^[13-15]. Examples of nonliving active inclusions include granular materials, suspensions, colloidal nano and micro particles, collective robots, while living and/or biological active inclusions include prokaryotic and eukaryotic cells, bacteria, terrestrial, aquatic, and aerial flocks^[13-15]. The far-from-equilibrium characteristics of active matter turn them into highly potential emerging materials and/or structures benefiting from unusual and/or tunable mechanical and rheological properties, collective behavior, mesoscale pattern formation, order-disorder phase transitions, and wave and oscillation propagation^[13-15]. These characteristics in living active matter systems enrich with dynamic and active organization, adaptation, regeneration, and spontaneous motion due to numerous internal and external stimuli^[13-15]. Many natural soft active materials comprise a large volume fraction of cellular inclusions embedded within fibrous biopolymeric networks. They are exemplified by blood clots, where a fibrin network enwraps and deforms by blood cells, such as red blood cells (RBCs) and platelets (Figure 1.10 and 1.13). Such clot-like

materials also encompass biological tissues, tumors, organoids, and bacterial biofilms^[12, 16-18]. Their formation often entails the self-assembly of cellular inclusions within their biopolymer fluid medium (Figure 1.13 and 1.14), a process sensitive to external stimuli.

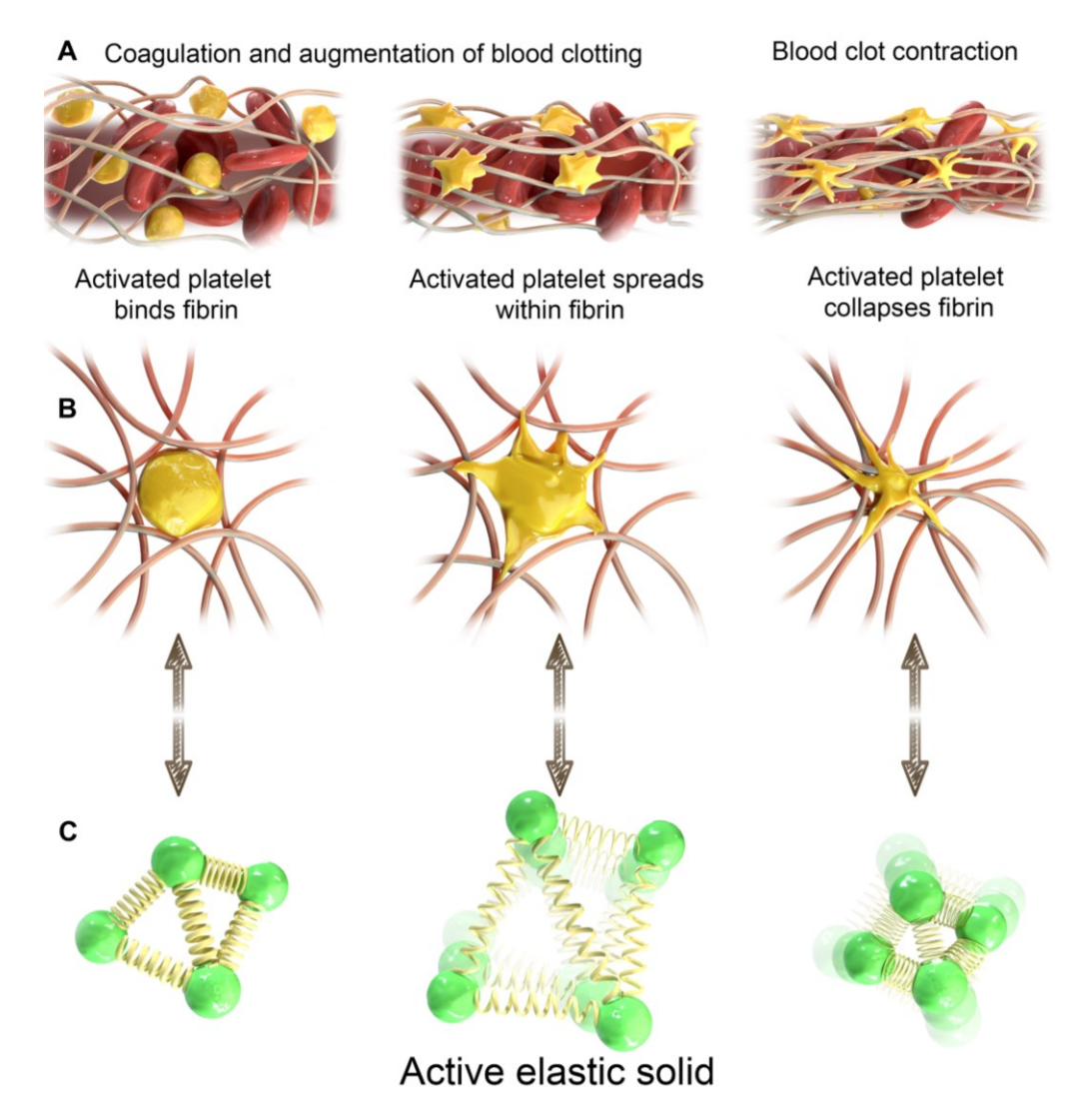


Figure 1. 13. Blood clot contraction and its analogy with active elastic solid behavior. (A) Progression from initiation of blood clot contraction to linear contraction phase and final mechanical stabilization. (B) Sequential steps involving fibrin receptor activation, activated platelet binding, spreading, deformation, and contraction, leading to fibrin collapse. (C) Analogy between the blood clot contraction process and the behavior of active elastic solid matter.

The formation of clot-like materials inherently is a self-assembly process of active soft inclusions (cells and/or spheroids) within their biological fluid medium under internal and external stimuli [11, 12, 16-18] (Figure 1.10, 1.13, and 1.14). Clot-like materials are transient microstructures,

blood clots for example formed through the hemostasis and/or thrombosis process as the primary body mechanism to stop bleeding [11, 12] (Figure 1.12). Bleeding, rebleeding, thrombosis, thromboembolism, and fibrinolysis can all be linked to the structure-property responses of blood clots which mostly stem from the three-dimensional architecture of fibrin mesh network (a fibrous extracellular matrix (ECM) protein) and the dispersion of entrapped red blood cells (RBCs) [11, 12, ^{19-21]}. However, unlike conventional polymeric materials, the formation and structure-property relations of clot-like materials under external stimulation remain relatively unexplored^[11, 12, 19-21], despite their profound implications in engineering and medicine. For instance, the ability to control how blood clots deform and fracture could help advance the treatments of hemorrhage and thrombosis. In not only blood clots but other clot-like materials such as plasma/cells tissues, the underlying mechanisms involved in the translation of micro-scale changes in the polymeric mesh architecture and cellular inclusion dispersions into meso- and/or macro-scale mechanical performance have yet to be understood^[11, 12, 19-21]. Therefore, a tunable experimental configuration is needed to systematically study these multiscale structure-property responses. Engineering clotlike materials comes with several challenges. Chemical strategies have been extensively used but limited by adverse side effects, toxicity, and specificity to the material system^[11, 12]. Alternatively, physical strategies such as magnetic, shearing, wave, and ultrasound have been used to manipulate soft active and/or granular material systems, such as the assembly and patterning of cells^[17, 22, 23]. However, none of these interesting studies have extended to the level of manipulating the threedimensional structure and mechanical properties of clot-like materials across length scales.

Ultrasound was used during fibrinolysis of fibrin clot which reduced the clot lysis time and decreased the diameter of fibers^[129]. Mechanical shear oscillation has been applied to study the microstructure and corresponding mechanical response of fibrin clots formed during perturbation^[130]. The effect of cells packing in fibrous networks due to different loading conditions on the mechanical responses of the blood clots was also explored to understand softening and stiffening differences with other tissues^[19]. The structure-property response of clot-like materials may accordingly be tuned during clot formation using external mechanical stimuli. To this end, mechanical agitation is a promising underexplored strategy, offering a facile, biocompatible, low-frequency and cost-effective way of stimulation^[17, 18, 22, 23]. Unlike ultrasound^[129], agitation yields no cavitation and thermal effects, and yet enables ordering, disordering, and phase transitioning of cellular, granular, and organoid inclusions ^[17, 18, 22, 23, 72, 73]. Extending the application of mechanical

agitation to clot-like materials could allow one to modulate the structure and mechanical properties without the need to change chemical compositions.

It is possible and can be hypothesized that at a certain level of applied mechanical agitation, the soft active inclusions (RBCs, cells) packed and/or clustered together within biopolymeric fluid (like plasma) during clotting (Figure 1.14A, B), whereas at another level of applied mechanical stimulus, most likely the higher range of agitations can non-uniformly disperse the inclusions (Figure 1.14A, C), resulting in two different clot microstructures (Figure 1.14D, E) and hence mechanical properties (Figure 1.14F, G). A comprehensive understanding of underlying mechanisms that govern vibration (mechanical agitation)-tuned structure-property response of clot-like materials is therefore needed so that method can be used as a scalable medical device and/or new therapeutic route in managing tumor therapy, thrombosis, hemostasis, drug-induced bleeding, and/or stopping surgical and traumatic hemorrhage. It can also be used to understand how the biophysical structure-property response of clots and tissues under various physiological conditions can alter embolization, disease and/or lead to cellular dysfunction. The vibration-induced system can also be used to engineer living materials, study cell (inclusion)-ECM interaction and explore other emerging biological, biomimetic, and bioengineering material systems^[11, 12, 19-21].

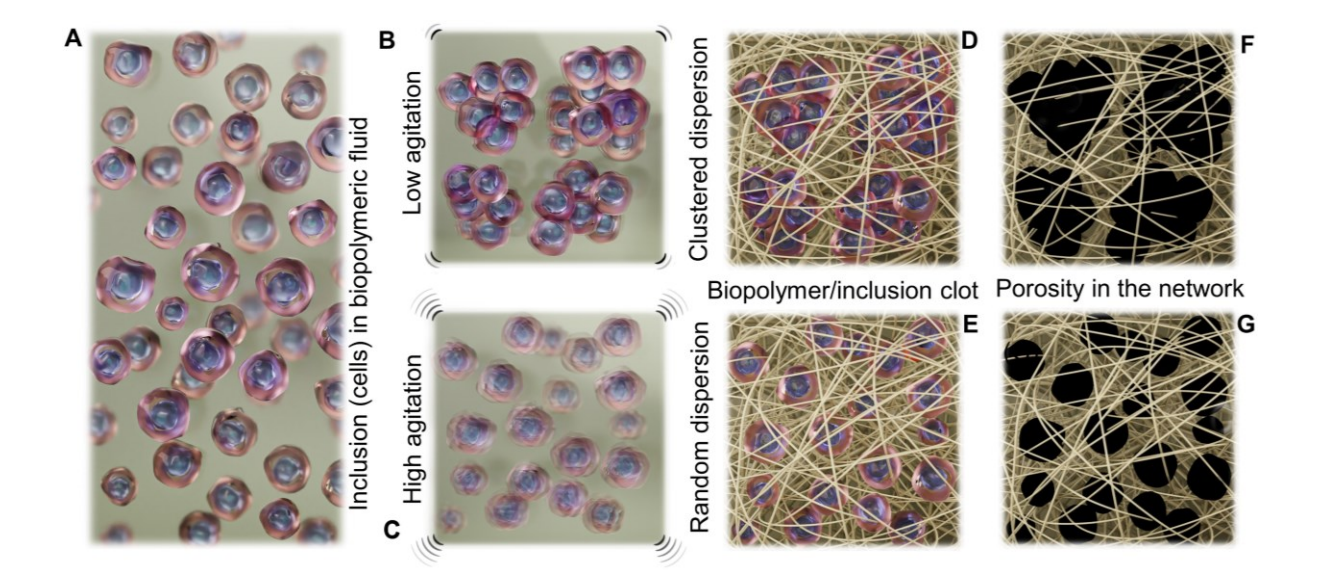


Figure 1. 14. Schematic of possible microstructures of clot-like materials under external mechanical agitations and experimental configurations. (A) Soft inclusions (cells) within biopolymeric medium; (B) inclusions clustering under low energy vibrations within biopolymeric medium; (C) non-uniformly dispersed inclusions under high energy vibrations within biopolymeric medium; (D) fixing the position of clustered inclusions due to clotting under low energy vibration; (E) fixing the position of randomly dispersed inclusions due to clotting under high energy vibration; (F) large porosities within biopolymeric network due to the inclusions clusters; G) homogenous porosities within biopolymeric network due to inclusion random dispersion.

1.4 Dissertation Objectives

Specific aim 1: Developing an assembly system to fabricate dense and segmented block-based architectured topologically interlocked materials/structures and understanding the underlying mechanics and physics of the process experimentally.

To accomplish this first specific aim, several objectives needed to be addressed. Firstly, it was imperative to investigate the vibration-induced assembly, crystallization, or interlocking of a monolayer panel using stiff polyhedral blocks, or "grains." This emphasis on stiff polyhedral blocks was essential as it facilitates easier interpretation of results and comparisons with models due to the absence of plastic yielding and their relatively high hardness. Additionally, it was necessary to comprehend the impact of various block geometries tessellated from the same medial section. Identifying limiting shapes that are impractical and unstable in this assembly process was

crucial to understanding the system's constraints. Characterizing the assembly phase diagram of this granular system through diverse combinations of applied vibration amplitudes and frequencies, along with employing object tracking image analysis, was another essential objective. This allowed for the evaluation of packing efficiency and the identification of different phase transitions within the system. Furthermore, it was required to determine the applicability of these findings to the construction of free-standing large pieces of materials or structures. This assessment would provide insights into the practical implications and potential real-world applications of the research.

Specific aim 2: Generating versatile discrete element models serves multiple purposes: Duplicating experimental assembly process and phase diagram characterization experiments and investigating underlying mechanisms at the grain level length scale using single individual block models.

To accomplish this aim, these models need to accurately replicate and capture the behavior observed in experimental setups, including the vibration-induced assembly and phase transitions. By adjusting parameters such as grain geometries and properties as well as vibration amplitudes and frequencies, the models need to simulate a wide range of experimental conditions, allowing for comprehensive exploration of the system behavior. Moreover, these models need to enable the study of individual block interactions, providing insights into the underlying mechanisms governing the packing, interlocking and phase transitions. Overall, versatile discrete element models are invaluable tools for both replicating experimental results and delving into the fundamental mechanisms driving granular assembly processes. They facilitate deeper insights and offer a platform for hypothesis testing and scenario exploration beyond the limitations of physical experiments.

Specific aim 3: Developing and investigating a physical strategy for engineering clot-like materials based on the principle of mechanical agitation, aiming to explore its efficacy in modulating a diverse range of material properties and mechanical performance experimentally and numerically.

This aim encompasses utilizing tailored agitating platforms and blood clots as a model system to explore the influence of agitation on stiffness, fracture toughness, lysis, and active contraction. The research will employ a combined experimental and simulation approach to uncover the underlying mechanism by which agitation-mediated cellular organization impacts

both microscopic structure and macroscopic mechanical responses within the fibrin network. Furthermore, the objective includes assessing the principle applicability across various material systems and validating its effectiveness through in vitro and in vivo animal experiments. Overall, this strategy can be a low-cost, noninvasive, scalable solution for manipulating and studying clot-like tissue and living material systems, with potential applications spanning various medical contexts. This approach could advance management of conditions related to thrombosis, hemostasis, and traumatic hemorrhage. It can also paves new avenues for tissue engineering and engineered living materials. The proposed agitation platform and models have broad applications beyond medicine, offering insights into the biophysics of active and granular matter. Overall, our research highlights the multifaceted potential of mechanical agitation as a versatile tool in both medical and bioengineering realms.

CHAPTER 2

Materials and Methods

This chapter presents the experimental and computational methodologies employed, along with the materials used throughout this dissertation. The chapter is structured into six main sections, each with several subsections. The first section covers the fabrication and design of diverse polyhedral blocks, as well as the synthesis of various clots containing cellular inclusions. The second section describes the experimental setups and configurations, encompassing mechanical agitation platforms, imaging systems, test specimens, lysis procedures, and in-vivo setups. The third section focuses on mechanical tests and characterizations. Moving on, the fourth section explains in-vitro cell culture and confocal imaging techniques applied to both agitation-mediated and native fibroblast cells, as well as fibrin and blood clots. In the fifth section, attention is given to short- and long-range spatial analyses of cells and fibrin fibers within agitation-mediated and native blood clots. Finally, the sixth section describes discrete element and finite element computational simulations.

2.1 Fabrication and Synthesis

This section outlines the systematic designs of polyhedral blocks and provides comprehensive details on their fabrication processes. Furthermore, it explains the systematic variation of clots laden with different cellular inclusions, accompanied by detailed descriptions of the fabrication procedures involved in incorporating these inclusions.

2.1.1 Polyhedral Blocks

Geometrical design: To design the individual blocks considered here in this study, we used a protocol developed by Dyskin et al. [36, 131], where individual blocks are constructed from their medial section, chosen to tessellate the plane (which becomes the medial plane in the TIM panel). We first considered $l \times l$ square medial sections for the individual blocks, which we then extruded to form $l \times l \times h$ square prism (Figure 2.1A). Based on this shape, truncated tetrahedra are produced from the square medial section by tilting one opposing pair surfaces of the square prism inward by an angle α , and the other remaining opposite pair surfaces outward by the same angle (Figure $(2.1A)^{[2]}$. We isolated the effect of geometry by fixing l = 5 mm and adjusting h from 4.7 mm (square prism) to 5 mm (truncated tetrahedron). In this way, the areal density ($\rho V/S=1.09 \text{ g/cm}^2$, ρ is the density, V is the volume of one block, and S is the area of medial section) of both square prism and truncated tetrahedron remains constant. We also consider hexagonal medial sections, which formed hexagonal prisms after extrusion (Figure 2.1B). The edge length of hexagonal medial section was set to a=3.25 mm, while the thickness h was adjusted from 4.3 mm (hexagon prism) to 5.3 mm (octahedron) to maintain a constant areal density. The truncated octahedra are created from the hexagonal medial section by tilting six side surfaces of the hexagonal prism: alternating every other surface inward and outward by the same interlocking angle $\alpha^{[2]}$. For each medial section, α was varied from 0° to 20°, creating truncated tetrahedron and octahedron (Figure 2.1A,B). Our objective was to work at the millimeter scale to ensure that the granular systems were thermodynamically athermal and far-from-equilibrium during applying external agitations. Then, blocks at millimetric size were chosen because they are relatively easy to fabricate with a high geometrical control. The assembly of these blocks into interlocking structures is shown on Figure 2.1C. We focused on these geometries because (i) the effect of different block geometries tessellated from the same medial section on the vibration-driven assembly and crystallization has to yet be explored; (ii) blocks that can interlock are superior to other tessellated blocks in generating high-performance mechanical responses for TIMs^[2]; (iii) the interlocking of these geometries achieves when they stand on one of their flat faces by which they are stable on the assembly platform (a flat substrate)—a practical advantage for the vibration-driven assembly

process. There are other geometries that tessellated by increasing α beyond 20°, which produces the limiting cases of tetrahedron (square medial section) and rhombohedron (hexagonal medial section) (Figure 2.1D)^[2]. However, in practice these geometries are highly unstable, and the blocks tilted on their side during the experiments.

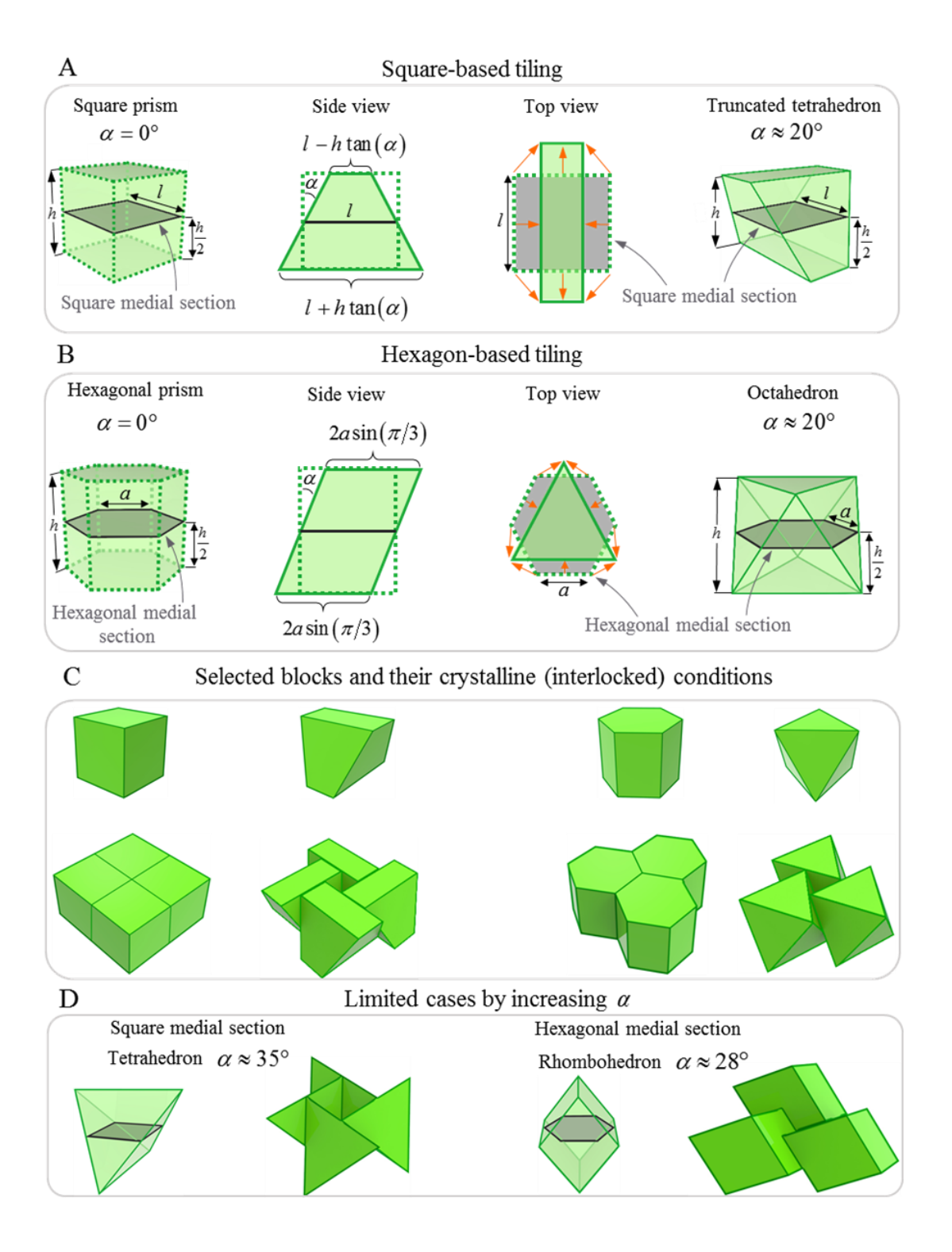


Figure 2. 1. Overview of four blocks categorized based on their medial section (A) square-based tiling; (B) hexagon-based tiling: For each category, the tessellation from the basic prism geometry to the truncated version; (C) the crystal and/or interlocked conditions for each geometry; (D) the limited geometries for vibration-driven assembly generated by increasing α in each medial section.

Fabrication: We produced the blocks described above using a replica casting method with calcium sulfate, using a method described in a previous report^[2, 132] and visualized in Figure 2.2 which creates dense and homogeneous blocks with uniform geometry and smooth surfaces. We used calcium sulfate (also known as gypsum or plaster of Paris) which is relatively easy to work with because it can be formed and cast at room temperature. In addition, the interpretation of the results and comparisons with models is made easier by the absence of plastic yielding and relatively high hardness compared to polymers. For this work, we used the strongest type of calcium sulfate plaster (CaSO₄ type V from Suprastone, Kerr Dental, Charlotte, NC) with an optimized casting method that maximizes density and strength^[132]. The density (ρ) of our calcium sulfate was 2.3 g/cm3, the measured modulus E=11 GPa, and the measured compressive and tensile strength were 90 and 31 MPa^[132]. Finally, we chose calcium sulfate because the lowest resonant frequency of the blocks (approximated by $(\pi/l)\sqrt{E/\rho} \sim 1.43$ MHz) was orders of magnitude higher than the frequency of the vibrations we used for assembly (order of 1 kHz). The modulus and density of the material also govern the time scale of the contact interactions which we wanted to be much smaller than other characteristic time scales in the problem.

Replica casting technique Cube Truncated tetrahedron Hexagon Octahedron 3D-printed polyhedra building blocks Metallic cast Mold cavities Molded CaSO₄ polyhedra building blocks CaSO₄ slurry Blotting paper Molded CaSO₄ polyhedra building blocks

Figure 2. 2. Replica casting technique used for producing calcium sulfate polyhedral blocks.

2.1.2 Clots Laden with Cellular Inclusions

Blood clot: Bovine blood was used as a model system for human blood in this study^[133-135]. The bovine whole blood (Lampire Inc.) was gender unspecified and collected in citrate-phosphate-dextrose solution anticoagulant (14% to volume of the final product), while it kept at 4°C and thawed at room temperature before usage. For the blood clot formation, we initiated the coagulation cascade (activating clotting factors and crosslinking fibrinogen into a fibrin network by adding the recalcification solution (sodium chloride (90 mM, Sigma Aldrich) and calcium chloride dihydrate (300 mM, Sigma Aldrich) mixed with the tissue factor by 249:1 volume ratio)

to the bovine whole blood samples, while the final blood volume to the recalcification solution volume remained constant by 9:1 (more details described in Refs [136, 137]).

Plasma clot: To obtain plasma, citrated whole blood was centrifuged at 300g for 15 min (room temperature). The separated platelet-rich plasma was carefully extracted (down to about 0.5 cm above the buffy coat) and again centrifuged at 1200g for 10 min (room temperature) to isolate the platelets. The separated plasma was carefully collected (without disturbing the platelet pellet) and kept at -80 °C while it was thawed at room temperature before use^[138, 139]. We formed the plasma clots using the same protocol and amount of recalcification solution as in blood clots experiments.

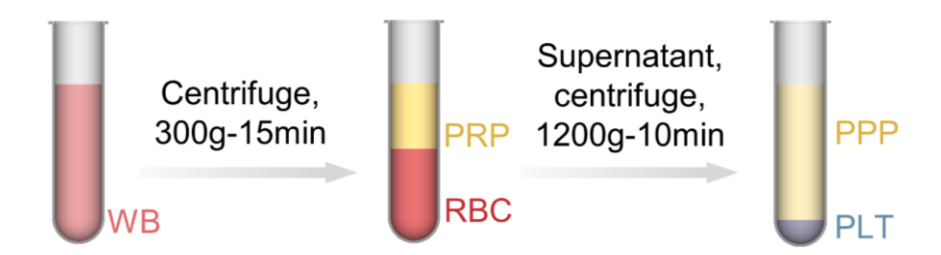


Figure 2. 3. Obtaining poor-platelet plasma (PPP) from whole blood clot (WB). Platelet rich plasma (PRP) first is separated from red blood cells (RBC) and then PPP is separated from platelets (PLT).

Fibroblast cells/Plasma clot: We used human vocal fold fibroblast cells for the study as fibrin scaffolds have been previously demonstrated to promote differentiation and proliferation of adipose-derived stem cell to fibroblast-like cells^[140]. They also exhibited attachment to the fibrin network, and whose interactions with the network were of interest for rheological studies and actin stains. Fibroblast cells were cultured at 37 °C and 5% CO₂ in high-glucose Dulbecco's modified eagle medium supplemented with 10% fetal bovine serum and 1% penicillin–streptomycin, which was changed twice weekly, and were grown to 80% confluency before each passage. Fibroblast cells of passage 15-20 were used, and for each sample, 1.79 × 107 cells were trypsinized, centrifuged, and then resuspended in 500 μL platelet-poor plasma to reach an approximate cell volume fraction of 15% (assuming each fibroblast cell is spherical with radius 10 μm).

Microgels/Plasma clot: To fabricate chondroitin sulfate sodium (CS)+ agarose microgels, we first prepared polyelectrolyte solutions by dissolving CS (20 wt.%) in deionized water and stirring overnight. Agarose powder (20 mg), CS (450 mg, 20 wt.%) and deionized water (0.53 mL)

were mixed and then heated at 90°C under stirring for 30 minutes. We then followed the batch emulsion method procedure to form microgels: The hot aqueous mixtures were added to a mineral oil solution containing Span80 (2 wt.%) at 90°C under constant stirring. The water-in-oil emulsion was stirred while cooled at room temperature for agarose gelation. The obtained microgels were then centrifuged at 4000 rpm for 3 minutes, and the supernatant was discarded. We removed mineral oil from microgels using the following steps: Ethanol (30%) was added to the microgel containers and mixed by vortex mixing for 1 minute; this mixture was then centrifuged, and the supernatant was discarded. This process was repeated twice with ethanol (30%) and thrice with deionized water^[141-143]. The mechanical properties of the CS+agarose microgels after jamming were measured by the rheology test (rheometer) at 1Hz oscillatory rate and 0.1% strain rate. The storage and loss moduli were 9 kPa and 0.5 kPa with 0.4 kPa yield stress at 15% yield strain. We used the same procedure as the plasma clot experiments for this material system (plasma/microgels) while the microgel volume fraction was fixed at 15~17%.

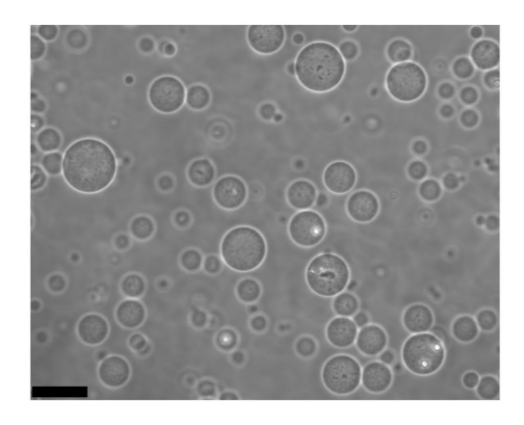


Figure 2. 4. Synthetized microgels under microscope; the scale bar is 50 μm.

2.2 Setups and Configurations

This section outlines the designs of vibrating and agitating platforms used for the assembly of polyhedral blocks, the engineering of clot-like materials, and in-vivo experiments. It also describes the experimental tools integrated with these platforms, such as image object tracking systems and laser vibrometers. Finally, it provides detailed information on the lysis test setup.

2.2.1 Vibrating Platform for Hard Architectured Materials

The experimental setup used to assemble and/or crystalize the hard polyhedral blocks consisted of a polymethylmethacrylate (PMMA, E=2.9 GPa) square assembly platform with edge walls of precise geometry that conform the geometry of the blocks to serve as assembly templates on each side, glued onto a voice coil with either a 45W/60W-RMS/peak power capacity and a frequency response range of 45 Hz~4 kHz, or a 120W/240W RMS/peak with a frequency response range of F₀~1 kHz (depending on which particular range of amplitudes and/or frequencies we explored in the experiments). The voice coil assembly platform was mounted on a tilting angle platform set to an angle of 10° directed along a direction aligned with the diagonal of the assembly platform (i.e., the lowest point of the platform was a corner of the platform). The tilt of the platform and the friction were such that the cubes did not move without vibrations. A laser vibrometer was used to calibrate the amplitude and frequency of the platform, and a high-speed camera was used to monitor the trajectory of the blocks during assembly. We explored the assembly response of the blocks subjected to a broad range of amplitude (1 to 100 µm with 5 µm intervals) and frequency (10~1000 Hz with 50 Hz intervals). Sixty four blocks were fed onto the vibrating platform in a way that was continuous but with random time intervals (0.1~1 second) for the drops and landing spots (Figure 2.5A). We used a sinusoidal waveform because it can be generated using a speaker without significant signal overshoot and also additional inertia of the assembly platform. Figure 2.5A,B shows a schematic of a high-speed camera view that was used to monitor the possible mechanisms involved in the vibration-driven assembly process and to measure the final packing factor at the actual steady-state condition (Figure 2.5C). Figure 2.5B also shows the mobility of the octahedron blocks toward their minimum potential energy position (the lowest corner of the platform).

Image analysis and object tracking: Once the assembly was complete (that is when the position of the blocks did not change anymore), the packing and/or interlocking efficiency was measured using image analysis, where the domain of blocks in the binarized images was closely captured by bounding contour (Figure 2.5C) using "boundary function". We defined the steady-state packing factor (PF) as the sum of the projected top surface area for each block divided by the bounding contour area (Figure 2.5C), which is the outer boundary of the block assembly. For each geometry, we conducted 400 combinations of amplitudes and frequencies and repeated these combinations five times and measured the average packing factor from these repetitions, which in total is 2000 tests. The obtained packing factor was then normalized by the theoretical maximum

packing factor for each block geometry. In this way, the unique packing and interlocking conditions of each geometry can be defined and comparable; for example, normalized packing factor 1 represents perfectly interlocked and/or crystalline for all geometries.

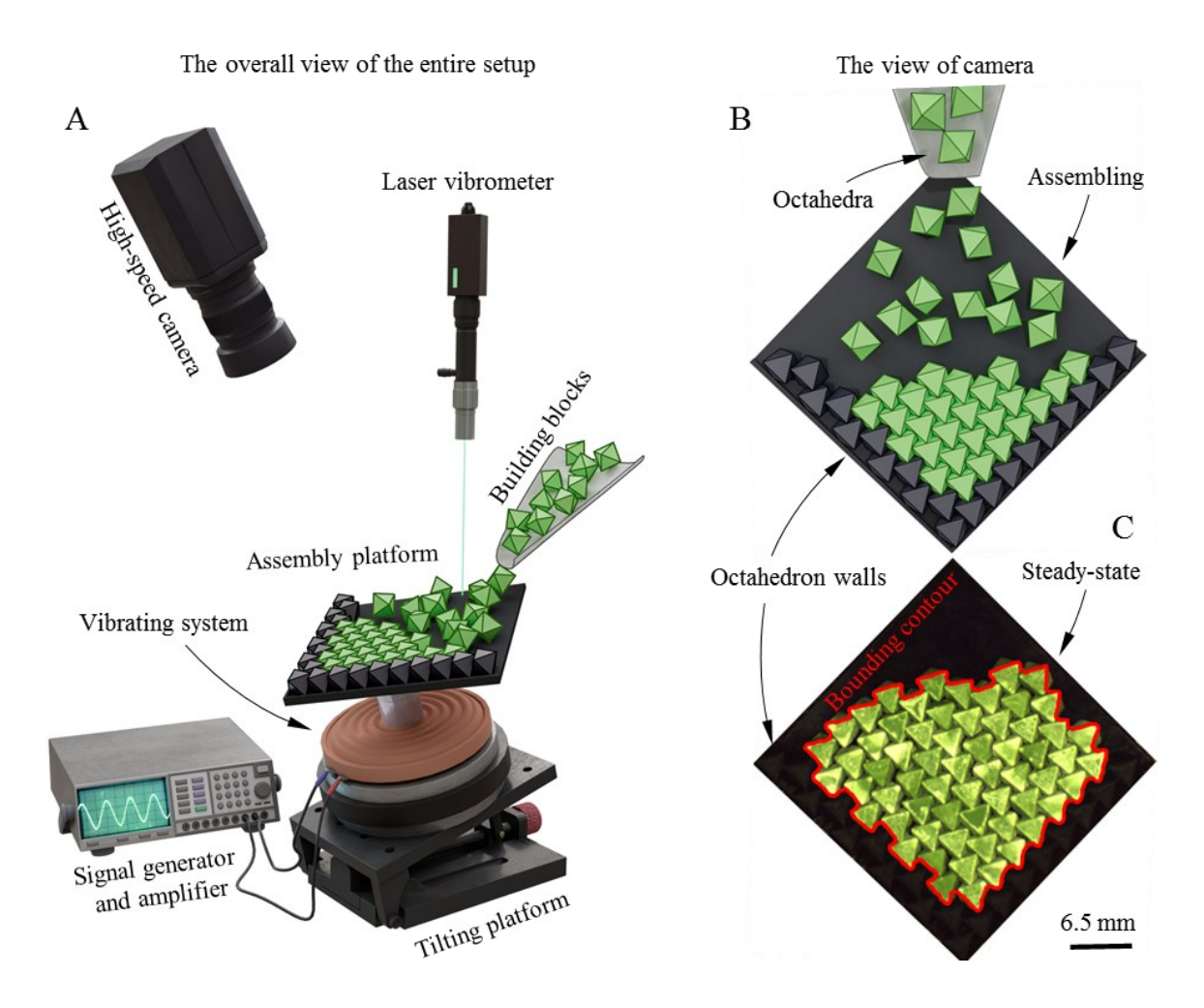


Figure 2. 5. (A) Schematic of the vibration-driven assembly process integrated with a high-speed camera and laser vibrometer. (B) Polyhedral blocks are randomly dropped on the tilted assembly platform with block-like walls (template) while it is vibrating. (C) Crystalline (interlocked) packing at steady-state condition measured by image analysis through overlaid bounding contour.

2.2.2 Vibrating Platform for Clot-like Materials

The experiments aimed to explore the effect of mechanical agitation, specifically vibrationdriven perturbation during clotting on the structure-property response of blood and cell-laden plasma clots. We therefore used a customized pure shear specimen to first apply a broad range of vibrations with different combinations of amplitudes and/or frequencies. Second, to conduct mechanical tests on vibration-generated and native clots.

Pure shear specimen: To make pure shear test specimens (Figure 2.6A), we designed a gelling mold, comprising two 3D-printed rigid hat-shaped parts (78 mm × 19 mm × 10 mm) with stuck dual lock strips placed inside two separated rectangular cavities (50 mm × 16 mm × 7 mm) of a flexible silicon mold (polydimethylsiloxane, 58 mm × 42 mm × 11 mm) to create a sealed substrate for adding recalcified blood. Two more 3D-printed rigid parts (78 mm × 19 mm × 6 mm) with stuck dual lock strips were placed onto the recalcified blood or plasma; these two parts were fixed by two binder clips (one clip on each side) to maintain the stability of the entire configuration. They were later gripped by the universal testing machine, while the silicone mold and binder clips were removed prior to testing (more details described in Ref [139]). The dual lock strips merged with blood clots or cell-laden clots enabling uniform loading. Once the recalcification solution was mixed with blood or cell-laden plasma, we immediately pour the recalcified blood or cell-laden plasma into the specimen and assembled it and then placed in a sealed Ziploc bag with saturated humidity inside to maintain hydration, preventing temperature modulation on thrombin activity, platelet contractility and RBC and cells membrane rigidity. The final clot sample size within the pure shear specimen was 40 mm × 4 mm × 3 mm. There were unnotched and notched pure shear specimens, while for the notched samples, 10 mm long pre-notch was introduced by polyester 0.1 mm thin film.

Vibrating platform: The under-hydration pure shear specimen was instantly transferred to an incubator at 37°C and fixed (by two binder clips) on a 3D-printed rigid substrate (100 mm (L) × 100 mm (W) × 3 mm (H)) which was glued onto a voice coil (speaker) with a 120 W/240 W RMS/peak with a frequency response range of $F_{0}\sim1$ kHz (Figure 2.6B). The 3D-printed rigid substrate was larger than the test specimen to ensure that vibration is applied uniformly. We used a laser vibrometer to calibrate amplitude and frequency of the vibrating platform under sinusoidal waveform which can be generated by a speaker without significant signal overshoot and inertia of the platform. We explored the perturbation effect generated by broad combinations of amplitude (1-25 μm with 5 μm intervals) and frequency (10-1000 Hz with 50 Hz intervals) during clotting on the mechanical response of blood clots. The vibration was applied for 10 min—an optimum time confirmed by our preliminary experiments and also enough time for a complete γ - γ crosslinking^[12, 130]. The specimen remained in the hydration bag within the incubator for 2 h more

to fully be crosslinked and coagulated. For each applied amplitude and/or frequency 5 unnotched and 5 notched.

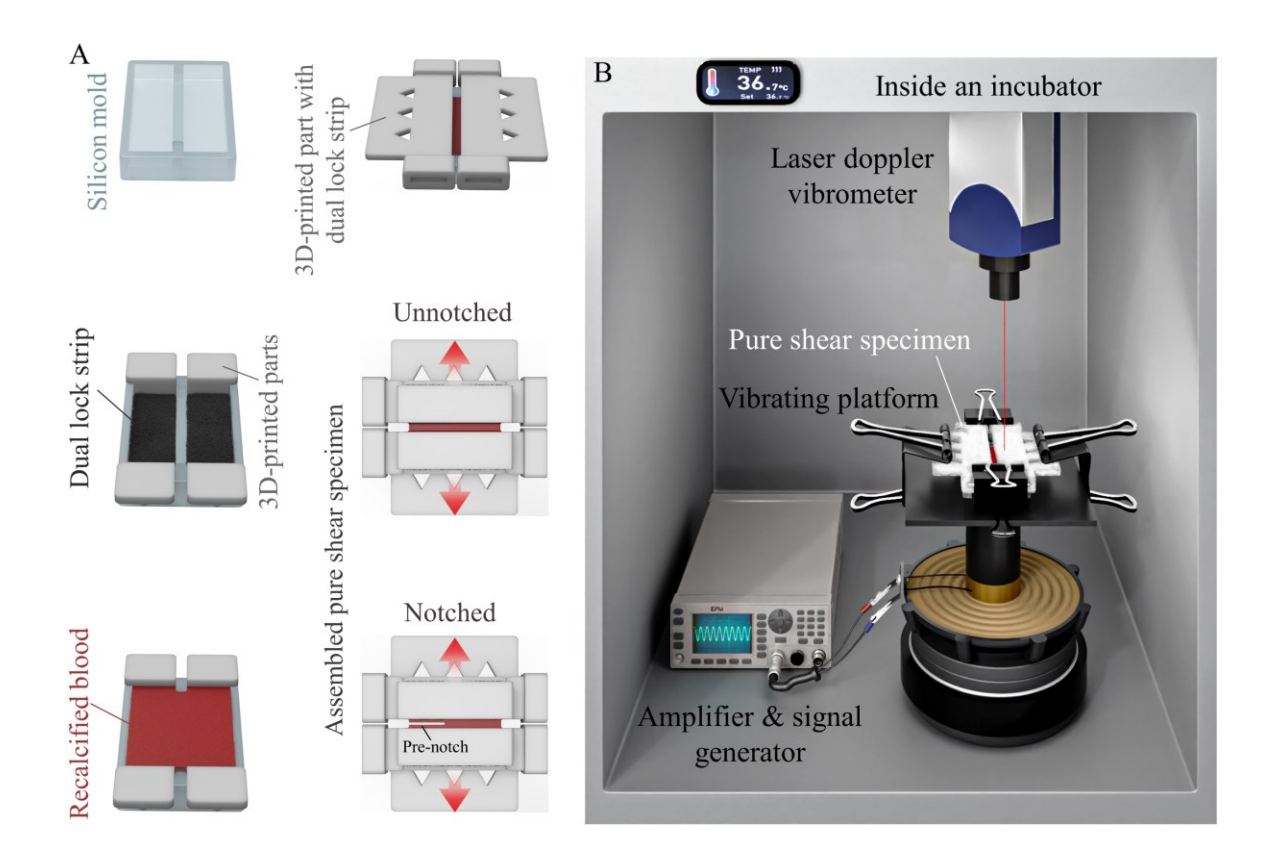


Figure 2. 6. (A) Schematics showing an agitating platform applies mechanical agitation during blood clotting in a pure-shear mold inside an incubator. (B) Step-by-step assembly of the unnotched and notched pure shear test specimen under tensile loading.

Sonication bath: To further validate the applicability of our methodology with other agitation sources, we used a sonication bath (BRANSON 2510) and prepared 5 unnotched and 5 notched samples for each sonicated and native blood clot pure shear specimen (Figure 2.7). We prepared these samples the same as in previous experiments; however, the sonicated samples were transferred to a sonication bath and sonicated for 10 minutes with 40 kHz. The rest of the process and testing protocols were the same as in previous experiments.



Figure 2. 7. Pure shear specimen within sonication bath to generated blood clots.

2.2.3 In-vivo

We used the rat liver puncture bleeding model^[144] to assess the safety and efficiency of our vibrating platform, which can be a remote device for generating on-demand blood clot properties. The objective was to measure the elastic properties of vibration-generated in-vivo blood clots on the volumetric hepatic injury. This experiment was approved by the McGill University Animal Care Committee (Protocol # 2019-8098) and performed according to the guidelines of the Canadian Council on Animal Care. The setup that we used is the same voice coil powered by an amplifier and signal generator in previous experiments; however, a Π-shape 3D-printed rigid part $(185 \text{ mm (L)} \times 52 \text{ mm (Ø)} \times 75 \text{ mm (H)})$ was glued on the coil (Figure 2.8A) while a 3D-printed cup-like biopsy rigid tube (10 mm (\emptyset) × 20 mm (H)) was attached to the Π -shape part (Figure 2.8A,B). The amplitude and frequency of this configuration was calibrated using the same laser vibrometer used in previous experiments (Figure 2.8A). The rats were anesthetized using isoflurane (4% isoflurane in oxygen) in an induction chamber while it maintained at 2% isoflurane using a nose cone during the surgery. A volume of 1 mL of saline was injected subcutaneously and then abdominal hair was removed. The rats were placed over a heating pad for the duration of the surgery and experiment. The liver was exposed via a laparotomy and then a volumetric injury of 4 mm diameter and 3 mm depth was made to the liver using a biopsy punch (Figure 2.8C). The vibrating cup-like biopsy tube was immediately placed on the punctured liver in a way that sealed the wound area without any blood leakage (Figure 2.8D) for 10 minutes (enough time to form a clot, same as previous experiments) at 7µm amplitude and 500Hz frequency for 5 vibrationenhanced samples across 5 rats trials and at 1.5µm amplitude and 1000Hz frequency for vibration-degraded samples across 5 rats trials, where these amplitudes and frequencies produced the highest and lowest mechanical properties in blood clot experiments, respectively. The 5 native samples were generated using the same cup-like biopsy tube without applying vibration. The generated blood clots were collected from the liver by a scalpel (Figure 2.8E) and stored in a sealed Petri dish with saturated humidity inside to maintain hydration. The rats were euthanized by 5% isoflurane induction followed by CO₂ inhalation. The blood clot samples were immediately transformed and tested using a rheometer which is described in the next section (Figure 2.8F).

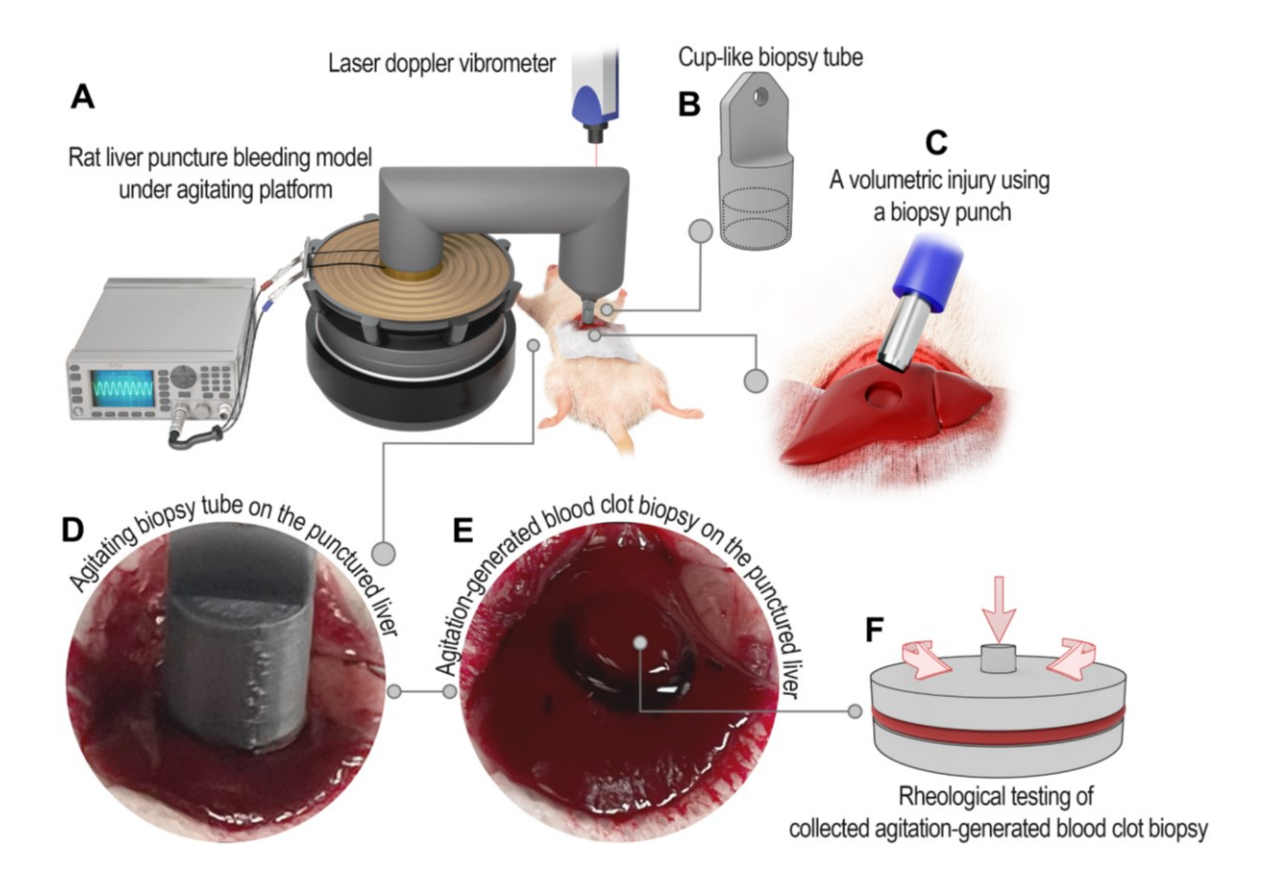


Figure 2. 8. Demonstration of agitation-mediated clotting with a rodent liver bleeding model in vivo. The agitation is applied with a customized in vivo agitating platform (A) and a cup-like biopsy tube (B). A volumetric injury is made with a biopsy punch (C) and receives agitation on site (D). The resulting clots (E) are tested with a rheometer (F).

2.2.4 Fibrinolysis

Our objective here was to comparatively examine the mass deduction (degradation) over incubation duration (time) of native and vibration-generated blood clots when they are under fibrinolysis condition. A couple of common methods have been used to readout fibrinolysis, yet they mostly are practical for plasma clots alone^[145]. We therefore devised a protocol to implement a fibrinolysis test on the whole blood clots. Although we used the same procedure to form native and vibration-induced blood clots, 3 samples for each group were prepared in a well plate containing 1ml blood with a final clot thickness of 2.5 mm. The samples were washed with phosphate-buffered saline (PBS) solution to remove all generated calcium and recalcification solution and then incubated within a transwell insert (Figure 2.9) pre-loaded with pre-warmed (37 °C) 400 ng/ml^[146] tissue plasminogen activator (t-PA) and 4 ml platelet-poor plasma solution. In this way, t-PA can activate plasmin enzymes from the plasminogen in the serum and plasma to breakdown the fibrinogen in blood clots (Figure 1.11A). We then measured the weight of blood clots (clot remained in transwell insert) every 10 minutes while all liquid remained in the chamber.

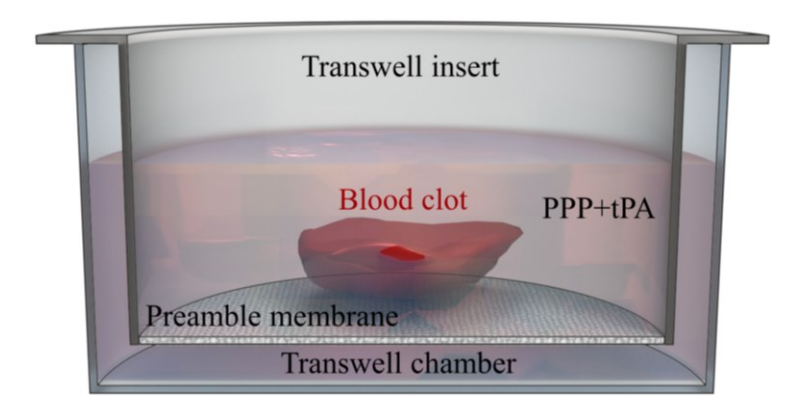


Figure 2. 9. Blood clots fibrinolysis test using a transwell.

2.3 Mechanical Characterizations

2.3.1 Elastic and Fracture Toughness Properties

For each applied amplitude and/or frequency 5 unnotched and 5 notched (10 mm long prenotch introduced by polyester 0.1 mm thin film) specimens were prepared and then tested at room temperature under uniaxial tensile loading with 3 mm/min displacement rate controlled by 10 N load cell in INSTRON universal machine. We calculated stress by dividing force from the load cell by the initial cross-sectional area of the specimen, which was measured using the image analysis in ImageJ. Similarly, the load cell displacement was divided by the initial height of the specimen to measure stretch. The elastic modulus (E) is the slope of linear (elastic) region of obtained unnotched stress-stretch results. We further used these unnotched results beside the notched samples data to measure the fracture toughness using the following equation [147]:

$$\Gamma' = H_0 \int_1^{\lambda_c} W d\lambda \tag{1}$$

where H_0 is the height of the specimen, λ_c is the stretch at the onset of crack propagation in the notched samples, and W is the strain energy density function which is the area under the stress-stretch curve of an unnotched sample up to λ_c .

2.3.2 Rheological Properties

Harvested blood clots from in-vivo experiments and fibroblast/plasma clots samples were tested using a single-head rotational rheometer (Discovery Hybrid HR-2, TA Instrument, DE) equipped with 10 mm and 20 mm parallel plates to determine the elastic storage modulus (G'). We run these time-sweep experiments with a rotational frequency of 1 Hz and a shear strain of 0.1% at the body temperature of 37°C. Each sample was placed on the center of the bottom plate, and the gap between the rheometer plates was adjusted using the Trios software (TA Instrument, DE) to ensure a complete filling and proper sample loading. Mineral oil sealing was applied to avoid sample dehydration during tests. We obtained the storage modulus (G') versus time and considered its plateau region as the shear modulus of our plasma/fibroblast clot material.

2.4 Cell Culture and Confocal Imaging

2.4.1 Fibroblast Cells

We used human vocal fold fibroblast cells for the study as fibrin scaffolds have been previously demonstrated to promote differentiation and proliferation of adipose-derived stem cell to fibroblast-like cells^[140]. They also exhibited attachment to the fibrin network, and whose interactions with the network were of interest for rheological studies and actin stains. Fibroblast cells were cultured at 37 °C and 5% CO2 in high-glucose Dulbecco's modified eagle medium supplemented with 10% fetal bovine serum and 1% penicillin-streptomycin, which was changed twice weekly, and were grown to 80% confluency before each passage. Fibroblast cells of passage 15-20 were used, and for each sample, 1.79×107 cells were trypsinized, centrifuged, and then resuspended in 500 µL platelet-poor plasma to reach an approximate cell volume fraction of 15% (assuming each fibroblast cell is spherical with radius 10 µm). Prior to resuspending cells for samples to be confocal imaging and then rheological testing, plasma was first combined with 3.3% of a 1.5 mg/mL solution of Alexa Fuor 488 or Alexa Fluor 547-conjugated human fibringen (Thermo Fisher). The cell suspensions were then added to 24-well plates and then quickly mixed with the recalcification solution. We prepared 9 samples for each native, agitation-enhanced and degraded group using the same agitation-perturbation procedure as our previous experiments (blood clots, plasma clots, and plasma/microgel clots). Samples were subsequently incubated for 1 hr at 37 °C and 5% CO₂ to allow for gelatin of the plasma/fibroblast clots.

A cell viability staining kit (LIVE/DEAD, Thermo Fisher Scientific) was used to assess the cell viability under agitation-perturbation. Plasma/fibroblast samples were removed from the 24-well plates following gelation, then cut into 4mm×4mm samples, placed in 35mm glass-bottom confocal dishes. These samples were cultured in the 2 mL culture medium for 24 hours prior to imaging, with medium replaced after 12 hours. The samples were washed twice with PBS then incubated in 1 mL staining solution containing 4 μM calcein AM and 4 μM ethidium homodimer-1 at 37 °C for 15 minutes. Lastly, samples were washed twice with PBS, and imaged under an LSM 800 Confocal Microscope linked with a Zeiss Axio Observer Z.1 fully motorized inverted microscopy (Advanced BioImaging Facility, McGill University) to obtain raw confocal Z-stack images. These images were collected through 488 nm excitation at 40x 1.30 NA oil immersion

plan apo-chromatic lens with 1610 x 1610 pixels. The optical resolution was 0.099µm in the xy plane and 0.1µm on the z-axis. We used ImageJ software to measure the porosity sizes of fibrin microstructure from confocal images for each group.

2.4.2 Blood Clots

We prepared whole blood fluorescently labelled by decorating the RBCs' surface with a Cy5 fluorescent probe using a DBCO-azide click reaction. The azide groups were grafted on the surface of RBCs through a reaction between primary amines on the cell surface and Nhydroxysuccinimide (NHS) esters based on the following steps. We first separated the RBCs from the plasma using the same procedure described above. The obtained RBCs were washed with PBS (to remove any endogenous amines contained on plasma proteins or other containments within the blood) and then resuspended in PBS (1:10 volume ratio). A stock solution of Azido-PEG4-NHS ester (click chemistry tools) dissolved in dimethyl sulfoxide (DMSO) (25 mg/mL) with a final concentration of 1 mg/mL and then incubated (1 hour, 37 °C) for reaction fulfillment. This mixture was then centrifuged, and the supernatant was gradually replaced with fresh PBS to remove the DMSO and unreacted products, precluding hemolysis. The modified RBCs were incubated (1 hour, 37 °C) with DBCO-Cy5 fluorescent probe (5 µg/mL, click chemistry tools) and then washed to remove the unreacted dye^[148]. Modified RBCs were then reconstituted in the separated plasma with 45% v/v of the blood consisting of the modified RBCs. A stock diluted solution of fluorescent dye-labelled fibrinogen (molecular probes fibrinogen from plasma, Alexa Fluor 488 conjugate (Thermo Fisher, Molecular Probes® F-13191)) added to the whole RBC-modified blood by 2% of blood volume to capture fibrin network under confocal microscopy. Three blood clot samples for each group of agitation-degraded (low), native, and agitation-enhanced (high) mechanical properties were then prepared on the microscope slide and incubated within moisturizing bags using the same procedure as in the experiments. We used LEICA SP8 multiphoton confocal microscope (Pharmacology & Therapeutics, McGill University) to capture raw confocal Z-stack images at 488 nm excitation with a 100x multi-immersion objective and a voxel size of $104 \times 104 \times 528$ nm.

2.5 Spatial Analysis

2.5.1 Vibration-mediated Cell Organization

Short-range analysis: The position (coordinates) of RBCs were also extracted using ImageJ. Our observations suggest that the spatial dispersion of RBCs for each group seemed different and followed a unique microstructural characteristic. It has been demonstrated that there is a close similarity between RBC and spherical dispersion; therefore, the following short- and long-range spatial analyses are reliable statistical tools to quantitively assess the RBC dispersions^[149]. We therefore spatially analyzed the degree of RBCs dispersion nonuniformity using nearest neighbor distance and radial distribution function across 3 different samples and regions of low, native, and high mechanical properties. The nearest neighbor distance (NND) function is an efficient means to assess short-range spatial analyses^[150, 151], which here indicates the distance between the centroid of each RBC with its nearest neighbor. The probability density function of the calculated first, second, and third NND for all RBCs represents the degree of dispersion non-uniformity.

Long-range analysis: We assessed the long-range spatial analyses through radial distribution function g(r) (pair correlation function), which here provides the variation of average RBC density along a distance from the centroid of an arbitrary RBC^[149-151]. To compute g(r), the number of RBCs in an imaginary circular shell with an inner (r) and outer (r + dr) radius are divided by the average number of RBCs expected in each shell. The mathematical expression can be defined based on the Ripley's K function (K(r)) (second-order intensity function) as^[149-151]:

$$g(r) = \frac{1}{4\pi r^2} \frac{dK(r)}{dr}$$
 (2)

where g(r)=1 represents the theoretical complete spatial random (CSR) dispersion, g(r)>1 can express clustering and/or agglomeration, and g(r)<1 demonstrates that the RBCs density is lower than the average value in the corresponding circular shell.

2.5.2 Microstructure of Fibrin Networks

We reconstructed 3D confocal images using an open-source Python package Qiber3D to characterize the fibrin network microstructure. This method can be operated without manual

interactions with the software, thus compatible with large datasets. It is advantageous over other methods such as 2D maximum-intensity projections. Raw 3D confocal image stacks were loaded for resampling using the Gaussian filter. After binarization and 3D reconstruction, the fiber segments were defined by fiber between two neighboring branch points (Figure 2.10). A fibrous network from one confocal image may consist of several collections of connected fiber segments. We conducted morphometric quantification^[148] and generated a database of structural parameters, including the spatial data of all the fiber segments, and their average diameters, lengths, and fiber directions. To extract the parameters from the database, we then developed a Python-based data processing script. In the fibrin network, several short fibers may laterally aggregate and crosslink, forming small clusters of fibers. The algorithm may identify the clusters as single fiber segments, which leads to an overestimation of average fiber segment diameters. Therefore, we adopted the interquartile range (IQR) method to identify and remove outliers statically. IQR value was calculated by subtracting the first quartile Q1 from the third quartile Q3. The lower limit was defined as Q1 minus 1.5*IQR, while the upper limit was obtained by Q3 plus 1.5*IQR. Data points beyond the upper and lower limits range were considered outliers and removed from the dataset.

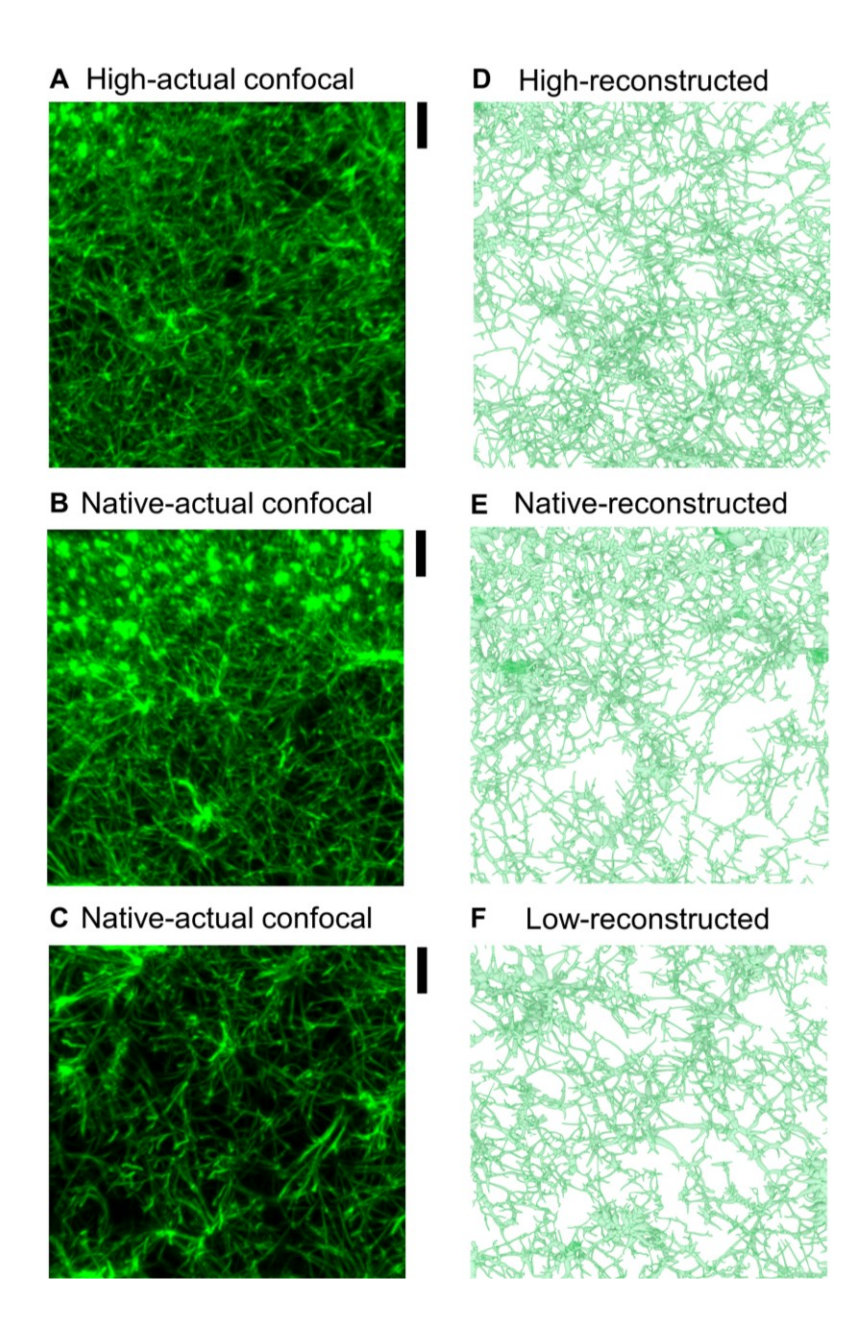


Figure 2. 10. Actual fibrin network confocal images of native and agitation-generated blood clots with their 3D reconstruction morphometric quantification. (A-C) Actual fibrin network confocal images for blood clots with high (agitation-enhanced), native, and low (agitation-degraded). (D-F) 3D reconstructed geometries of fibrin network from their confocal images for blood clots with high (agitation-enhanced), native, and low (agitation-degraded).

2.6 Simulations

2.6.1 Discrete Element Modeling

Assembly of blocks: We used discrete element modeling (DEM) to better understand the phase transition and crystallization (interlocking) of each building block geometry during vibration-driven assembly process. The open-source C++/ Python DEM solver Granoo that we used is particularly developed to model polyhedral granular blocks^[152-154]. A contact model that explicitly captures surface roughness was not used here. Instead, we used a linear frictional contact model based on the GJK-EPA algorithm^[155]. This algorithm detects collision and compute penetration distance between colliding blocks, from which a contact force is computed. We used a linear contact model where the contact is governed by a single contact stiffness, which is an acceptable approximation for intermittent contacts (this approximation of the contact also led to good agreements with the experiments). The experimental physical dimensions and properties were directly duplicated into the DEM simulations. The block-on-block static and dynamic friction coefficients were 0.4 and 0.33, and the block-on-platform static and dynamic friction coefficients were 0.38 and 0.27 (Figure 2.11 and 2.12). The block-on-block contact stiffnesses was set at 150 kN/mm and the block-on-platform contact stiffnesses was set at 700 kN/mm. The block-on-block and block-on-platform coefficients of restitution were 0.3 and 0.4. These values and more details for experimental measurement of these properties are described in Ref [156]. These DEM simulations were first compared with the experimental results for validation. We non-uniformly dispersed and randomly dropped 64 building blocks onto the vibrating tilted (10°) platform subjected to gravitational acceleration and vertical sinusoidal displacement during 100 seconds which was adequate time to capture the response of the system for any applied vibration amplitudes and/or frequencies for each building blocks geometry.

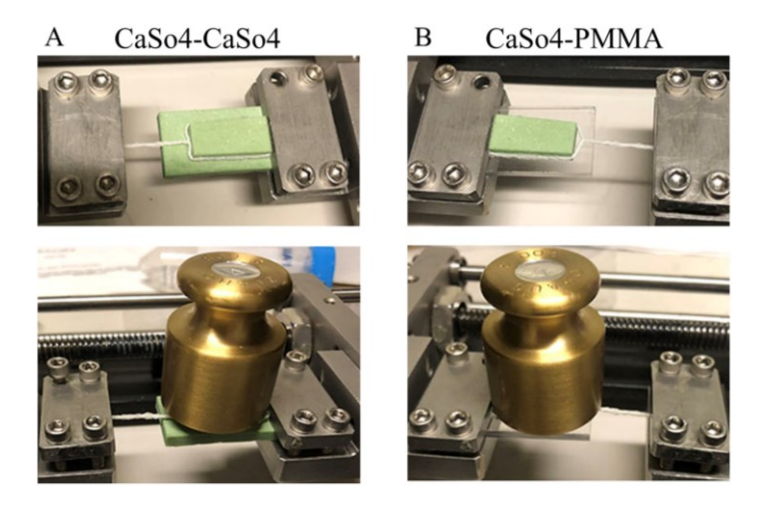


Figure 2. 11. Coefficients of friction tests using the ASTM D1894 standard for calcium sulfate (CaCo4) on either the same calcium sulfate (CaSO4) or polymethyl methacrylate (PMMA) material.

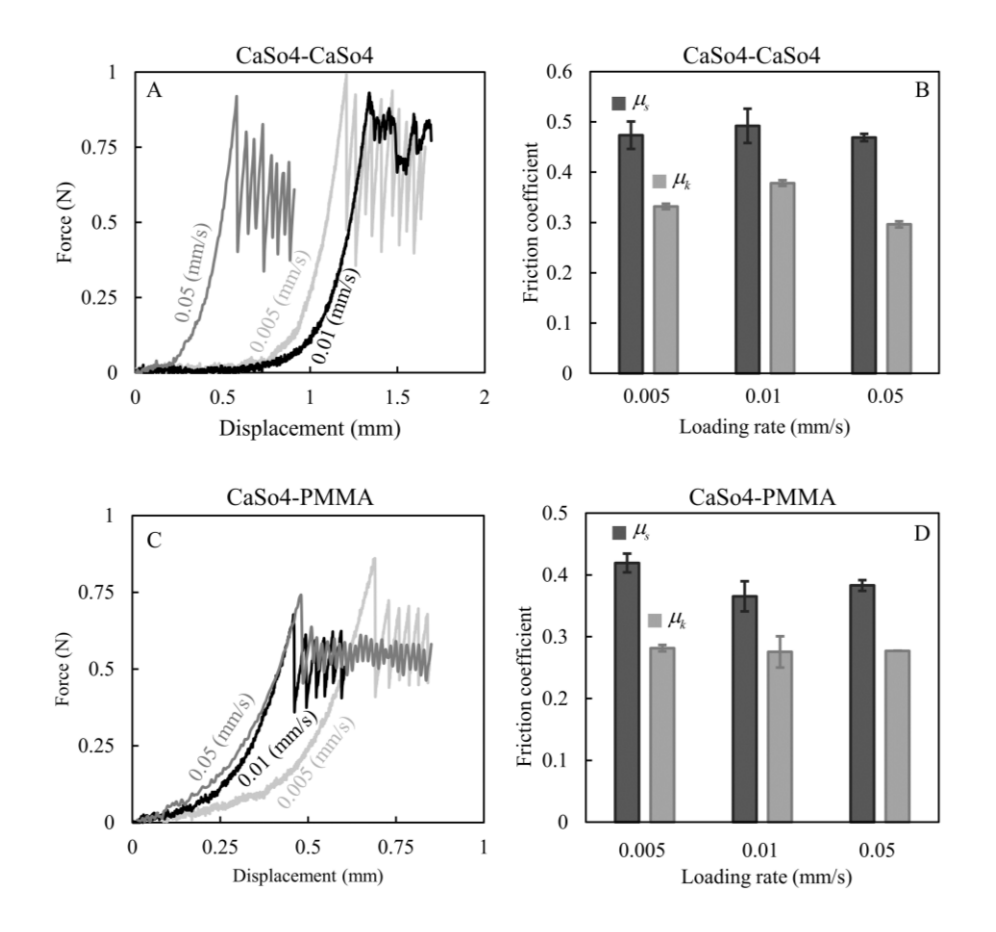


Figure 2. 12. Force-displacment curves in the ASTM D1894 standard tests and obtained frinction coefficients for calcium sulfate (CaCO4) on either the same calcium sulfate (CaSO4) or polymethyl methacrylate (PMMA) material.

Mechanisms of individual blocks: The assembly process suggests that the bouncing of individual grain (polyhedral block) can be a key mechanism to overcome friction and enable the grain motion of grain on the assembly platform. Therefore, we considered a model based on the bouncing of one particle on the platform, with critical bouncing height and critical bouncing time as potential criteria for the phase transition lines in the assembly process. For this study we have used DEM simulation to predict average bouncing characteristics as function of vibration parameters. We considered a single-sphere bouncing on a harmonic vibrating rigid platform (Figure. 2.13) to predict the bouncing height and bouncing duration, and to explore how they are governed by vibration parameters and other key properties. We used a spherical geometry because the polyhedral geometries can create more nonlinearities and obscure the effect of physical parameters due to its angular features and harder to predict bouncing directions. The bouncing of a sphere on a vibrating substrate is a seemingly simple problem, but in fact, it is a complex and difficult phenomenon that generally leads to chaotic behavior^[157-159]. Here we studied this phenomenon using the discrete element method to be consistent with the other modeling approaches. More than 6000 combinations of sphere contact stiffness, coefficient of restitution, density, and applied amplitude-frequency were examined. The total time in these models was set at five seconds, which was sufficient to measure an average height of the bounce. We used the actual physical parameters that were experimentally measured by a calcium sulfate cube.



Figure 2. 13. Schematic of an individual sphere bouncing on a vibrating rigid platform.

In addition to bouncing, rotation also promotes interactions among polyhedral blocks and is another effective block-based mechanism observed in the vibration-driven crystallization and/or interlocking process, steering blocks toward the available vacancies. This mechanism is not well understood for platonic and non-platonic blocks; therefore, we used a single-block DEM simulation for each geometry with the same dimensions and physical properties as in experiments. Our objective was to capture the conditions in which a single-block rotates from a misaligned static

equilibrium condition to perfectly align position (producing interlocking and/or crystallization) or transition from rotation to chaotic fashion (fluttering). We used this single-block DEM simulation to explore the rotation-based mechanism of each block geometry based on the initial misaligned angle, applied vibration amplitudes and/or frequencies. The single block that we placed at the corner of a tilted (10°) rigid platform with block-like walls (the same shape as the blocks) has an initial misaligned angle (θ) (Figure. 2.14). This configuration initially was subjected to only gravity, and the rotated block was settled by contact (friction) with block-like walls in a static equilibrium condition. The platform was then subjected to a vertical sinusoidal displacement for 5 seconds which was adequate time to capture the rotation response of block for any applied vibration amplitudes and/or frequencies. This model replicates a local configuration where a block interacts with nearest neighbors and/or the assembly platform and will be interlocked and/or crystalline when it rotates from misaligned position.

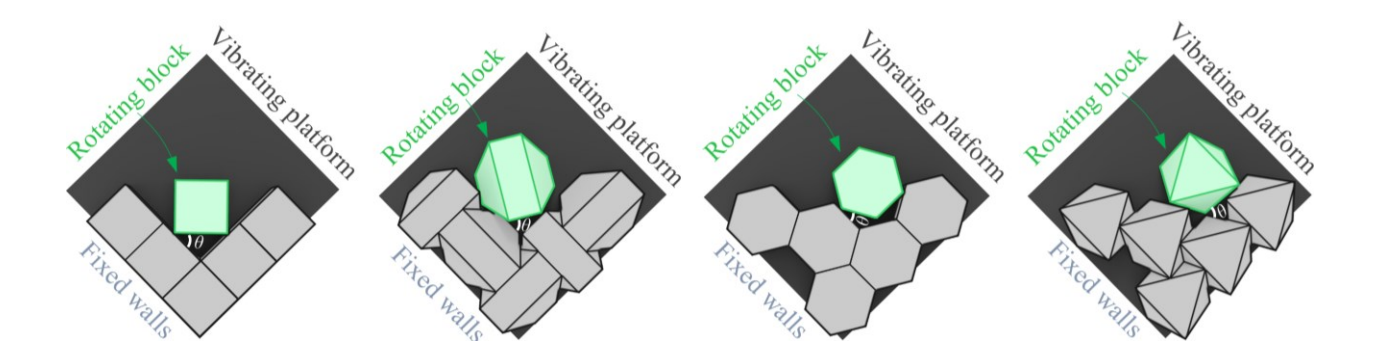


Figure 2. 14. Schematics of the single-block DEM models rotating due to the vibration of the tilted rigid platform.

2.6.2 Finite Element Modeling

We used a hybrid element simulation approach, which includes continuum deformable 3D elements for the RBCs and 3D truss elements as linkage network. Our objective was to compute the structure-property elastic response of soft inclusion/fibrous network clot material systems. Beam, truss, and spring elements can be used for the modelling of fibrous chains and networks^[19, 20, 160, 161]. We tested these three elements and due to the micro-scale thickness and length of the linkages, and our tensile loading in the elastic regime, there was no difference between their results.

We implemented the non-uniform sequential mobile packing (NSMP) algorithm^[151], in MATLAB, where we defined the size of required representative volume element (RVE) (40, 80, 120, 160), the diameter of RBC (8μm) with invariable size, the desired volume fractions (0%, 1%, 2.5%, 5%, 10%, 15%), and type of distributions such as randomly dispersed misoriented RBCs or randomly clustered misoriented RBCs. The NSMP was then defined the required inter-inclusion distances and its collision check function based on RVE size, RBC diameter and its invariable size (more details in REF [151]). The non-uniform sequential mobile packing (NSMP) algorithm^[151], which we implemented in MATLAB, is well suited to mimic our experimental observations into a 3D geometry as representative volume element (RVE) with either non-uniform or clustered dispersion of RBCs (for more details see Ref [151]), where all RBCs in the non-uniform RVE are randomly and non-uniformly distributed (Figure 2.15A), and clustered RVE has more agglomerated RBCs beside non-uniformly dispersed RBCs (Figure 2.15B). The non-uniform RBC dispersion indeed represents vibration-enhanced blood clots with higher mechanical properties, while RVEs with more clustered RBCs can simulate the native blood clots. The generated RBC coordinates (non-uniform dispersion and clustered dispersion) were then randomly connected by the Delaunay triangulation algorithm in MATLAB to create the coordinates of linkages which each linkage will be a 3D truss element. These coordinates (RBCs and linkages) were transferred into the finite element package ABAQUS using customized PYTHON scripts. The created geometry of RBCs and connected linkages (3D truss elements) were merged while the intersecting boundaries were removed; in this way, we removed the part of linkages connected to the RBCs' centers and therefore, the linkages are randomly connected to the different regions on the outer surface of the RBCs (Figure 2.15C). This connection (RBC with linkage) was modelled as perfectly bonded; given that this is a study of the elastic behavior, this approach is suitable^[151].

Although these simulations were run in a static linear elastic solution, a diminutive seed size was used for RBC elements with sizes less than 1/10th of the RBC diameter. The isotropic linear elastic properties of RBCs were designated based on Suresh and coworkers^[162] study as Young's modulus E_{RBC} =450 Pa and Poisson's ratio v_{RBC} =0.495. Young's modulus and Poisson's ratio of linkages were defined following Weisel and coworkers^[163] study as $E_{Linkage}$ =14.5 MPa and $v_{Linkage}$ =0.45. We then categorized these models into (i) RBC models, where RVEs with different RBC volume fractions and dispersion (non-uniform and clustered) were generated and (ii) linkage net models, where the length, diameter and number of linkages vary. The maximum achievable

RBC volume fraction for non-uniform dispersion was 15%, and for clustered dispersion was 5%. It is useful to highlight that NSMP and other available geometry generation algorithms are limited in generating non-uniform and clustered dispersion and/or misoriented high volume fractions complex shapes like an RBC^[151]; therefore, exploring higher RBC volume fractions remained limited in this study. For each case, we generated three different random microstructure trials to take this effect also into account. All nodes located in the outer side of the RVE were all together subjected to 0.5% normal strain, while the nodes on the corresponding opposite side were fixed, and the elastic modulus was computed from obtained stress-strain curve.

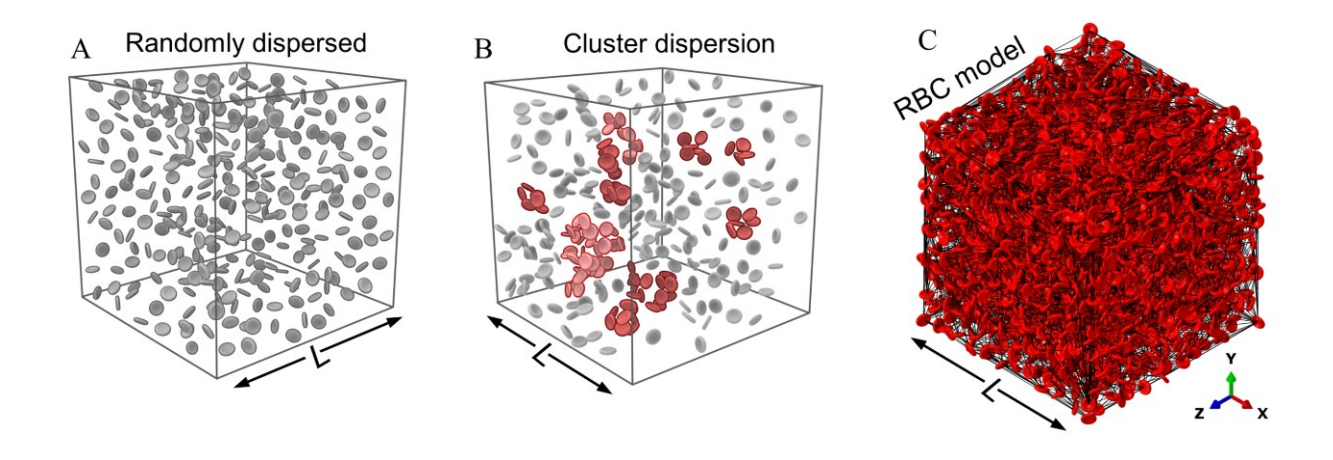


Figure 2. 15. Hybrid element computational models—geometry generation, verification and validation, and results. (A) non-uniformly dispersed RBCs within a representative volume element (RVE); (B) Clustered (agglomerated) RBCs beside non-uniformly distributed RBCs within an RVE; (C) RBC model includes RBCs and connected linkage networks.

CHAPTER 3

Agitation-Driven Fabrication of Dense Architectured Panels

Architectured materials are an emerging class of material with unusual structural behavior which can surpass the performance of traditional materials. Fully dense block-based architectured materials are based on polyhderal blocks that must be assembled into materials and structures, which represents challenges that hamper the broader application of these materials. An underused yet promising fabrication pathway is vibration-assisted assembly at the macro-scale, a process

where individual building blocks are organized into a pre-designed and ordered structure. Understanding and optimizing the vibration-assisted of these material systems can be used as guidelines in the physics and mechanics of other complex granular media. In this chapter, we propose a vibration-induced assembly route enabling scalable, rapid, low-energy fabrication of these materials. We showed that the cubic grains can be self-crystalized using this technique and used as a free-standing architectured component. The self-assembly applications of these materials include armor and protective suits, transformable and freeform structures, biomedical, aerospace and astronautics materials.

Highlights of this chapter include:

- Vibration-assisted assembly is an efficient fabrication method for granular matter.
- Vibrations can crystalize polyhedral grains into large 2D monolayer panels.
- Vibration amplitude and frequency are critical parameters in the assembly process.
- The states of blocks are characterized into three regimes and two phase transitions.

3.1 Experimental Assembly

Figure 3.1A-D shows an example of a successful assembly where we used image analysis to track individual cubes. The cubes moved toward the lowest corner of the platform from the combined action of vibrations and gravity. The evolution of packing efficiency (Figure 3.1D) was measured at each video frame by computing the packing factor, which we measured using image analysis: The images were first binarized, then the boundary and projected top surface area of cubes were measured by the sum of white pixels area. We defined the steady-state packing factor as the sum of the projected top surface area for each cube divided by the bounding contour area (Figure 2.4), which is the closest outer boundary of the assembly of cubes. The bounding contour was computed using a "boundary" function similar to a convex hull function, but allowing for concave contours that could closely match the domain of the cubes.

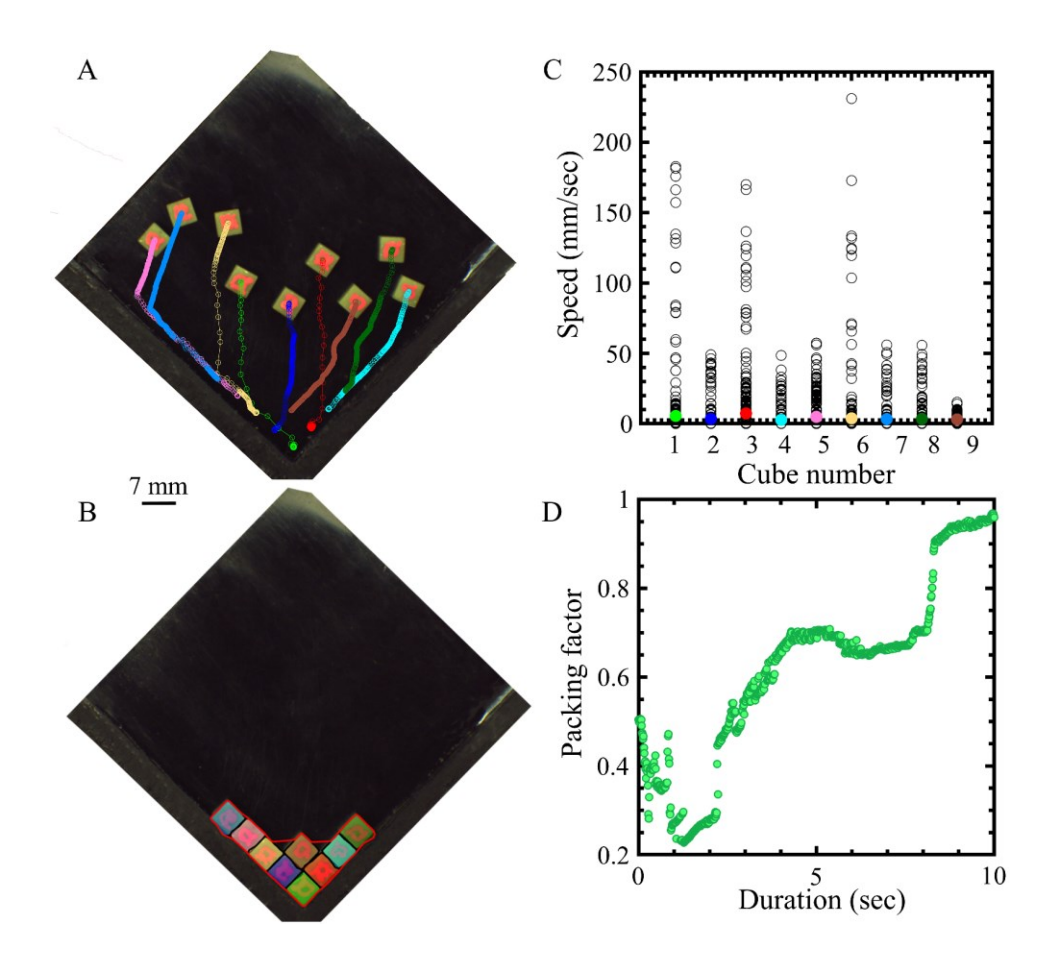


Figure 3. 1. Example of results obtained on 9 cubes dropped on a vibrating platform (A=10 μm and f=600 Hz). (A) Trajectories of individual cubes by video recording and tracking the trajectory; (B) packed position of each cube; (C) instantaneous and average (filled color markers) speed of each cube; (D) evolution of packing factor versus duration of the vibrations.

A broad range of combinations of vibration amplitude and frequency was explored experimentally. For each combination of parameters, we repeated the experiment five times, and we computed an average packing factor from these experiments. The results were quite repeatable and the deviation from the mean never exceeded 5% of the mean value, indicating that the system at steady state is not dependent on the initial conditions and therefore memoryless. In addition, Figure 3.1 shows that while the cubes have different trajectories and speeds, their average speed is almost equal, which suggests a common underlying mechanism driving their phase transition.

Depending on the vibration parameters for the platform, the cubes did not always assemble in a crystalline structure. We identified three main regimes for this system (Figure 3.1): At low vibration amplitude and/or frequency; the cubes did not move on the platform. In this "static"

regime, the applied energy originating from vibrations was not sufficient to overcome frictional forces. At higher amplitude and/or frequency, the cubes bounced on the surface, which overcame friction and enabled more mobility. The general trajectory of the cubes was towards the lowest corner of the assembly platform, where they assembled into a 2D crystal. At higher combinations of amplitudes and frequencies, the system entered a "fluttering" regime where the cubes bounced indefinitely in a chaotic fashion that precluded assembly. Fig. 3A shows an experimental map of these different regimes as function of a normalized frequency $f\sqrt{l/2g}$ and amplitude 2A/l, where f is applied frequency, l is the size of cubes (edge length), g is the gravitational acceleration and A is the vibration amplitude. The size of block is an important parameter for vibration-induced assembly. For this reason, the vibration amplitude and the frequency were normalized using the size of the blocks I as the characteristic length. A colormap in the assembly region represents the measured packing factors for the assembly at steady state. Within this region, the packing factor increased progressively as amplitude and/or frequency was increased from the static-packing transition line, and reached a maximum of 1 (i.e., perfect packing) near the packing-fluttering transition line. The assembly process can be interpreted as a competition between vibration of the platform and friction between the blocks and the platform. For example, we expect that decreasing friction between cubes and the platform can shift the static-packing phase transition toward lower amplitudes and frequencies. Figure 3.1also shows snapshots of the cubes at each regime.

The packing of granular matter subjected to vibrations has often been predicted as function of dimensionless relative acceleration $\Gamma = A\omega^2/g$ ($\omega = 2\pi f$ and A is the vibration amplitude)^[56, 57, 68], where there is an "irreversibility point", after which the packing factor was led to the steady-state condition^[56, 57, 68]. We fitted this model to our experiment, which predicted a critical acceleration for the static-packing boundary at $\Gamma = 3.8$ and for the packing-fluttering boundary at $\Gamma = 21$. However, these empirical values have no obvious physical significance, and the model did not capture the entire static-packing and packing-fluttering phase transition lines. These two phase transitions do have two different slopes, implying that there could be a distinctive mechanism governing each boundary. Γ also depends on the shape of the grain and experimental protocol, making this model inadequate for assessing the individual effect of amplitude and frequency on the phase transition and packing regimes^[56, 57, 68]. For example, Jaeger and coworkers reported $\Gamma \approx 3$ for spherical beads^[56, 57], while Neudecker et al. reported various values ($\Gamma \approx 1.5 \sim 5$) for tetrahedra^[68]. These

values are empirical, and therefore the relative acceleration model provides limited insight into the mechanics of assembly.

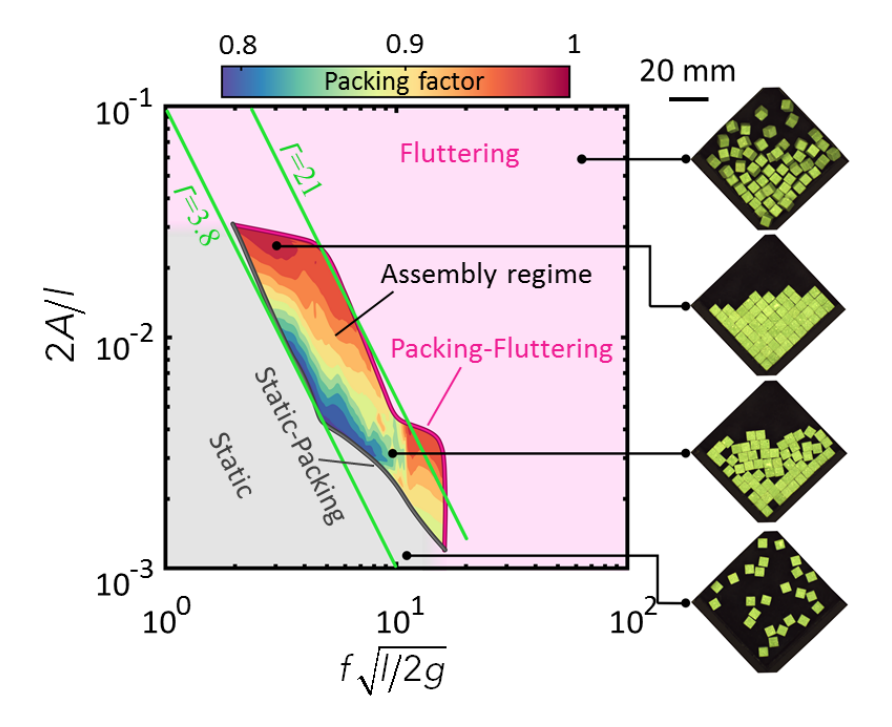


Figure 3. 2. Experimental phase diagram showing the different states of the cubes as function of dimensionless frequency and dimensionless amplitude. This map show three main regimes: static, packing (contoured region showing final packing factor) and fluttering. The two green lines show the predictions from fitted relative acceleration models.

Figure 3.3 shows that the self-assembled and/or -crystallized cubes can be released from the assembly platform and used as a dense architectured panel.

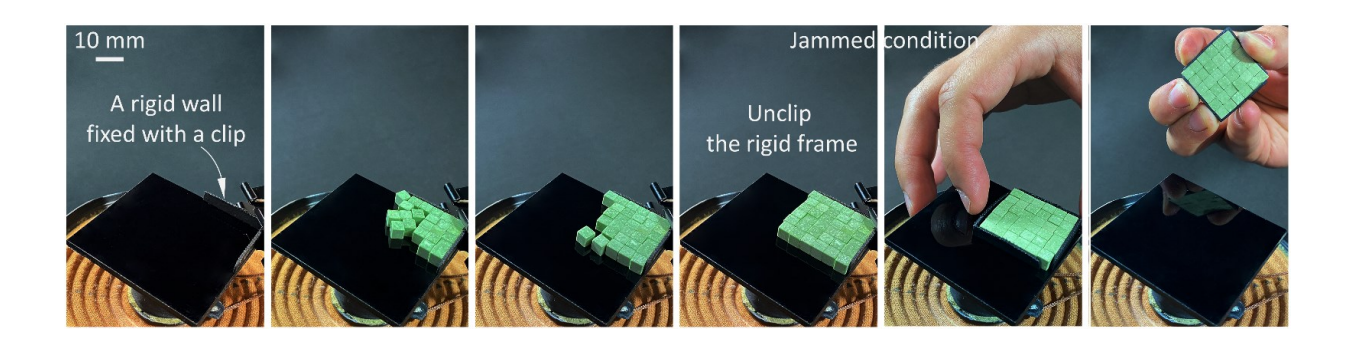


Figure 3. 3. The self- crystallization and/or assembly process of hard cubes into dense free-standing monolayer as a large piece material and/or structure.

3.2 Discrete Element Modeling

For a better understanding of the assembly process, we used discrete element models (DEM), with the open-source C++/ Python DEM solver Granoo which is particularly well suited to the modeling of polyhedral grains^[152-154]. The parameters for the DEM simulations were taken directly from the experiments. A broad range of combinations of vibration amplitude and frequencies was applied in the simulations, and the steady-state packing factor was measured using the same method as in experiments. Figure 3.4A shows the DEM-generated map of the different regimes as function of dimensionless vibration amplitude and frequency. The average packing factor in the DEM models was repeatable and memoryless, with a deviation of the packing factor of less than 10% across five different initial conditions for the cubes. Figure 3.4A also shows snapshots of the cubes in the DEM models at each regime. The contours represent the variation of the steady-state average packing factor. The highest packing factor region (i.e., 1) is in low range frequencies and/or higher range amplitudes, an observation which is consistent with the experiments. Figure 3.4B overlays the assembly map predicted by DEM with the assembly map measured experimentally. There is good overall agreement between the two contours, although the DEM simulation slightly overestimates the combinations of amplitudes and frequencies required to achieve assembly. Figure 3.4B also displays the error between experimental and DEM packing factors, which remains within about 10%.

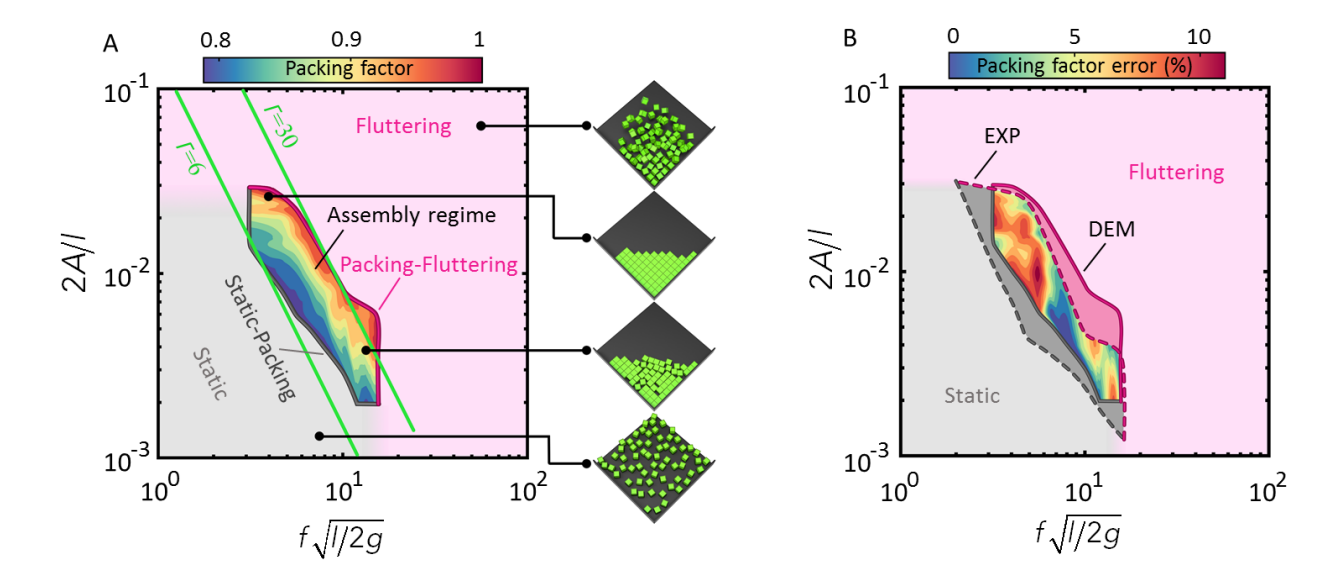


Figure 3. 4. (A) DEM phase diagram showing the different states of the cubes as function of dimensionless frequency and dimensionless amplitude. This map show three main regimes: static, packing (contoured region showing final packing factor) and fluttering. The two green lines show the predictions from fitted relative acceleration models; (B) comparisons between experimental and DEM assembly maps; the contoured region shows the percent error between experimentally measured packing factor and packing factor predicted from DEM simulation.

In the following section, we sought mechanics-based models for the interaction of single grains with the substrate to gain a more fundamental understanding of the assembly process. The findings can inform more sophisticated models for the transitions and assembly of the granular system, and in turn be used to optimize the material assembly process.

3.3 Bouncing of Individual Grains

3.3.1 Bouncing Model

We considered a single-sphere bouncing on a harmonic vibrating rigid platform (Figure 3.5A) to predict the bouncing height and bouncing duration, and to explore how they are governed by vibration parameters and other key properties. We used a spherical geometry because the cube itself can create more nonlinearities and obscure the effect of physical parameters due to its angular features and harder to predict bouncing directions. The bouncing of a sphere on a vibrating substrate is a seemingly simple problem, but in fact, it is a complex and difficult phenomenon that generally leads to chaotic behavior^[157-159]. Here we studied this phenomenon using the discrete

element method to be consistent with the other modeling approaches. More than 6000 combinations of sphere contact stiffness, coefficient of restitution, density, and applied amplitude-frequency were examined. The total time in these models was set at five seconds, which was sufficient to measure an average height of the bounce. We used the actual physical parameters that were experimentally measured by a calcium sulfate cube. Figures 3.5B-D show the trajectory of the bouncing sphere for different combinations of the relative acceleration $\Gamma = A\omega^2/g$. For $\Gamma \le 1$, the sphere bounces a few times and then stays in contact with the platform (Figure 3.5B). At higher $\Gamma(\Gamma \ge 1)$, the sphere takes off from the platform is a seemingly periodic fashion (Figure 3.5C). At yet even greater platform acceleration ($\Gamma >> 1$), the sphere enters a chaotic regime of bouncing, which can be characterized as an athermal far-from-equilibrium state (Figure 3.5D). These results are consistent with previous models for bouncing objects [157-159]. Next, we used these DEM results to compute the dimensionless time-averaged height of the bouncing sphere as function of dimensionless amplitude and frequency (Figure 3.5E). A 3D regression in MATLAB was used to fit a surface on these results with the *R*-square of 0.98:

$$\frac{\langle h' \rangle}{D'} = 7.5 \left(\frac{2A}{D'}\right)^2 \left(f\sqrt{\frac{D'}{2g}}\right)^{2.1} \tag{3}$$

where $\langle h' \rangle$ is the time averaged height, D' is the diameter of the sphere, g is gravitational acceleration, A is vibration amplitude, and f is vibration frequency. We also computed the average bounce duration of the bouncing sphere $\langle t \rangle$ as function of dimensionless amplitude and frequency (Figure 3.5F). The obtained equation from 3D regression (r=0.93) based on non-dimensionalized average bounce duration is:

$$\langle t \rangle \sqrt{\frac{2g}{D'}} = 1.4 \left(\frac{2A}{D'}\right)^{0.21} \left(f\sqrt{\frac{D'}{2g}}\right)^{0.29} \tag{4}$$

We also assessed the non-dimensionalized average bounce height and duration as function of the dimensionless relative acceleration (Γ) of the platform (Figure 3.5G,H). The fitted curves to these two data sets show that the R-square for bounce height and duration versus Γ is 0.92 and 0.62. These values are much lower than the R-square of fitted surfaces (Figure 3.5E,F), showing that bounce height and duration cannot be predicted by relative acceleration only. The contribution

of amplitude and frequency must be considered separately in the context of a vibration-induced assembly.

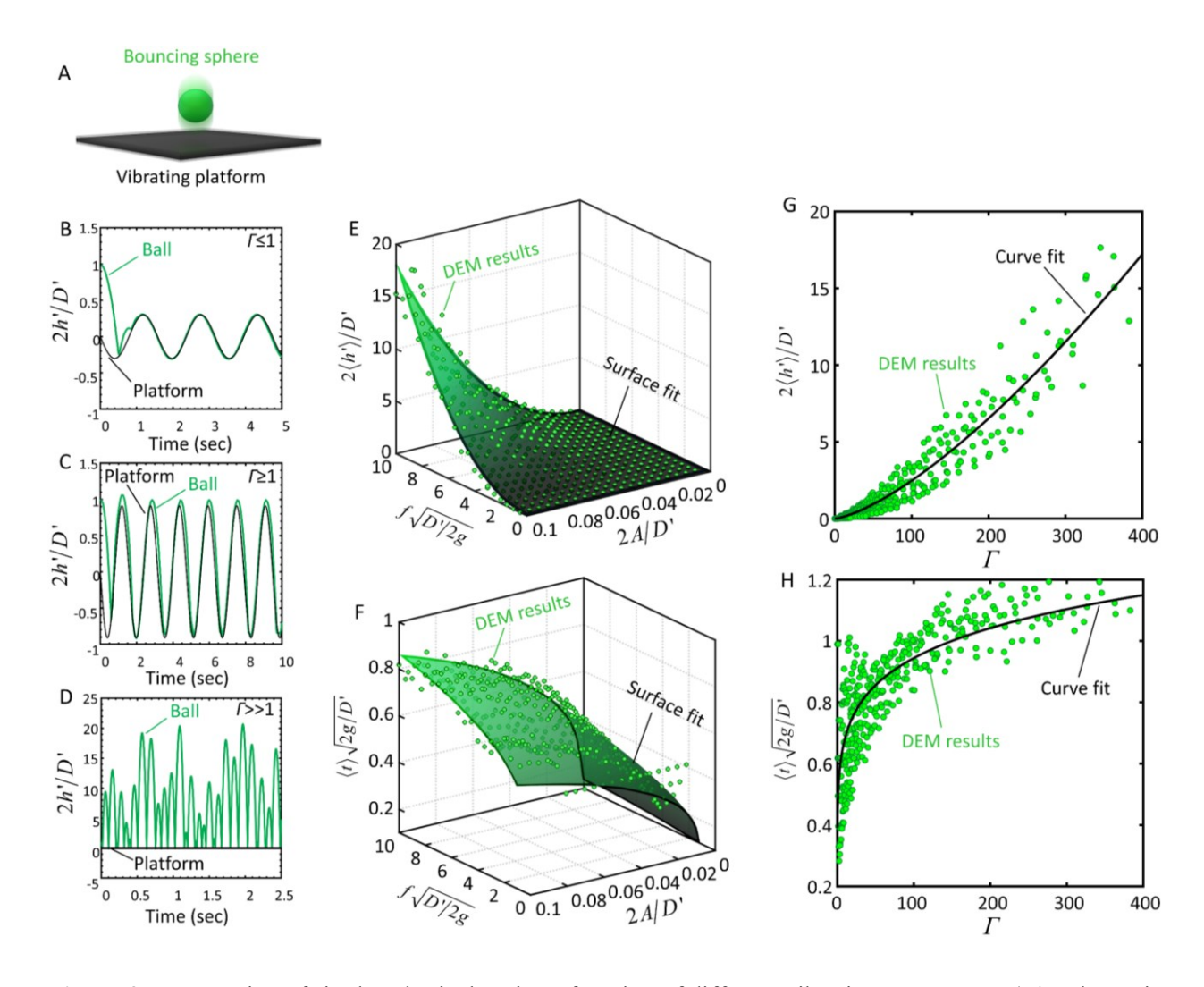


Figure 3. 5. Bouncing of single spherical grain as function of different vibration parameters. (A) Schematic of an individual sphere bouncing on a vibrating rigid platform; (B-D) predictions from the DEM model under various regimes; (E and F) DEM-predicted average bounce height and bounce duration for the sphere as function of amplitude and frequency with fitted 3D surfaces; (G and H): Bounce height and bounce duration as function of Γ , together with curve fit.

3.3.2 Rotation Model

In addition to bouncing, the assembly process and Figure 3.1 suggest that the rotation of individual cubes is also an effective packing and assembly mechanism allowing cubes to better fill available vacancies as well as promoting interactions among cubes. To explore this mechanism, we used a $4.8\times4.8\times4.8$ mm single-cube DEM model with an initial rotation angle (θ) at the corner of a 10° tilted rigid platform (Figure 3.6A). The system was subject to gravity and to a sinusoidal displacement applied vertically to the rigid platform. Before applying vibration, the rotated cube initially was in a static equilibrium condition due to friction with the walls. This condition duplicate a local configuration where a cube is in contact with its neighbors (or with the assembly platform) but where it is jammed in a mis-rotated position. Our objective was to capture the conditions in which individual cubes rotate from a static equilibrium condition to properly align and assemble. These rotation-based mechanisms can be assessed as function of initial rotation angle, friction, amplitude, and frequency using the single-cube model. We ran 9000 models for different combinations of these parameters. Each simulation captured 5 seconds of physical interactions between the cube and the corner walls—enough time to capture the rotation of the cube for any applied amplitude-frequency response of the rigid platform. Since there were many parameters and combinations, we used the actual physical parameters that were experimentally measured on calcium sulfate cubes. Figure 3.6B shows the result, in the form of a rose plot showing the state of the cube (static, rotating to assemble or fluttering) as function of Γ and the initial mis-rotation angle of the cube θ . At low Γ magnitudes and/or high initial mis-rotation angles (θ), the cube did not rotate (static). At higher Γ magnitudes and/or lower initial mis-rotation angles, the cube rotated (rotating). At high Γ magnitudes, the system entered a fluttering regime. The rose plot displayed a rotation symmetry that reflect the symmetry of the cube. While the transition static-to-rotating depended on the mis-rotation angle of the cube θ , the rotating-fluttering transition only depended on Γ . From these DEM results, the static-rotating transition can be fitted with equation (3) at θ =45° which is the least favorable initial angle to assembly.

$$\frac{A}{l} = 0.015 \left(f \sqrt{\frac{l}{2g}} \right)^{-0.94} \tag{5}$$

The rotating-fluttering transition at θ =45° can be captured with:

$$\frac{A}{l} = 0.035 \left(f \sqrt{\frac{l}{2g}} \right)^{-1.03} \tag{6}$$

Equation (3) and (4) are compared with the many-cube experiments in the next section.

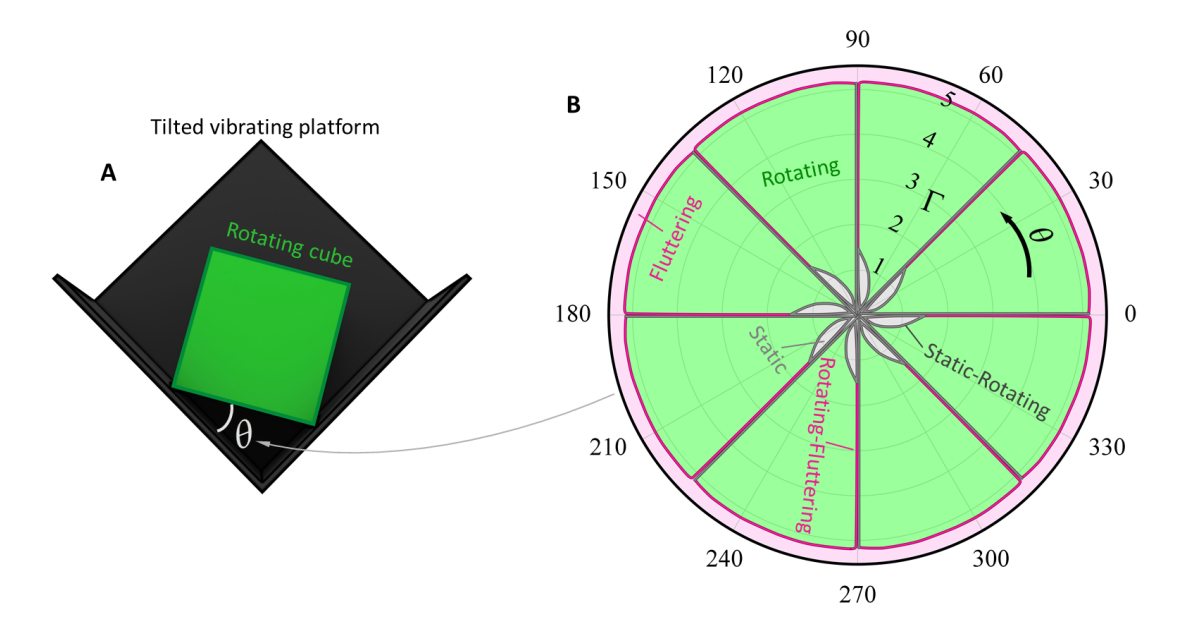


Figure 3. 6. (A) Schematic of the single-cube DEM model rotating due to the vibration of the rigid platform; θ is the initial cube rotation angle; (B) cube rotation map as function of dimensionless relative acceleration and its initial rotation angle. The rotation map shows the three main regimes: static, rotating, and fluttering regimes.

CHAPTER 4

Agitation-Induced Assembly of Topologically Interlocked Materials

In chapter, we examined a vibration-driven configuration to rapidly interlock platonic and non-platonic polyhedral granular building blocks into a monolayer interlocked material and/or structure. We used two basic medial section shapes, including square and hexagon, to form hard topological interlocking convex blocks. We study the physics and mechanics involved in the interlocking of far-from-equilibrium granular systems for different grain geometries and their basic medial section shape. We show that a self-interlocked dense architectured material and/or structure can be free-standing; these material systems can be re-fragmented and again be re-fabricated using

this scalable and low-energy fabrication process. The results show that maximum acceleration normalized by gravity cannot fully capture packing nor the phase transitions and that instead, amplitude and frequency must be considered independently. In addition, we used discrete element modeling to capture the experimental results, and we used the single-block models to assess the effective mechanisms governing the packing and phase transition of the polyhedral blocks. We found that rotation only influences packing while the bouncing is effective on both packing and phase transitions. We showed that the chaotic phase transition of a shape is the main reason to ease the self-interlocking process. We found a geometry with a lower out-of-plane moment of inertia can fully be interlocked in a broader range of vibration amplitudes and frequencies. Our findings can be applied to assess the governing mechanisms in the shape-dependency, re-fragmentation, re-crystallization and re-reconfigurability of other granular far-from-equilibrium systems including "Granulobots", other fabrication and agitation methods such levitation, and for the rapid assembly of versatile anisotropic and/or hybrid macroscale topologically interlocked materials, structures, components, and armors.

Highlights of this chapter include:

- Vibration-driven assembly is an efficient interlocking method for polyhedral block-based materials.
- Polyhedral blocks can be self-crystalized into large topologically interlocked panels.
- Polyhedral blocks interlocking regime and its phase transition can be captured by singleblock models.
- Polyhedral blocks with a lower moment of inertia can be self-interlocked in wider vibration range.

4.1 Experimental Interlocking

We interpolated the discrete experimental results to get an assembly map composed of continuous boundaries (Figure 4.1A-D). Three main regimes and phase transitions between these regimes were identified for this system based on the dimensionless applied amplitudes and frequencies: A "Static" regime was observed at low vibration amplitudes and/or low frequencies. In this regime the blocks did not move on the platform due to insufficient applied vibrational energy for overcoming frictional forces, disabling packing factor measurements. An "Assembly"

regime was observed at higher vibration amplitudes and/or frequencies. In this regime the blocks bounced and rotated on the platform substrate, enabling movement and the assembly of the blocks into a panel. A steady-state packing factor (PF) could be measured at end of this regime. Finally, a "Fluttering" regime was observed at higher vibration amplitudes and/or frequencies. The blocks in this regime bounced and overturned constantly in a chaotic manner that prevented packing. Figure 4.1 shows these regimes and phases transitions as well as snapshots of the blocks at each regime based on the dimensionless amplitude 2A/h and frequency $f\sqrt{h/2g}$, where A and f are applied vibration amplitude and frequency, h is the height of blocks, and g is the gravitational acceleration. Figure 4.1A-D shows that each block geometry has a unique amplitude-vibration range for the assembly regime; however, the variation of packing factor followed a common trend. The packing factor gradually increased by increasing both amplitude and frequency together from static-assembly phase transition boundary toward the assembly-fluttering transition and reached perfectly interlocked and/or crystalline (PF=1) near this boundary. Square prisms (Figure 4.1A) produced the widest assembly regime among other geometries in this study, while hexagonal prism (Figure 4.1C) has the largest maximum packing factor region (PF=1). In addition, increasing α from 0° to 20° in both square- and hexagon-based tiling narrows assembly regimes and maximum packing factor regions (PF=1); however, octahedron (Figure 4.1D) is superior to both square prism and truncated tetrahedron in maximum packing factor region (PF=1). Truncated tetrahedron (Figure 4.1B) has the narrowest assembly regime and maximum packing factor region (PF=1) with the widest fluttering regime, which reflects that this geometry is more difficult to assemble. Figure 4.1 demonstrates that hexagon-based tiling geometries have the largest maximum packing factor region (PF=1); therefore, they are easier to perfectly be crystallized and/or interlocked than squarebased tilting geometries.

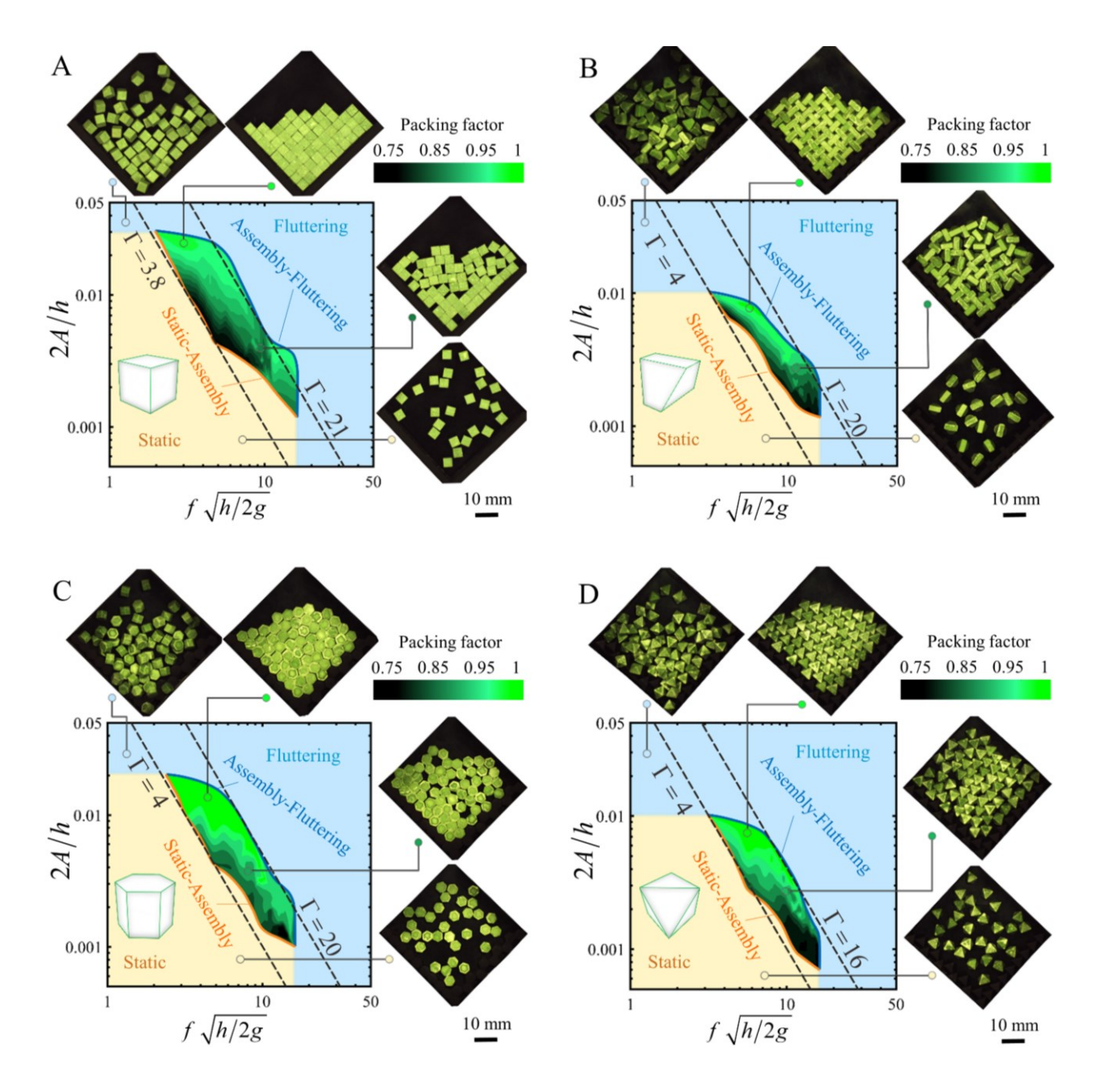


Figure 4. 1. Experimental assembly phase diagrams demonstrating the various states of the blocks based on normalized vibration amplitude and frequency (A) square prism; (B) truncated tetrahedron; (C) hexagonal prism; (D) octahedron. These assembly diagrams indicate three main regimes: static, assembly (contoured region representing normalized steady-state packing factor quantified by the colorbar) and fluttering, as well as two phase transitions: static-assembly and assembly-fluttering. The two dash lines exhibit the predictions of fitted critical relative acceleration criterion normalized by gravitational acceleration. For each geometry, the snapshots show the blocks in different regimes: fluttering, high and low packing factor, and static regime.

The phase transitions of granular blocks and their steady-state packing due to vibrations have traditionally been predicted based on critical relative acceleration of vibrating system normalized by gravitational acceleration $\Gamma = A\omega^2/g$ ($\omega = 2\pi f$ and A is the vibration amplitude). Figure 4.1 shows the predictions of this model fitted to phase transitions (static-assembly and assemblyfluttering) for each block geometry. The closest critical acceleration to the static-assembly boundary was at Γ =3.8 for square prism and Γ =4 for other remaining blocks. The closest critical acceleration to the assembly-fluttering boundary was at Γ =21 for square prism, Γ =20 for truncated tetrahedron and hexagon prism, and $\Gamma=16$ for octahedron. These predictions were closer to hexagon-based tiling geometries than square-based tiling geometries. However, this model did not predict the entire phases transition boundaries for any block geometries. In addition, these values are obtained from empirical fitting and have no clear physical significance and insights into the mechanics of assembly. For example, the static-assembly and assembly-fluttering transitions are function of the geometry of the blocks, an effect which is not captured by accelerations only. The assembly process is a complex phenomenon that results from a fine balance between the energy provided by mechanical vibrations, geometry of the blocks, inertia of the blocks and contact interaction including elasticity and friction. Changes in any of these parameters can potentially impact the assembly results, for example decreasing friction between blocks and the platform would probably shift the static-packing phase transition toward lower amplitudes and frequencies. The tilt angle of the assembly platform can also impact the assembly process. Figure 4.2 shows the assembly diagram obtained using 5° and 10° tilt angles, on square prisms and octahedra. The 10° tilt angle slightly extended the assembly regime in terms of both amplitude and frequency range (Figure 4.2), because the higher titled angle facilitated the onset of motion in the blocks. Higher angles however led to individual blocks titling on their side, which hindered assembly. The dimensions of the blocks varied within 2-5% around their mean values. It is not clear whether these slight variations in size and shape apparently affected the phase diagram of assembly nor the packing factor of interlocking and/or crystallization."

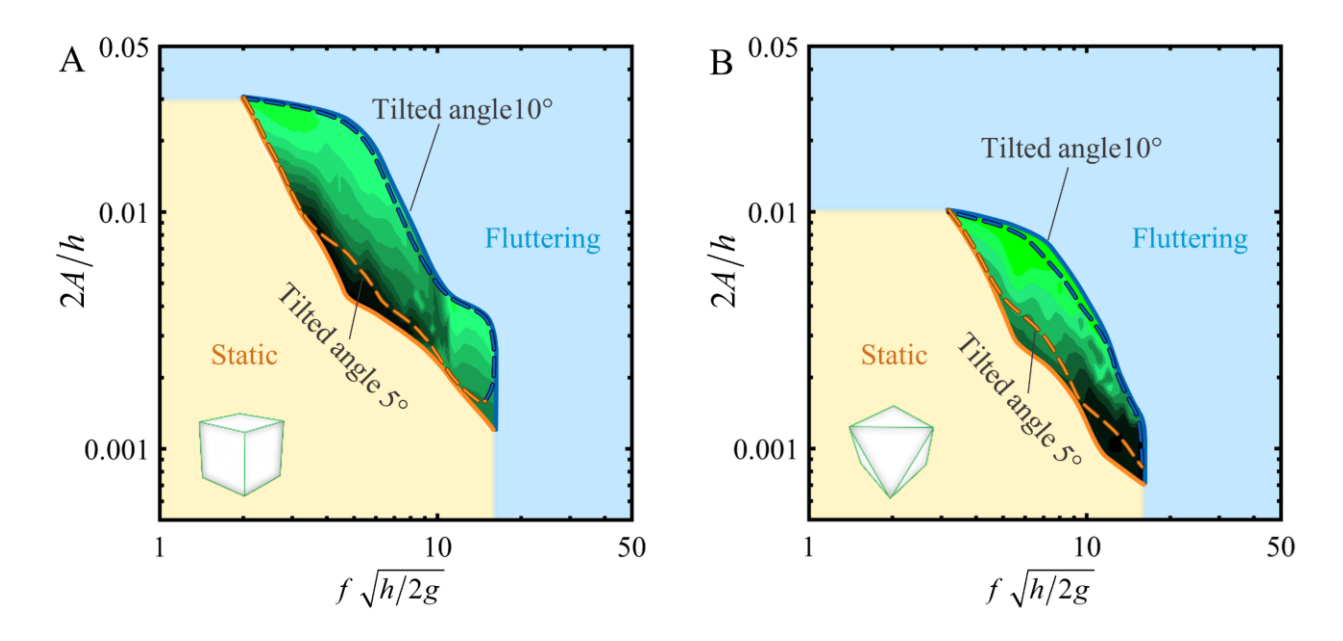


Figure 4. 2. Comparisons between experimental assembly phase diagrams for two different assembly platform tilted angles (5 and 10 degrees); (A) square prism; (B) octahedron.

Figure 4.3 shows that meso-scale polyhedral granular blocks can be self-interlocked and/or -crystallized into macro-scale TIMs using vibration-driven assembly and can be released from assembly platform to be used as a large-piece free-standing stiff architectured panel.

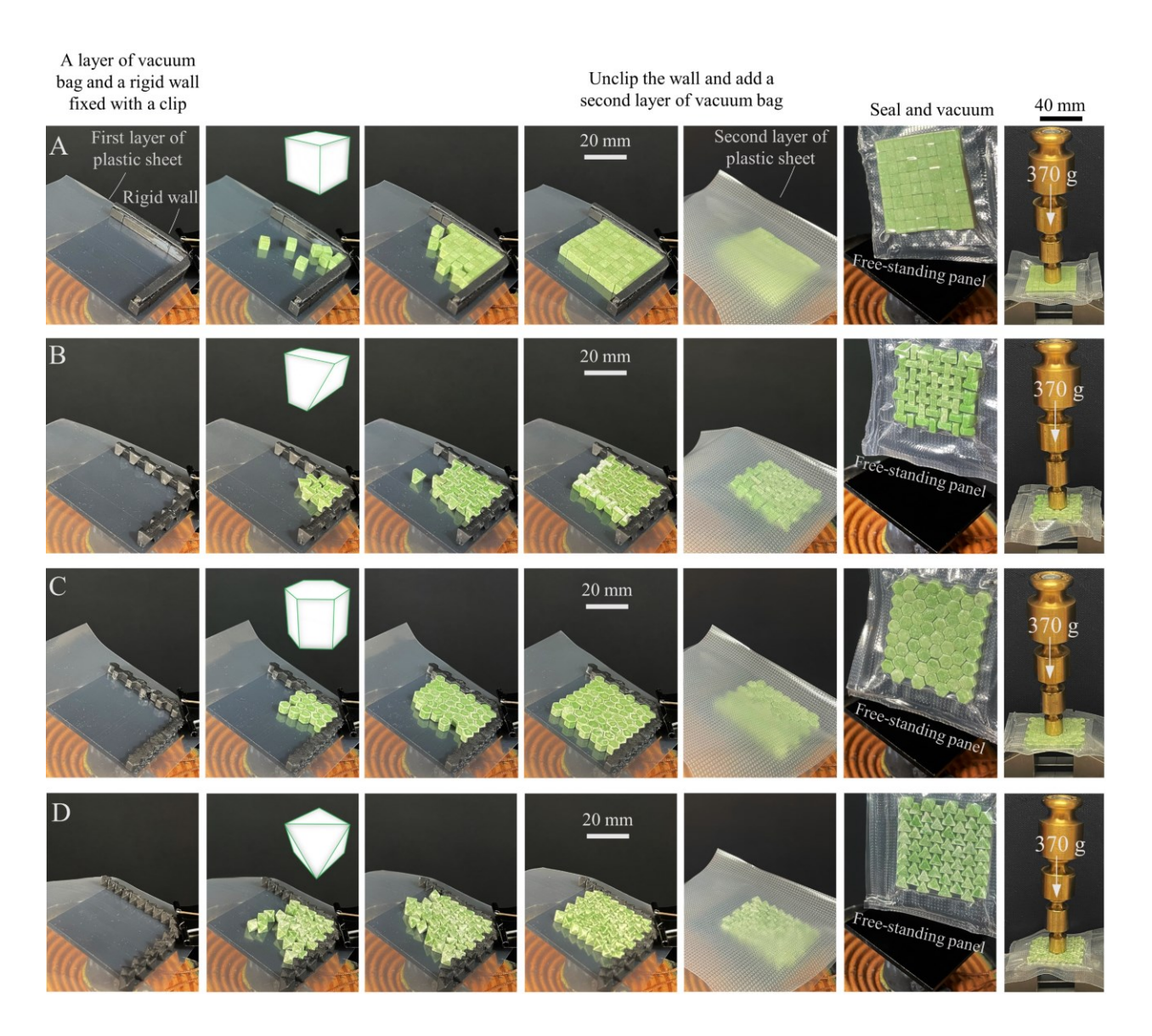


Figure 4. 3. The self-interlocking and/or crystallization process of (A) square prism, (B) truncated tetraheron, (C) hexagon prism, and (D) octahedron blocks into dense free-standing TIM monolayer as a large piece material and/or structure.

4.2 Discrete Element Models

Figure 4.4A-D shows the DEM-generated assembly phase diagrams based on the dimensionless vibration amplitude and frequency for different block geometries, together with snapshots at each of the regimes. The DEM simulations duplicated the phase transition contours from the experiments quite accurately. The packing factors predicted by the DEM simulation were repeatable and independent of the initial dropping position of blocks and consistent with experiments. We repeated each simulation (for each applied vibration amplitude and/or frequency) five times with randomly dispersed block positions, the packing factor was memoryless, and its deviation from the mean did not exceed 10% for each block geometry. In agreement with the experiments, the maximum packing factor region (PF=1) in DEM was also achieved by high vibration amplitudes and/or low frequencies for each block geometry. The DEM-generated packing factor also is increased from the static-assembly to the assembly-fluttering phase transition boundary. We used the same method as the experiments to interpolate continuous domains from the discrete modeling results to get an assembly map shown on Figure 4.4. The square prism (Figure 4.4A) has the largest assembly regime; the truncated tetrahedron (Figure 4.4B) has the smallest assembly regime and largest fluttering regime. DEM also properly captured the effects of increasing α from 0° to 20° in both square- and hexagon-based tiling, creating smaller assembly regimes and maximum packing factor regions, as well as wider fluttering regimes. The critical relative acceleration criterion did not fit experimental transition well nor DEM predictions. In the following section, we use DEM to capture the rotation and bouncing mechanisms of individual blocks to create a fundamental understanding of the assembly process.

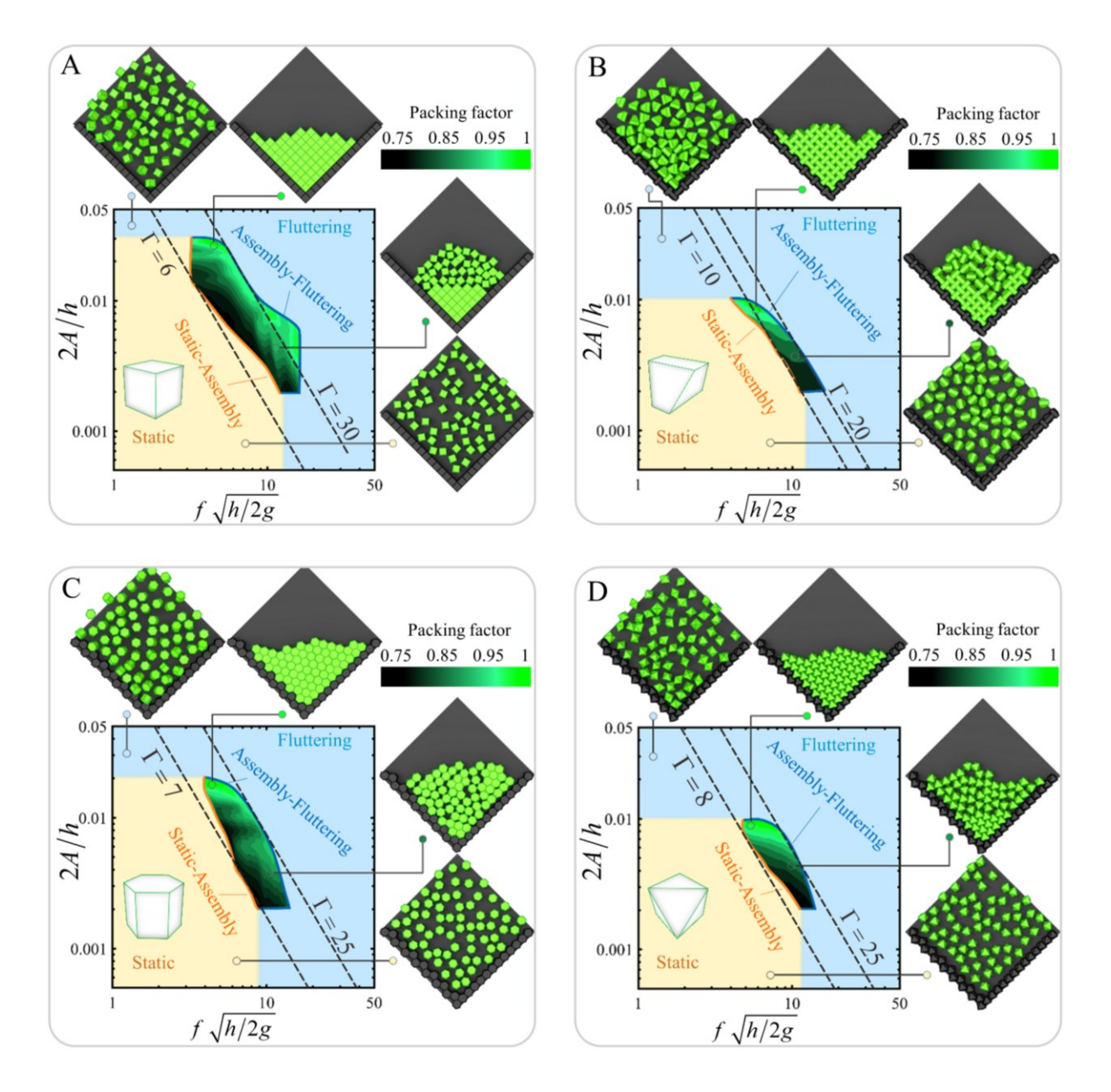


Figure 4. 4. DEM-generated phase diagrams indicating the various states of the blocks based on normalized vibration amplitude and frequency (A) square prism; (B) truncated tetrahedron; (C) hexagonal prism; (D) octahedron. These assembly phase diagrams show three main regimes: static, assembly and fluttering. as well as two phase transitions: static-assembly and assembly-fluttering. The contours quantified by the colorbar represent the variation of the steady-state normalized average packing factor, which was measured by the bounding contour the same as experiments. The two dash lines exhibit the predictions of fitted critical relative acceleration criterion normalized by gravitational acceleration. For each geometry, the snapshots show the blocks in different regimes: fluttering, high and low packing factor, and static regime.

4.2.1 Rotation Mechanism

In addition to bouncing, rotation also promotes interactions among polyhedral blocks and is another effective block-based mechanism observed in the vibration-driven crystallization and/or interlocking process, steering blocks toward the available vacancies. This mechanism is not well understood for polyhedral blocks; therefore, we used a single-block DEM simulation for each geometry with the same dimensions and physical properties as in experiments. Our objective was to capture the conditions in which a single-block rotates from a misaligned static equilibrium condition to perfectly align position (producing interlocking and/or crystallization) or transition from rotation to chaotic fashion (fluttering). We used this single-block DEM simulation to explore the rotation-based mechanism of each block geometry based on the initial misaligned angle, applied vibration amplitudes and/or frequencies. The single block that we placed at the corner of a tilted (10°) rigid platform with block-like walls (the same shape as the blocks) has an initial misaligned angle (θ) (Figure 4.5). This configuration initially was subjected to only gravity, and the rotated block was settled by contact (friction) with block-like walls in a static equilibrium condition. The platform was then subjected to a vertical sinusoidal displacement for 5 seconds which was adequate time to capture the rotation response of block for any applied vibration amplitudes and/or frequencies. This model replicates a local configuration where a block interacts with nearest neighbors and/or the assembly platform and will be interlocked and/or crystalline when it rotates from misaligned position. The polar plots in Figure 4.5 show the radial phase diagram for each block geometry indicating the state of single block (static, rotating to assembly or fluttering) based on Γ and the initial misaligned angle of the block (θ). These polar plots exhibit that the rotation of each block is independent of the medial section geometry because each block has a unique rotation symmetry regardless of their geometry transformation from the same medial section (square prism to truncated tetrahedron and hexagonal prism to octahedron). For all block geometries, the misaligned angle θ governs the static-rotating transition, while Γ governs the rotating-fluttering boundary. The results can be fitted with expression:

$$\frac{A}{h} = C \left(f \sqrt{\frac{h}{2g}} \right)^n \tag{5}$$

A general form of power equation (2) can be fitted to radial phase transitions based on the applied vibration amplitudes and frequencies for all block geometries. The constant values (C and n) for each block geometry and phase transition are indicated in Figure 4.6.

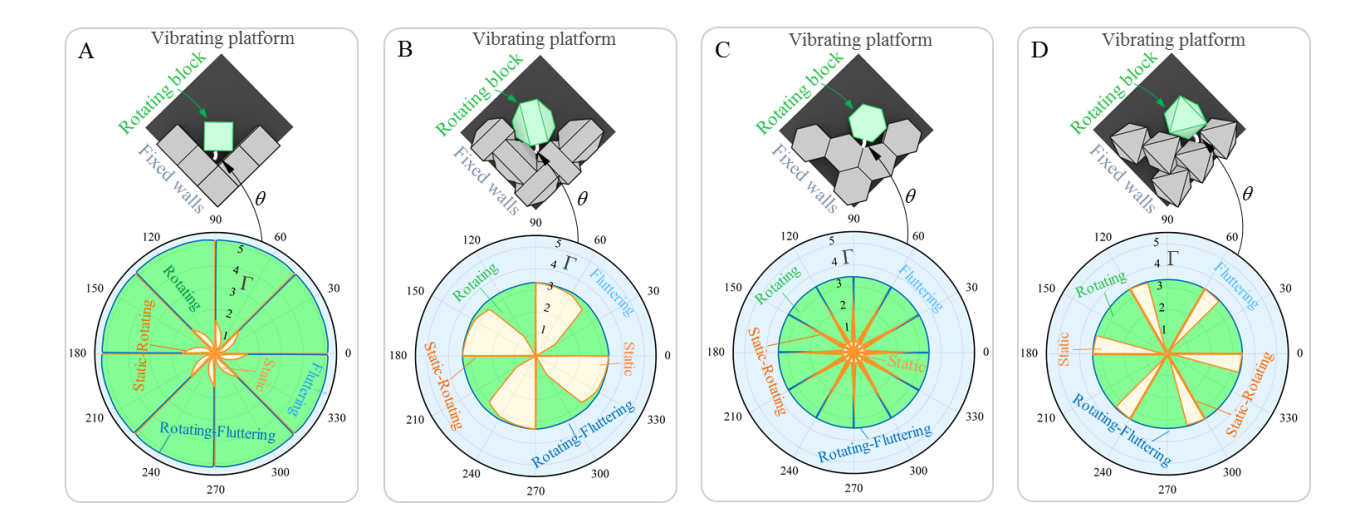


Figure 4. 5. Schematics of the single-block DEM models rotating due to the vibration of the tilted rigid platform. Radial phase diagrams computed by these single-block DEM models as function of dimensionless critical relative acceleration (Γ) and initial misaligned angle (θ) for each block. (A) Square prism; (B) truncated tetrahedron; (C) hexagonal prism; (D) octahedron.

Figure 4.6 indicates the constant values for the rotation model. These values are different for each block geometry and phase transition boundaries (static-rotating and rotating-fluttering).

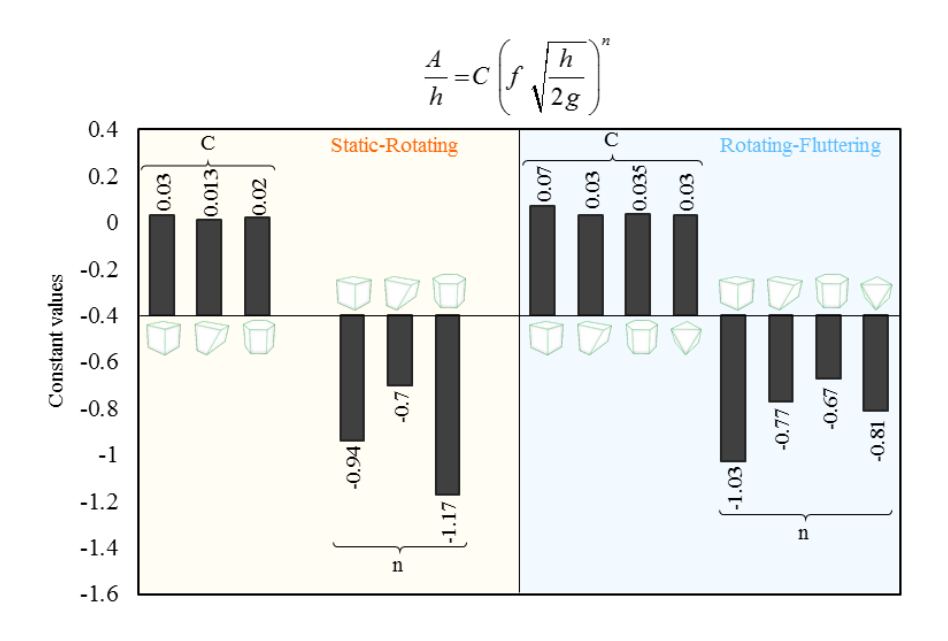


Figure 4. 6. The constant values of the rotation model for each block geometry and phase transitions.

CHAPTER 5

Agitation-Mediated Structure-Property Relation of Biopolymers Laden with Soft Cellular Inclusions

This chapter explores an emerging class of soft active matter, specifically those resembling blood clots, wherein soft cellular inclusions are embedded within a biopolymeric matrix. Notable examples include tumors, muscles, organoids, and biofilms. Unlike conventional polymeric materials, the formation and structure-property relations of clot-like materials remain relatively unexplored, despite their profound implications for engineering and medicine. For instance, the mechanical properties of blood clots govern critical events like rupture, which can lead to fatal hemorrhage or stroke conditions. These clot-like materials present unique challenges, primarily due to the high volume fraction and sensitivity of cellular inclusions. To tune their structure and properties, chemical alterations can induce cytotoxicity and other side effects in vivo. Alternatively, physical strategies are appealing for modulating structure-property relations without changing biochemical compositions. While wave-based approaches such as vibration, sound and ultrasound have been developed for controlling cellular assembly and patterning similar granular materials,

their application to macroscopic three-dimensional clot-like materials remains unexplored, particularly in the form of mechanical agitation.

To address this gap and develop new strategies to engineer clot-like materials, we propose a principle based on mechanical agitation. Through tailored agitating platforms and blood clots as a model system, we demonstrate that agitation can effectively modulate a broad spectrum of material properties and mechanical performance, including stiffness, fracture toughness, lysis, and active contraction. Our combined experimental and simulation approach elucidates the mechanism by which agitation-mediated cellular organization influences both microscopic structure and macroscopic mechanical responses within the fibrin network. Moreover, we showcase the applicability of this principle across various material systems and in in vivo animal experiments.

5.1 Agitation-mediated Mechanical Properties of Blood Clots

The experiments first aimed to explore the effect of mechanical agitation, specifically vibration-driven perturbation during clotting on the structure-property response of bovine blood clots. Our objective was to assess elastic response and fracture toughness to ensure that both smalland large-strain mechanical performance of the blood clots were covered. We therefore synthesized blood clot within a pure shear test specimen (for more details see clot synthesis in Materials and Methods chapter) (Figure. 2.5A). This under-hydration specimen was fixed on a 3D-printed rigid substrate which was glued onto a voice coil (speaker) inside an incubator at 37°C (Figure. 2.5B). We used a laser vibrometer to calibrate amplitude and frequency of the vibrating platform under sinusoidal waveform. We explored the perturbation effect generated by the broad combinations of amplitudes (1-25 μm with 5 μm intervals) and frequencies (10-1000 Hz with 50 Hz intervals) during clotting on the mechanical response of blood clots. The vibration was applied for 10 min an optimum time confirmed by our preliminary experiments (Figure. 5.1A) and also enough time for a complete γ - γ crosslinking^[12, 130]. For each applied amplitude and/or frequency 5 unnotched and 5 notched (10 mm long pre-notch introduced by polyester 0.1 mm thin film) pure shear specimens were prepared and then tested at room temperature under uniaxial tensile loading. The representative stress-stretch curves of unnotched and notched specimens for native and agitationmediated samples are shown in Figure 5.1B. The elastic modulus and fracture toughness were characterized to capture both small- and large-deformation behaviors, respectively. Our result shows that agitation could either degrade or enhance the mechanical properties of blood clots

(Figure 5.1C). Compared with the non-treatment native clots (7.02±1.5kPa, 9.59±2.27Jm⁻²), the agitation-degraded clots exhibit significantly lower elastic modulus (3.16±0.62kPa) and fracture toughness (5.04±1.22Jm⁻²), while the agitation-enhanced clots are much stiffer (12.37±0.45kPa) and tougher (20.22±6.88Jm⁻²).

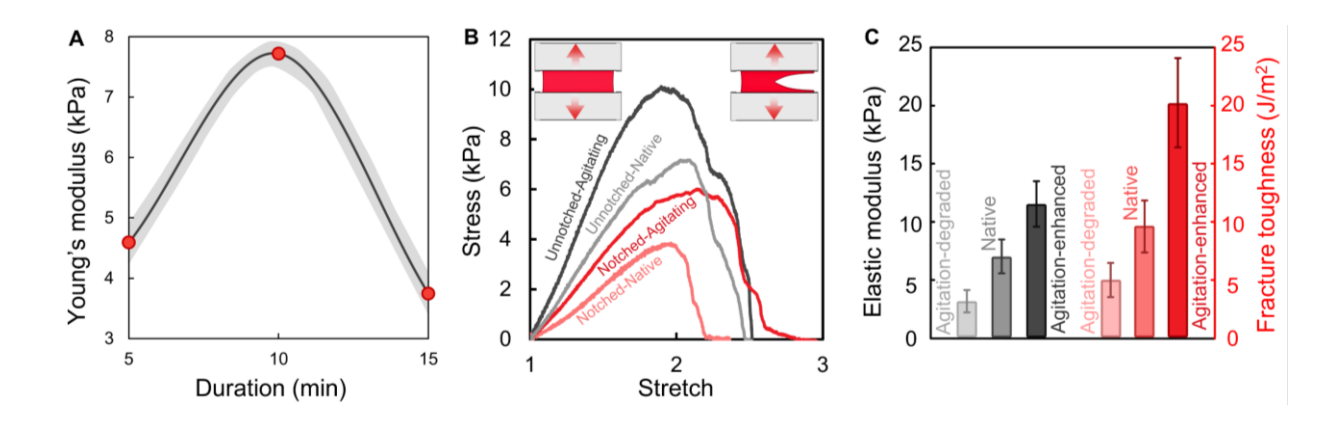


Figure 5. 1. (A) Preliminary results for the variation of typical agitation-generated blood clots as function of the duration of applied agitation. (B) Stress-stretch responses of the unnotched and notched pure-shear specimens with and without the agitation treatment. (C) Elastic modulus and fracture toughness for agitation-degraded or enhanced blood clots, compared to native clots without agitation. Data are shown as means \pm SD for n=5 independent experiments.

To further reveal the coupling between agitation conditions and mechanical properties, we experimented with various combinations of amplitudes (A, ranging from 1 to 25µm with 5µm intervals) and frequencies (f, ranging from 10 to 1000Hz with 50Hz intervals). The measured elastic modulus and fracture toughness were normalized by the properties of the native blood clots without agitation treatment. We plotted these results in phase diagrams (Figure 5.3A,B) as function of dimensionless amplitudes (2A/D) and frequencies ($f\sqrt{D/2g}$), where g is gravitational acceleration and D is the diameter of an RBC (\sim 8µm). The phase diagrams delineate two distinct regimes: a "perturbation" regime where the agitation is tamable to tune the mechanical properties, and a "splashing" regime where the blood splashes out of mold, impairing clot formation.

Upon examination of the phase diagrams (Figure 5.2A,B), we found that low-frequency agitation ($0 < f \lor D/2g < 0.05$) had minimal effect on the mechanical properties, and the agitation of mid-range amplitudes (1 < 2A/D < 4) and/or frequencies ($0.2 < f \lor D/2g < 0.4$) significantly enhanced the elastic modulus and fracture toughness, up to 1.6 and 2.0 times that of native clots, respectively.

However, further increasing the frequencies and amplitudes resulted in a notable decrease in clot stiffness and toughness, halving their values, eventually pushing the system into the "splashing" regime. The agitation approach achieved modulation of the elastic modulus and fracture toughness of blood clots within a range of approximately 400%, that is, a fourfold difference from agitation-degraded to agitation-enhanced properties. Notably, there is a positive correlation between variations in the elastic moduli and their corresponding fracture toughness of blood clots (Figure 5.2C).

Following our previous blood clot synthesis and experiments, we used a hydrophilic polymer square container made of polymethyl methacrylate (PMMA) (50mm × 50mm × 20mm) (Figure 5.3D). This container facilitated blood adhesion to its surfaces, thereby inducing prestress/strain within the clot. The PMMA container was mounted on the same agitation setup within the incubator and then 15ml recalcified blood was added. We applied agitation-induced perturbation for 10 minutes at 7µm amplitude (2A/D=1.75) and 500Hz frequency ($f\sqrt{D/2}g=0.3$) for 5 agitation-enhanced samples and at 1.5μm amplitude (2A/D=0.35) and 1000Hz frequency $(f\sqrt{D/2g}=0.6)$ for agitation-degraded samples, where these amplitudes and frequencies produced the highest and lowest mechanical properties in blood clot experiments, respectively. The 5 native samples were generated within the same PMMA container without applying agitation. We then placed the specimens in the hydration bags within the incubator for 2 hours more to fully be crosslinked and coagulated. After removing the samples from the incubator, each specimen was individually placed on a calibrated grid, and an image was captured of the blood clot within the PMMA mold. We then carefully detached the blood clot from PMMA mold using a spatula. It was then repositioned onto the same calibrated grid, which had been moistened with phosphatebuffered saline (PBS), and another image of the blood clot was taken. During image processing using ImageJ we identified the four corners of the blood clots both within the PMMA mold and after their removal (Figure 5.2D,C).

As soft active materials, blood clots undergo contraction through platelet function, deforming the fibrin network (Figure 1Error! No text of specified style in document.13). As depicted in Figure 5.2F, clot contraction displays in-plane isotropy (in the x and y directions), with agitation-degraded clots exhibiting the most pronounced contraction, while agitation-enhanced clots display minimal contraction. These observations likely stem from differing elastic moduli

among these clots, suggesting the potential utility of agitation in modulating clot contraction—a pivotal process underlying wound healing and tissue regeneration.

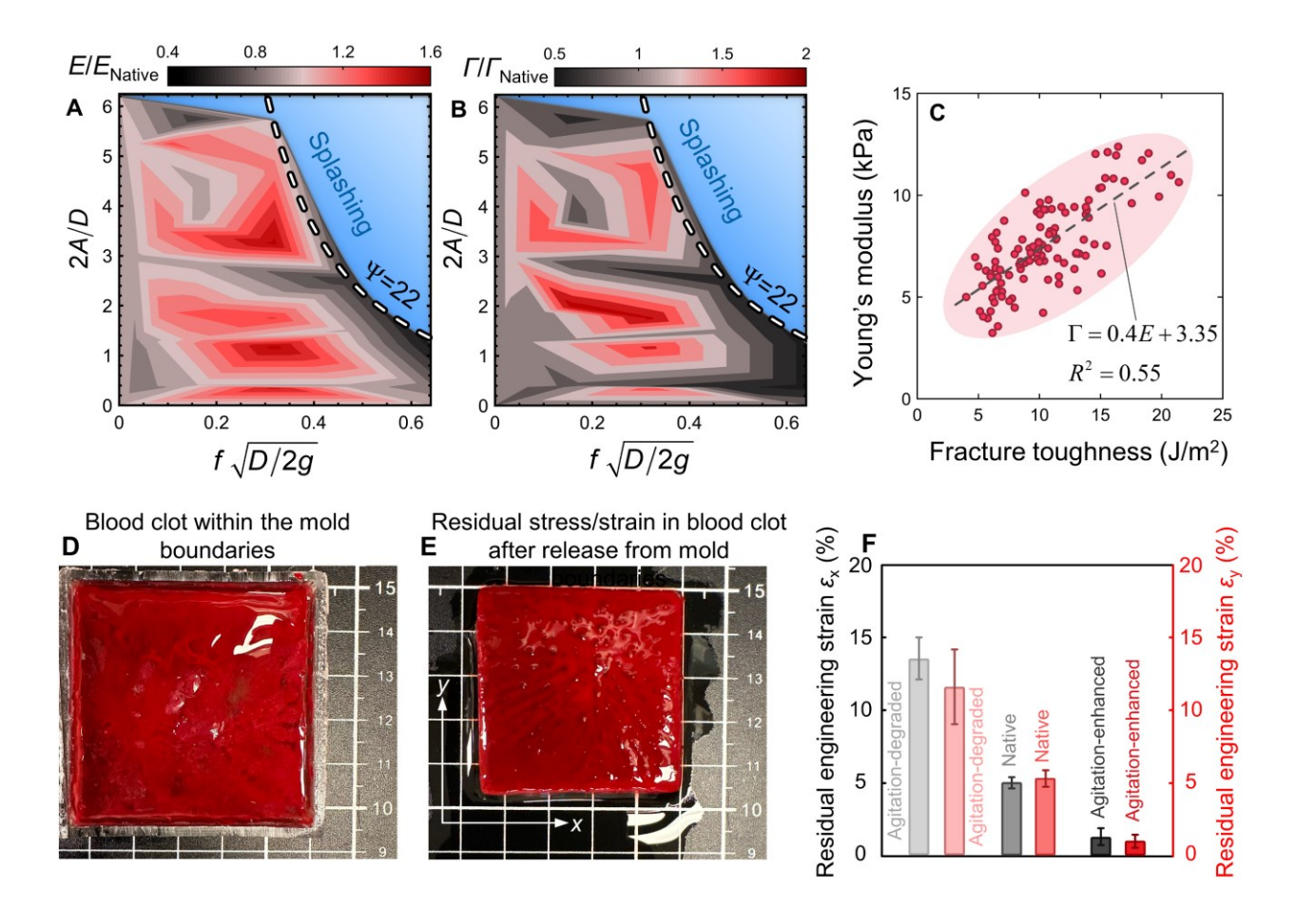


Figure 5. 2. Agitation-mediated mechanical properties of clot-like materials. Normalized elastic properties (A) and fracture toughness (B) of blood clot samples as function of dimensionless applied agitation amplitudes and/or frequencies. (C) Correlation between the elastic modulus of native and agitation-generated blood clots and their corresponding fracture toughness. (D, E) Contraction strain tests on the native and agitation-tuned confined blood clots. (D) Blood clot adhered to the PMMA mold walls (boundaries), producing pre-stress/strain; (E) detached blood clot from the PMMA mold. (F) Contraction strains of native and agitation-mediated blood clots released from the gelling mold. Data are shown as means \pm SD for n=3 independent experiments.

We further examined the other forms of mechanical agitation to prove this concept. We used a sonication bath (BRANSON 2510) and prepared 5 unnotched and 5 notched samples for each sonicated and native group. We prepared these samples the same as in previous experiments;

however, the sonicated samples were transferred to a sonication bath and sonicated for 10 minutes. The rest of the process and testing protocols were the same as in previous experiments. Figure 5.3 shows differences between both elastic and fracture properties of sonicated and native blood clots, implying that different forms of mechanical stimuli during clotting can vary the mechanical properties of blood clots. The sonication bath however is limited to a certain range of amplitude and/or frequency whereas the vibrating platform introduced in this study covers a wide range of mechanical agitations, enabling tuning a broad range of mechanical responses.

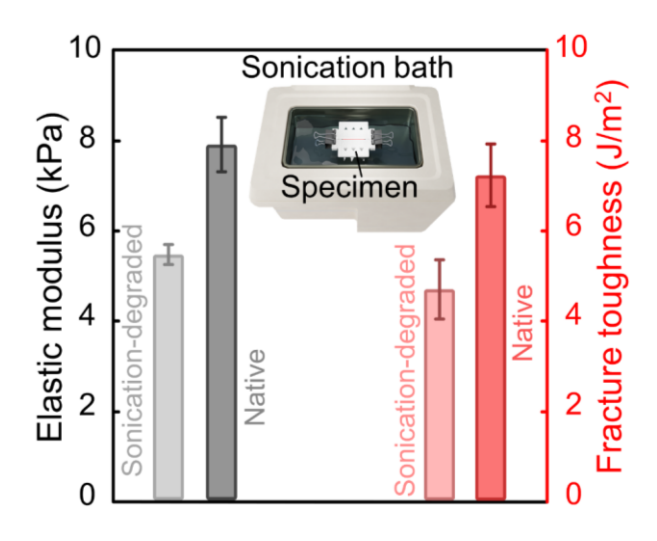


Figure 5. 3. Elastic modulus and fracture toughness of native and sonication bath-generated blood clots.

5.2 In-vivo Experiments

To further validate the effectiveness of our methodology in vivo, we tested it with a rat liver puncture bleeding model^[144]. We modified the agitating platform (Figure 5.4A-B) to apply agitation directly to the bleeding liver following a volumetric injury (Figure 5.4C). Guided by the phase diagram, we applied 10-minute agitations corresponding to the highest and lowest mechanical properties of blood clots (Figure 5.4A-B). Specifically, the agitation-enhanced conditions are 7µm amplitude (2A/D = 1.75) and 500Hz frequency ($f\sqrt{D}/2g = 0.3$), while the agitation-degraded conditions are 1.5µm amplitude (2A/D=0.35) and 1000Hz frequency ($f\sqrt{D}/2g = 0.6$). The formed blood clots were sequentially harvested for rheological tests (Figure 5.4D-F). Figure 5.4G shows the average storage moduli (G) for the agitation-enhanced and degraded groups normalized by the native group (Figure 5.4H). The formation of stiffer and tougher clots

under agitation could benefit wound management by minimizing risk rebleeding. These results prove the effectiveness of the agitation principle in manipulating the mechanical properties of blood clots in vitro and in vivo.

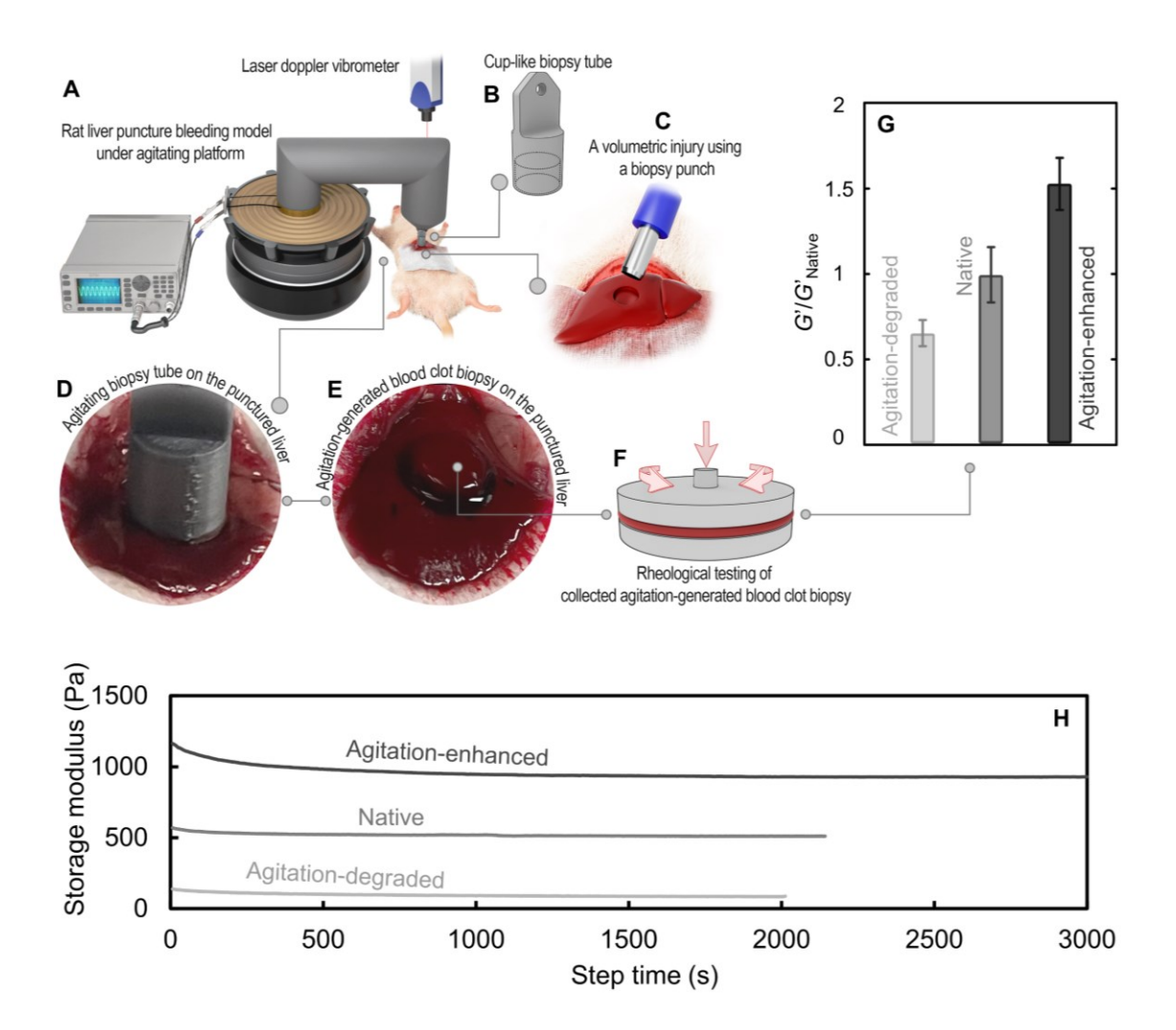


Figure 5. 4. (A-F) Demonstration of agitation-mediated clotting with a rodent liver bleeding model in vivo. The agitation is applied with a customized in vivo agitating platform (A) and a cup-like biopsy tube (B). A volumetric injury is made with a biopsy punch (C) and receives agitation on site (D). The resulting clots (E) are tested with a rheometer (F), displaying normalized storage moduli of native and in-vivo agitation-mediated blood clots (G). Typical obtained storage modulus curves in rheology testes for in-vivo agitation generated blood clots.

5.3 Extending to Clot-like Materials

To demonstrate the universal applicability of the agitation-mediated principle, we varied the inclusions within the fibrin network. A better understanding of the underlying mechanisms involved in fabricating fibrin network architecture can be used to explore the implications of agitation-induced perturbation on other fibrous and biopolymeric materials. For reference, we extracted the RBCs and platelet-rich plasma from blood and obtained the platelet-poor plasma to form plasma clots during agitation-driven perturbation. Our objective was to experimentally study agitation-induced perturbation influences on the mechanical responses of plasma clots as a representative of natural fibrous material system. Figure 5.5A shows the elastic modulus and fracture toughness of native and agitating specimens normalized by native group; it also highlights that the agitation-induced perturbation do not independently affect the mechanical performance of the fibrin network.

We then considered and mimicked the effect of RBCs (or other inclusions/cells) dispersion on the fibrin network mechanical responses by adding microgels (another material model) to the plasma and applying agitation-induced perturbation during clot formation. Microgels expand some concepts of the gels while borrowing some characteristics from wet and/or soft granular matter in a way which can be consistent with RBCs or other cells (inclusions). The diameter of the microgels varies from 10~50 µm (Figure 2.4)—large enough to represent other soft and/or wet granular materials or cells within a biofluid and/or biomonomer also small enough in a way that mimics RBCs dispersion. Figure 5.5B shows the elastic modulus and fracture toughness of plasma/microgels clots for native and agitation-generated specimens normalized by native group. Figure 5.5A,B reveal that microgels dispersion due to the agitation-induced perturbation can both amplify and/or degrade the mechanical performance of plasma/microgels clots depending on the applied agitation amplitude and frequency range.

RBCs and microgels do not have nuclei; we therefore extend this concept by replicating our previous experiments with the typical cells with nuclei, human vocal fold fibroblast cells and adding them to the plasma. Since our agitating platform has manipulated the tensile mechanical properties of soft inclusion/clot-like material systems, our objective was first to assess regulating the shear properties of these material systems. Second, to explore whether the cells with and without nuclei can behave like soft inclusions under agitation-steered perturbation and be used as

blocks to tune the mechanical performance of a typical natural fibrous clot like plasma. Finally, to examine the safety and effect of our agitating platform on the cells viability and morphology within plasma clot. Figure 5.5C shows the average storage modulus (G') at the plateau normalized by native group results for agitation-degraded, native and agitation-enhanced groups (Figure 5.5D). In addition to our understanding from RBCs and microgel so far, Figure 5.5 demonstrates that soft cells and/or inclusions can be used as blocks to modulate the structure-property response of fibrous materials under mechanical agitations. At this point, it is useful to highlight that although there are analogies between RBCs, microgels, and fibroblast cells, their geometry, size, density, volume fraction and properties differ. Their degree of dispersion nonuniformity and architectural effect on the fibrin network can therefore be in a distinct fashion, resulting in different mechanical responses.

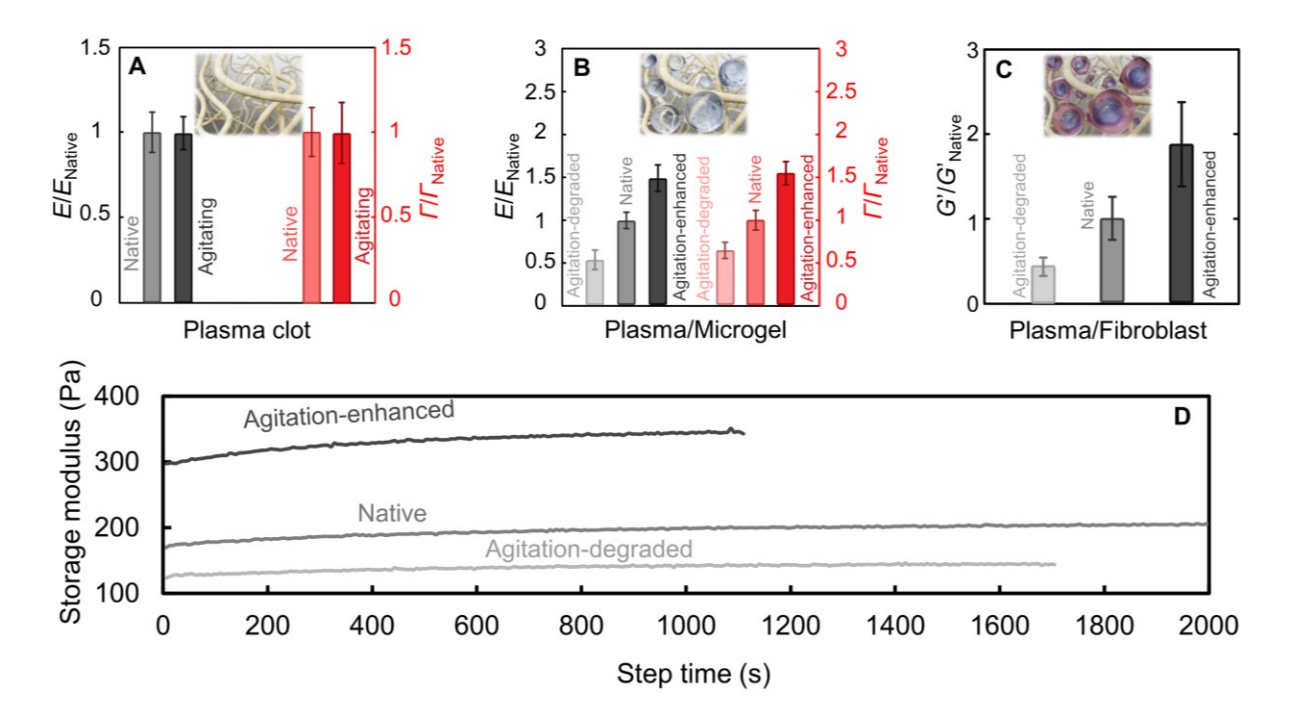


Figure 5. 5. (A) normalized elastic modulus and fracture toughness of native and agitation-mediated plasma clots. (B) Normalized elastic properties and fracture toughness of native and agitation-mediated plasma/microgel clots. (C) normalized average storage modulus of native and agitation-mediated plasma/fibroblast clots. (D) Typical obtained storage modulus curves in rheology testes for plasma/fibroblast cells clots. Data are shown as means ± SD for n=5 independent experiments.

5.4 Microstructure Characterization

It has been demonstrated that the RBCs dispersion can change the fibrin network microstructure^[163], which may result in meso- and/or macro-scale mechanical responses of the blood clots. We here explored the confocal microscopy images to understand the synergistic effect of agitation-induced perturbation and resulting RBCs dispersion on the microstructural changes of the fibrin network. The findings can inform an indirect role of the RBCs in the microstructure of the fibrin network and in turn be used to tune and optimize the mechanical performance of the blood clots depending on therapeutic targets. The confocal imaging allowed for precise visualization of the spatial organization of RBCs within the fibrin network, elucidating their dispersion patterns and potential clustering. Quantitative analysis of the imaging data was performed to provide insights into the relationship between clot microstructure, RBC arrangement, and the mechanical properties of the clot. It has also been demonstrated that there is a close similarity between RBC and spherical dispersion; therefore, the following short- and long-range spatial analyses are reliable statistical tools to quantitively assess the RBC dispersions [149]. We therefore spatially analyzed the degree of RBCs dispersion nonuniformity using nearest neighbor distance and radial distribution function across 3 different samples and regions of agitationdegraded (low), native, and agitation-enhanced (high) mechanical properties. The nearest neighbor distance (NND) function is an efficient means to assess short-range spatial analyses^[151], which here indicates the distance between the centroid of each RBC with its nearest neighbor. The probability density function of the calculated first, second, and third NND for all RBCs represents the degree of random dispersion. For a random dispersion, a high sharp density peak in the first NND is expected, while this peak tends to gradually decrease in the second and third NND^[151]. In addition, the range of centroid-to-centroid nearest neighbor distances is expected to increase from the first nearest neighbor to the third one^[151].

Agitation-mediated cell organization: We propose that agitation-induced perturbations influence the dispersion and/or packing of cells, which create downstream effects on the structure of the biopolymer network. We tested this mechanism by characterizing the microstructure of blood clots and plasma/fibroblast clots using a confocal microscope. The clots were either enhanced or degraded by agitation and compared to native counterparts without agitation. We stained RBCs and fibrin fibers to visualize the dispersion of RBCs within the fibrin network

(Figure 5.6). The spatial dispersion of RBCs for each group exhibited different microstructural characteristics (Figure 5.6 and Figure 5.7A-C). We quantified them with kernel density estimations of RBCs for first, second, and third nearest neighbor distance (NND) as function of the normalized centroid-to-centroid nearest neighbor distances (d/\overline{R}) (Figure 5.7D-F) (histograms are shown in Figure 5.8). These observations imply that the RBCs in the low group are more packed and/or closer to each other; conversely, the RBCs in the high group have more distance from each other compared with the native and low groups. The degree of random dispersion for the native group is intermediate between low and high groups. We further verified these findings by the box-and-whisker diagram (Figure 5.7G), while the width and length of boxes and whiskers indicate the variation of data spread and skewness.

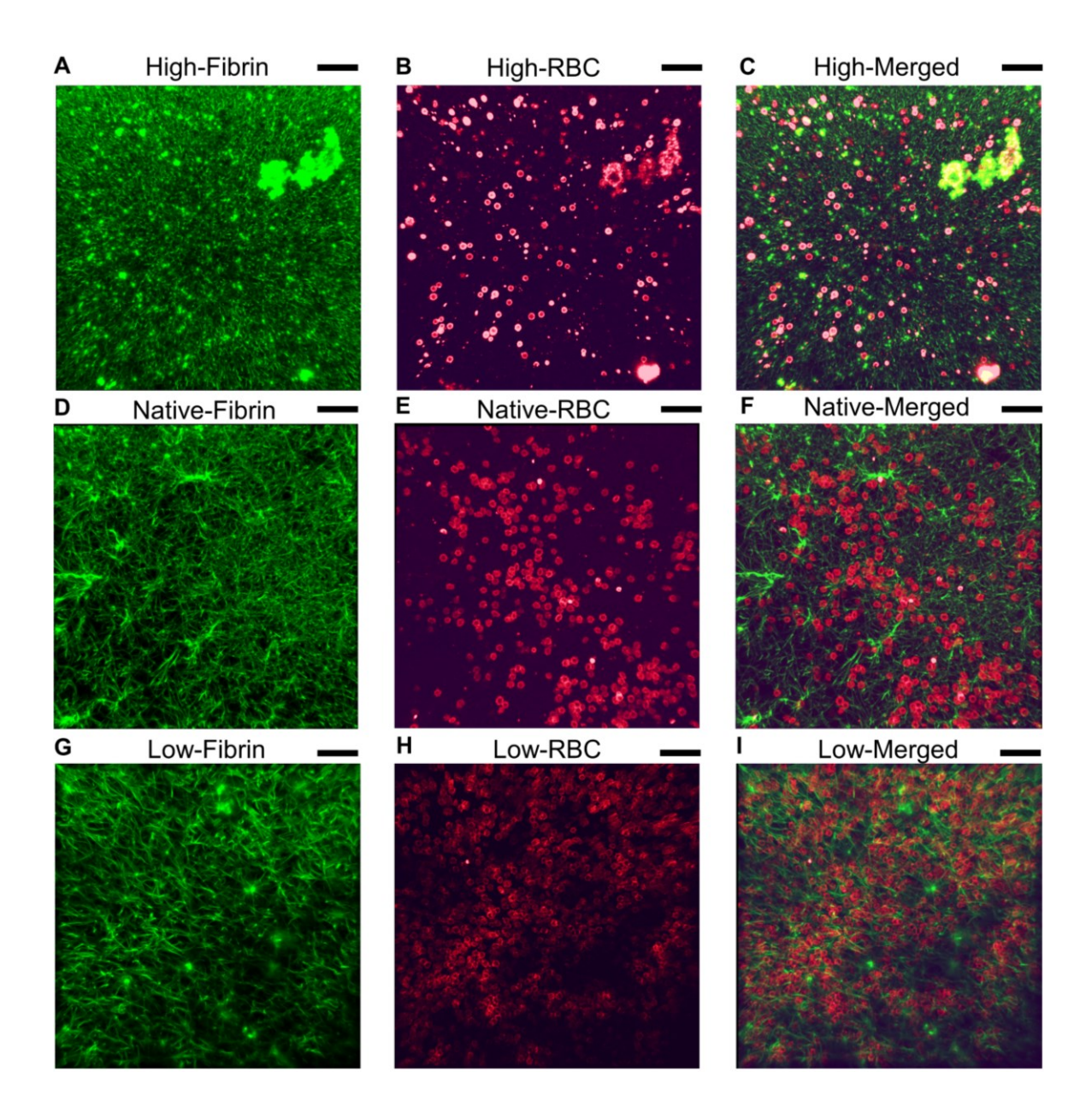


Figure 5. 6. Confocal images of native and agitation-generated blood clots. (A) Fibrin network of agitation-enhanced blood clots; (B) click-chemistry labelled RBCs for agitation-enhanced blood clots; (C) merged image of agitation-enhanced blood clots. (D-F) Fibrin network, RBCs and merged image of native group. (G-I) Fibrin network, RBCs and merged image of agitation-degraded group. Scale bars are 30μm. Fibrin fibers and RBCs were stained as green and red respectively.

We assessed the long-range spatial analyses through radial distribution function g(r) (pair correlation function), which here provides the variation of average RBC density along a distance from the centroid of an arbitrary RBC^[149, 151]. g(r)=1 represents the theoretical complete spatial

random (CSR) dispersion, g(r)>1 can express clustering and/or agglomeration, and g(r)<1 demonstrates that the RBCs density is lower than the average value in the corresponding circular shell (Figure 5.7H). We further confirmed these observations by kernel density estimation as function of radial distribution function g(r) shown in Figure 5.7I (histograms are shown in Figure 5.9). The high group has the highest and sharpest density without any second peak, narrowed toward CSR. Although the low and native group seems to follow the same trend, the second peak of native group happens at 1.5 < g(r) < 2, which is remarkably lower than the low group second peak at 2 < g(r) < 2.5.

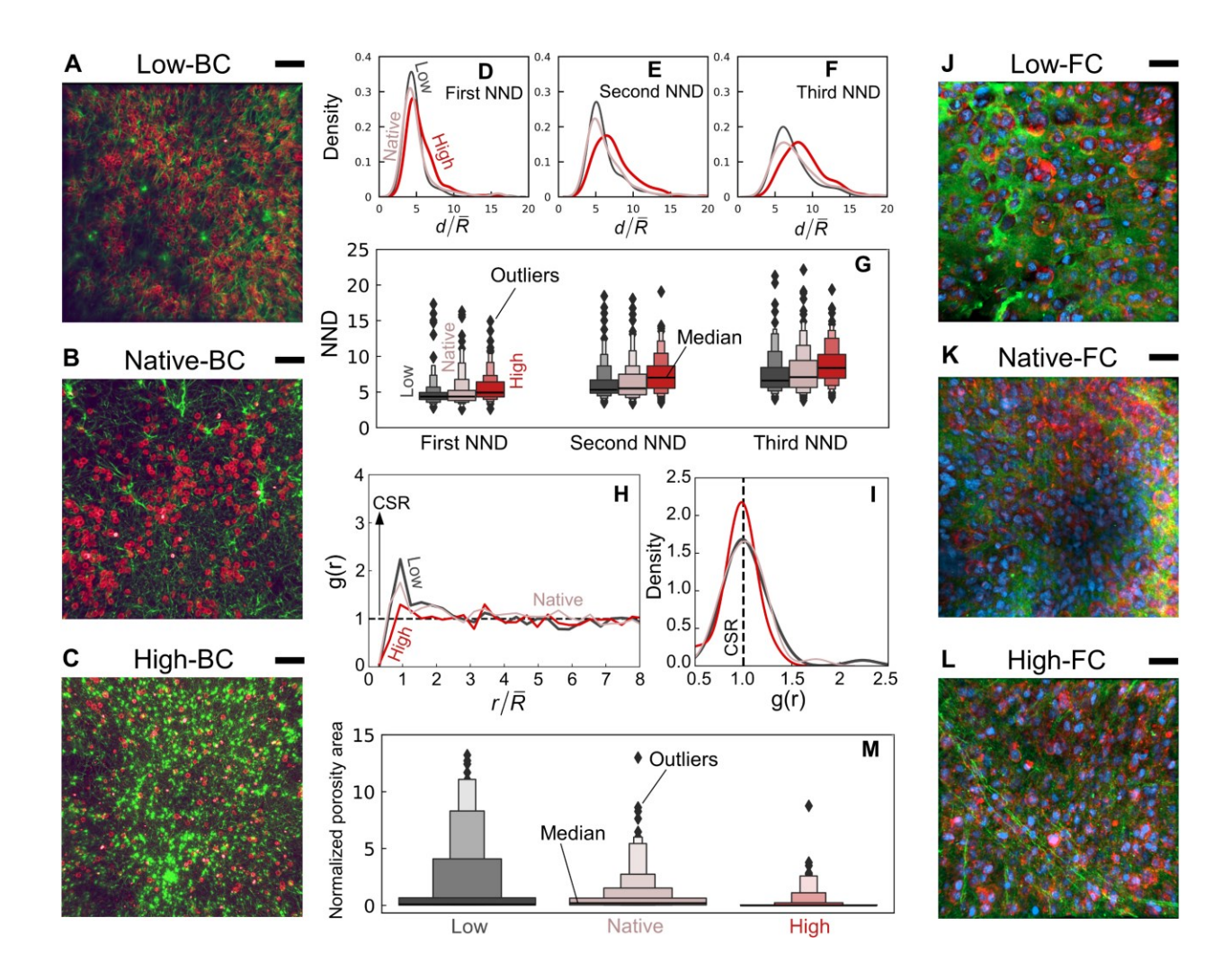


Figure 5. 7. Three-dimensional confocal microscopy image stacks with morphometric quantifications and spatial analyses. (A) Blood clot (BC) with low (agitation-degraded) mechanical properties; (B) native blood clot group; (C) blood clot with high (agitation-enhanced) mechanical properties. The scale bars are 30μm and fibrin fibers and RBCs were stained as green and red respectively. First (D), second (E), and third (F) nearest neighbor distance (NND) density distributions of RBCs and their box-and-whisker diagram (G). (H) Radial distribution function g(r) (pair correlation function) as function of a long-range normalized distance of RBCs; (I) kernel density estimation of radial distribution function g(r) for RBCs. CSR denotes complete spatial random. Nucleus and actin structure confocal images for agitation-degraded (Low) (J), native (K), and agitation-enhanced (High) (L) plasma/fibroblast cells clots (FC) on day 1. Scale bars are 40μm and Fibrin fibers, nucleus, and actin were stained as green, blue, and red respectively. (M) The normalized average porosity area in plasma/fibroblast cells clots for agitation-degraded (Low), native, and agitation-enhanced (High) groups. Data are shown as means ± SD for n=3 independent experiments.

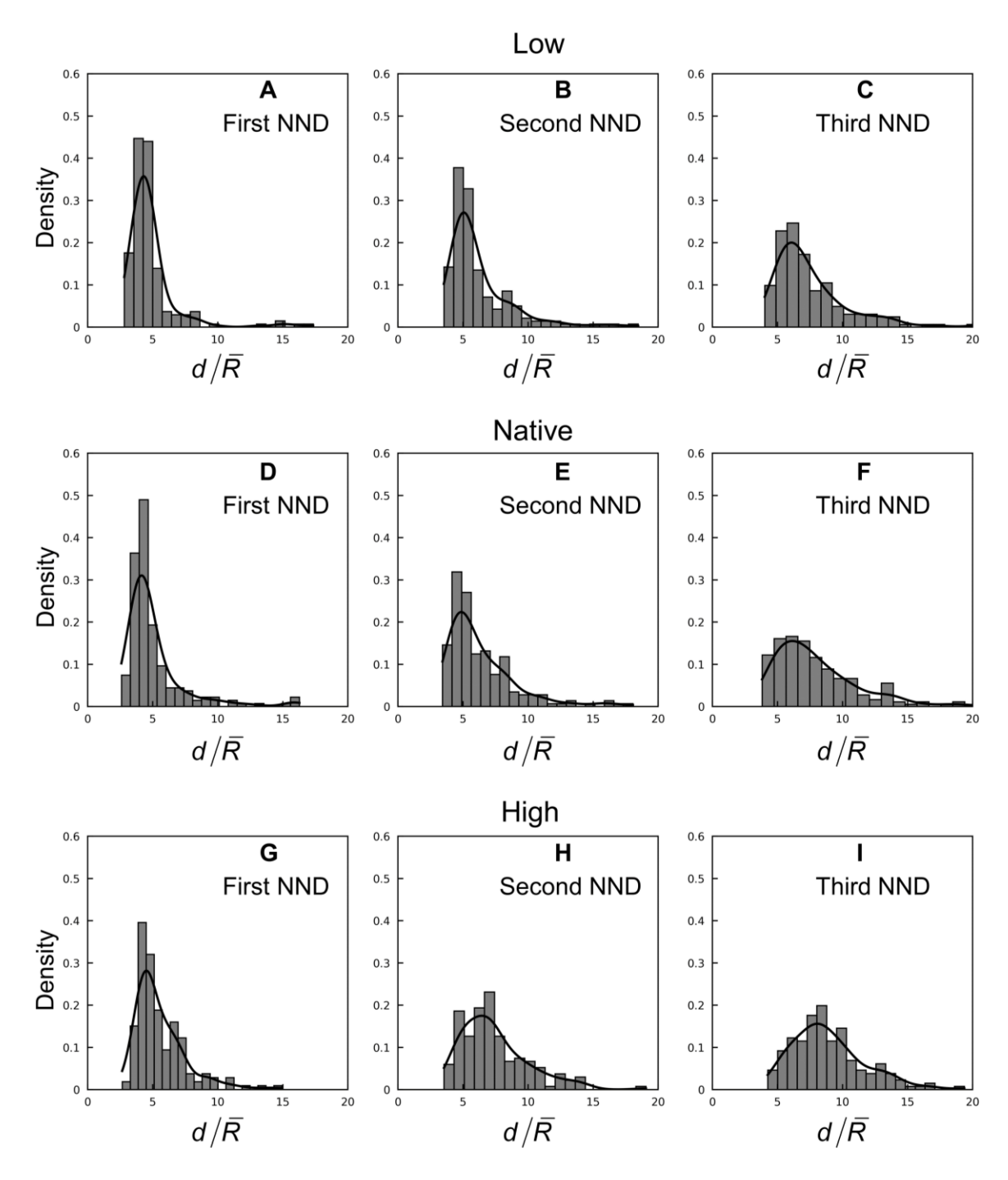


Figure 5. 8. The histograms of first, second, and third nearest neighbor distance (NND) density distributions of RBCs. (A-C) Agitation-degraded (low), (D-F) native and (G-I) agitation-enhanced (high) blood clots, where d is centroid-to-centroid nearest neighbor distances and \overline{R} is the average of RBC radii.

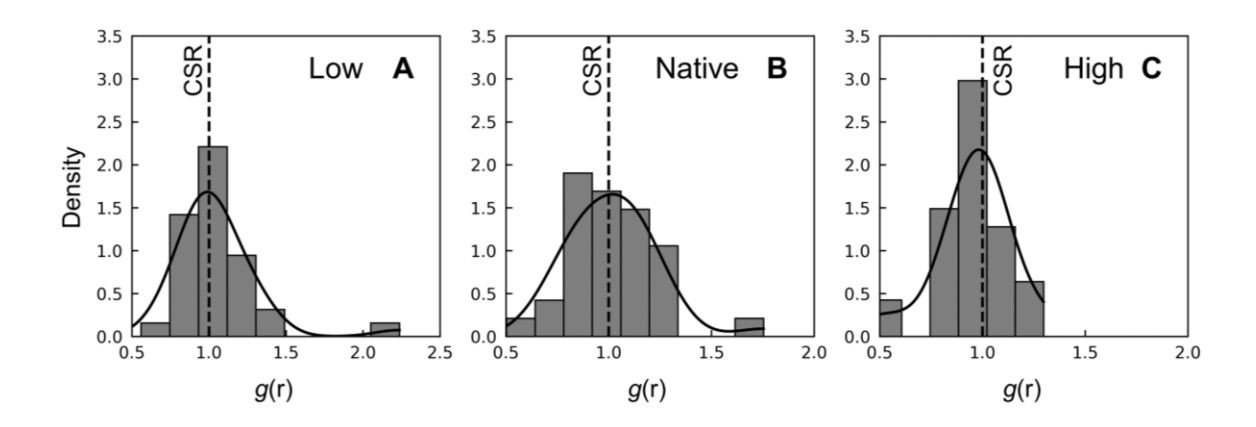


Figure 5. 9. The histograms of kernel density estimations of radial distribution function g(r) (pair correlation function) of RBCs. (A) Agitation-degraded (low), (B) native and (C) agitation-enhanced (high) blood clots.

The same trend can happen to the agitation-generated and native plasma/fibroblast clots. We stained cells nuclei to recognize single cells, cell clusters and actin membrane to evaluate cell spreading and morphology within the stained fibrin network (Figure 5.7J-L). Figure 5.10 show the fibrin network, cells nuclei and actin membrane for high, native, and low groups on day 1. Similar to blood clot samples, these figures reveal a distinct fibroblast cell dispersion for each group, resulting in different porosity fashions in fibrin microstructure. Figure 5.7M shows the average porosity area in the fibrin microstructure of plasma/fibroblast clots normalized by the average area of a single fibroblast cell ($\approx 300~\mu m^2$) low, native, and high groups on day 1. Figure 5.8M indicates that more cells agglomerated in low groups so that there are larger porosities within the fibrin network compared to native and high groups. The cells in the high group are less clustered or more dispersed, and therefore the fibrin microstructure in this group has smaller porosity sizes. These observations are consistent with the blood clot samples.

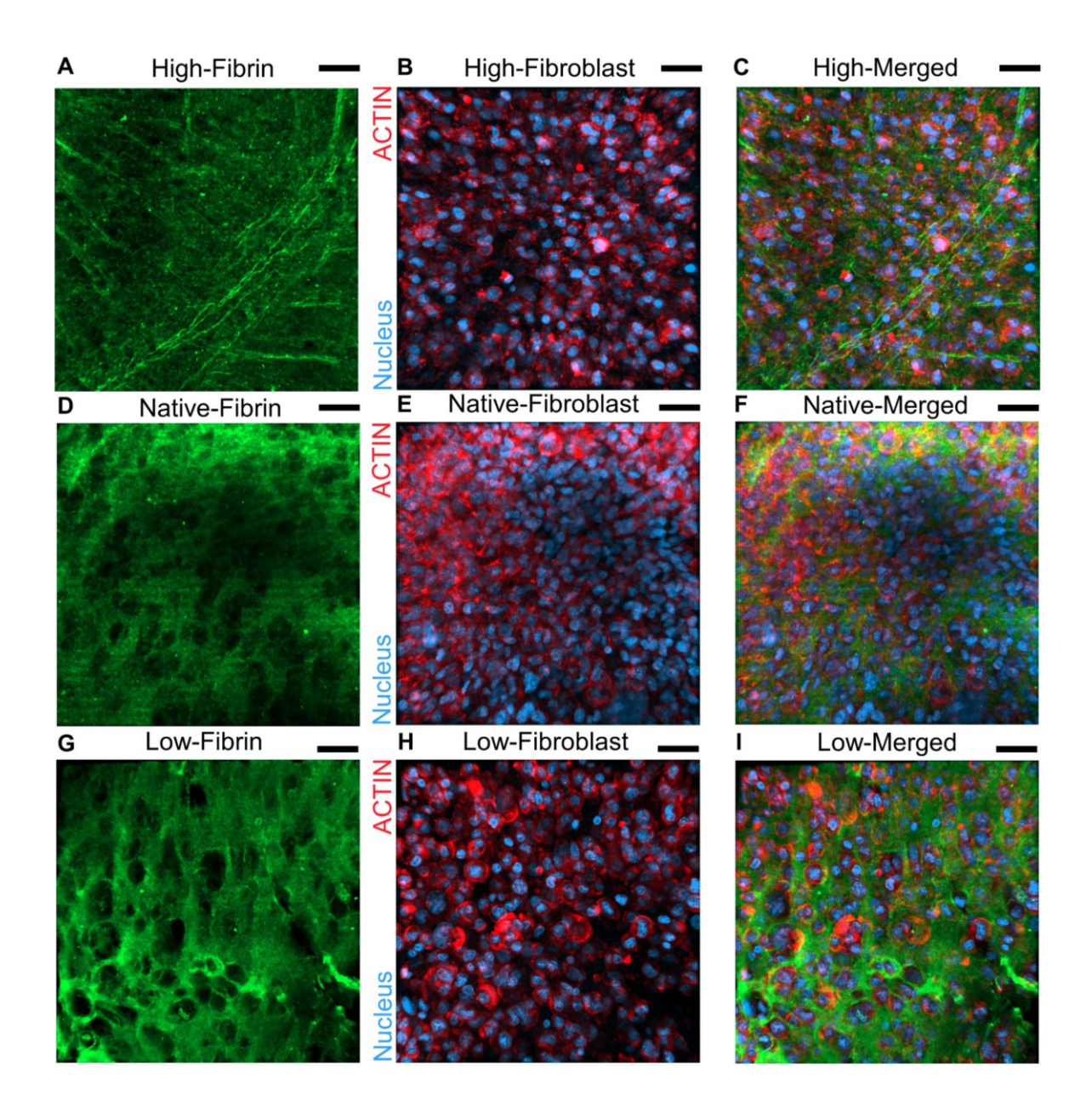


Figure 5. 10. Nucleus and actin member confocal images of native and agitation-generated plasma/fibroblast cells clots. (A-C) Agitation-enhanced (high), (D-F) native, and (G-I) agitation-degraded (low) plasma/fibroblast cells clots on day 1. Scale bars are 40μm. Fibrin fibers, nucleus, and actin were stained as green, blue, and red respectively.

We also studied the effect of agitation-perturbation on the fibroblast cells viability and morphology within plasma/fibroblast clots for agitation-enhanced and -degraded (high and low mechanical properties) cases using confocal z-stack imaging. Figure 5.11A,B show the merged z-stack confocal images of fibroblast cells viability for high and low groups on day 1. These figures beside their dead reference image (Figure 5.11C), exhibit that generated agitation-perturbation by our agitating platform is not invasive for fibroblast cells (Figure 5.11D).

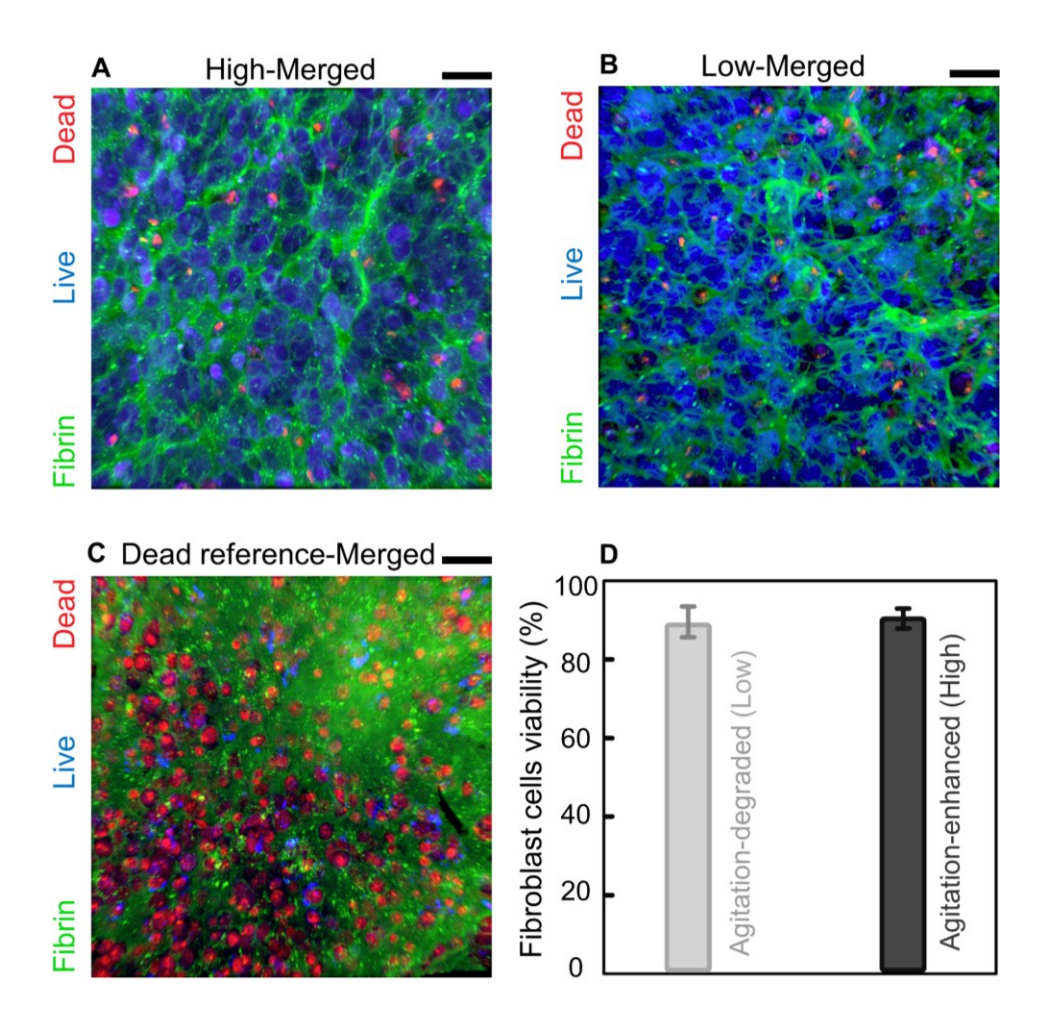


Figure 5. 11. Cell viability confocal images for the agitation-generated plasma/fibroblast cells clots on day 1. (A) agitation-enhanced (high) and (B) agitation-degraded (Low) groups; (C) dead reference control group. Scale bars are 80μm. Fibrin fibers, live cells, and dead cells were stained as green, blue, and red respectively. (D) The fibroblast cells viability percentages within the crosslinked plasma for both agitation-degraded (low) and agitation-enhanced (high) groups.

Microstructure of fibrin networks: In addition to cell spatial organization, we characterized the microstructural features of fibrin network including fiber diameter, length and orientation using 3D reconstruction morphometric quantifications of confocal images for native and agitation-generated blood clots (Figure 5.12). The average of obtained fiber diameters and lengths from confocal image analyses are plotted in the box-and-whisker for native and agitation-generated blood clot samples (shown in Figure 5.13A,B). These figures exhibit an inverse correlation between fiber diameters and lengths in low, native, and high groups, resulting from the porosity size and dispersion in fibrin networks. The high group benefits from larger diameters and shorter lengths. In addition to the dimensions of the fibers, the results suggest that the orientation of fibers may also be in play, which we have studied and shown in Figure 5.13C,D. Figure 5.13C,D shows the low and native groups are in close agreement with CSR with respect to *θ* angle orientation; however, fibers in the high group are mostly aligned in the range of 60°< θ_i <120°, while maximum alignment happens at θ_i =90°. Similarly, the orientation of fibers in low and native groups with respect to *φ* angle correlates well with the CSR (Figure 5.13C,D), while the high group benefits from more aligned fibers in 90°< φ <180° and 180°< φ <270° range.

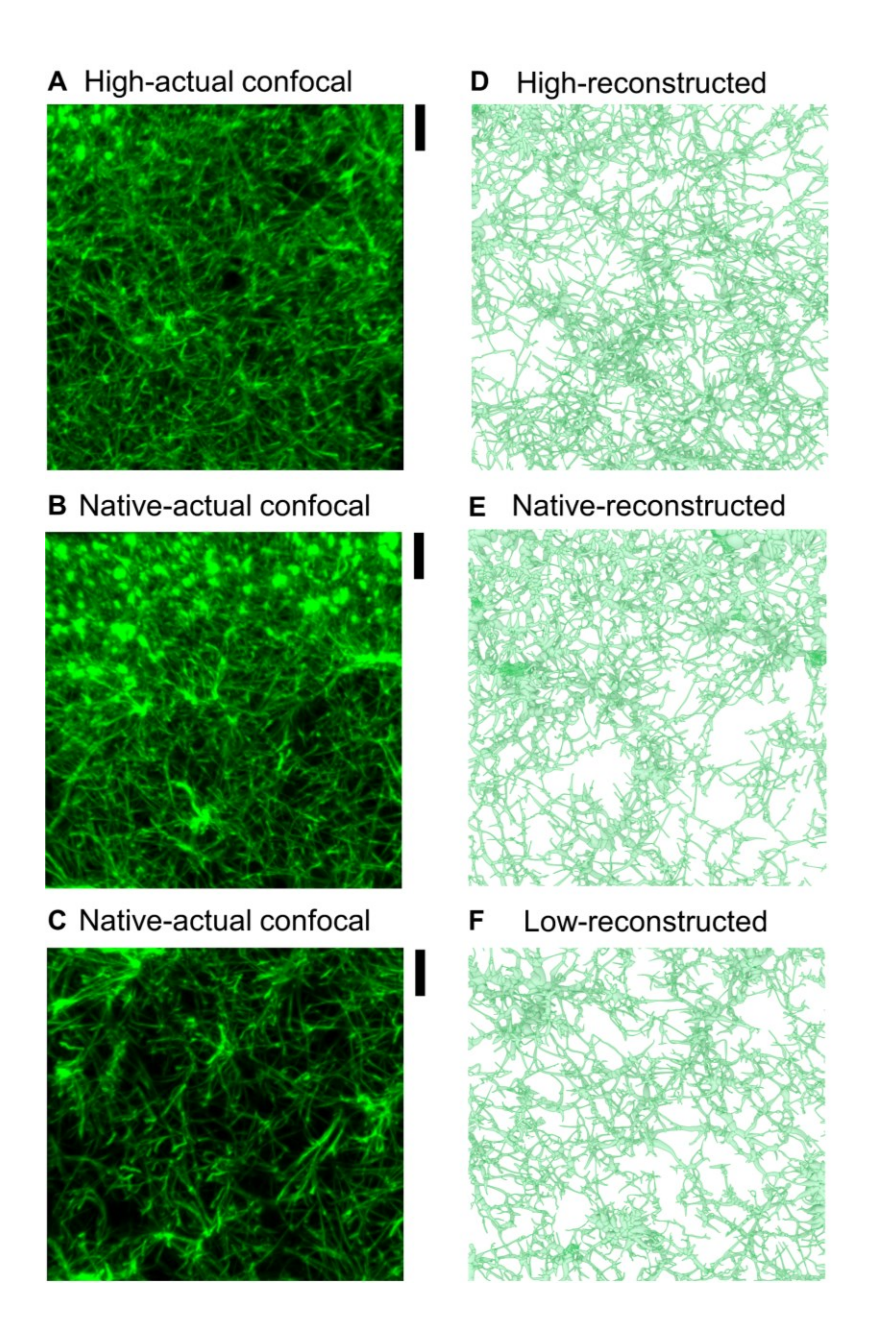


Figure 5. 12. Actual fibrin network confocal images of native and agitation-generated blood clots with their 3D reconstruction morphometric quantification. (A-C) Actual fibrin network confocal images for blood clots with high (agitation-enhanced), native, and low (agitation-degraded). (D-F) 3D reconstructed geometries of fibrin network from their confocal images for blood clots with high (agitation-enhanced), native, and low (agitation-degraded).

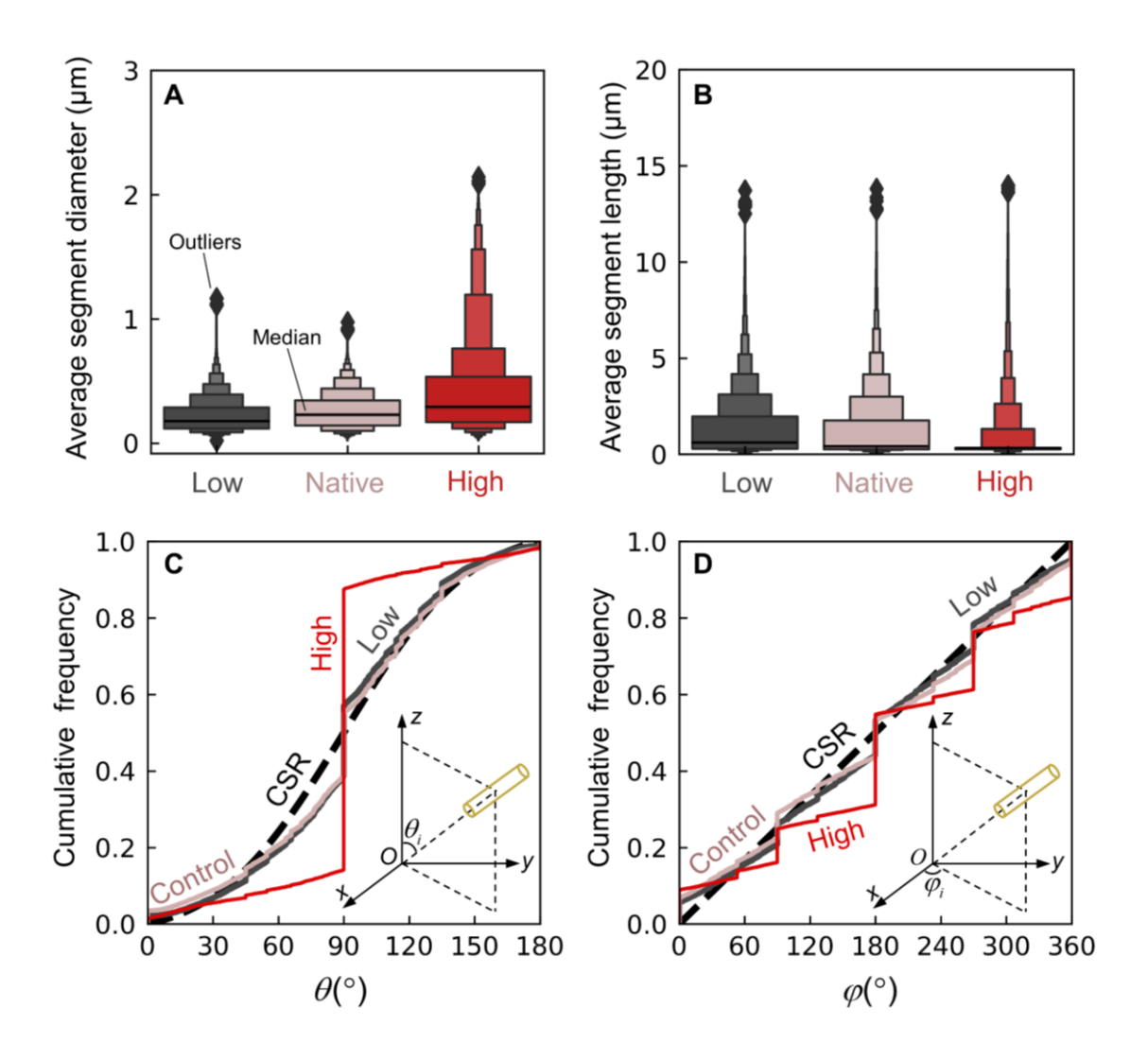


Figure 5. 13. Box-and-whisker diagram of fiber diameters (A) and lengths (B). Cumulative frequency of fiber orientations as function θ (C) and φ (D) angles. CSR stands for complete spatial random. Data are shown as means \pm SD for n=3 independent experiments.

To further verify these findings, we comparatively examine the mass reduction (degradation) of native and agitation-generated blood clots during fibrinolysis condition. We therefore devised a protocol to implement a fibrinolysis test on the whole blood clots (Figure 5.14A). We used the same procedure to form native and agitation-generated blood clots. Figure 5.14B shows the mass reduction percentage of each group versus incubation time, implying a strong connection between the structure-property response of blood clots with the ease of their degradation.

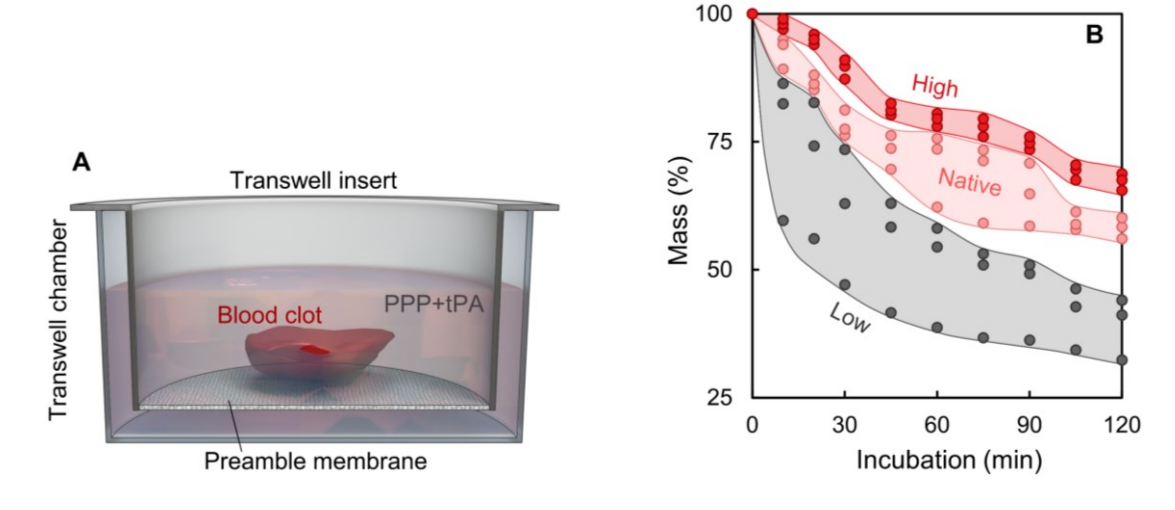


Figure 5. 14. (A) Blood clots fibrinolysis test using a transwell. (B) Mass reduction percentage versus incubation duration for fibrinolysis tests of agitation-mediated and native blood clots. Data are shown as means \pm SD for n=3 independent experiments.

Figure 5.14 also indicates that our agitating platform that can form blood clots with low mechanical properties can offer a new therapeutic route for fibrinolysis and/or thrombotic disorders. We experimentally verified the correlation between the agitation-driven inclusion dispersion and microstructural characteristics of the fibrin network. The agitation-induced perturbation can disperse or agglomerate soft inclusions (here in this study, RBCs, microgels, and fibroblast cells) within biofluids and/or biomonomers (here in this study, blood and plasma) which can indirectly adjust the microstructure of the biopolymeric and fibrous network (here in this study, fibrin network), resulting in different meso- and/or macro-scale mechanical performance

In the following, we sought computational models for effective microarchitectures (RBC dispersion, fiber diameter, and length) underlying the variation of the elastic response of clot-like materials (soft distributed cells/inclusion embedded within a fibrous network) to establish a design guideline for these material systems.

5.5 Hybrid Element Modeling

To compute the structure-property elastic response of soft inclusion/fibrous network clot material systems, we further built a hybrid element model where RBC and linkages are modeled with 3D deformable continuum elements and 3D truss elements, respectively. Fibrous chains and networks can be modeled using beam, truss, and spring elements^[20, 161, 164]. Three elements yielded

similar results in our simulation, likely due to the micro-scale thickness and length of linkages and the tensile loading in the elastic regime. Our model can recapitulate the cell dispersion and fiber geometry of blood clots. Based on micro-characterization results, we generated two types of RVEs: One RVE with randomly dispersed RBCs represents the agitation-enhanced blood clots (Figure 5.15A), and the other with clustered RBCs simulates the agitation-degraded blood clots (Figure 5.15B). By incorporating the linkages between RBCs, our model could simulate the structure and mechanics of blood clots (Figure 5.15C). To prove so, we first examined the linkage length in the two models. The maximum achievable RBC volume fraction for non-uniform dispersion was 15%, and for clustered dispersion was 5%. It should be noted that non-uniform sequential mobile packing and other available geometry generation algorithms are limited in generating non-uniform and clustered dispersion and/or misoriented high volume fractions complex shapes like an RBC^[151]; therefore, exploring higher RBC volume fractions remained limited in this study. For each case, we generated three different random microstructure trials to take this effect also into account. All nodes located in the outer side of the RVE were all together subjected to 0.5% normal strain, while the nodes on the corresponding opposite side were fixed, and the elastic modulus was computed from obtained stress-strain curve.

Figure 5.15D shows a typical histogram of the length of linkages (L_1) normalized by the length of fiber segment ($L_{\rm sf} = 1 \mu {\rm m}$) measured experimentally^[165]. We found a good agreement between the generated models and experimental measurements. Additionally, we validated our model by varying the RVE size (L) and analyzing the resulting elastic moduli under unidirectional tensile loading. Figure 5.15E shows the convergence (deviation < 10%) of the elastic modulus of blood clots normalized by that of RBC-free plasma clot (13.5kPa) when L is 15 times of the RBC diameter ($D = 8 \mu {\rm m}$). With the model validated geometrically, we next studied the impact of cell dispersion and volume fraction on the elastic modulus of clots. Figure 5.15F plots simulations of randomly dispersed and clustered RBC clots, alongside the experimental results derived from native clots without agitation treatment. We found agreement between them at low RBC contents, from 0% (plasma clot) to 2.5% RBC volume fraction, where the clot stiffness decreases. The results suggest that the RBC-free plasma clot could be stiffer than blood clots and that the native blood clots are closer to the dispersion with clustered RBC than randomly dispersed one. These findings are in agreement with our experimental results and literature reports^[12]. When the RBC content further increases, these computational and experimental results diverge. The randomly

dispersed RBC model yielded significantly higher stiffness than the clustered RBC model and the native clots. Specifically, at 15% RBC volume fraction, the randomly dispersed model surpasses that of the native clot by 47%, a finding consistent with our experiments of native and agitationenhanced blood clots. Furthermore, our model enables a parametric study to investigate the correlation between microstructural characteristics of fibrin networks and their mechanical behavior. Figure 5.15G, H illustrate the computed stress fields in the RVEs with RBCs (15% volume fraction) and without RBCs (linkage net) under unidirectional tensile loading. These images reveal high stress concentration through the linkages, while the RBCs remain less-stressed due to their compliance response. As another demonstration, we used the linkage net model (RBCfree) to study how various combinations of linkage length, diameter, and number influence the elastic responses. Figure 4I shows a contour map of the elastic modulus of the linkage net model normalized by that of a fibrin fiber as functions of linkage length (L_1) normalized by fibrin segment length ($L_{\rm sf} = 1 \mu {\rm m}$) and linkage cross-section diameter ($D_{\rm l}$) normalized by the average fibrin diameter (D_f = 250nm) obtained for native group in this study. Consistent with our experimental results, the network stiffens with shorter linkages and larger diameters. This trend correlates with the quantity of linkages in the model, indicating that a stiffer network comprises more thickly packed fibers. The significant difference between elastic moduli of RBCs and linkages can turn this model into a representative for other cell-based and clot-like material systems since it has been reported that there is no remarkable difference between RBCs and spherical inclusion dispersions^[149] and also demonstrated in this study for spherical microgels and fibroblast cells.

To compare our models with experiments, we isolated RBCs from blood and then prepared and tested native blood clot pure shear samples with various RBC volume fractions up to our geometry generation algorithm limitation (1%, 2.5%, 5%, 10%, 15%, while 0% represents plasma clot) and 5 replicates for each volume fraction. Figure 5.15F compares the elastic modulus of blood clot normalized by the elastic modulus of plasma clot versus different RBC volume fractions extracted from experiments, non-uniform, and clustered RBC dispersion simulations across 3 different random microarchitecture trails. There is a good overall agreement between experiments and both non-uniform and clustered dispersion from 0% (plasma clot) up to 2.5% RBC volume fraction, while the clustered model is nearly correlated with experiments up to 5% RBC volume fraction. The results of our models in Figure 5.15F also demonstrate that by increasing the RBC volume fraction, the native blood clots in experiments are closer to the dispersion with more RBC

clusters than non-uniformly dispersed one—a finding that matches with our experimental observations. It has been reported that the plasma clot elastic properties are higher than regular blood clots^[12], as shown in our experimental results and captured by our numerical simulations in Figure 5.15F. Figure 5.15G, H highlight typical computed stress counters in the RVEs with RBCs (15% volume fraction) and without RBCs (linkage net) under applied normal deformation which reveals high stress concentration through the chains while the RBCs remain less-stressed due to their compliance response.

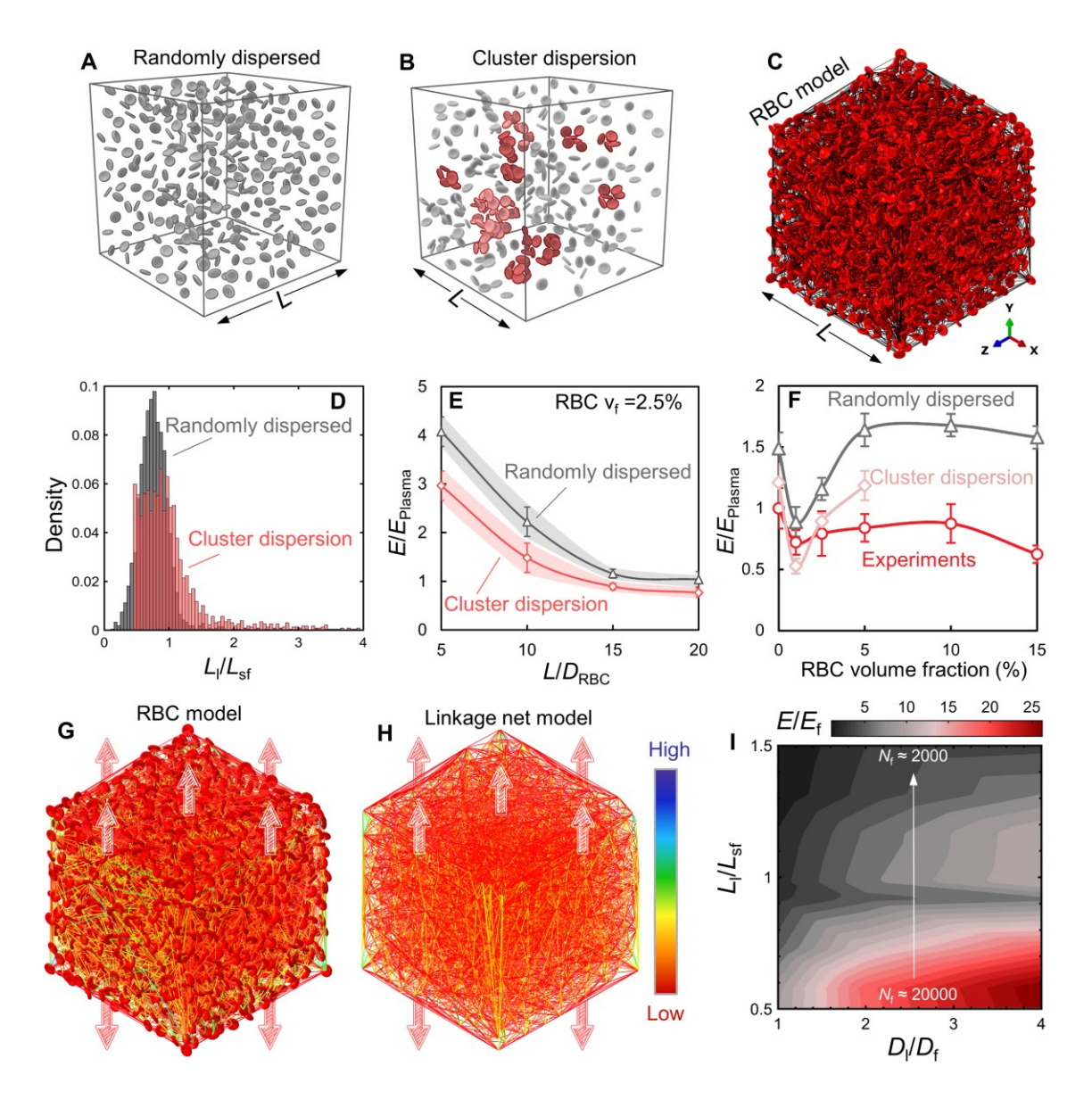


Figure 5. 15. Hybrid element computational models of blood clots. (A) Randomly dispersed RBCs within a representative volume element (RVE); (B) clustered (agglomerated) RBCs beside randomly distributed RBCs within an RVE; (C) RBC model includes RBCs and connected linkage networks; (D) statistical analysis of linkage networks length distribution for both random and clustered cases (L_{sf}, fibrin segment length); (E) size assessment of RVEs for both randomly dispersed and clustered distributions for RBC model; (F) comparisons of computed normalized elastic (Young's) moduli for random and cluster dispersion models and experiments native clots versus RBCs volume fractions; (G) stress contours within RBC model and (H) linkage networks model under tensile loading (indicated by arrows); (I) variation of normalized elastic (Young's) modulus of linkage networks model as function of linkage number and normalized linkage length and diameter. Data are shown as means ± SD for n=3 independent simulations and experiments.

CHAPTER 6

Discussions

This chapter covers the links between hard and soft inclusions under mechanical agitations. Then, it discusses results and predictions of vibration-generated assembly phase diagrams for polyhedral blocks using the mechanics of single-block models. It also explores potential applications of vibration-driven topologically interlocked materials and structures. Furthermore, it reviews and discusses the findings and potential applications of engineering clot-like materials through mechanical agitation perturbations. Lastly, it highlights the possible future work based on this dissertation.

6.1 Similarities and Differences between Hard and Soft Inclusions

The agitation-generated phase diagrams presented in Figure 4.1 for hard inclusions demonstrated three main regimes: a static regime where there were no changes in block packing, an assembly regime where various ordered and disordered block packings or arrangements could be achieved, and a fluttering regime where chaotic behaviors precluded block packing. Similarly, the agitation-generated phase diagrams for soft inclusions, presented in Figure 5.2A,B, demonstrated a regime (low amplitudes and/or frequencies) where there were no changes in mechanical properties, essentially representing the static regime observed in hard inclusions. Additionally, there was a perturbation regime (higher amplitudes and/or frequencies) where soft inclusion clustering or packing occurred, leading to degraded mechanical properties, and soft inclusion dispersion happened for enhanced mechanical properties, corresponding to the assembly regime in the hard inclusions phase diagram. At higher amplitudes and/or frequencies, a chaotic splashing regime was achieved, analogous to the fluttering regime in the hard inclusions phase diagram.

Both hard and soft inclusions were stimulated within air and fluid media, creating a shift in the dimensionless phase diagrams. For instance, the phase diagrams for hard inclusions were responsive to a lower range of amplitudes and higher range of frequencies, while soft inclusions were responsive to a higher range of amplitudes and a lower range of frequencies.

6.2 Predicting Many-cube Transition Lines with Single-grain Models

Figure 6.1 shows the experimental assembly map presented in Figure 3.2 with the addition of the four models described above (relative acceleration, bounce height, bounce duration, rotation). The relative acceleration model properly captured the upper side (high amplitudes) of the static-packing boundary, but not the lower side (low amplitudes). The bounce height model has the advantage to be a phenomenological model based on grain motion. This model captured the lower side of both the static-packing and packing-fluttering transitions, but it shows some discrepancies with the upper side of these boundaries. The bounce duration model produced predictions with the largest errors, which suggest that bounce duration is not an effective metrics for phase transition and packing. Finally, the rotation model could capture some of the lower sections of the phase transitions but was less accurate for the upper sections. However, considering that this model has no fitting parameter, rotation captures the overall transitions reasonably well. In addition, the overlap between rotation and bounce height model in high packing factor regions suggests that both rotation and bouncing are the key mechanisms for vibration-driven assembly.

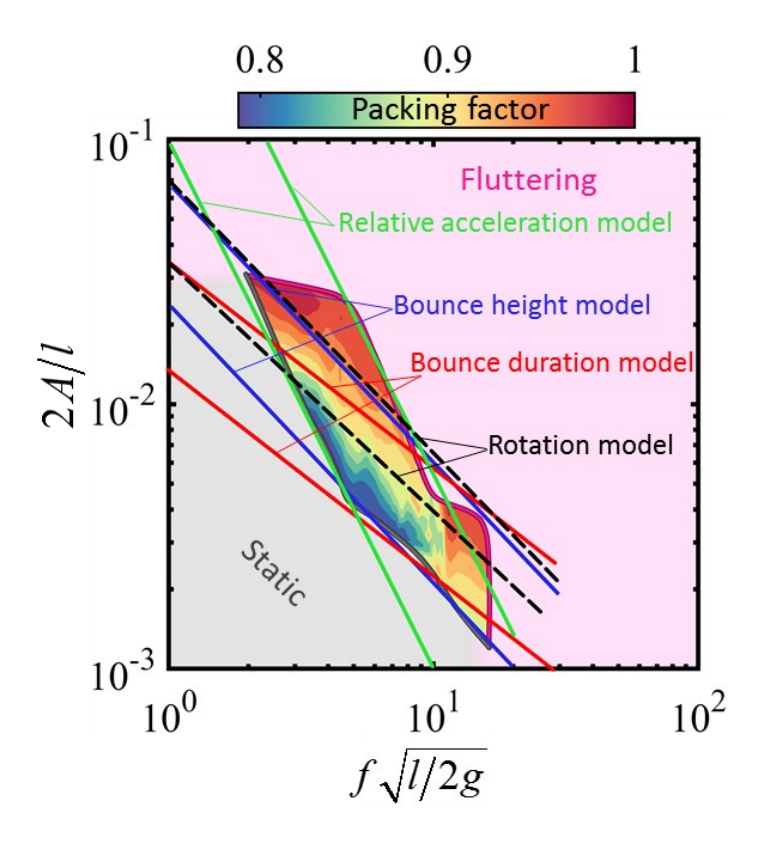


Figure 6. 1. Comparison between experimental phase transition boundaries (i.e., static-packing and packing-fluttering) and packing regime with relative acceleration, bounce height, bounce duration, and rotation models.

In summary, the relative acceleration model and the bounce height model could properly capture the slope of phase transitions, but their main weakness is that empirical parameters must be used to fit the experiments. The rotation model captures the phase transitions relatively well, with the main advantage to be a purely phenomenological model.

6.3 Assembly Phase Diagram Assessments with Individual Block Mechanics

In this section, we assess the effect of block-based mechanisms on the phase transitions and compare these models with the critical relative acceleration criterion. We also seek effective regimes, phase transitions, and geometrical dynamic characteristics, making a geometry an easier block for vibration-driven assembly than another geometry. In addition to the critical relative acceleration criterion, the two DEM-generated models presented above (bounce height and

rotation) were superimposed to the experimental assembly phase diagrams indicated in Figure 4.1 and shown in Figure 6.2A-D. The critical relative acceleration criterion predicts the transition boundaries of hexagon-based tiling geometries (Figure 6.2C,D) more precisely than square-based tiling geometries (Figure 6.2A,B). This empirical model is based on the vibrating system, and therefore, it does not consider the block geometry and/or the mechanisms involved in phase transitions. In contrast to the critical relative acceleration criterion, the bounce height model has advantages based on the phenomenological model of block mechanism; however, this model also has a fitting parameter that varies by changing block geometry. Figure 6.2A-D. exhibits that the bounce height model was more successful in predicting the phase transitions of square-based tiling geometries (Figure 6.2A,B) than hexagon-based tiling geometries (Figure 6.2C,D). The rotation model is purely phenomenological based on the actual geometry of block and its rotation mechanism; therefore, there is no fitting parameter and/or dependency on block geometry in this model. The overall trends of transition boundaries were nearly captured while this model captures the high packing factor regions reasonably well for all block geometries implying that the rotation mechanism may not utterly be involved in the phase transitions, but it is one of the key mechanisms in the assembly regime. In addition, the overlap between rotation and bounce height model in high packing factor regions for all geometries, suggests that both rotation and bouncing are the key mechanisms for vibration-driven assembly.

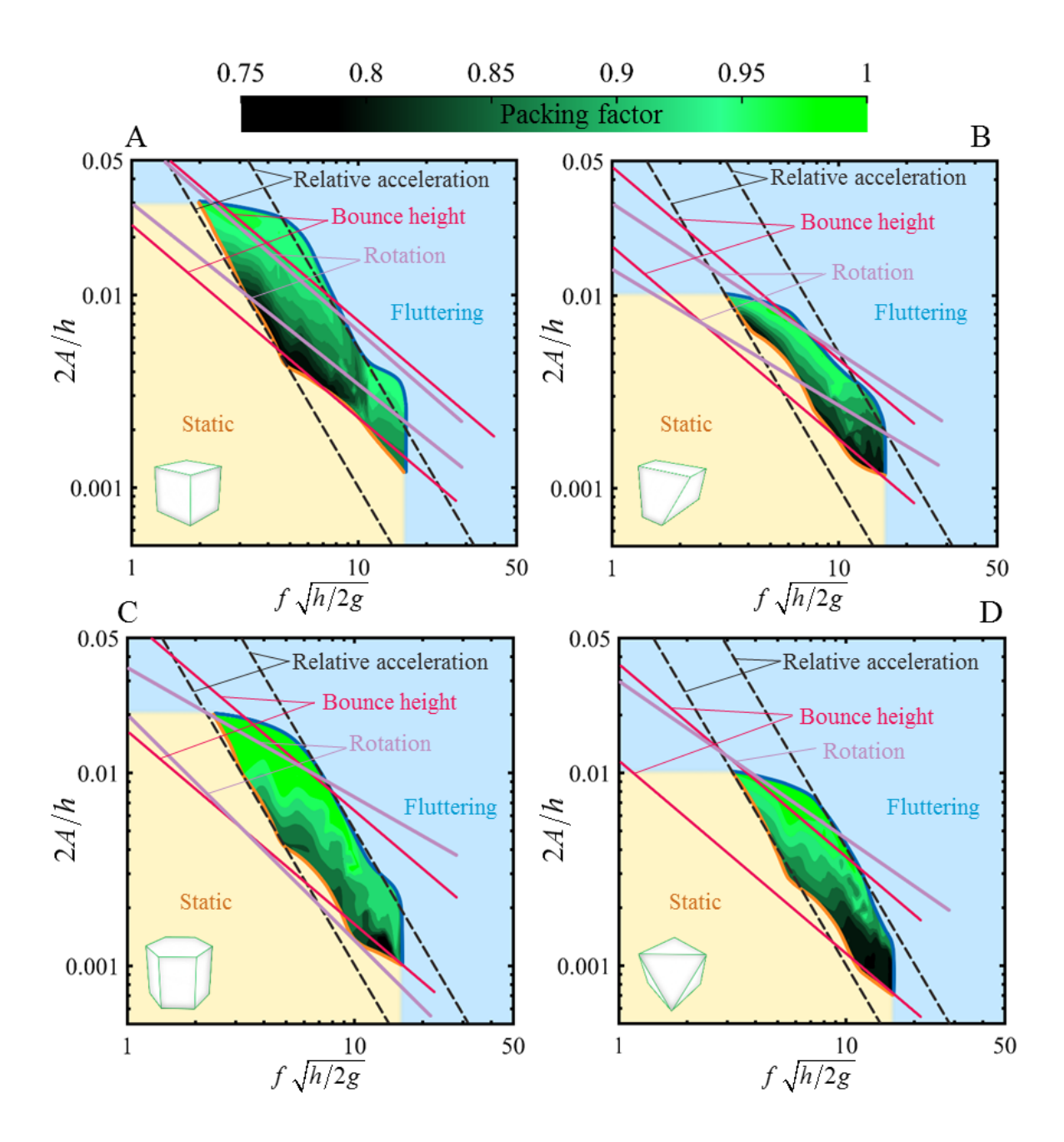


Figure 6. 2. Comparison between experimental phase transition boundaries (i.e., static-assembly and assembly -fluttering) and assembly regime with critical relative acceleration, bounce height, and rotation models. (A) Square prism; (B) truncated tetrahedron; (C) hexagonal prism; (D) octahedron.

6.4 Assembly of Polyhedral Blocks

A block can be assembled easier than another one with a different geometry when it has a wider assembly regime with a broader range of vibration amplitudes and frequencies in the

assembly phase diagram. Figure 6.3A shows that the static-assembly boundary is nearly the same for block geometries used in this study; however, their assembly-fluttering boundary is different. For example, the static regime for truncated tetrahedron is the smallest due to its largest fluttering regime. Therefore, a block with the wider fluttering regime is more difficult to be self-interlocked and/or -crystallized due to its instability during assembly process (truncated tetrahedron and octahedron). In a perfectly interlocked packing arrangement (PF=1), finished assemblies of truncated tetrahedra and of octahedra appeared to be more stable because of geometrical interlocking. However, these two geometries are also less stable during the assembly process because of their dynamic characteristics and also their narrow PF=1 region in terms of amplitude and frequency range (Figure 4.1). From dropping point to steady-state condition, we showed that blocks might bounce and/or rotate to reach the platform wall or other blocks or perfectly be crystalline and/or interlocked. During this process, a geometry like truncated tetrahedron or octahedron is more unstable than a square and hexagonal prism due to their dynamic characteristics and geometrical angular features, which include the moment of inertia. We showed that bouncing has an additional role in assembly-fluttering transition (Figure 6.2), and due to the angular features of each block geometry, the out-of-plane moment of inertia can be more effective in instability of a block than rotation and in-plane moment of inertia (I_{zz}) . We therefore explored the area of PF=1 regions (Figure 4.1) for each block as function of the normalized out-of-plane moment of inertia $(I_{xx} \text{ and } I_{yy})$ (Figure 6.3B). The lower the out-of-plane moment of inertia, the larger the maximum packing factor region (PF=1) in terms of amplitude and frequency range, implying that perfectly interlocked assemblies (PF=1) by hexagon-based geometries can be achieved in a broader range of amplitude and frequency due to their lower out-of-plane moment of inertia compared to squarebased geometries (higher out-of-plane moment of inertia). Figure 6.3B and Figure 6.2 also imply that by increasing the out-of-plane moment of inertia, the block-based models are further needed to capture different states of the phases diagram, while the critical relative acceleration model is more prices for geometries with the lower out-of-plane moment of inertia.

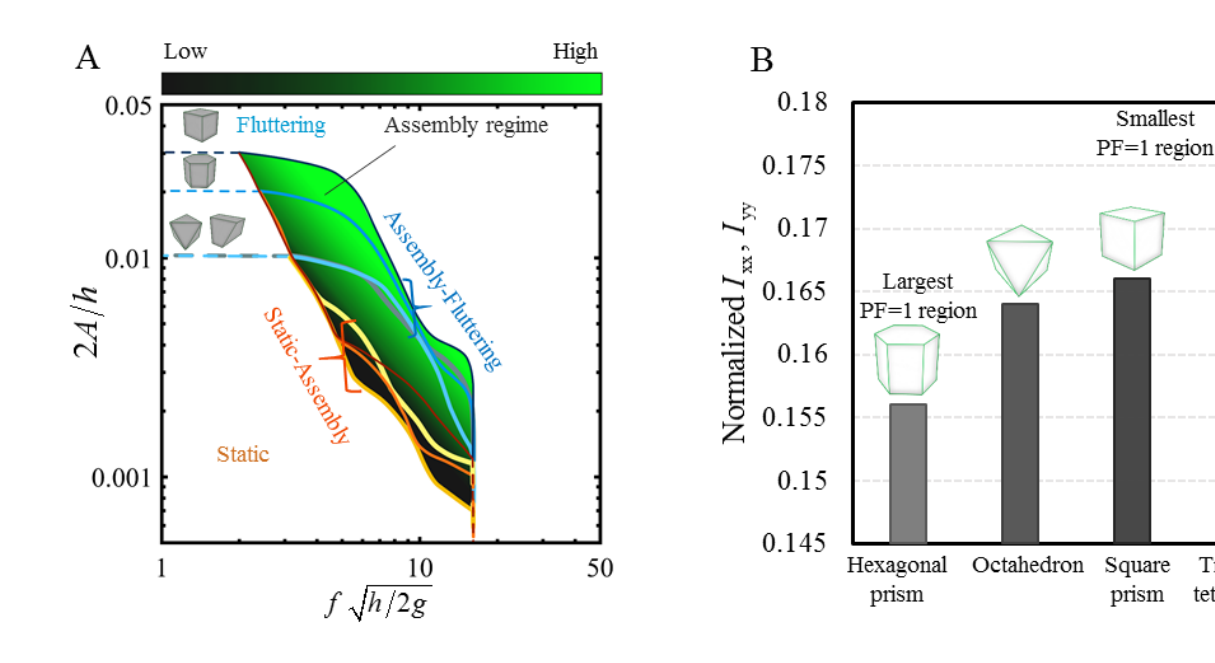


Figure 6. 3. (A) Comparisons of assembly phase diagrams for four block geometries; (B) normalized out-of-plane moment of inertia (I_{xx} and I_{yy}) for each geometry verse their maximum packing factor regions (PF=1).

Truncated

tetrahedron

We assembled stiff square- and hexagon-based polyhedral blocks into free-standing topologically interlocked and/or crystalline monolayers by combining vibration and gravity. We identified three regimes and two-phase transitions for the assembly phase diagram of each block geometry experimentally and numerically. We generated DEM models to duplicate the experiments and complemented these simulations with single-block DEM models to study the effective mechanisms involved in the assembly and phase transitions of each polyhedral block geometry. The physics and mechanics underlying the shape-dependency of athermal out-ofequilibrium material systems can be studied in meso- and macro-scale using the vibration-driven assembly method presented in this study. This method can also be an efficient and promising pathway for self-crystallization and/or -interlocking of polyhedral granular blocks in different length scales. It can offer new high-potential routes enabling scalable, rapid, and low-energy fabrication method for block-based architectured materials and/or structures in different environments and atmospheres—topologically interlocked materials (TIMs) was a prominent example in this study. The assembly method in this study can be used to frequently re-fragment and then again re-fabricate versatile anisotropic and/or hybrid TIM transformable and freeform structures, components, and armors. The assembly method is very robust, especially if a

"crystallization front" is created and maintained during assembly by controlling the feeding rate of the blocks onto the assembly platform. In this condition, it would be possible to scale the process to many more blocks using a larger assembly platform. The vibration-driven method in this study can also have biomedical applications including tissue regeneration and healing and manipulating blood clot properties. In addition, it can be used to form and assess decentralized and reconfigurable robots made by granular blocks^[166-171]. The principal mechanisms and findings in this study can also be used for other wave-based agitation methods for granular materials such as levitation^[59,67,172]. We did not study the effect of different waveforms (signal shapes) and also large size and shape variations. These two parameters need to systematically be studied in future studies.

Up to this point, we have studied the mechanics and physics of vibration-driven assembly of athermal, far-from-equilibrium active polyhedral grains, focusing on their transformation into stable, reversible, or reconfigurable interlocked crystals. In the following chapter, we aim to extend our understanding to far-from-equilibrium active soft inclusions, with the goal of achieving similar stabilization and translating the application of this system.

6.5 Clot-like Materials

We examined the vibration-induced perturbation during clot formation to efficiently tune the mechanical performance blood clots (as a representative of clot-like materials) based on the vibration amplitudes and/or frequencies. The relationship between the structure-property response of blood clots with blood clot degradation (fibrinolysis) was also characterized. We decoupled the effect of the vibration-induced perturbation on the RBCs and fibrin mesh network by replicating vibration-driven blood clot formation using similar material models, including plasma/microgels (spheroids) and plasma/fibroblast cells. We introduced soft inclusions (RBCs, microgels and fibroblast cells) as biological blocks to regulate the microarchitecture of a natural fibrous material like plasma (fibrin) clot using a mechanical stimulus resulting in tunable mechanical performance. We further examined the safety and efficiency of the vibrating platform on cells viability and the potential application of the vibrating platform as a remote device for tuning on-site and/or-demand blood clot properties through in-vivo experiments. The effect of applied vibration-driven perturbation on the possible states of blood clots microarchitecture was assessed through the spatial analyses of RBCs and fibroblast cells dispersions and fibrin mesh network. These experimental findings were then complemented with a hybrid element computational model to further explore

the effect of geometrical features of clot microarchitecture on the meso- and/or macro-scale mechanical responses.

At a certain level of applied mechanical agitation, the soft active inclusions (RBCs, cells) packed and/or clustered together within biopolymeric fluid (like plasma) during clotting (Figure 6.4A, B), whereas at a different level of applied mechanical stimulus, most likely the higher range of agitations can non-uniformly disperse the inclusions (Figure 6.4A, C), resulting in two different clot microstructures (Figure 6.4D, E) and hence mechanical properties (Figure 6.4F, G). Here we presented a strategy for engineering clot-like materials utilizing mechanical agitation. By adjusting the levels of mechanical agitation, we could finely tune both the organization of soft active inclusions during clotting (Figure 6.4A-C) and the microstructure of the polymeric network (Figure 6.4D-G), thereby modulating the macroscopic mechanical behavior of the clot.

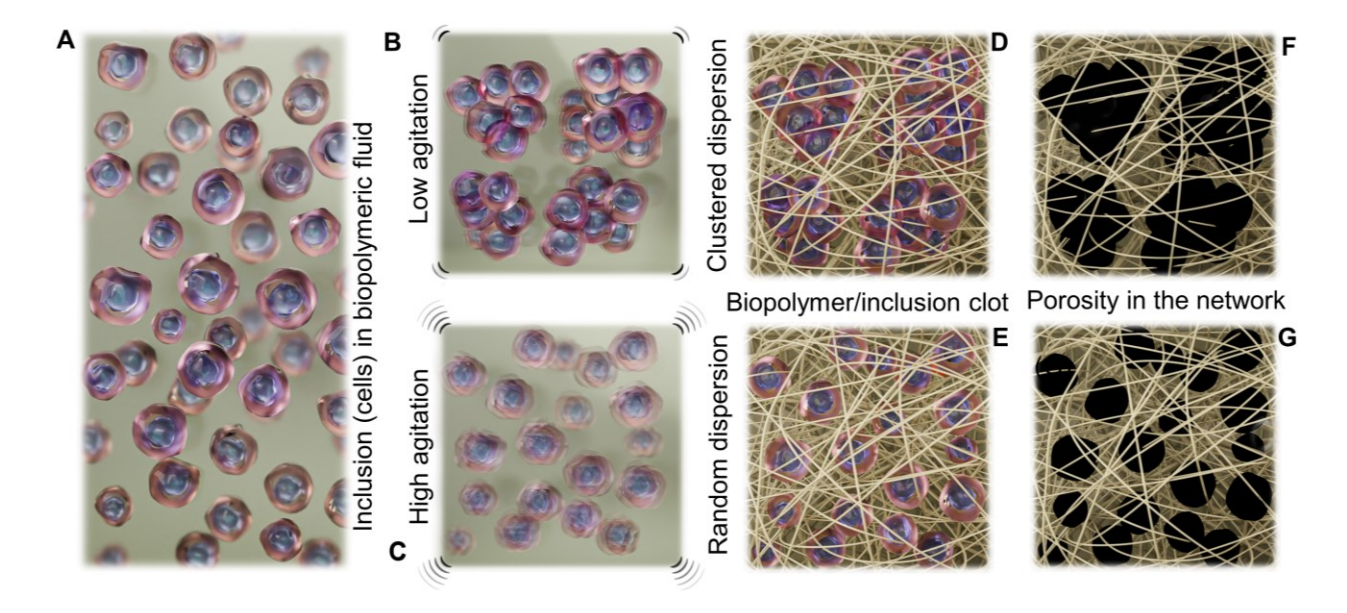


Figure 6.4. Schematic of possible microstructures of clot-like materials under external mechanical agitations. (A) Soft inclusions (cells) within biopolymeric medium; (B) inclusions clustering under low energy vibrations within biopolymeric medium; (C) non-uniformly dispersed inclusions under high energy vibrations within biopolymeric medium; (D) fixing the position of clustered inclusions due to clotting under low energy vibration; (E) fixing the position of randomly dispersed inclusions due to clotting under high energy vibration; (F) large porosities within biopolymeric network due to the inclusions clusters; G) homogenous porosities within biopolymeric network due to inclusion random dispersion.

We verified with short- and long-range spatial analyses that vibration-degraded (Low) groups had more clustered and/or agglomerated RBCs, and vibration-enhanced (High) groups had more dispersed RBCs. Similar to the plasma/fibroblast clots, the fibrin microstructure in the blood clots can have larger porosities in vibration-degraded (Low) groups due to the RBC clusters and/or agglomerations while the RBCs were more dispersed in the vibration-enhanced (High); therefore, their fibrin microstructures had smaller porosities. The clusters and/or agglomerations can be due to the discocyte shape of RBCs; however, there are other disorders and/or diseases, including rouleaux formation (stacks of RBCs), malaria and sickle cell diseases^[173,174] which the vibration-induced perturbation method in this study can deal with them. For example, at mid-range amplitudes and/or frequencies where the RBCs were non-uniformly dispersed, the applied energy and/or perturbation originating from vibrations can overcome the macromolecular bridging (causing rouleaux formation) among RBCs^[173,174].

We experimentally verified that the vibration-induced perturbation can non-uniformly and/or homogeneously disperses soft inclusions (here in this study, RBCs, microgels, and fibroblast cells) within biofluids and/or biomonomers (here in this study, blood and plasma) while this dispersion can indirectly adjust the architectural and microstructural characteristics of the biopolymer mesh network (here in this study, fibrin mesh network), resulting in different meso-and/or macro-scale mechanical performance. The biophysical properties of blood clots forming within the human body vary based on physiological boundary conditions^[175-179]. For instance, generated blood clots in the arterial environment are subjected to high blood pressure (≈100 mmHg) and high fluid shear stress (≈240 Pa), which aligns the fibrin microstructures with the flow direction^[175-179]. The blood clots which are formed under the low blood pressure (≈20 mmHg) and low fluid shear stress (≈87 Pa) environment of the venous have more random microstructures^[175-179]. The physiological boundary conditions in arterial and venous environments are also mechanical agitations similar to the vibration-induced perturbations in this study. Our experimental configurations and findings here in this study can be an onward step toward demystifying blood clot embolization.

We have shown in this part of study that the fibrin network microarchitecture changes through different RBCs, microgels, and fibroblast cells dispersions, resulting in various meso-and/or macro-scale mechanical responses experimentally and numerically. However, fibrin mesh microarchitecture and thus its meso- and/or macro-scale mechanical properties can also be

manipulated through multiple myeloma, diabetes, nephrotic syndrome, deep vein thrombosis, atrial fibrillation and stroke^[12]. A comprehensive understanding of the relationship between fibrin mesh microarchitectural characteristics and their mechanical responses was therefore needed and had yet to be established.

These vibration-enhanced mechanical responses of blood clots at the wound sites can hamper rebleeding caused by the rupture; meanwhile, it can shed light on the possible treatment for drug-induced bleeding and/or bleeding disorders like hemophilia and wound closure. The higher mechanical properties can be interesting both mechanics- and clinic-wise but can vibration-degraded properties here in this study be useful, and/or can fibrinolysis be linked to the structure-property response of clot were two questions we tackled. Our findings indicated that our vibrating platform that can form blood clots with low (vibration-degraded) mechanical properties can offer a new therapeutic route for fibrinolysis and/or thrombotic disorders.

We have introduced a mechanical stimulus platform to tune the structure-property response of soft inclusion (cells)/fibrous clot-like material systems without adding any chemical and/or biochemical agents. We used prokaryotic and eukaryotic cells/inclusions (RBCs, microgels, fibroblast cells) as blocks subjected to vibration-driven perturbations to efficiently regulate their dispersions as function of applied vibration amplitudes and/or frequencies, resulting in altering the microarchitecture of the fibrin network. We mechanically manipulated the self-assembly formation of these clot-like material systems. Fibrin networks with more irregular large porosities due to inclusions clusters and/or agglomerations have lower elastic properties and fracture resistance, while non-uniformly dispersed inclusions generated more homogenously dispersed small porosities in fibrin networks, resulting in high elastic performance and fracture toughness. The findings revealed how microstructural features of soft inclusions (cells)/fibrous clot-like materials markedly determine their meso- and/or macro-scale mechanical properties. We demonstrated that vibration-generated blood clots with lower structure-property response degraded more easily. The safety and efficiency of this vibrating platform approach on the cells viability and in-vivo rat liver puncture bleeding model was here in this study examined. We generated hybrid element simulations to duplicate the vibration-generated microstructures of blood clots and complement our experimental findings by assessing the role of geometrical characteristics of the fibrin network architecture on the meso- and/or macro-scale mechanical properties.

We used our linkage net model (RBC-free) for this purpose and examined different combinations of linkage length, diameter, and number on the elastic responses. In agreement with our experimental observations, the network with the longer linkage length has lower elastic performance, while the higher diameter causes higher elastic properties. The microstructure with the high number of linkages indeed had a more packed and shorter range of linkages, but even in such an arrangement, the diameter of the linkage plays a pivotal role. The model allows for defining the detailed properties of inclusions and linkages while capture the spatial distribution that can turn this model into a representative for other cell-based and clot-like material systems. The model also enables virtual experiments, allowing flexibility for exploring nonlinearities and local damage progression.

To conclude, this part of the study established the use of mechanical agitation to mechanically engineer clot-like materials with the underlying mechanism revealed governing the agitation-mediated approach. Our strategy provides a low-cost, low-energy, noninvasive, rapid, scalable, remote solution for manipulating and studying clot-like tissue and living material systems, with potential applications spanning various medical contexts. This approach could advance management of conditions related to thrombosis, hemostasis, and traumatic hemorrhage. It also paves new avenues for tissue engineering and engineered living materials. The proposed agitation platform and models have broad applications beyond medicine, offering insights into the biophysics of active and granular matter. Overall, our research highlights the multifaceted potential of mechanical agitation as a versatile tool in both medical and bioengineering realms.

6.6 Discussion on Limitations and Scale-Up Challenges

In the case of dense architectured materials, scaling up vibration-assisted assembly from laboratory setups to industrial manufacturing poses complexities. Efficient energy use at larger scales becomes critical, as increased amplitudes and frequencies may be necessary to overcome higher inertia and friction. Maintaining uniform vibration across larger platforms is challenging, potentially impacting the consistency of the crystalline structures formed. Additionally, continuous feeding and precise placement of polyhedral blocks are essential, requiring advanced automation to avoid defects in large-scale production. Geometric constraints further complicate scalability. Certain block shapes, such as truncated polyhedra, exhibit narrower assembly regimes than simpler geometries. Even slight dimensional variations can disrupt the assembly process at larger scales,

necessitating rigorous quality control to ensure uniform mechanical properties. Moreover, different materials respond variably to mechanical agitation, requiring customized approaches for various applications

For soft cell-laden materials, similar challenges arise when integrating vibration-based methodologies into 3D bioprinting, as seen in technologies like MIMIX Biotherapeutics' CymatiX system^[180]. These systems use acoustic waves to assemble cells into high-resolution patterns. Scaling this process introduces the need for consistent resonance across larger constructs to maintain uniform cell distribution. Additionally, building multi-layered structures demands precise alignment, as any deviation can compromise structural integrity. Cell viability also becomes a concern at larger scales. While acoustic methods are generally gentle, prolonged or intensified exposure could stress delicate cells or organoids. Material compatibility is another factor; different hydrogels may respond inconsistently to acoustic stimulation, necessitating optimized formulations to ensure mechanical stability and biocompatibility. Increasing fabrication throughput without sacrificing pattern fidelity will likely require parallel processing, which involves synchronizing multiple acoustic systems—a complex task demanding sophisticated control mechanisms

Addressing these limitations involves exploring multi-directional agitation, adaptive control systems, and hybrid fabrication approaches. Implementing real-time feedback systems and developing robust computational models could enhance scalability and consistency for both hard and soft materials. By overcoming these challenges, vibration-assisted and acoustic bioprinting methodologies could revolutionize the manufacturing of architectured materials and bioengineered tissues, enabling applications in aerospace, biomedical engineering, and regenerative medicine.

CHAPTER 7

Concluding Remarks

The conclusion of this dissertation is classified into two parts: the vibration-driven assembly of polyhedral stiff blocks and the engineering of soft clot-like materials through mechanical agitation. Regarding the vibration-induced crystallization of polyhedral blocks into topologically interlocked materials, several key findings emerged:

- **Self-Crystallization and Interlocking**: Different polyhedral granular building blocks can self-crystallize and interlock into topologically interlocked materials, which can be immediately used as free-standing large pieces of materials or structures.
- Assembly Phase Diagram: Through experiments and DEM simulations, the assembly
 phase diagram of the system was established. Static, assembly, and fluttering regimes,
 along with their phase transition boundaries, were identified. Optimum packing occurred
 near the assembly-fluttering transition for all block geometries.
- **Re-Fragmentation and Re-Fabrication**: The crystallized and/or interlocked polyhedral granular building blocks can be re-fragmented by the fluttering regime and re-fabricated by the assembly regime. A wider fluttering regime makes self-interlocking and/or crystallization more challenging.
- Geometric Effects on Assembly: Basic geometries with square and hexagonal medial sections (square and hexagonal prisms) have wider assembly regimes compared to their truncated versions (truncated tetrahedron and octahedron). Hexagon-based tiling geometries have wider maximum packing factor regions than square-based tiling geometries.
- **Dynamic Characteristics**: The out-of-plane moment of inertia significantly influences the perfect interlocking and/or crystallization of building blocks. Geometries with a lower out-of-plane moment of inertia exhibit wider maximum packing factor regions.
- **Distinct Phase Transitions**: Each building block geometry has distinct static-assembly and assembly-fluttering phase transitions. Hexagon-based tiling geometries align with the critical relative acceleration criterion, whereas square-based tiling geometries partly correlate with bounce height and rotation models.

• Rotation and Fluttering Onset: The onset of rotation and fluttering was captured by a single-block rotation model, correlating well with phase transition boundaries and maximum packing factor regions.

Transitioning to the agitation-mediated engineering of soft clot-like materials, this dissertation addressed fundamental questions surrounding their formation and mechanical properties by proposing mechanical agitation as a platform to form and tune the structure-property responses of clot-like materials. Experiments were complemented by hybrid elements computational models to study the microstructural features' effects on the meso- and macro-scale mechanical responses of clots.

Key findings include:

- New Design Strategy: Cellular inclusions can be used as building blocks to indirectly alter
 the biopolymeric network's microarchitecture under mechanical agitation, enhancing or
 degrading mechanical performance.
- **Agitation-Tuned Performance**: Fundamental principles of agitating systems were established, demonstrating that mechanical properties such as elastic modulus and fracture toughness can be enhanced or degraded significantly. Blood clots' elastic modulus and fracture toughness were modulated by approximately 400%, indicating a fourfold difference from agitation-degraded to agitation-enhanced properties.
- Micro-to-Macro Translation: Agitation-steered dispersion of soft cellular inclusions
 affects the biopolymeric architecture's microstructural features, influencing meso- and
 macro-scale mechanical responses. This was supported by experimental spatial analysis
 and computational simulations.
- Universal Applicability: The mechanical agitation platform and models are generalizable for various clot-like materials and cellular inclusion types, offering new therapeutic routes for diseases and conditions like thrombosis, hemostasis, embolism, and more.

In conclusion, this dissertation contributes novel insights into the vibrational assembly of polyhedral blocks and the mechanical engineering of soft clot-like materials. These findings not

only advance our understanding of complex material systems but also offer promising avenues for biomedical applications and biomimetic material design.

The potential future works can be outlined in two categories:

(i) Assembly and Crystallization of Polyhedral Stiff Blocks and Soft Cellular Inclusions:

Three-Dimensional Vibration-Driven Crystallization: The polyhedral building blocks in this study were self-interlocked in a monolayer arrangement, and their final three-dimensional crystal form will be layer-by-layer monolayer assemblies. They could interlock only in-plane. However, three-dimensional interlocked crystals require specific building block shapes to interlock in three dimensions and out-of-plane. Using three-dimensional vibration-driven techniques to create densely architectured materials with polyhedral blocks will achieve 3D interlocking crystals. This approach will allow the study of underlying micro-scale mechanisms for the mechanical properties of different crystals at a macroscale level. Thus, the multiscale mechanisms and properties can be tuned through mechanical stimuli.

Bidirectional and Tridirectional Agitation-Induced Assembly: This study only investigated unidirectional mechanical vibration or agitation for both hard and soft inclusions. Future work could explore the effects of bidirectional and tridirectional vibrations or agitations on the assembly of granular polyhedral blocks or cell-laden clot-like materials, expanding beyond this dissertation.

Surface Functionalization: In this dissertation, the surfaces of the hard and soft inclusions were not explored. Future work could evaluate the impact of chemical or physical surface functionalization of stiff polyhedral blocks and soft cellular inclusions on the agitation-steered assembly process and their macroscale mechanical responses.

(ii) Engineering Clot-Like Materials:

Soft and Porous Cell-Laden Polyhedral Blocks: One potential future biomedical application of this work, which was not explored in this dissertation, is the non-uniform and homogeneous dispersion of cells throughout a large piece of porous material for tissue regeneration. Soft cell-laden porous polyhedral blocks can be assembled into a large, free-standing, architectured porous material system with well-dispersed cells using the agitation-driven fabrication method proposed in this study.

Stem Cells and Mechanical Agitation: It has been shown that mechanical agitation can be used for cell patterning; however, using this technique to tune the mechanical properties and

proliferation of cell-laden tissue has not been explored. Future research should investigate the use of stem cells and the influence of mechanical agitation on cellular differentiation, aiming to engineer and regenerate biological tissues from clot-like materials.

Fatigue and Nonlinear Rupture of Blood Clots: The fatigue and nonlinear rupture of blood clots is a crucial topic in hemostasis and hemorrhage management. Understanding this topic is pivotal in both engineering and medicine to mitigate life-threatening risks. Therefore, it is essential to study how mechanical agitation, resulting cellular organization, and fibrin microarchitecture affect the fatigue properties and viscoelasticity of blood clots under various loading conditions.

Bibliography

- 1. Barthelat, F. (2015). Architectured materials in engineering and biology: Fabrication, structure, mechanics and performance. *International Materials Reviews*, 60(8), 413-430.
- 2. Mirkhalaf, M., Zhou, T., & Barthelat, F. (2018). Simultaneous improvements of strength and toughness in topologically interlocked ceramics. *Proceedings of the National Academy of Sciences*, 115(37), 9128-9133.
- 3. Studart, A. R. (2016). Additive manufacturing of biologically-inspired materials. *Chemical Society Reviews*, 45(2), 359-376.
- 4. Siegmund, T., Barthelat, F., Cipra, R., Habtour, E., & Riddick, J. (2016). Manufacture and mechanics of topologically interlocked material assemblies. *Applied Mechanics Reviews*, 68(4), 040803.
- 5. Mirkhalaf, M., & Zreiqat, H. (2020). Fabrication and mechanics of bioinspired materials with dense architectures: Current status and future perspectives. *JOM*, 72, 1458-1476.
- 6. Svenson, S. (2004). Controlling surfactant self-assembly. *Current Opinion in Colloid & Interface Science*, 9(3-4), 201-212.
- 7. Manoharan, V. N. (2015). Colloidal matter: Packing, geometry, and entropy. Science, 349.
- 8. Behringer, R. P., & Chakraborty, B. (2018). The physics of jamming for granular materials: A review. *Reports on Progress in Physics*, 82, 012601.
- 9. Damasceno, P. F., Engel, M., & Glotzer, S. C. (2012). Predictive self-assembly of polyhedra into complex structures. *Science*, 337(6093), 453-457.
- 10. van Anders, G., Klotsa, D., Ahmed, N. K., Engel, M., & Glotzer, S. C. (2014). Understanding shape entropy through local dense packing. *Proceedings of the National Academy of Sciences*, 111(45), E4812-E4821.
- 11. Guo, B., Dong, R., Liang, Y., & Li, M. (2021). Haemostatic materials for wound healing applications. *Nature Reviews Chemistry*, *5*(11), 773-791.
- 12. Qiu, Y., Myers, D. R., & Lam, W. A. (2019). The biophysics and mechanics of blood from a materials perspective. *Nature Reviews Materials*, 4(5), 294-311.
- 13. Marchetti, M. C., Joanny, J. F., Ramaswamy, S., Liverpool, T. B., Prost, J., Rao, M., & Simha, R. A. (2013). Hydrodynamics of soft active matter. *Reviews of Modern Physics*, 85, 1143-1189.

- 14. Aranson, I. S., & Tsimring, L. S. (2006). Patterns and collective behavior in granular media: Theoretical concepts. *Reviews of Modern Physics*, 78, 641-692.
- 15. Needleman, D., & Dogic, Z. (2017). Active matter at the interface between materials science and cell biology. *Nature Reviews Materials*, 2.
- Flemming, H.-C., Wingender, J., Szewzyk, U., Steinberg, P., Rice, S. A., & Kjelleberg, S. (2016). Biofilms: An emergent form of bacterial life. *Nature Reviews Microbiology*, 14, 563-575.
- 17. Guex, A. G., Di Marzio, N., Eglin, D., Alini, M., & Serra, T. (2021). The waves that make the pattern: A review on acoustic manipulation in biomedical research. *Materials Today Bio*, *10*, 100110.
- 18. Asghar, W., El Assal, R., Shafiee, H., Anchan, R. M., Demirci, U. (2015). Engineering cancer microenvironments for in vitro 3-D tumor models. *Materials Today*, 18, 539-553.
- van Oosten, A. S. G., Chen, X., Chin, L., Cruz, K., Kamsma, D., Yang, W., ... & Weitz, D. A. (2019). Emergence of tissue-like mechanics from fibrous networks confined by close-packed cells. *Nature*, 573, 96-101.
- 20. Shivers, J. L., Bai, Y., Nguyen, N., Roman, B., Jacobi, I., & Boudaoud, A. (2020). Compression stiffening of fibrous networks with stiff inclusions. *Proceedings of the National Academy of Sciences*, 117, 21037-21044.
- 21. Davidson, M. D., Hosseini, V., Nelson, M. T., Ni, R., Paiva, A. E., Watanabe, M., ... & Lutolf, M. P. (2021). Programmable and contractile materials through cell encapsulation in fibrous hydrogel assemblies. *Science Advances*, 7, eabi8157.
- 22. Hong, S.-H., Lee, J. B., Ko, H. S., Lee, W., Lee, S., Lee, J., ... & Kim, W. (2020). Surface waves control bacterial attachment and formation of biofilms in thin layers. *Science Advances*, 6, aaz9386.
- Armstrong, J. P. K., Burke, M., Carter, B. M., Davis, S. A., Perriman, A. W., & Perriman,
 A. W. (2018). Engineering anisotropic muscle tissue using acoustic cell patterning.
 Advanced Materials, 30, 1802649.
- 24. Wegst, U. G., Bai, H., Saiz, E., Tomsia, A. P., & Ritchie, R. O. (2015). Bioinspired structural materials. *Nature Materials*, 14(1), 23-36.
- 25. Barthelat, F., Yin, Z., & Buehler, M. J. (2016). Structure and mechanics of interfaces in biological materials. *Nature Reviews Materials*, 1(4), 16007.

- 26. Dunlop, J. W., Weinkamer, R., & Fratzl, P. (2011). Artful interfaces within biological materials. *Materials Today*, 14(3), 70-78.
- 27. Bahmani, A., Li, G., Willett, T. L., & Montesano, J. (2019). Three-dimensional micromechanical assessment of bio-inspired composites with non-uniformly dispersed inclusions. *Composite Structures*, *212*, 484-499.
- 28. Barthelat, F., & Zhu, D. (2011). A novel biomimetic material duplicating the structure and mechanics of natural nacre. *Journal of Materials Research*, 26(10), 1203-1215.
- 29. Habelitz, S., Marshall, S. J., Marshall Jr, G. W., & Balooch, M. (2001). Mechanical properties of human dental enamel on the nanometre scale. *Archives of Oral Biology*, 46(2), 173-183.
- 30. Aizenberg, J., Weaver, J. C., Thanawala, M. S., Sundar, V. C., Morse, D. E., & Fratzl, P. (2005). Skeleton of Euplectella sp.: Structural hierarchy from the nanoscale to the macroscale. *Science*, 309(5732), 275-278.
- 31. Alheit, B., Bargmann, S., & Reddy, B. D. (2021). Dynamic mechanical behaviour of suture interfaces as inspiration for architectured hierarchical interlocking composites. *Journal of the Mechanics and Physics of Solids*, 157, 104620.
- 32. Yin, Z., Hannard, F., & Barthelat, F. (2019). Impact-resistant nacre-like transparent materials. *Science*, *364*(6447), 1260-1263.
- 33. Mirkhalaf, M., Sunesara, A., Ashrafi, B., & Barthelat, F. (2019). Toughness by segmentation: Fabrication, testing and micromechanics of architectured ceramic panels for impact applications. *International Journal of Solids and Structures*, 158, 52-65.
- 34. Estrin, Y., Bréchet, Y., Dunlop, J., & Fratzl, P. (2019). *Architectured materials in nature and engineering*. Cham, Switzerland: Springer Nature Switzerland AG.
- 35. Yin, Z., Dastjerdi, A., & Barthelat, F. (2018). Tough and deformable glasses with bioinspired cross-ply architectures. *Acta Biomaterialia*, 75, 439-450.
- 36. Dyskin, A. V., Estrin, Y., Kanel-Belov, A. J., & Pasternak, E. (2001). A new concept in design of materials and structures: Assemblies of interlocked tetrahedron-shaped elements. *Scripta Materialia*, 44, 2689-2694.
- 37. Djumas, L., Simon, G. P., Estrin, Y., & Molotnikov, A. (2017). Deformation mechanics of non-planar topologically interlocked assemblies with structural hierarchy and varying geometry. *Scientific Reports*, 7, 1-11.

- 38. Williams, A., & Siegmund, T. (2021). Mechanics of topologically interlocked material systems under point load: Archimedean and Laves tiling. *International Journal of Mechanical Sciences*, 190, 106016.
- 39. Karuriya, A. N., & Barthelat, F. (2023). Granular crystals as strong and fully dense architectured materials. *Proceedings of the National Academy of Sciences*, 120(1), e2215508120.
- 40. Wang, Y., Li, L., Hofmann, D., Andrade, J. E., & Daraio, C. (2021). Structured fabrics with tunable mechanical properties. *Nature*, *596*, 238-243.
- 41. Kim, D. Y., & Siegmund, T. (2021). Mechanics and design of topologically interlocked irregular quadrilateral tessellations. *Materials & Design*, 212, 110155.
- 42. Dalaq, A. S., & Barthelat, F. (2020). Manipulating the geometry of architectured beams for maximum toughness and strength. *Materials & Design*, 194, 108889.
- 43. Gravish, N., Franklin, S. V., Hu, D. L., & Goldman, D. I. (2012). Entangled granular media. *Physical Review Letters*, *108*, 208001.
- 44. Murphy, K. A., Reiser, N., Choksy, D., Singer, C. E., & Jaeger, H. M. (2016). Freestanding load-bearing structures with Z-shaped particles. *Granular Matter*, 18, 26.
- 45. Barés, J., Zhao, Y., Renouf, M., Dierichs, K., & Behringer, R. (2017). Structure of hexapod 3D packings: Understanding the global stability from the local organization. In *EPJ Web of Conferences* (Vol. 140, p. 06021). EDP Sciences.
- 46. Jaeger, H. M., Nagel, S. R., & Behringer, R. P. (1996). Granular solids, liquids, and gases. *Reviews of Modern Physics*, 68, 1259–1273.
- 47. Radjai, F., Roux, J.-N., & Daouadji, A. (2017). Modeling granular materials: Century-long research across scales. *Journal of Engineering Mechanics*, *143*, 04017002.
- 48. Onoda, G. Y., & Liniger, E. G. (1990). Random loose packings of uniform spheres and the dilatancy onset. *Physical Review Letters*, *64*, 2727–2730.
- 49. Behringer, R. P., Chakraborty, B., Clark, A. H., Kondic, L., & Kramar, M. (2014). Statistical properties of granular materials near jamming. *Journal of Statistical Mechanics: Theory and Experiment, 2014*, P06004.
- 50. Hascoet, E., Herrmann, H. J., & Loreto, V. (1999). Shock propagation in a granular chain. *Physical Review E*, *59*, 3202–3206.

- 51. Daraio, C., Nesterenko, V. F., Herbold, E. B., & Jin, S. (2006). Energy trapping and shock disintegration in a composite granular medium. *Physical Review Letters*, *96*, 058002.
- 52. Porter, M. A., Kevrekidis, P. G., & Daraio, C. (2015). Granular crystals: Nonlinear dynamics meets materials engineering. *Physics Today*, 68(11), 44–50.
- 53. Brown, E., Rodenberg, N., Amend, J., Mozeika, A., Steltz, E., Zakin, M. R., ... & Lipson, H. (2010). Universal robotic gripper based on the jamming of granular material. Proceedings of the National Academy of Sciences, 107, 18809–18814.
- 54. Athanassiadis, A. G., Miskin, M. Z., Kaplan, P., Rodenberg, N., Lee, S. H., Merritt, J., ... & Jaeger, H. M. (2014). Particle shape effects on the stress response of granular packings. *Soft Matter*, *10*(1), 48–59.
- 55. Kraft, D. J., Ni, R., Smallenburg, F., Hermes, M., Yoon, K., Weitz, D. A., ... & Kegel, W. K. (2012). Surface roughness directed self-assembly of patchy particles into colloidal micelles. *Proceedings of the National Academy of Sciences*, 109, 10787-10792.
- 56. Nowak, E. R., Knight, J. B., Ben-Naim, E., Jaeger, H. M., & Nagel, S. R. (1998). Density fluctuations in vibrated granular materials. *Physical Review E*, *57*, 1971-1982.
- 57. Knight, J. B., Fandrich, C. G., Lau, C. N., Jaeger, H. M., & Nagel, S. R. (1995). Density relaxation in a vibrated granular material. *Physical Review E*, *51*, 3957-3963.
- 58. Richard, P., Nicodemi, M., Delannay, R., Ribiere, P., & Bideau, D. (2005). Slow relaxation and compaction of granular systems. *Nature Materials*, 4(2), 121-128.
- 59. Lim, M. X., Souslov, A., Vitelli, V., & Jaeger, H. M. (2019). Cluster formation by acoustic forces and active fluctuations in levitated granular matter. *Nature Physics*, 15(5), 460-464.
- 60. An, X. Z., Yang, R. Y., Dong, K. J., Zou, R. P., & Yu, A. B. (2005). Micromechanical simulation and analysis of one-dimensional vibratory sphere packing. *Physical Review Letters*, 95, 205502.
- 61. Philippe, P., & Bideau, D. (2003). Granular medium under vertical tapping: Change of compaction and convection dynamics around the liftoff threshold. *Physical Review Letters*, *91*(10), 104302.
- 62. Amirifar, R., Dong, K., Zeng, Q., & An, X. (2018). Self-assembly of granular spheres under one-dimensional vibration. *Soft Matter, 14*(45), 9856-9869.
- 63. Amirifar, R., Dong, K., Zeng, Q., & An, X. (2019). Bimodal self-assembly of granular spheres under vertical vibration. *Soft Matter, 15*(30), 5933-5944.

- 64. López-González, F., Herrera-González, A. M., & Donado, F. (2022). Study of the transition from amorphous to crystalline phase in a granular system under shearing and vibration. *Physica A: Statistical Mechanics and Its Applications*, 590, 126756.
- 65. Baker, J., & Kudrolli, A. (2010). Maximum and minimum stable random packings of platonic solids. *Physical Review E*, 82(6), 061304.
- 66. Götz, M., Fey, T., & Greil, P. (2012). Vibration assisted self-assembly processing of ceramic-based composites with modular meta-structure. *Journal of the American Ceramic Society*, 95(1), 95-101.
- 67. Lim, M. X., Murphy, K. A., & Jaeger, H. M. (2019). Edges control clustering in levitated granular matter. *Granular Matter*, *21*, 77.
- 68. Neudecker, M., Ulrich, S., Herminghaus, S., & Schröter, M. (2013). Jammed frictional tetrahedra are hyperstatic. *Physical Review Letters*, 111(2), 028001.
- 69. Asencio, K., Acevedo, M., Zuriguel, I., & Maza, D. (2017). Experimental study of ordering of hard cubes by shearing. *Physical Review Letters*, 119(22), 228002.
- 70. Ramaioli, M., Pournin, L., & Liebling, T. M. (2007). Vertical ordering of rods under vertical vibration. *Physical Review E*, 76(2), 021304.
- 71. Jaoshvili, A., Esakia, A., Porrati, M., & Chaikin, P. M. (2010). Experiments on the random packing of tetrahedral dice. *Physical Review Letters*, *104*(18), 185501.
- 72. Bahmani, A., Pro, J. W., Hannard, F., & Barthelat, F. (2022). Vibration-driven fabrication of dense architectured panels. *Matter*, *5*(3), 899-910.
- 73. Bahmani, A., Pro, J. W., & Barthelat, F. (2022). Vibration-induced assembly of topologically interlocked materials. *Applied Materials Today*, 29, 101601.
- 74. Behera, R. P., & Le Ferrand, H. (2021). Impact-resistant materials inspired by the mantis shrimp's dactyl club. *Matter, 4*(10), 2831-2849.
- 75. Bouville, F., Maire, E., Meille, S., Van de Moortèle, B., Stevenson, A. J., & Deville, S. (2014). Strong, tough and stiff bioinspired ceramics from brittle constituents. *Nature Materials*, *13*(5), 508-514.
- 76. Nelson, I., & Naleway, S. E. (2019). Intrinsic and extrinsic control of freeze casting. Journal of Materials Research and Technology, 8(3), 2372-2385.
- 77. Mirkhalaf, M., Dastjerdi, A. K., & Barthelat, F. (2014). Overcoming the brittleness of glass through bio-inspiration and micro-architecture. *Nature Communications*, *5*, 3166.

- 78. Amini, A., Khavari, A., Barthelat, F., & Ehrlicher, A. J. (2021). Centrifugation and index matching yield a strong and transparent bioinspired nacreous composite. *Science*, 373(6560), 1229-1234.
- 79. Mirkhalaf, M., Tanguay, J., & Barthelat, F. (2016). Carving 3D architectures within glass: Exploring new strategies to transform the mechanics and performance of materials. *Extreme Mechanics Letters*, 7, 104-113.
- 80. Boncheva, M., & Whitesides, G. M. (2005). Making things by self-assembly. *MRS Bulletin*, 30(10), 736-742.
- 81. Whitesides, G. M., & Grzybowski, B. (2002). Self-assembly at all scales. *Science*, 295(5564), 2418-2421.
- 82. Boncheva, M., Bruzewicz, D. A., & Whitesides, G. M. (2003). Millimeter-scale self-assembly and its applications. *Pure and Applied Chemistry*, 75(5), 621-630.
- 83. Whitesides, G. M., & Boncheva, M. (2002). Beyond molecules: Self-assembly of mesoscopic and macroscopic components. *Proceedings of the National Academy of Sciences*, 99(8), 4769-4774.
- 84. Brammer, L. (2004). Developments in inorganic crystal engineering. *Chemical Society Reviews*, 33(8), 476-489.
- 85. Rebek Jr, J. (2005). Simultaneous encapsulation: molecules held at close range. *Angewandte Chemie International Edition*, 44(14), 2068-2078.
- 86. Hartgerink, J. D., Beniash, E., & Stupp, S. I. (2001). Self-assembly and mineralization of peptide-amphiphile nanofibers. *Science*, *294*(5547), 1684-1688.
- 87. Hall, N. (Ed.). (2000). The new chemistry. Cambridge University Press.
- 88. Hollingsworth, M. D. (2002). Crystal engineering: from structure to function. *Science*, 295(5564), 2410-2413.
- 89. Cohn, M. B., Boehringer, K. F., Noworolski, J. M., Singh, A., Keller, C. G., Goldberg, K. A., & Howe, R. T. (1998, September). Microassembly technologies for MEMS. In *Microelectronic Structures and MEMS for Optical Processing IV* (Vol. 3513, pp. 2-17). International Society for Optics and Photonics.
- 90. Shet, S., Revero, R. D., Booty, M. R., Fiory, A. T., Lepselter, M. P., & Ravindra, N. M. (2006). Microassembly techniques: A review. *MATERIALS SCIENCE AND TECHNOLOGY-ASSOCIATION FOR IRON AND STEEL TECHNOLOGY-*, 1, 451.

- 91. Grzybowski, B. A., Jiang, X., Stone, H. A., & Whitesides, G. M. (2001). Dynamic, self-assembled aggregates of magnetized, millimeter-sized objects rotating at the liquid-air interface: Macroscopic, two-dimensional classical artificial atoms and molecules. *Physical Review E*, 64(1), 011603.
- 92. Bowden, N., Oliver, S. R., & Whitesides, G. M. (2000). Mesoscale self-assembly: capillary bonds and negative menisci. *The Journal of Physical Chemistry B*, 104(12), 2714-2724.
- 93. Israelachvili, J. N. (2011). *Intermolecular and surface forces*. Academic press.
- 94. Feddema, J. T., Xavier, P., & Brown, R. (1999). Micro-assembly planning with van der Waals force. In *Proceedings of the 1999 IEEE International Symposium on Assembly and Task Planning (ISATP'99)* (Cat. No. 99TH8470) (pp. 32-38). IEEE.
- 95. Feddema, J. T., Xavier, P., & Brown, R. (1998). Assembly planning at the micro scale (No. SAND-98-0896C; CONF-980537-). Sandia National Labs., Albuquerque, NM (United States).
- 96. Kooij, E. S., Brouwer, E. M., Wormeester, H., & Poelsema, B. (2002). Ionic strength mediated self-organization of gold nanocrystals: An AFM study. *Langmuir*, 18(20), 7677-7682.
- 97. Adams, M., Dogic, Z., Keller, S. L., & Fraden, S. (1998). Entropically driven microphase transitions in mixtures of colloidal rods and spheres. *Nature*, *393*(6683), 349.
- 98. Burns, M. M., Fournier, J. M., & Golovchenko, J. A. (1990). Optical matter: crystallization and binding in intense optical fields. *Science*, *249*(4970), 749-754.
- 99. Korda, P., Spalding, G. C., Dufresne, E. R., & Grier, D. G. (2002). Nanofabrication with holographic optical tweezers. *Review of Scientific Instruments*, 73(4), 1956-1957.
- 100. Lamoreaux, S. K. (1997). Demonstration of the Casimir force in the 0.6 to 6 μ m range. *Physical Review Letters*, 78(1), 5.
- 101. Wu, H., Thalladi, V. R., Whitesides, S., & Whitesides, G. M. (2002). Using hierarchical self-assembly to form three-dimensional lattices of spheres. *Journal of the American Chemical Society*, 124(48), 14495-14502.
- Khunsin, W., Amann, A., Kocher-Oberlehner, G., Romanov, S. G., Pullteap, S., Seat,
 H. C., ... & Sotomayor Torres, C. M. (2012). Noise-Assisted Crystallization of Opal Films.
 Advanced Functional Materials, 22(9), 1812-1821.

- Collino, R. R., Ray, T. R., Fleming, R. C., Sasaki, C. H., Haj-Hariri, H., & Begley,
 M. R. (2015). Acoustic field controlled patterning and assembly of anisotropic particles.
 Extreme Mechanics Letters, 5, 37-46.
- 104. Clark, T. D., Boncheva, M., German, J. M., Weck, M., & Whitesides, G. M. (2002). Design of three-dimensional, millimeter-scale models for molecular folding. *Journal of the American Chemical Society*, 124(1), 18-19.
- 105. Gracias, D. H., Kavthekar, V., Love, J. C., Paul, K. E., & Whitesides, G. M. (2002). Fabrication of Micrometer-Scale, Patterned Polyhedra by Self-Assembly. *Advanced Materials*, *14*(3), 235-238.
- 106. Jager, E. W., Smela, E., & Inganäs, O. (2000). Microfabricating conjugated polymer actuators. *Science*, 290(5496), 1540-1545.
- 107. Green, P. W., Syms, R. R. A., & Yeatman, E. M. (1995). Demonstration of three-dimensional microstructure self-assembly. *Journal of Microelectromechanical Systems*, *4*(4), 170-176.
- 108. Harsh, K. F., Bright, V. M., & Lee, Y. C. (1999). Solder self-assembly for three-dimensional microelectromechanical systems. *Sensors and Actuators A: Physical*, 77(3), 237-244.
- 109. Syms, R. R. A., Gormley, C., & Blackstone, S. (2000). Improving yield, accuracy and complexity in surface tension self-assembled MOEMS. *Sensors and Actuators*, 2839, 1-11.
- 110. Yeh, H. J., & Smith, J. S. (1994). Fluidic self-assembly for the integration of GaAs light-emitting diodes on Si substrates. *IEEE Photonics technology letters*, *6*(6), 706-708.
- 111. Cohn, M. B., Kim, C. J., & Pisano, A. P. (1991, June). Self-assembling electrical networks: An application of micromachining technology. In *TRANSDUCERS'91: 1991 International Conference on Solid-State Sensors and Actuators. Digest of Technical Papers* (pp. 490-493). IEEE.
- 112. Cohn, M. B., Boehringer, K. F., Noworolski, J. M., Singh, A., Keller, C. G., Goldberg, K. A., & Howe, R. T. (1998, September). Microassembly technologies for MEMS. In *Microelectronic Structures and MEMS for Optical Processing IV* (Vol. 3513, pp. 2-17). International Society for Optics and Photonics.

- 113. Majumder, U., & Reif, J. H. Design and Simulation of Novel Magnetic Tiles Capable of Complex Self-Assemblies.
- 114. Cohn, M. B. (1994). U.S. Patent No. 5,355,577. Washington, DC: U.S. Patent and Trademark Office.
- 115. Zheng, W., Buhlmann, P., & Jacobs, H. O. (2004). Sequential shape-and-solder-directed self-assembly of functional microsystems. *Proceedings of the National Academy of Sciences*, 101(35), 12814-12817.
- 116. Terfort, A., & Whitesides, G. M. (1998). Self-Assembly of an Operating Electrical Circuit Based on Shape Complementarity and the Hydrophobic Effect. *Advanced materials*, 10(6), 470-473.
- 117. Srinivasan, U., Liepmann, D., & Howe, R. T. (2001). Microstructure to substrate self-assembly using capillary forces. *Journal of Microelectromechanical Systems*, 10(1), 17-24.
- 118. Xiong, X., Hanein, Y., Wang, W., Schwartz, D. T., & Böhringer, K. F. (2001). Controlled part-to-substrate micro-assembly via electrochemical modulation of surface energy. In *Transducers' 01 Eurosensors XV* (pp. 1012-1014). Springer, Berlin, Heidelberg.
- 119. Grzybowski, B. A., Stone, H. A., & Whitesides, G. M. (2000). Dynamic self-assembly of magnetized, millimetre-sized objects rotating at a liquid–air interface. *Nature*, 405(6790), 1033.
- 120. Grzybowski, B. A., Winkleman, A., Wiles, J. A., Brumer, Y., & Whitesides, G. M. (2003). Electrostatic self-assembly of macroscopic crystals using contact electrification. *Nature materials*, *2*(4), 241.
- 121. Gouldstone, A., Van Vliet, K. J., & Suresh, S. (2001). Nanoindentation: Simulation of defect nucleation in a crystal. *Nature*, *411*(6838), 656.
- 122. Mallory, S. A., Valeriani, C., & Cacciuto, A. (2018). An active approach to colloidal self-assembly. *Annual review of physical chemistry*, 69, 59-79.
- 123. Pawar, A. B., & Kretzschmar, I. (2010). Fabrication, assembly, and application of patchy particles. *Macromolecular rapid communications*, 31(2), 150-168.
- 124. Wachs, A. (2019). Particle-scale computational approaches to model dry and saturated granular flows of non-Brownian, non-cohesive, and non-spherical rigid bodies. *Acta Mechanica*, 230(6), 1919-1980.

- 125. Wachs, A., Girolami, L., Vinay, G., & Ferrer, G. (2012). Grains3D, a flexible DEM approach for particles of arbitrary convex shape—Part I: Numerical model and validations. *Powder Technology*, 224, 374-389.
- 126. Rakotonirina, A. D., Delenne, J. Y., Radjai, F., & Wachs, A. (2019). Grains3D, a flexible DEM approach for particles of arbitrary convex shape—Part III: extension to non-convex particles modelled as glued convex particles. *Computational Particle Mechanics*, 6(1), 55-84.
- 127. Smeets, B., Odenthal, T., Vanmaercke, S., & Ramon, H. (2015). Polygon-based contact description for modeling arbitrary polyhedra in the Discrete Element Method. *Computer Methods in Applied Mechanics and Engineering*, 290, 277-289.
- 128. Shi, Z., Sun, J., Chen, S., & Jia, S. (2019). Investigation on the self-assembly of magnetic core-shell nanoparticles under soft-magnet element by using discrete element method. *Journal of Magnetism and Magnetic Materials*, 475, 152-159.
- 129. Chernysh, I. N., Everbach, C. E., Purohit, P. K., & Weisel, J. W. (2015). Molecular mechanisms of the effect of ultrasound on the fibrinolysis of clots. *Journal of Thrombosis and Haemostasis*, 13(4), 601-609.
- 130. Münster, S., Jawerth, L. M., Fabry, B., & Weitz, D. A. (2013). Structure and mechanics of fibrin clots formed under mechanical perturbation. *Journal of Thrombosis and Haemostasis*, 11(3), 557-560.
- 131. Dyskin, A. V., Estrin, Y., Kanel-Belov, A. J., & Pasternak, E. (2003). Topological interlocking of platonic solids: A way to new materials and structures. *Philosophical magazine letters*, 83(3), 197-203.
- 132. Cavelier, S., Mirmohammadi, S. A., & Barthelat, F. (2021). Titanium meshreinforced calcium sulfate for structural bone grafts. *J. Mech. Behav. Biomed. Mater.*, 118, 104461.
- Sugerman, G. P., Kakaletsis, S., Thakkar, P., Chokshi, A., Parekh, S. H., & Rausch,
 M. K. (2021). A whole blood thrombus mimic: constitutive behavior under simple shear.
 Journal of the Mechanical Behavior of Biomedical Materials, 115, 104216.
- 134. Sugerman, G. P., Parekh, S. H., & Rausch, M. K. (2020). Nonlinear, dissipative phenomena in whole blood clot mechanics. *Soft Matter, 16*(43), 9908-9916.

- 135. Malone, F., McCarthy, E., Delassus, P., Fahy, P., Kennedy, J., Fagan, A. J., & Morris, L. (2018). The mechanical characterisation of bovine embolus analogues under various loading conditions. *Cardiovascular Engineering and Technology*, 9, 489-502.
- Hun Yeon, J., Chan, K. Y., Wong, T. C., Chan, K., Sutherland, M. R., Ismagilov, R. F., ... & Kastrup, C. J. (2015). A biochemical network can control formation of a synthetic material by sensing numerous specific stimuli. *Scientific Reports*, *5*(1), 1-9.
- 137. Liu, S., Bao, G., Ma, Z., Kastrup, C. J., & Li, J. (2021). Fracture mechanics of blood clots: Measurements of toughness and critical length scales. *Extreme Mechanics Letters*, 48, 101444.
- 138. Araki, J., Jona, M., Eto, H., Aoi, N., Kato, H., Suga, H., ... & Yoshimura, K. (2012). Optimized preparation method of platelet-concentrated plasma and noncoagulating platelet-derived factor concentrates: maximization of platelet concentration and removal of fibrinogen. *Tissue Engineering Part C: Methods*, 18(3), 176-185.
- 139. Liu, S., Bahmani, A., Ghezelbash, F., & Li, J. (2024). Fibrin clot fracture under cyclic fatigue and variable rate loading. *Acta Biomaterialia*.
- 140. Park, H., Karajanagi, S., Wolak, K., Aanestad, J., Daheron, L., Kobler, J. B., ... & Zeitels, S. M. (2010). Three-dimensional hydrogel model using adipose-derived stem cells for vocal fold augmentation. *Tissue Engineering Part A*, 16(2), 535-543.
- 141. Hirsch, M., Charlet, A., & Amstad, E. (2021). 3D printing of strong and tough double network granular hydrogels. *Advanced Functional Materials*, *31*(5), 2005929.
- 142. Muir, V. G., Qazi, T. H., Shan, J., Groll, J., & Burdick, J. A. (2021). Influence of microgel fabrication technique on granular hydrogel properties. *ACS Biomaterials Science & Engineering*, 7(9), 4269-4281.
- 143. Huo, R., Bao, G., He, Z., Li, X., Ma, Z., Yang, Z., ... & Li, J. (2023). Tough transient ionic junctions printed with ionic microgels. *Advanced Functional Materials*, 33(20), 2213677.
- 144. Bao, G., Gao, Q., Cau, M., Ali-Mohamad, N., Strong, M., Jiang, S., ... & Li, J. (2022). Liquid-infused microstructured bioadhesives halt non-compressible hemorrhage. *Nature Communications*, *13*(1), 5035.
- 145. Longstaff, C. (2018). Measuring fibrinolysis: from research to routine diagnostic assays. *Journal of Thrombosis and Haemostasis*, 16(4), 652-662.

- 146. Amiral, J., Laroche, M., & Seghatchian, J. (2018). A new assay for global fibrinolysis capacity (GFC): Investigating a critical system regulating hemostasis and thrombosis and other extravascular functions. *Transfusion and Apheresis Science*, 57(1), 118-126.
- 147. Long, R., & Hui, C.-Y. (2016). Fracture toughness of hydrogels: Measurement and interpretation. *Soft Matter*, *12*, 8069–8086.
- 148. Nagahama, K., Kimura, Y., & Takemoto, A. (2018). Living functional hydrogels generated by bioorthogonal cross-linking reactions of azide-modified cells with alkynemodified polymers. *Nature Communications*, *9*, 2195.
- 149. Roychowdhury, S., Draeger, E. W., & Randles, A. (2023). Establishing metrics to quantify spatial similarity in spherical and red blood cell distributions. *Journal of Computational Science*, 71, 102060.
- 150. Illian, J., Penttinen, A., Stoyan, H., & Stoyan, D. (2008). Statistical analysis and modelling of spatial point patterns. John Wiley & Sons.
- 151. Bahmani, A., Nooraie, R. Y., Willett, T. L., & Montesano, J. (2023). A sequential mobile packing algorithm for micromechanical assessment of heterogeneous materials. *Composites Science and Technology*, 237, 110008.
- 152. André, D., Charles, J. L., Iordanoff, I., & Néauport, J. (2014). The GranOO workbench, a new tool for developing discrete element simulations, and its application to tribological problems. *Advances in Engineering Software*, 74, 40-48.
- 153. André, D., Charles, J. L., & Iordanoff, I. (2015). 3D Discrete Element Workbench for Highly Dynamic Thermo-mechanical Analysis: GranOO. John Wiley & Sons.
- 154. André, D., Girardot, J., & Hubert, C. (2019). A novel DEM approach for modeling brittle elastic media based on distinct lattice spring model. *Computer Methods in Applied Mechanics and Engineering*, 350, 100-122.
- 155. Bergen, G. V. D. (1999). A fast and robust GJK implementation for collision detection of convex objects. *Journal of graphics tools*, 4(2), 7-25.
- 156. Farkas, N., & Ramsier, R. D. (2006). Measurement of coefficient of restitution made easy. *Physics education*, 41(1), 73.
- 157. Barroso, J. J., Carneiro, M. V., & Macau, E. E. (2009). Bouncing ball problem: stability of the periodic modes. *Physical Review E*, 79(2), 026206.

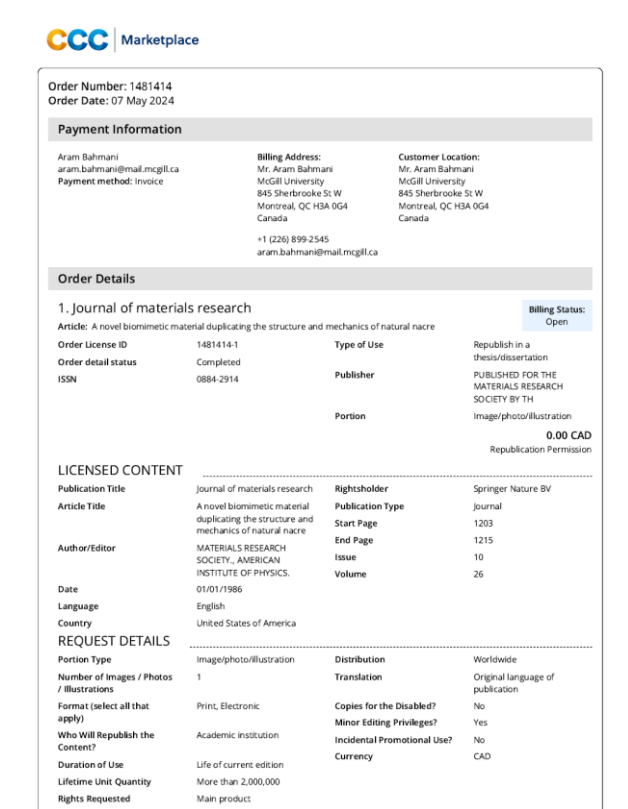
- 158. Jiang, Z. H., Liang, Z. J., Wu, A. C., & Zheng, R. H. (2018). Effect of collision duration on the chaotic dynamics of a ball bouncing on a vertically vibrating plate. *Physica A: Statistical Mechanics and its Applications*, 494, 380-388.
- 159. Leine, R. I., & Heimsch, T. F. (2012). Global uniform symptotic attractive stability of the non-autonomous bouncing ball system. *Physica D: Nonlinear Phenomena*, 241(22), 2029-2041.
- 160. Sun, Y., Myers, D. R., Nikolov, S. V., Oshinowo, O., Baek, J., Bowie, S. M., ... & Alexeev, A. (2021). Platelet heterogeneity enhances blood clot volumetric contraction: An example of asynchrono-mechanical amplification. *Biomaterials*, 274, 120828.
- 161. Ban, E., Wang, H., Franklin, J. M., Liphardt, J. T., Janmey, P. A., & Shenoy, V. B. (2019). Strong triaxial coupling and anomalous Poisson effect in collagen networks. *Proceedings of the National Academy of Sciences*, *116*(14), 6790-6799.
- 162. Dao, M., Lim, C. T., & Suresh, S. (2003). Mechanics of the human red blood cell deformed by optical tweezers. *Journal of the Mechanics and Physics of Solids*, 51(11-12), 2259-2280.
- 163. Weisel, J. W., & Litvinov, R. I. (2019). Red blood cells: the forgotten player in hemostasis and thrombosis. *Journal of Thrombosis and Haemostasis*, 17, 271-282.
- 164. Britton, S., Kim, O., Pancaldi, F., Xu, Z., Litvinov, R. I., Weisel, J. W., & Alber, M. (2019). Contribution of nascent cohesive fiber-fiber interactions to the non-linear elasticity of fibrin networks under tensile load. *Acta biomaterialia*, 94, 514-523.
- 165. Collet, J. P., Shuman, H., Ledger, R. E., Lee, S., & Weisel, J. W. (2005). The elasticity of an individual fibrin fiber in a clot. *Proceedings of the National Academy of Sciences*, 102(26), 9133-9137.
- 166. Saintyves, B., Spenko, M., & Jaeger, H. M. (2024). A self-organizing robotic aggregate using solid and liquid-like collective states. *Science Robotics*, 9(86), eadh4130.
- 167. Zimmermann, C. J., Schraeder, T., Reynolds, B., DeBoer, E. M., Neeves, K. B., & Marr, D. W. (2022). Delivery and actuation of aerosolized microbots. *Nano Select*, *3*(7), 1185-1191.
- 168. Wang, W., Giltinan, J., Zakharchenko, S., & Sitti, M. (2017). Dynamic and programmable self-assembly of micro-rafts at the air-water interface. *Science advances*, 3(5), e1602522.

- 169. Niu, R., Du, C. X., Esposito, E., Ng, J., Brenner, M. P., McEuen, P. L., & Cohen, I. (2019). Magnetic handshake materials as a scale-invariant platform for programmed self-assembly. *Proceedings of the National Academy of Sciences*, *116*(49), 24402-24407.
- 170. Miskin, M. Z., Cortese, A. J., Dorsey, K., Esposito, E. P., Reynolds, M. F., Liu, Q., ... & Cohen, I. (2020). Electronically integrated, mass-manufactured, microscopic robots. *Nature*, *584*(7822), 557-561.
- 171. Gardi, G., Ceron, S., Wang, W., Petersen, K., & Sitti, M. (2022). Microrobot collectives with reconfigurable morphologies, behaviors, and functions. *Nature communications*, *13*(1), 2239.
- 172. Lim, M. X., & Jaeger, H. M. (2023). Acoustically levitated lock and key grains. *Physical Review Research*, *5*(1), 013116.
- 173. Wagner, C., Steffen, P., & Svetina, S. (2013). Aggregation of red blood cells: from rouleaux to clot formation. *Comptes Rendus. Physique*, *14*(6), 459-469.
- 174. Swanepoel, A. C., Emmerson, O., & Pretorius, E. (2017). Effect of progesterone and synthetic progestins on whole blood clot formation and erythrocyte structure. *Microscopy and Microanalysis*, 23(3), 607-617.
- 175. Pivkin, I. V., Richardson, P. D., & Karniadakis, G. (2006). Blood flow velocity effects and role of activation delay time on growth and form of platelet thrombi. *Proceedings of the National Academy of Sciences*, 103(46), 17164-17169.
- 176. Safar, M. E. (2018). Arterial stiffness as a risk factor for clinical hypertension. *Nature Reviews Cardiology*, 15(2), 97-105.
- 177. Colace, T. V., Muthard, R. W., & Diamond, S. L. (2012). Thrombus growth and embolism on tissue factor-bearing collagen surfaces under flow: role of thrombin with and without fibrin. *Arteriosclerosis, thrombosis, and vascular biology*, 32(6), 1466-1476.
- 178. Eberhardt, R. T., & Raffetto, J. D. (2014). Chronic venous insufficiency. *Circulation*, 130(4), 333-346.
- 179. Tansey, E. A., Montgomery, L. E., Quinn, J. G., Roe, S. M., & Johnson, C. D. (2019). Understanding basic vein physiology and venous blood pressure through simple physical assessments. *Advances in physiology education*.
- 180. https://3dprintingindustry.com/news/mimix-biotherapeutics-launches-its-cymatix-acoustic-3d-bioprinter-181312/

Copyright and Licence Permissions

Please note that reused or reproduced figures which I myself, Aram Bahmani, was the author of the paper or those from open-access journals and publishers, including AAAS (Science), the Proceedings of the National Academy of Sciences of the United States of America (PNAS), and Nature, among others, did not require a license or copyright documentation for reuse or reproduction in my PhD dissertation. The figure license or copyright documentation reproduced or reused in this dissertation are listed below:

Figure 1.1A



NEW WORK DETAILS				
Title	PhD Candidate	Institution Name	McGill Univers	ity
Instructor Name	Francois Barthelat, Jianyu Li	Expected Presentation Date	2024-12-15	
ADDITIONAL DETAIL:	S			
The Requesting Person / Organization to Appear on the License	Aram Bahmani			
REQUESTED CONTEN	NT DETAILS			
Title, Description or Numeric Reference of the Portion(s)	Figure 1	Title of the Article / Chapter the Portion Is From	A novel biomin duplicating the mechanics of	e structure
Editor of Portion(s)	Barthelat, Francois; Zhu, Deju	Author of Portion(s)	Barthelat, Fra Deju	ncois; Zhu,
Volume / Edition	26	Publication Date of Portion	2011-05-28	
Page or Page Range of	1203-1215			
Total Items: 1		o	Subtotal: order Total:	0.00
			raci rotai.	0.00
of Works pursuant to the Licenses		h any applicable Publisher Terms ar Center, Inc. ("CCC") on behalf of the		
	granted by Copyright Clearance	Center, Inc. ("CCC") on behalf of the		
Works through CCC's applicable M	granted by Copyright Clearance arketplace transactional licensing	Center, Inc. ("CCC") on behalf of the services (each, a "Service").		
Works through CCC's applicable M 1) Definitions. For purposes of the	granted by Copyright Clearance larketplace transactional licensing ese General Terms, the following	Center, Inc. ("CCC") on behalf of the services (each, a "Service").	applicable Rights	holders of
Works through CCC's applicable M 1) Definitions. For purposes of th "Dicense" is the licensed use the Usenfirmation. "Order Confirmation" is the con Confirmation Terms" are addition.	symmeted by Copyright Clearance- larketplace transactional licensing ese General Terms, the following ser obtains via the Marketplace p firmation CCC provides to the al term's set forth on specific Ordi	Center, Inc. ("CCC") on behalf of the services (each, a "Service"). definitions apply:	applicable Rights saction, as set for vlarketplace trans te General Terms to	th in the G
Works through CCCs applicable M 1) Definitions. For purposes of th "License" is the licensed use the U- Confirmation. "Order Confirmation" is the con Confirmation Terms" are addition- terms applicable to a particular CC	is granted by Copyright Clearance, and explace transactional licensing ese General Terms, the following ser obtains via the Marketplace p firmation CCC provides to the al terms see forth on specific Ordi- Cransactional Resning service, of copyright rights in the Works for	Center, inc. ("CCC") on behalf of the services (each, a "Service"). definitions apply: latform in a particular licensing tran User at the conclusion of each !! er Confirmations not set forth in the er Confirmations not set forth in the er Confirmations not set forth in the set of the set o	applicable Rights saction, as set for warketplace trans to General Terms to	nth in the G saction. "G hat can in
Works through CCCs applicable M 1) Definitions. For purposes of th "License" is the licensed use the U- Confirmation. "Order Confirmation" is the con Confirmation Terms" are addition. The confirmation of th	granted by Copyright Clearance, larketplace transactional licensing ese General Terms, the following ser obtains via the Marketplace p firmation CCC provides to the lat terms set forth on specific Critic Ctransactional licensing service - it oppyright rights in the Works for infirmations.	Center, Inc. ("CCC") on behalf of the services (each, a "Service"). definitions apply: datform in a particular licensing tran User at the conclusion of each ! er Confirmations not set forth in the and/or any Rightsholder-specific ter	applicable Rights saction, as set for Warketplace trans trans. the Marketplace	holders of rith in the o saction. "(that can in platform, v
Works through CCCs applicable M 1) Definitions. For purposes of th "Uceras" is the licensed use the Uconfilmation. "Order Confirmation" is the con Confirmation Terms" are addition: terms applicable to a particular Coff "Rightsholder(s)" are the holders of are displayed on specific Order Co "Terms" means the terms and con "User" or "you" is the person or et "User" or "you" is the person or et	is granted by Copyright Clearance and explace transcribed in the control licensing seer obtains via the Marketplace p filmation CCC provides to the all terms set forth on specific Ordi- ce Transactional Terming service. Copyright rights in the Works To infirmations. didions set forth in these General multip making the use granted un- corbet right part who the User	Center, inc. ("CCC") on behalf of the services (each, a "Service"). definitions apply: latform in a particular licensing tran User at the conclusion of each ! for Confirmations not set forth in the article and set of the transfer and set in the set of the transfer and set of the transfer and set of the set of set of set set of set set of set set set set set set set set	applicable Rights saction, as set for Marketplace trans e General Terms t ms. the Marketplace infirmation Terms	holders of rth in the o saction. "(" that can in platform, v collectivel g the Tern
Works through CCS applicable M (1) Definitions. For purposes of th "Liversea" is the licensed use the U- Confirmation: "Order Confirmation" is the con- Confirmation are addition terms applicable to a particular CO "Rightsuboldersty," are the holders are are displayed on specific Order Co "Terms" means the terms and con "User" or you's is the person or en "User" or you's is the person or en	is granted by Copyright Clearance and an advertised to the control licensing sees General Terms, the following seer obtains via the Marketplace per firmation CCC provides to the alterns see forth on specific Order Currancational Seering service of copyright rights in the Works for informations. Or the control will be controlled to the control of the	Center, inc. ("CCC") on behalf of the services (each, a "Service"). definitions apply: latform in a particular licensing tran User at the conclusion of each ! er Confirmations not set forth in the and/er any lightsholder-specific ter er which a User obtains licenses via Terms and any additional Order Co let the relevant License. Where the autherized to accept the General !	applicable Rights saction, as set for Marketplace trans e General Terms t ms. the Marketplace infirmation Terms	holders of rth in the G saction. "G that can in- platform, v collectivel g the Term
Works through CCS applicable M (1) Definitions, For purposes of the "Liversea" is the licensed use the te Confirmation. "Order Confirmation" is the con- Confirmation are addition, terms applicable to a particular Co- "Rightsholderisy," are the holders or en diplayed on specific Order Co "Terms" means the terms and con- tierms on specific Order Co "Terms" means the terms and con- behalf of a User is a freelancer or person shall be deemed jointly at Vorkis)" are the copyright protect (2) Description of Service, CCS:	is granted by Copyright Clearance and steeplace transcriptional licensing seer obtains via the Marketplace p filmation CCC provides to the all terms set forth on specific Ordi- cal terms set forth on specific Ordi- cal terms set forth on specific Ordi- cal Copyright rights in the Works for filmations. dictions set forth in these General multip making the use granted un- corber third party who the User set for purposes of such Terms. Marketplace enables Users to on Marketplace enab	Center, inc. ("CCC") on behalf of the services (each, a "Service"). definitions apply: latform in a particular licensing tran User at the conclusion of each ! er Confirmations not set forth in the and/er any lightsholder-specific ter er which a User obtains licenses via Terms and any additional Order Co let the relevant License. Where the autherized to accept the General !	applicable Rights saction, as set for Marketplace trans to the Marketplace in firmation Terms person accepting ferms on the Use we Works in acco	holders of rth in the C saction. "C that can in platform, v collectivel g the Term r's behalf,
Works through CCS applicable M (1) Definitions. For purposes of th "Tuctersa" is the licensed use the U Confirmation. "Order Confirmation" is the con- Confirmation and the confirmation is the con- Confirmation Terms applicable to a particular CO "Rightsaholdersty," are the holders are displayed on specific Order Co "Terms" means the terms and con- "User" or "you" is the person or en- "User" or "you" is the person or en- "Viser" or "Viser"	ig anted by Copyright Clearance and an advantage of the Copyright of the C	Center, inc. ("CCC") on behalf of the services (each, a "Service"). definitions apply: latform in a particular licensing tran User at the conclusion of each ! er Confirmations not set forth in the another any high-inder specific ter er which a User obtains licenses via Terms and any additional Order Co fer the relevant License. Where the authorized to accept the General 1 refer Confirmations.	applicable Rights saction, as set for darketplace trans General Terms time. The Marketplace trans time. The Marketplace infirmation Terms person accepting person accepting errors on the Use Works in according to the Marketplace in the event Order time. In the event are Rightsholders sinse, in the event are Rightsholders	nth in the of saction. "On that can in platform, of collectivel g the Tern r's behalf, rdance with Confirmatic confarmatic confarmatic confarmatic confarmatic confarmatic confarmatic
Works through CCCs applicable M 1) Definitions. For purposes of th 1) Definitions. For purposes of th 1) Definitions. For purposes of th 1) Confirmation: 1"Cortex* of the Identification 1"Cortex* of the Identification 1"Cortex* of Confirmation I the 1"Ghishabletos a particular Cortex* of 1"Ghishabletos", are the holders are digitallyed on specific Order Co 1"Grams" means the terms and con 1"Dest" of "you" is the person or en 1"Dest" or "you" is the person or en 1"Dest" or "you" is the 1"Dest" or "you"	ig annet by Copyright Clearance and an advantage of the Copyright of the C	Center, inc. ("CCC") on behalf of the services (each, a "service"). definitions apply: latform in a particular licensing tran User at the conclusion of each ! er Confirmations not set forth in the and/or any lightshode-spedic fer er which a User obtains licenses via Terms and any additional Order Co fer the relevant. License. Where the authorized to accept the General 1 refer Confirmations. busin Licenses to use one or mor pyright rightsholder identified in th n connection with the relevant. Lice shall govern. User acknowledges it also govern. User acknowledges it hall govern. User acknowledges it and so were acknowledges it an	applicable Rights saction, as set for saction,	rth in the C saction. "C hat can in platform, v collectivel g the Tern r's behalf, rdance wit confirmati c of any co have com ht to super

Figure 1.1B

May 06, 2024

This Agreement between McGill University -- Aram Bahmani ("You") and Elsevier ("Elsevier") consists of your license details and the terms and conditions provided by Elsevier and Copyright Clearance Center.

License Number 5783400766609 License date May 06, 2024 Licensed Content Publisher Elsevier Licensed Content Publication Archives of Oral Biology Mechanical properties of human dental enamel Licensed Content Title on the nanometre scale S Habelitz, S.J Marshall, G.W Marshall, M Licensed Content Author Balooch Licensed Content Date Feb 1, 2001 Licensed Content Volume 46 Licensed Content Issue 2 Licensed Content Pages 11 Start Page 173

183

Figure 1.1D

End Page

May 06, 2024

This Agreement between McGill University -- Aram Bahmani ("You") and Elsevier ("Elsevier") consists of your license details and the terms and conditions provided by Elsevier and Copyright Clearance Center.

License Number 5783350731887

License date May 06, 2024

Licensed Content Publisher Elsevier

Licensed Content Publication Journal of the Mechanics and Physics of Solids

Dynamic mechanical behaviour of suture interfaces

Licensed Content Title as inspiration for architectured hierarchical

interlocking composites

Licensed Content Author B. Alheit, S. Bargmann, B.D. Reddy

Licensed Content Date Dec 1, 2021

Licensed Content Volume 157

Licensed Content Issue n/a

Licensed Content Pages 1

Start Page 104620

End Page 0

Figure 1.2

May 06, 2024

This Agreement between McGill University -- Aram Bahmani ("You") and Elsevier ("Elsevier") consists of your license details and the terms and conditions provided by Elsevier and Copyright Clearance Center.

License Number	5783411088651
License date	May 06, 2024
Licensed Content Publisher	Elsevier
Licensed Content Publication	Acta Biomaterialia
Licensed Content Title	Tough and deformable glasses with bioinspired cross-ply architectures
Licensed Content Author	Zhen Yin,Ahmad Dastjerdi,Francois Barthelat
Licensed Content Date	Jul 15, 2018
Licensed Content Volume	75
Licensed Content Issue	n/a
Licensed Content Pages	12
Start Page	439

450

Figure 1.5A

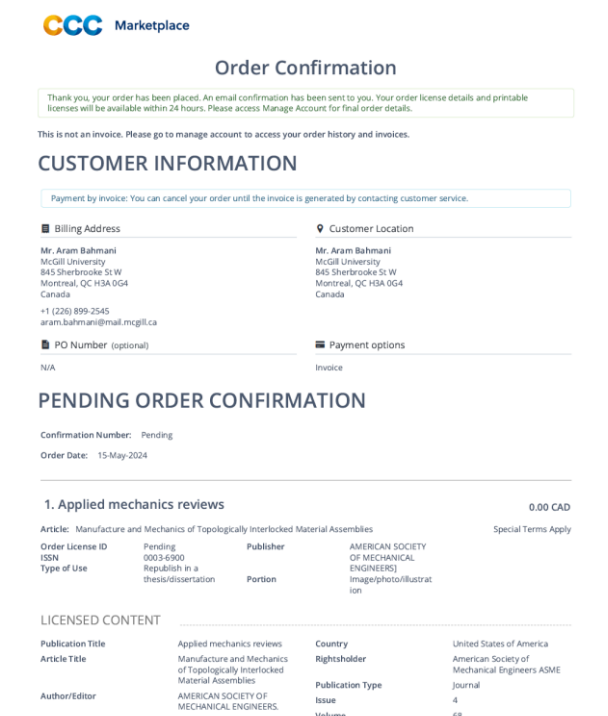
End Page

May 07, 2024

This Agreement between McGill University -- Aram Bahmani ("You") and Elsevier ("Elsevier") consists of your license details and the terms and conditions provided by Elsevier and Copyright Clearance Center.

License Number 5783421433275 License date May 07, 2024 Licensed Content Publisher Elsevier Licensed Content Publication International Journal of Solids and Structures Toughness by segmentation: Fabrication, testing and Licensed Content Title micromechanics of architectured ceramic panels for impact applications Mohammad Mirkhalaf, Amanul Sunesara, Behnam Licensed Content Author Ashrafi, François Barthelat Licensed Content Date Feb 1, 2019 Licensed Content Volume 158 Licensed Content Issue n/a Licensed Content Pages 14 Start Page 52

Figure 1.5B-G



Portion Type	Image/photo/illustration	Distribution	Worldwide
Number of Images / Photos / Illustrations	4	Translation	Original language of publication
Format (select all that apply)	Print, Electronic	Copies for the Disabled?	No
Who Will Republish the	Academic institution	Minor Editing Privileges?	Yes
Content?		Incidental Promotional Use?	No
Duration of Use	Life of current edition	Currency	CAD
Lifetime Unit Quantity Rights Requested	Up to 2,000,000 Main product		
NEW WORK DETAILS			
Title	PhD candidate	Institution Name	McGill University
Instructor Name	Francois Barthelat, Jianyu Li	Expected Presentation Date	2024-12-15
ADDITIONAL DETAIL:	S		
Order Reference Number	N/A	The Requesting Person / Organization to Appear on	Aram Bahmani
		the License	
REQUESTED CONTEN	NT DETAILS		
Title, Description or Numeric	NT DETAILS Figures 6, 10, 12, 14		Manufacture and Mechanics of Topologically Interlocked
Title, Description or Numeric Reference of the Portion(s)	Figures 6, 10, 12, 14 Siegmund, Thomas; Barthelat, Francols; Cipra, Raymond;	the License Title of the Article / Chapter	of Topologically Interlocked Material Assemblies Siegmund, Thomas; Bartheli
Title, Description or Numeric Reference of the Portion(s) Editor of Portion(s)	Figures 6, 10, 12, 14 Siegmund, Thomas; Barthelat,	Title of the Article / Chapter the Portion Is From	of Topologically Interlocked Material Assemblies
REQUESTED CONTENT Title, Description or Numeric Reference of the Portion(s) Editor of Portion(s) Volume / Edition Page or Page Range of Portion	Figures 6, 10, 12, 14 Siegmund, Thomas; Barthelat, Francois; Cipra, Raymond; Habtour, Ed; Riddick, Jaret	Title of the Article / Chapter the Portion Is From	of Topologically Interlocked Material Assemblies Siegmund, Thomas; Bartheli Francois; Cipra, Raymond;
Title, Description or Numeric Reference of the Portion(s) Editor of Portion(s) Volume / Edition Page or Page Range of	Figures 6, 10, 12, 14 Siegmund, Thomas; Barthelat, Francois; Cipra, Raymond; Habtour, Ed; Riddick, Jaret 68	the License Title of the Article / Chapter the Portion is From Author of Portion(s) Issue, if Republishing an	of Topologically Interlocked Material Assemblies Siegmund, Thomas; Barthel Francois; Cipra, Raymond; Habtour, Ed; Riddick, Jaret
Title, Description or Numeric Reference of the Portion(s) Editor of Portion(s) Volume / Edition Page or Page Range of Portion	Figures 6, 10, 12, 14 Siegmund, Thomas; Barthelat, Francois; Cipra, Raymond; Habtour, Ed; Riddick, Jaret 68	the License Title of the Article / Chapter the Portion Is From Author of Portion(s) Issue, if Republishing an Article From a Serial Publication Date of Portion	of Topologically Interlocked Material Assemblies Siegmund, Thomas; Barthel, Francois; Cipra, Raymond; Habtour, Ed; Riddick, Jaret 4
Title, Description or Numeric Reference of the Portion(s) Editor of Portion(s) Volume / Edition Page or Page Range of Portion SPECIAL RIGHTSHOL Permission is granted for the sp	Figures 6, 10, 12, 14 Siegmund, Thomas; Barthelat, Francist; Opra, Raymond; Habbour, Ed; Riddick, Jaret 68 4 DER TERMS AND COND beelfic use of the ASME Figures 6, 10, 174daton. As Is outloang; we require size.	Title of the Article / Chapter the Portion is From Author of Portion(s) Issue, if Republishing an Article From a Serial Publication Date of Portion ITONS 2,14 ONLY as stated herein and do	of Topologically Interlocked Material Assemblies Siegmund, Thomas; Barthel, Francois; Cipra, Raymond: Habtour, Ed. Riddick, Jaret 4 2016-07-14 es not permit further use of the

Figure 1.9

SPRINGER NATURE LICENSE TERMS AND CONDITIONS

May 09, 2024

This Agreement between McGill University -- Aram Bahmani ("You") and Springer Nature ("Springer Nature") consists of your license details and the terms and conditions provided by Springer Nature and Copyright Clearance Center.

License Number 5784870429042 License date May 09, 2024 Licensed Content Publisher Springer Nature Licensed Content Publication Computational Particle Mechanics

Grains3D, a flexible DEM approach for particles of arbitrary convex shape—Part III: extension to non-convex particles modelled as glued convex particles Licensed Content Title

Licensed Content Author Andriarimina Daniel Rakotonirina et al

Licensed Content Date Jun 23, 2018

Type of Use Thesis/Dissertation

Requestor type academic/university or research institute

print and electronic

figures/tables/illustrations

Number of figures/tables/illustrations

Will you be translating?

Circulation/distribution 50000 or greater

Author of this Springer Nature no

Title of new work PhD candidate

McGill University Institution name

Expected presentation date

McGill University 845 Sherbrooke St W

Requestor Location

Montreal, QC H3A 0G4 Canada Attn: McGill University

Terms and Conditions

Springer Nature Customer Service Centre GmbH Terms and Conditions

The following terms and conditions ("Terms and Conditions") logether with the terms specified in your [Rights, link] constitute the License ("License") between you as Licenses and Springer Nature Customer Service Centre GmbH as Licenson By clicking 'accept' and completing the transaction for your use of the material ("Licensed Material"), your confirm your acceptance of and obligation to be bound by these Terms and Conditions.

1. Grant and Scope of License

1. 1. The Licensor grants you a personal, non-exclusive, non-transferable, non-sublicensable, revocable, world-wide License to reproduce, distribute, communicate to the public, make available, broadcast, electronically transmit or create derivative works using the Licensed Material for the purpose(s) specified in your Rights.link Licence Details only. Licenses are granted for the specific use requested in the order

Figure 1.12

SPRINGER NATURE LICENSE TERMS AND CONDITIONS

May 11, 2024

This Agreement between McGill University -- Aram Bahmani ("You") and Springer Nature ("Springer Nature") consists of your license details and the terms and conditions provided by Springer Nature and Copyright Clearance Center.

License Number 5786010351701

May 11, 2024 License date

Springer Nature Licensed Content Publisher

Licensed Content Publication Nature Reviews Chemistry

Haemostatic materials for wound healing Licensed Content Title

applications

Licensed Content Author Baolin Guo et al

Licensed Content Date Sep 17, 2021

Type of Use Thesis/Dissertation

Requestor type academic/university or research institute

Format print and electronic

Portion figures/tables/illustrations

Number of figures/tables/illustrations

Would you like a high resolution image with

Will you be translating?

Circulation/distribution 50000 or greater

no

Author of this Springer Nature content

Title of new work PhD candidate

McGill University Institution name

Expected presentation date Dec 2024

Portions Figure in Box 1

McGill University 845 Sherbrooke St W

Requestor Location

Montreal, QC H3A 0G4 Canada Attn: McGill University

0.00 CAD Total

Terms and Conditions

Springer Nature Customer Service Centre GmbH Terms and Conditions

The following terms and conditions ("Terms and Conditions") together with the terms specified in your [RightsLink] constitute the License ("License") between you as Licensee and Springer Nature Customer Service Centre GmbH as Licensor. By clicking 'accept' and completing the transaction for your use of the material ("Licensed Material"), you confirm your acceptance of and obligation to be bound by these Terms and Conditions.

1. Grant and Scope of License

1. 1. The Licensor grants you a personal, non-exclusive, non-transferable, non-sublicensable, revocable, world-wide License to reproduce, distribute, communicate